

**Growth, Characterization and Applications of Variable  
Oxygen Deficient Oxide Hetero–nanostructures  
(Au–ZnO and Au–GeO<sub>2</sub>)**

*By*

**Arnab Ghosh**

**(PHYS07201004002)**

**INSTITUTE OF PHYSICS, BHUBANESWAR**

*A thesis submitted to the*

*Board of studies in Physical Sciences*

*In partial fulfillment of the requirements*

*For the Degree of*

**DOCTOR OF PHILOSOPHY**

*of*

**HOMI BHABHA NATIONAL INSTITUTE**



**March, 2016**

# HOMI BHABHA NATIONAL INSTITUTE

## Recommendations of the Viva Voce Board

As members of the Viva Voce Board, we certify that we have read the dissertation prepared by Mr. Arnab Ghosh entitled “**Growth, Characterization and Applications of Variable Oxygen Deficient Oxide Hetero-nanostructures (Au-ZnO and Au-GeO<sub>2</sub>)**” and recommend that it may be accepted as fulfilling the dissertation requirement for the Degree of Doctor of Philosophy.

\_\_\_\_\_ *S. Varma* Date: 22/3/16

**Chairperson – Prof. S. Varma**

\_\_\_\_\_ *P. V. Satyam* Date: 22/3/16

**Guide / Convener – Prof. P. V. Satyam**

\_\_\_\_\_ *P. V. Satyam* Date: 22/3/16

**Member1 (Thesis examiner) – Prof. Dipak Kumar Goswami**

\_\_\_\_\_ *D. K. Goswami* Date: 22/3/16

**Member2 – Prof. S. K. Patra**

\_\_\_\_\_ *G. Tripathy* Date: 22/3/16

**Member3 – Prof. G. Tripathy**

Final approval and acceptance of this dissertation is contingent upon the candidate's submission of the final copies of the dissertation to HBNI.

I hereby certify that I have read this dissertation prepared under my direction and recommend that it may be accepted as fulfilling the dissertation requirement.

Date: 22/3/16

Place: Bhubaneswar

*P. V. Satyam*  
डॉ. पी.वी. सत्यम / Dr. P.V. Satyam  
प्रोफेसर / Professor  
भौतिकी संस्थान / Institute of Physics  
भुवनेश्वर / Bhubaneswar

## Statement by author

This dissertation has been submitted in partial fulfillment of requirements for an advanced degree at Homi Bhabha National Institute (HBNI) and is deposited in the Library to be made available to borrowers under rules of the HBNI. Brief quotations from this dissertation are allowable without special permission, provided that accurate acknowledgement of source is made. Requests for permission for extended quotation from or reproduction of this manuscript in whole or in part may be granted by the Competent Authority of HBNI when in his or her judgment the proposed use of the material is in the interests of scholarship. In all other instances, however, permission must be obtained from the author.

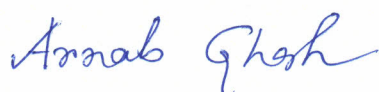


---

Arnab Ghosh  
Institute of Physics  
Bhubaneswar

## Declaration

I, Arnab Ghosh, hereby declare that the investigation presented in the thesis has been carried out by me. The work is original and has not been submitted earlier as a whole or in part for a degree / diploma at this or any other University / Institution.



---

Arnab Ghosh  
Institute of Physics  
Bhubaneswar



## Certificate

This is to certify that the thesis entitled “**Growth, Characterization and Applications of Variable Oxygen Deficient Oxide Hetero-nanostructures (Au-ZnO and Au-GeO<sub>2</sub>)**”, which is being submitted by **Mr. Arnab Ghosh** in partial fulfillment of the degree of **Doctor of Philosophy in Physics** of **Homi Bhabha National Institute** is a record of his own research work carried out by him. He has carried out his investigations for the last five years on the subject matter of the thesis under my supervision at **Institute of Physics, Bhubaneswar**. To the best of our knowledge, the matter embodied in the thesis has not been submitted for the award of any other degree.



**Signature of the candidate:**

Arnab Ghosh

Institute of Physics

Bhubaneswar



**Signature of the supervisor:**

Prof. P. V. Satyam

Professor

Institute of Physics

Bhubaneswar

**Date:** 22/03/2016

## Acknowledgments

I could not able to finish my thesis without the proper guidance of my committee members, ample help from group members and support from my family. Now, I want to show my sincere gratitude to those who have helped me finishing this thesis work in different regards.

First and foremost, I would like to show my heartfelt gratitude to my thesis supervisor Prof. P. V. Satyam for giving me the opportunity to work in his group and for his constant encouragement towards my research focus. In his group, I have enjoyed the freedom that he has given to me to do research work according to my area of interest. It is my proud privilege to show my appreciation and obligation to him for his continuous support both academically and socially whenever I needed, as well as for giving me enthusiastic motivation behind this thesis work. I must thank him for providing a well equipped electron microscopy laboratory and also for arranging several necessary experiments for this thesis work through his contacts and collaborations. I have learnt various skills (technical, writing and communication) from him which I needed to develop not only for this thesis work but also for my ensuing future. He is very soft, sensible and broad minded person I have ever come across. I truly consider myself fortunate being a PhD scholar under his guidance. I eternally thank him and his family for their affection and hospitality, during this 5 years stay at IOP, which will be unforgettable for my entire life time.

I would like to thank Dr. Bikash Kumar Jena (Scientist at IMMT, BBSR) for allowing me doing all electrochemical measurements in his laboratory. He always considers me like his own student and has given several fruitful suggestions throughout. I also would like to thank his group members (Mr. Aneeya K. Samantara and Dr. Subas C. Sahu) for their help in carrying out measurements according to my availability.

I extend my great depth of gratitude and indebtedness to Dr. Pawan Kumar Tyagi (Assistant Professor at DTU) for his contribution to setup chemical vapor deposition (CVD) system at IOP as our group facility. He has been known to me since my Masters days at IIT Bombay,

that time he was finishing his PhD. Even though he is quite senior to me still he is like my good friend. He has given me invaluable suggestions and supported me continuously for this thesis work. I have used his lab facility (MFC) for more than 2 years, till we have procured in our Lab, to grow various nanostructures using CVD.

It is my great pleasure to thank Prof. Samit K. Ray (IIT KGP) for allowing me doing all photoluminescence (PL) and photodetection measurements in his Lab. I must thank his group members especially Mr. Rajshekhar Bar and Mr. S. Mukherjee for their enormous patience and labor in doing all PL, photodetection and for some important XRD measurements.

I would like to thank Prof. T. Som (IOP, SUNAG Lab) and his group members (especially Mr. Mohit Kumar) for allowing and helping in doing various experiments (like UV-Vis, Field emission, AFM etc.) for several times. I would like to thank Prof. T. Chini and Dr. P. Das from SINP, Kolkata for their help in carrying out cathodoluminescence (CL) experiments on the Au-ZnO samples. I wish to thank Prof. S. Varma (IOP) for allowing me to do XPS in here Lab. I would like to thank Dr. R. Sathyavathi and Prof. D. N. Rao and his group at University of Hyderabad and Ajit Dash (IMMT, BBSR) for their support and help to perform various SERS experiments. I also would like to acknowledge Mr. Tapan for XPS measurements. I would like to thank Department of Science and Technology and SINP, India for facilitating the experiments at the Indian Beamline, Photon Factory, KEK, Japan.

My thesis committee members guided me through all these years. Thanks to Prof. Shikha Varma, Prof. Goutam Tripathy and Prof. Suresh Kumar Patra for their continuous cooperation, support and timely suggestions at every stage of my thesis work.

I am very much thankful to all the Directors, IOPB for their every support and kindness during my whole stay at IOPB. I would like to thank our group postdocs Dr. Rajib Biswal, Dr. Bipul Rakshit and Dr. T. Arun for their valuable discussions as well as in other aspects.

It was a great pleasure for me to spend last four years working in the electron microscopy group at IOP. I would like to acknowledge the individual help and support from our HR-TEM and FE-SEM group members. I express my earnest thanks to all my colleagues for creating the nice academic atmosphere, Dr. Ashutosh Rath, Dr. Jatis K. Dash, Dr. Raghavendra R. Juluri, Mr. Puspendu Guha, Mr. Anjan Bhukta and Miss Paramita Maity. Everyone has helped me one way or the other. It is my innermost urge to thank Ashutosh da and Raghav da for being the tireless supporters since the days I have started journey in research, for their

patience to teach an inexperienced graduate student from the scratch of electron microscopy. They gave me the moral support and initial ideas I needed to move on. A special thanks to my junior cum lab mate Mr Puspendu Guha, who has helped me in every regards throughout my thesis work, starting from experiments, writing papers all the way to writing thesis. Without enormous cooperation from Puspendu, thesis could have been delayed. I wish all my lab juniors (Puspendu and Paramita) the good luck for the remaining parts of their PhD works.

I also would like to thank all my teachers who taught me in the pre-doctoral course work and all the experimental condensed matter group faculties at IOP, for their generous support.

I have enjoyed the company of all my colleagues (seniors, juniors and batch mates) and many more; I would like to thank them for all their help in making my stay a pleasant experience here at IOPB. Multiple cheers go to all scholars (starting from 2010 Predoc batch to 2015 batch) in the IOP campus. I feel so lucky to be a part of such a beautiful fraternity.

Without friends, life would be dreary. I am greatly obliged to all my good friends at IOP and outside IOP, who have encouraged and made me focused to finish my thesis in time.

No experimental work would be successful without skilled technical support. In this regard I would like to thank two persons, Mr. S. R. Mohanty (Soumya) and Mr. B. K. Dash for providing each and every requirement for our Lab. Special thanks to Soumya bhai for his continuous, quick and reliable helps.

I acknowledge the excellent library and computer facilities provided by the IOP and the timely help of all the academic as well as non academic staff.

Finally, but not the least, I would love to express my deepest gratitude to my family members where basic source of my energy resides. My family includes my parents, my brother and my beloved wife Mrs. Arpita Ghosh. I must acknowledge my wife Arpita for her constant encouragement and for being cooperative in every situation through this tough journey of my PhD life. They always have believed in me and continuously motivated me to move forward. Without their sacrifice, love and support these accomplishments wouldn't have been possible.

***TO MY PARENTS AND BELOVED WIFE***

## List of Publications

1. \*Study of Faceted Au nanoparticle capped ZnO nanowires: Antireflection, Surface Enhanced Raman Spectroscopy and Photoluminescence aspects.  
**Arnab Ghosh**, R. R. Juluri, P. Guha, R. Sathyavathi, A. Dash, B. K. Jena and P. V. Satyam,  
*J. Phys. D: Appl. Phys.* **48**, 055303 (2015).
2. \*Simple growth of faceted Au–ZnO hetero-nanostructures on silicon substrates (Nanowires and Triangular Nanoflakes): A shape and defect driven enhanced photocatalytic performance under visible light.  
**Arnab Ghosh**, P. Guha, A. K. Samanata, B. K. Jena, R. Bar, S. K. Ray and P. V. Satyam,  
*ACS Appl. Mater. Interfaces* **7** (18), 9486 (2015).
3. \*Tuning work function of randomly oriented ZnO nanostructures by capping with faceted Au nanostructure and oxygen defects: Enhanced field emission experiments and DFT studies.  
**Arnab Ghosh**, P. Guha, R. Thapa, S. Sinthika, M. Kumar, B. Rakshit, T. Dash, R. Bar, S. K. Ray and P. V. Satyam,  
*Nanotechnology* **27**, 125701 (2016).
4. \*Novel large scale growth of Au-GeO<sub>2</sub> nano/micro-wires: Surface-plasmons and oxygen-defects mediated visible-light photodetection.  
**Arnab Ghosh**, P. Guha, S. Mukherjee, R. Bar, S. K. Ray and P. V. Satyam,  
*To be submitted*, 2016.



5. \*Role of native oxide on Si substrate towards Au catalyzed growth of ZnO nanowires:  
Transition of growth mode from VLS to VS or vice versa  
**Arnab Ghosh**, P. Guha, A. Bhukta and P. V. Satyam,  
*Manuscript under preparation.*
  
6. Growth of Ag nanostructures on high-index Si (5 5 12) surfaces under UHV conditions: effect of prior surface treatment before deposition  
A. Bhukta, P. Guha, **Arnab Ghosh**, P. Maiti and P. V. Satyam,  
*Appl. Phys. A* **122**, 356 (2016).
  
7. Silver endotaxy in silicon under various ambient conditions and their use as surface enhanced Raman spectroscopy substrates.  
R. R. Juluri, **Arnab Ghosh**, A. Bhukta, R. Sathyavathi and P. V. Satyam,  
*Thin Solid Films* **586**, 88 (2015).
  
8. Multilayer Ge Nanocrystals embedded within Al<sub>2</sub>O<sub>3</sub> matrix for high performance floating gate memory devices.  
R. Bar, R. Aluguri, S. Manna, **Arnab Ghosh**, P. V. Satyam and S. K. Ray,  
*Appl. Phys. Lett.* **107**, 093102 (2015).
  
9. Sandwiched graphene with nitrogen, sulphur co-doped CQDs: Efficient metal free material for energy storage and conversion application.  
A. K. Samantara, S. C. Sahu, **Arnab Ghosh** and B. K. Jena,  
*J. Mater. Chem. A* **3**, 16961 (2015).
  
10. Coherently Embedded Ag Nanostructures in Si: 3D Imaging and their application to SERS.  
R. R. Juluri, A. Rath, **Arnab Ghosh**, A. Bhukta, Sathyavathi R., Narayana rao D., K. Mueller, K. Frank, M. Schowalter, T. Grieb, F. Krause, A. Rosenauer and P. V. Satyam,  
*Sci. Rep.( Nature)* **4**, 4663 (2014).

- 11.** Study of initial stages of growth of Au-assisted epitaxial Ge nanowires on clean Ge(100) Surface.  
A. Rath, J. K. Dash, R. R. Juluri, **Arnab Ghosh**, T. Grieb, M. Schowalter, F. F. Krause, K. Müller, A. Rosenauer and P. V. Satyam,  
*CrystEngComm.* **16**, 2486 (2014).
- 12.** Facile synthesis of single crystalline n-/p- type ZnO nanorods by lithium substitution and their photoluminescence, electrochemical and photocatalytic properties.  
I. Thakur, S. Chatterjee, S. Swain, **Arnab Ghosh**, S. K. Behera and Y. S. Chaudhary,  
*New J. Chem.* **39**, 2612 (2015).
- 13.** Substrate Symmetry Driven Endotaxial Silver Nanostructures by Chemical Vapor Deposition.  
R. R. Juluri, A. Rath, **Arnab Ghosh** and P. V. Satyam,  
*J. Phys. Chem. C* **117** (25), 13247 (2013).
- 14.** A bioinspired approach for shaping Au nanostructures: The role of biomolecule structures in shape evolution.  
S. C. Sahu, A. K. Samantara, **Arnab Ghosh** and B. K. Jena,  
*Chem. Eur. J.* **19**, 8220 (2013).
- 15.** Polarity selective etching: A self-assisted route for fabricating high density of c-axis oriented tapered GaN nanopillars.  
**Arnab Ghosh**, H. P. Bhasker, A. Mukherjee, T. Kundu, B. P. Singh, S. Dhar, S. De and A. Chowdhury,  
*J. Appl. Phys.* **110**, 033528 (2011).
- 16.** Photoluminescence study on irradiated yttria stabilized zirconia.  
R. Halder, P. Sengupta, V. Sudarsan, A. Ghosh, **Arnab Ghosh**, A. Bhukta, G. Sharma, I. Samajdar and G. K. Dey,  
*J. Nucl. Mater.* **456**, 359 (2015).

17. Electron irradiation induced buckling, morphological transformation, and inverse Ostwald ripening in nanorod filled inside carbon nanotube.  
A. Singh, R. Kumari, V. Kumar, L. Krishnia, Z. Naqvi, A. K Panwar, U. M. Bhatta, **Arnab Ghosh**, P. V. Satyam and P. K. Tyagi,  
*Appl. Surf. Sci.* **360**, 1003 (2016).
18. Good's Buffer Derived Highly Emissive Carbon Quantum Dots: Excellent Biocompatible Anticancer Drug Carrier.  
A. K. Samantara, S. Maji, **Arnab Ghosh**, B. Bag, R. Dash and B. K. Jena,  
*J. Mater. Chem. B* (Accepted, 2016).
19. Polysaccharide-capped silver Nanoparticles inhibit biofilm formation and eliminate multi-drug-resistant bacteria by disrupting bacterial cytoskeleton with reduced cytotoxicity towards mammalian cells.  
S. Sanyasi, R. K. Majhi, S. Kumar, M. Mishra, **Arnab Ghosh**, M. Suar, P. V. Satyam, H. Mohapatra , L. Goswami and C. Goswami,  
*Sci. Rep.( Nature)* (Revised version submitted, 2016).

## Conference Presentations

1. \*Single step growth of Au-ZnO hetero-nanostructures and their application as efficient cold field Emitter: Experimental study and DFT simulation.  
**Arnab Ghosh**, P. Guha, R. Thapa, S. Sinthika, M. Kumar, B. Rakshit, T. Dash and P. V. Satyam,  
*NANOSA-2015*, 24<sup>th</sup> – 28<sup>th</sup> August 2015, MPI-PKS, Germany.
2. \*Structural characterization of simultaneously grown two types of Au-ZnO hetero-nanostructures (Nanowires and triangular nanoflakes) using electron microscopy.  
**Arnab Ghosh**, R. R. Juluri, P. Guha, M. Kumar and P.V. Satyam,  
*EMSI-2015*, 8<sup>th</sup> – 10<sup>th</sup> July 2015, Mumbai, India.

3. \*Optical, photo-electrochemical and field emission properties of Au-ZnO Nanowires.  
**Arnab Ghosh**, R. R. Juluri, P. Guha and P. V. Satyam,  
*PSI-2014*, 24<sup>th</sup> – 28<sup>th</sup> February 2014, Puri, India.
  
4. \*Structure and optical properties of 1D ZnO nanostructures on Si substrate.  
**Arnab Ghosh**, R. R. Juluri and P. V. Satyam,  
*EMSI-2013*, 3<sup>rd</sup> – 5<sup>th</sup> July 2013, Kolkata, India.
  
5. Role of vacuum level on surface morphological modifications in Au/Si(100) system:  
 An in-situ and ex-situ TEM study.  
 A. Rath, J. K. Dash, R. R. Juluri, **Arnab Ghosh** and P. V. Satyam,  
*EMSI-2012*, 2<sup>nd</sup> – 4<sup>th</sup> July 2012, IISc Bangalore, India.
  
6. Shape Transition in Au/Si (100) System: Role of Surface oxide and Vacuum level.  
 A. Rath , J. K. Dash , R. R. Juluri1, **Arnab Ghosh**, A. Rosenauer and P. V. Satyam,  
*ICANN-2011*, 8<sup>th</sup> – 10<sup>th</sup> December 2011, IIT Guwahati, India.

(\*) Indicates the papers on which this thesis work is based upon.

# Synopsis

The field of nanoscience and nanotechnology is an expanding inter-disciplinary paradigm which encompasses diverse fields of science and engineering, which resulted in diversified potential device applications at the nano/subatomic scale. Almost all materials exhibit unique physical, chemical and mechanical properties stemming from their nanoscale dimension, that are significantly different from their bulk properties [1-2]. With the emerging area of nanoscience and nanotechnology, one-dimensional (1D) inorganic semiconductor nanostructures (NSs) of various morphologies (such as nanowires, nanotubes, nanoflakes, nanobelts etc.) have gathered great deal of interest not only due to their fundamental importance in basic scientific research but also due to their potential technological applications [2-5]. Among the inorganic semiconductor NSs, 1D oxide semiconductor (OS) NSs are the focus of current research interests, due to their special shapes, compositions that enabled stable chemical and physical properties [5-8]. This thesis work is based on two different classes of high direct bandgap oxide semiconductors (OS), one is group II-VI semiconductor zinc oxide (ZnO) having bandgap  $\approx 3.37$  eV and other is group IV-VI germanium oxide (GeO<sub>2</sub>) having bandgap of  $\approx 5.0$  eV [9,10]. The applications of these wide direct bandgap OS NSs (ZnO and GeO<sub>2</sub>) towards photonic, optoelectronic, photovoltaic device applications are hindered by some apparent drawbacks, such as, limited wavelength response ( $\lambda < 380$  nm, UV range) and fast radiative recombination rate of photo-generated electron-hole pairs [11-16]. Hence, efforts are being made to enhance their visible light absorption capability and also restrain radiative recombination of photogenerated charge carriers for their practical optoelectronic and photocatalytic device applications. To overcome these drawbacks and improve the visible light driven performances, various approaches have been adopted such as, various elemental n-type doping to engineer the bandgap [11,17], hybridization with noble metal nanoparticles (like, Au, Ag) [12,14,15,18], creation of oxygen vacancy [13,16], coupling with other semiconductors [19,20], annealing in different ambiances [21], etc. Among all the pathways, noble metal hybridization and oxygen vacancies introduction as self-doping without impurities in these NSs become popular

methods because of easy tunability of properties, large scale integration viability and stability without disturbing the host matrix. Recently hybrid semiconductor-metal nanostructures have attracted great research attention because they provide tunable physical and chemical properties superior to their individual properties [12,14,15,22]. It has been reported that metal nanoparticles (NPs), particularly Au NPs enhance visible light absorption and populate conduction band of oxide semiconductor by transferring hot electron utilizing their the surface plasmon resonance (SPR) properties [12,15,23]. Alternatively, Au NPs also serve as a passive sink for photogenerated electrons, hindering their recombination processes in the semiconductor matrix i.e., improving visible-light driven properties [12,14,15,24]. On the other hand, presence of oxygen vacancy in NS prompted a decrease in bandgap, and also serve as electron trap centers to restrain the recombination processes, which in turn enhance visible light driven device performances [13,16]. However, synthesis of such oxygen deficient or metal NPs conjugated ZnO hybrid/hetero-nanostructures usually involves a complicated multistep post-growth chemical process with harsh reaction conditions [12-18]. Therefore, it is indispensable to develop a rational, simple and inexpensive growth/synthesis protocol for the scalable synthesis of ZnO nanostructures/hetero-nanostructures (NSs/HNs) having improved visible-light harnessing capability from solar spectrum. First part as well as majority of this thesis work devoted on simple *single step* catalyzed growth of faceted Au NP capped ZnO hetero-nanostructures (HNs) of various size, morphology, areal density and oxygen vacancy concentration on native oxide Si(100), (110), (111) and single crystalline ZnO(0001) substrates using chemical vapor deposition (CVD) technique [25-27]. In the present thesis work, influence of native oxide on Si substrates towards metal (Au) catalyzed growth of ZnO HNs, on the growth modes (vapor-liquid-solid  $\rightarrow$  VLS or vapor-solid  $\rightarrow$  VS) has been reported [27]. Then the Au-ZnO HNs coated Si substrate's performance as active substrate for surface enhanced Raman scattering (SERS) to detect crystal violet (CV) molecules under the excitation of visible LASERs (green and red) has been reported[25]. Here, we have suggested a correlation between antireflection and SERS activity of plasmonic substrates [25]. Furthermore, we have studied the visible light driven photocatalytic application towards degradation of organic pollutants (rhodamine B and phenol) following their high visible photoresponse of the as-grown samples [26]. Enhanced photocatalytic performance offered by triangular nanoflakes of Au-ZnO HNs is attributed to the presence of high oxygen vacancies in them. Presence of oxygen vacancies has been studied by photoluminescence (PL) and X-ray photoelectron spectroscopy (XPS) measurements [26]. To further add, several experiments combined with first principle density functional theory



(DFT) calculations, a method of tailoring work function of ZnO HNs is proposed and corresponding enhanced field emission (FE) performances are studied [28]. We have demonstrated the best FE properties in terms of turn-on field and field enhancement factor offered by Au-ZnO HNs/Si samples having high oxygen vacancy following their lower work function and tapered geometry, compared to the reported values so far on different kinds of ZnO based NSs [28].

Recently, one-dimensional (1D) GeO<sub>2</sub> nanostructures of various morphologies have drawn a lot of attention for their applicability in various field of applications, such as in Li-ion energy storage devices (as high-performance anode material) [29-31], photocatalytic, photovoltaic along with optical fibers and waveguides applications [32-34]. A part of this thesis work reports a simple and inexpensive technique to grow large scale production of GeO<sub>2</sub> nanostructures (NSs). Last part of this thesis work deals with simple *single step* growth of Au nanoparticles capped GeO<sub>2</sub> hybrid nano/micro-wires (N/MWs) on Ge(100) substrates in two different ambiances via decomposition of the substrate and simultaneous active oxidation processes without any external supply of source vapor [35]. We also have studied the ambiance dependency, particularly to check the role of oxygen partial pressure on Au-GeO<sub>2</sub> hetero nano/micro-wires (N/MWs) growth via VLS mechanism [35]. We have explored visible light photodetection application of these as-grown oxygen deficient N/MWs in the presence of Au NP at the tip of individual N/MWs [35].

This thesis is organized in eight (8) chapters. A brief introduction and motivation to the novel growth method and possible applications of *single step* grown hybrid oxide semiconductors-metal (such as Au-ZnO and Au-GeO<sub>2</sub> hetero-nanostructures) along with variable oxygen vacancy related defects, are discussed in chapter 1. It is also discussed the role of oxygen vacancies and Au NPs associated with these hetero-nanostructures towards various applications, such as SERS, visible-light driven enhanced photocatalysis, field emission properties with tailored work function and visible light photodetection.

Second chapter describes working principles and instrumentations of all the major experimental techniques that have been used for the materials growth, characterizations and their viable applications related to this thesis work. Field emission based scanning electron microscopy (SEM) with energy dispersive X-ray detector (EDX) and back-scattered electron (BSE) detector attachments, Transmission electron microscopy (TEM), high resolution TEM (HRTEM), X-ray diffraction (XRD), UV-Vis absorption/reflectance spectroscopy,

photoluminescence (PL), X-ray photoelectron spectroscopy (XPS), field emission (FE), photo-electrochemical measurements, current voltage (I-V) measurements and surface enhanced Raman spectroscopy (SERS) have been used extensively to study the growth mechanism, characterization and applications of the as-grown hetero-nanostructures.

In chapter 3, we have explicitly discussed the growth of faceted Au NPs capped ZnO hetero-nanostructures (randomly aligned) of various shape, size and morphology via *single step* Au catalyzed chemical vapor transport processes (particularly VLS and VS modes) on native oxide coated, different oriented Si substrates. We have shown the catalyst layer thickness and substrates position dependency on the morphology, areal density and dimensionality of the as-grown Au-ZnO HNs. We have proposed growth mechanisms involved in the formation of two different morphology HNs (nanowires  $\rightarrow$  NWs and triangular nanoflakes  $\rightarrow$  TNFs) simultaneously. Nanowires (NWs) are having uniform in diameter with hexagonal cross-section whereas triangular nanoflakes (TNFs) are of gradually tapered from the base with rectangular cross-sections. This is achieved by varying substrates position in the CVD chamber, which enable variable temperature and Zn/O vapor pressure (availability of the growth species: Zn and O vapor) keeping all other growth parameters remain same. Using detailed electron microscopy study, vapor-solid (VS) mechanism is proposed for the growth of only ZnO NSs on substrates where Au was deposited in MBE conditions on atomically cleaned Si surfaces (in UHV). In case, where Au thin film was deposited on native oxide coated Si substrates under high vacuum conditions, the growth of Au-ZnO HNs is proposed using a combined VLS–VS mechanism. So, controlling the interfacial oxide between catalyst layer and Si substrates, growth modes can be altered. At the end of this chapter we have showed the growth of oriented/aligned Au-ZnO NWs on lattice matched oxygen terminated ZnO(0001) substrate.

In chapter 4, surface enhance Raman spectroscopy (SERS) measurements using faceted Au capped Au-ZnO HNs (NWs and TNFs), as active substrates are presented to detection of low concentration crystal violet (CV) molecule for two different excitation wavelengths (514 nm and 632 nm). Reflectance spectra indicate that the Au-ZnO HNs coated Si surfaces have improved optical antireflection (as low as 0.50 % reflectance) properties through optical impedance match between air and Si substrate is observed in the wavelength range of 250–1000 nm. It has been found that the sample from each category (NWs or TNFs) with higher density of HNs and lower reflectance (i.e., 5 nm Au cases) has exhibits higher AEF in terms of Raman signal strength with proper excitation wavelength. A correlation

between the reflectance and SERS AEF has been proposed. Higher SERS activity towards CV detection is also observed when LSPR (i.e., reflectance minima) lies in between the excitation wavelength and the vibrational mode of analyte molecule. These Au-ZnO HNs coated Si substrates yielded high SERS activity for CV, implying their potential in SERS based detection of biomolecules.

In chapter 5, visible-light driven enhanced photocatalytic performances of Au-ZnO HNs grown on Si(110) substrates towards the degradation of rhodamine B and phenol are systematically presented. From the PL, CL and XPS measurements, Au-ZnO TNFs/Si(110) found to have more oxygen related defect states compared to Au-ZnO NWs/Si(110) which perhaps due to  $\approx$  eight (8) times larger average surface area of TNF compared to NW ( $TNF_{ASA}/NW_{ASA} \approx 8$ ). The TNFs sample has shown one order of magnitude less charge-transfer resistance ( $R_{ct}$ ) compared to NWs sample, owing to their higher oxygen related defect states leading to enhancement in visible-light induced photocurrent densities ( $\approx 4$  times). Following higher oxygen defects and less  $R_{ct}$  of TNFs sample, these found to have better photocatalytic degradation of  $5 \times 10^{-6}$  Molar RhB with average degradation rate constant of  $0.0305 \text{ min}^{-1}$  and photonic efficiency 0.11 %. In contrast, NWs sample has exhibited  $\approx 5.3$  times poorer photocatalytic degradation performance, with average degradation rate constant of  $0.0058 \text{ min}^{-1}$  and photonic efficiency 0.021 %. We have further cross-checked the enhance photocatalytic property of TNFs sample over NWs sample by studying the degradation of standard organic pollutant (phenol). Role of oxygen vacancies in conjunction with the presence of Au NPs at the apex of HNs have been discussed elaborately. Reusability of both the samples up to five (5) cycles of operations were checked, showing very good stability and no further treatment is involved before using them in the next cycle. This high photocatalytic property and robustness of the Au-ZnO TNFs sample could endow its use in harnessing visible part of the solar spectrum towards the degradation of organic compounds and microorganisms in water.

Chapter 6 presents local work function ( $\Phi$ ) modulation of ZnO HNs by combined effect of faceted Au nanostructures at the tip and varying oxygen vacancies ( $O_{vac}$ ) in them probed by experiments and also qualitatively verified by DFT calculations. The field emission (FE) properties of non-aligned Au-ZnO HNs having two different morphologies (NWs of uniform diameter and TNFs of tapered morphology) and oxygen vacancies have been explored. TNFs with tapered geometry having more  $O_{vac}$  exhibits enhanced FE performances with lower turn-on field and  $\approx 4$  times higher field enhancement factor  $5.16 \times$

$10^5$  compared to NWs sample with less  $O_{vac}$ . Using Kelvin probe force microscopy (KPFM) technique local  $\Phi$  of TNFs sample with high  $O_{vac}$  is found out to be  $4.7 \pm 0.1$  eV, which is  $\approx 0.34$  eV less in comparison with NWs sample. DFT calculations suggested that HNs with higher oxygen vacancies will have lower effective  $\Phi$  (tunneling barrier) because of excess unshared d-electrons of Zn atoms (nearest of O vacancy site) and charge transfer induced electronic band structure modification, which lead to increase in electron donating capability i.e., improvement in field emission behavior. Enhanced FE behavior of TNFs sample compared to NWs sample is attributed to the presence of higher oxygen vacancies in TNFs. Excellent FE properties including very high  $\beta$ , low turn-on field of 0.52 Volt/ $\mu\text{m}$  and emission stability for 4 hrs (at current density of 0.9 mA/cm<sup>2</sup>), offered by high oxygen deficient Au-ZnO TNFs sample could be useful for FE based device applications.

Chapter 7 deals with a novel large scale growth of Au-GeO<sub>2</sub> nano/micro-wires (N/MWs) of variable dimensionality and defect densities, on  $\approx 5$  nm Au coated native oxide Ge(100) substrates using a simple horizontal tube furnace without any external supply of source precursors. It has been demonstrated the role of ambience and catalyst layer on the growth via conducting growth experiments with and without  $\approx 5$  nm Au layer on Ge substrate under various ambiances (such as low vacuum, 40 sccm Ar and O<sub>2</sub> and in air atmospheric). Visible-light photodetector device application of highly oxygen deficient N/MWs grown in Ar ambience, following their lower reflectance in the visible spectral regime is demonstrated. Photodetector performance was studied by fabricating an Al<sub>2</sub>O<sub>3</sub>/Au-GeO<sub>2</sub> N/MWs/SiO<sub>2</sub>/p-type Si(100) device structure with top and bottom aluminum (Al) contact. This visible-light detection is attributed to the oxygen vacancy induced defect states and plasmonically generated hot electron injection from Au to conduction band of GeO<sub>2</sub>. Function of Au nanoparticles present at the tip of the as-grown Au-GeO<sub>2</sub> NWs on photodetection was further complemented by showing further increase in photoresponse and decrease in the reflectance after putting  $\approx 4$  nm Au layer on the as-grown sample.

Summary and conclusions are given in chapter 8.

## References

- [1] C. N. R. Rao, P. J. Thomas and G. U. Kulkarni, Nanocrystals: Synthesis, Properties and Applications (Springer, 2007, ISBN: 978-3-540-68751-1).

- [2] P. Alvisato, *Science* **271**, 933 (1996).
- [3] P. D. Yang et al., *Adv. Mater.* **12**, 323 (2002).
- [4] Y. N. Xia et al., *Adv. Mater.* **15**, 353 (2003).
- [5] R. K. Joshi and J. J. Schneider, *Chem. Soc. Rev.* **41**, 5285 (2012).
- [6] T. Zhai et al., *Sensors* **9**, 6504 (2009).
- [7] S. Zhuiykov, *Nanostructured Semiconductor Oxides for the Next Generation of Electronics and Functional Devices* (Elsevier, 2013, ISBN: 978-1-78242-220-4).
- [8] Y. W. Heo et al., *Mater. Sci. Eng. R-Rep.* **47**, 1 (2004).
- [9] M. H. Huang, S. Mao, H. Feick, H. Q. Yan, Y. Y. Wu, H. Kind, E. Weber, R. Russo and P. D. Yang, *Science* **292**, 1897 (2001).
- [10] D. Kuzum et al., *IEEE Trans. Electron Dev.* **58**, 1 (2011).
- [11] S. Liu, C. Li, J. Yu and Q. Xiang, *CrystEngComm* **13**, 2533 (2011).
- [12] M. D. L. Peralta et al., *ACS Appl. Mater. Interfaces* **4**, 4807 (2012).
- [13] J. Wang et al., *ACS Appl. Mater. Interfaces* **4**, 4024 (2012).
- [14] W. He et al., *J. Am. Chem. Soc.* **136**, 750 (2014).
- [15] M. Wu et al., *ACS Appl. Mater. Interfaces* **6**, 15052 (2014).
- [16] S. A. Ansari, M. M. Khan, S. Kalathil and M. H. Cho, *Nanoscale* **5**, 9238 (2013).
- [17] A. Asahi, T. Morikawa, T. Ohwaki, K. Aoki and Y. Taga, *Science* **293**, 269 (2001).
- [18] C. Gu et al., *Cryst. Growth Des.* **9**, 3278 (2009).
- [19] H. Yin et al., *ACS Appl. Mater. Interfaces* **6**, 14851 (2014).
- [20] S. Jung and K. Yong, *Chem. Commun.* **47**, 2643 (2011).
- [21] Q. Zhao et al., *Appl. Phys. Letter.* **88**, 033102 (2006).
- [22] J. Zeng et al., *Adv. Mater.* **22**, 1936 (2010).

- [23] X. Lang, X. Chen and J. Zhao, *Chem. Soc. Rev.* **43**, 473 (2014).
- [24] C. Clavero, *Nature Photonics* **8**, 95 (2014).
- [25] A. Ghosh, R. R. Juluri, P. Guha, R. Sathyavathi, A. Dash, B. K. Jena and P. V. Satyam, *J. Phys. D: Appl. Phys.* **48**, 055303 (2015).
- [26] A. Ghosh, P. Guha, A. K. Samantara, B. K. Jena, R. Bar, S. Ray and P. V. Satyam, *ACS Appl. Mater. Interfaces* **7**, 9486 (2015).
- [27] A. Ghosh, P. Guha, A. Bhukta and P. V. Satyam (To be submitted, 2016).
- [28] A. Ghosh, P. Guha, R. Thapa, S. Selvaraj, M. Kumar, B. Rakshit, T. Dash, R. Bar, S. K. Ray and P. V. Satyam, *Nanotechnology* **27**, 125701 (2016).
- [29] Y. Lin et al., *J. Phys. Chem. Lett.* **4**, 999 (2013).
- [30] Y. Son et al., *Nano Lett.* **14**, 1005 (2014).
- [31] X. L. Wang et al., *J. Am. Chem. Soc.* **133**, 20692 (2011).
- [32] L. Nejaty-Moghadam et al., *J. Mater. Sci. Mater. Electron.* **26**, 6386 (2015).
- [33] S. Sakaguchi and S. Todoroki, *Appl. Opt.* **36**, 6809 (1997).
- [34] N. Bose, M. Basu and S. Mukherjee, *Mater. Res. Bull.* **47**, 1368 (2012).
- [35] A. Ghosh, P. Guha, S. Mukherjee, R. Bar, S. K. Ray and P. V. Satyam (To be submitted, 2016).



# Contents

<b>Statement by author</b>	<b>iii</b>
<b>Declaration</b>	<b>iv</b>
<b>Certificate</b>	<b>v</b>
<b>Acknowledgments</b>	<b>vi</b>
<b>List of Publications</b>	<b>x</b>
<b>Synopsis</b>	<b>xiv</b>
<b>List of Figures</b>	<b>xxv</b>
<b>Chapter 1: Introduction</b>	<b>1</b>
<b>Chapter 2: Experimental Techniques</b>	<b>11</b>
2.1 Introduction	11
2.2 Thin film and nanostructures growth method	11
2.2.1 Thermal evaporation at high vacuum (HV) (physical vapor deposition (PVD) technique)	12
2.2.2 Thermal evaporation using molecular beam epitaxy (MBE)	13
2.2.3 Chemical vapor deposition (CVD) technique	14
2.2.4 Growth mechanisms	15
2.2.4.1 Vapor-liquid-solid (VLS) mechanism	15
2.2.4.2 Vapor-solid (VS) mechanism	18
2.2.4.3 Solid-liquid-solid (SLS) mechanism	19
2.3 Characterization and application techniques	20
2.3.1 Transmission electron microscope (TEM)	20
2.3.1.1 Instrumentation	21
2.3.1.2 Diffraction and imaging	24
2.3.1.3 Beam (electrons)-specimen interaction	25
2.3.1.4 Sample preparation (mechanical process)	27
2.3.2 Focused ion beam – scanning electron microscope (FIB – SEM) cross beam system	28
2.3.2.1 Scanning electron microscope (SEM)	30
2.3.2.2 Focused ion beam (FIB)	33
2.3.3 X-ray diffraction (XRD)	35
2.3.4 Photoluminescence (PL)	36

2.3.5 Cathodoluminescence (CL)	38
2.3.6 Reflectance	39
2.3.7 X-ray photoelectron spectroscopy (XPS)	39
2.3.8 Surface enhanced Raman spectroscopy/scattering (SERS)	40
2.3.8.1 Mechanisms	42
2.3.8.2 Distance dependence	43
2.3.9 Electrochemistry	44
2.3.10 Field emission (FE)	45
2.3.11 Visible light photodetector (I-V) characteristics	47
2.4 References	47
<b>Chapter 3: Au Catalyzed Vapor-Liquid-Solid (VLS) Growth of Faceted Au-ZnO Hetero-nanostructures on Low Index Silicon Surfaces: Role of Native Oxide at the Interface</b>	<b>51</b>
3.1 Introduction	51
3.2 Experimental	54
3.3 Results and discussion	57
3.3.1 Growth of Au-ZnO HNs (Nanowires and Triangular nanoflakes) on native oxide coated Si substrates	57
3.3.2 Role of catalyst layer thickness on the dimensionality of Au- ZnO hetero-nanostructures	61
3.3.3 Proposed growth models	69
3.3.4 Role of native oxide at the interface of catalyst Au layer and Si substrate	72
3.3.5 Growth of vertically oriented Au-ZnO nanowires	75
3.4 Summary	77
3.5 References	78
<b>Chapter 4: SERS Applications of Au-ZnO Hetero-nanostructures/Si</b>	<b>81</b>
4.1 Introduction	81
4.2 Experimental	82
4.3 Results and discussion	83
4.3.1 Morphological properties	83
4.3.2 Optical properties	84
4.3.3 SERS substrates: detection of CV (Crystal Violet) molecules	87
4.4 Summary	91
4.5 References	91
<b>Chapter 5: Faceted Au-ZnO Hetero-nanostructures on Silicon Substrates (Nanowires and Triangular Nanoflakes): A Shape and Defect Driven Enhanced Photocatalytic Performance under Visible Light</b>	<b>94</b>
5.1 Introduction	94
5.2 Experimental	96
5.2.1 Structural and optical characterization	96
5.2.2 Photo-electrochemical measurements	96

5.2.3 Photocatalytic activity	97
5.3 Results and discussion	97
5.3.1 Morphological and structural characterization	97
5.3.2 Optical studies	99
5.3.3 Photo-electrochemical analysis	101
5.3.4 Photocatalytic degradation of rhodamine B and phenol	104
5.3.5 Plausible photocatalytic degradation mechanism	108
5.4 Summary	109
5.5 References	109
<b>Chapter 6: Tuning Work Function of Randomly Oriented ZnO Nanostructures by Capping With Faceted Au Nanostructure and Oxygen Defects: Enhanced Field Emission Experiments and DFT Studies</b>	<b>113</b>
6.1 Introduction	113
6.2 Experimental	115
6.3 Results and discussion	116
6.3.1 Morphological and structural properties	116
6.3.2 Optical properties	117
6.3.3 Field emission properties	119
6.3.4 DFT results	125
6.4 Summary	127
6.5 References	128
<b>Chapter 7: Novel Large Scale Growth of Au-GeO<sub>2</sub> Nano/Micro-wires: Surface-plasmons and Oxygen-defects Mediated Visible-light Photodetection</b>	<b>132</b>
7.1 Introduction	132
7.2 Experimental	134
7.3 Results and discussion	135
7.3.1 Morphological and structural properties	135
7.3.1.1 Growth mechanism	140
7.3.2 Optical properties	141
7.3.3 Visible-light photodetector applications	143
7.4 Summary	146
7.5 References	146
<b>Chapter 8: Summary and Conclusions</b>	<b>150</b>

# List of Figures

<b>1.1</b>	Stick and ball representation of ZnO wurtzite structure showing tetrahedral coordination (using VESTA) [42]. (b) Hexagonal ZnO with common low index planes.	<b>3</b>
<b>1.2</b>	$2 \times 2 \times 2$ unit cells of $\text{GeO}_2$ crystal structures, (a) Hexagonal and (b) tetragonal rutile-like (drawn using VESTA) [46].	<b>4</b>
<b>2.1</b>	High vacuum coating unit (M/s Vacuum Techniques Pvt. Ltd) installed at Institute of Physics, Bhubaneswar.	<b>13</b>
<b>2.2</b>	Schematic illustration of the single zone horizontal quartz tube furnace, that is used as Chemical Vapor Deposition (CVD) setup for the work in this thesis.	<b>15</b>
<b>2.3</b>	Schematic illustration of the VLS growth mechanism for metal-assisted nanowire; impinging of vapors, alloy formation, nucleation and formation of vertically oriented nanowires.	<b>16</b>
<b>2.4</b>	Schematic of the Au-Zn alloy droplet with ZnO layer on substrate.	<b>17</b>
<b>2.5</b>	Schematic of VS growth mechanism, impinging of vapors, formation of seed and formation of nanowires.	<b>18</b>
<b>2.6</b>	Schematic illustration of the SLS growth mechanism for metal assisted Si nanowires growth.	<b>19</b>
<b>2.7</b>	A schematic diagram of (a) filament and illumination part, (b) diffraction pattern formation and image formation [22].	<b>22</b>
<b>2.8</b>	Parallel-beam operation in the TEM: the basic principle illustrated (left) and the practical situation in most TEMs (right) [22].	<b>22</b>
<b>2.9</b>	200 keV JEOL HRTEM installed at Institute of Physics, Bhubaneswar.	<b>23</b>
<b>2.10</b>	A schematic diagram showing the geometry of diffraction pattern formation [22].	<b>25</b>
<b>2.11</b>	Schematic presentation of various signals generated when a high-energy beam of electrons interacts with a thin specimen. Most of these signals can be detected in different types of TEM.	<b>26</b>
<b>2.12</b>	A schematic diagram of procedure to prepare a typical planar TEM specimen.	<b>27</b>
<b>2.13</b>	A schematic diagram of procedure to prepare a typical XTEM specimen.	<b>28</b>
<b>2.14</b>	FIB-SEM crossbeam system installed at Institute of Physics, Bhubaneswar.	<b>29</b>
<b>2.15</b>	Schematic representation of various signals generated as a result of the electron-specimen interaction in a SEM.	<b>32</b>
<b>2.16</b>	Illustration of TEM lamella preparation utilizing FIB.	<b>35</b>

<b>2.17</b>	Schematic representation of X-ray diffraction occurring in a crystal with spacing $d$ .	<b>36</b>
<b>2.18</b>	Schematic of the process occurring during photoluminescence in a direct band gap semiconductor after excitation at frequency $\nu_{\text{excitation}}$ .	<b>38</b>
<b>2.19</b>	Energy level diagram showing the states involved in Raman signal. (b) Model of LSPRs at the spherical nanoparticle surface [47].	<b>42</b>
<b>2.20</b>	1D potential energy barrier for an electron near a metal surface [55]. (b) A schematic illustration of field emission phenomenon, showing the emission from the tip of an emitter. The emitters can have different tip geometry such as, Au-ZnO NW, Au-ZnO TNF.	<b>46</b>
<b>3.1</b>	Schematic of growth setup (a) with one side open quartz boat (used for all growth carried out for this thesis work) and (b) with both side closed quartz boat. Except quartz boat geometry else are exactly same for both the setup (to show more growth species availability leads to triangular nanoflakes (TNFs) growth. So, for nanowires growth optimized growth species supply is required.	<b>54</b>
<b>3.2</b>	Schematic representations of Au thin film deposited on commercially available silicon substrate with $\approx 2 - 3$ nm native oxide (above) and Au nanoparticles (NPs) formed after air annealing at $800^\circ\text{C}$ for 30 min (below).	<b>55</b>
<b>3.3</b>	SEM image of Au nanoparticles (NPs) formed after air annealing at $800^\circ\text{C}$ of 1 nm Au/SiO <sub>2</sub> /Si(100); inset represents corresponding size distribution histogram of Au NPs. (b and g) show low-magnification SEM micrographs of as-grown Au-ZnO nanowires (NWs) and triangular nanoflakes (TNFs) on the previous substrate, respectively; corresponding inset figures show high resolution SE images of a single NW and TNF with faceted Au NP at the tip. (c and h) present cross-sectional SEM images of the corresponding NWs and TNFs samples, respectively; corresponding insets show high resolution BSE images (Z-contrast images) of individual Au-ZnO NW and TNF. (d and i) depict low-magnification TEM micrographs of a single Au-ZnO NW and TNF with faceted Au particle at the tip of each, respectively. (e and j) are the selected area electron diffraction (SAED) pattern from individual NW and TNF, respectively. (f and k) present HRTEM images taken from the highlighted regions of Au-ZnO NW in panel (d) and Au-ZnO TNF in panel (i), respectively.	<b>58</b>
<b>3.4</b>	SEM image of Au nanoparticles (NPs) formed after air annealing at $800^\circ\text{C}$ of 1 nm Au/SiO <sub>2</sub> /Si(110); inset represents corresponding size distribution histogram of Au NPs. (b and g) show low-magnification SEM micrographs of as-grown Au-ZnO nanowires (NWs) and triangular nanoflakes (TNFs) on the previous substrate, respectively; corresponding inset figures show high resolution SE images of a single NW and TNF with faceted Au NP at the tip. (c and h) present cross-sectional SEM images of the corresponding NWs and TNFs samples, respectively; corresponding insets show high resolution BSE images (Z-contrast images) of individual Au-ZnO NW and TNF. (d and i) depict low-magnification TEM micrographs of a single Au-ZnO NW and TNF with faceted Au particle at the tip of each, respectively. (e and j) are the selected area electron diffraction (SAED) pattern from individual NW and TNF, respectively. (f and k) present	

- HRTEM images taken from the highlighted regions of Au-ZnO NW in panel (d) and Au-ZnO TNF in panel (i), respectively.
- 3.5** SEM image of Au nanoparticles (NPs) formed after air annealing at 800 °C of 1 nm Au/SiO<sub>2</sub>/Si(111); inset represents corresponding size distribution histogram of Au NPs. (b and g) show low-magnification SEM micrographs of as-grown Au-ZnO nanowires (NWs) and triangular nanoflakes (TNFs) on the previous substrate, respectively; corresponding inset figures show high resolution SE images of a single NW and TNF with faceted Au NP at the tip. (c and h) present cross-sectional SEM images of the corresponding NWs and TNFs samples, respectively; corresponding insets show high resolution BSE images (Z-contrast images) of individual Au-ZnO NW and TNF. (d and i) depict low-magnification TEM micrographs of a single Au-ZnO NW and TNF with faceted Au particle at the tip of each, respectively. (e and j) are the selected area electron diffraction (SAED) pattern from individual NW and TNF, respectively. (f and k) present HRTEM images taken from the highlighted regions of Au-ZnO NW in panel (d) and Au-ZnO TNF in panel (i), respectively.
- 3.6** SEM image of Au nanoparticles (NPs) formed after air annealing at 800 °C of 5 nm Au/SiO<sub>2</sub>/Si(100); inset represents corresponding size distribution histogram of Au NPs. (b and g) show low-magnification SEM micrographs of as-grown Au-ZnO nanowires (NWs) and triangular nanoflakes (TNFs) on the previous substrate, respectively; corresponding inset figures show high resolution SE images of a single NW and TNF with faceted Au NP at the tip. (c and h) present cross-sectional SEM images of the corresponding NWs and TNFs samples, respectively; corresponding insets show high resolution BSE images (Z-contrast images) of individual Au-ZnO NW and TNF. (d and i) depict low-magnification TEM micrographs of a single Au-ZnO NW and TNF with faceted Au particle at the tip of each, respectively. (e and j) are the selected area electron diffraction (SAED) pattern from individual NW and TNF, respectively. (f and k) present HRTEM images taken from the highlighted regions of Au-ZnO NW in panel (d) and Au-ZnO TNF in panel (i), respectively.
- 3.7** SEM image of Au nanoparticles (NPs) formed after air annealing at 800 °C of 5 nm Au/SiO<sub>2</sub>/Si(110); inset represents corresponding size distribution histogram of Au NPs. (b and g) show low-magnification SEM micrographs of as-grown Au-ZnO nanowires (NWs) and triangular nanoflakes (TNFs) on the previous substrate, respectively; corresponding inset figures show high resolution SE images of a single NW and TNF with faceted Au NP at the tip. (c and h) present cross-sectional SEM images of the corresponding NWs and TNFs samples, respectively; corresponding insets show high resolution BSE images (Z-contrast images) of individual Au-ZnO NW and TNF. (d and i) depict low-magnification TEM micrographs of a single Au-ZnO NW and TNF with faceted Au particle at the tip of each, respectively. (e and j) are the selected area electron diffraction (SAED) pattern from individual NW and TNF, respectively. (f and k) present HRTEM images taken from the highlighted regions of Au-ZnO NW in panel (d) and Au-ZnO TNF in panel (i), respectively.

59

60

62

64



- 3.8** SEM image of Au nanoparticles (NPs) formed after air annealing at 800 °C of 5 nm Au/SiO<sub>2</sub>/Si(111); inset represents corresponding size distribution histogram of Au NPs. (b and g) show low-magnification SEM micrographs of as-grown Au-ZnO nanowires (NWs) and triangular nanoflakes (TNFs) on the previous substrate, respectively; corresponding inset figures show high resolution SE images of a single NW and TNF with faceted Au NP at the tip. (c and h) present cross-sectional SEM images of the corresponding NWs and TNFs samples, respectively; corresponding insets show high resolution BSE images (Z-contrast images) of individual Au-ZnO NW and TNF. (d and i) depict low-magnification TEM micrographs of a single Au-ZnO NW and TNF with faceted Au particle at the tip of each, respectively. (e and j) are the selected area electron diffraction (SAED) pattern from individual NW and TNF, respectively. (f and k) present HRTEM images taken from the highlighted regions of Au-ZnO NW in panel (d) and Au-ZnO TNF in panel (i), respectively. 65
- 3.9** Shows comparison of the XRD patterns obtained from the as-grown ZnO NWs samples grown on 5 nm Au coated (pre-annealed) three different oriented silicon substrates as Si(100), Si(110) and Si(111). (b) Shows comparison of the XRD patterns obtained from the as-grown ZnO TNFs samples grown on 5 nm Au coated (pre-annealed) three different oriented silicon substrates as Si(100), Si(110) and Si(111). (c) and (d) show comparison (1 nm and 5 nm Au as catalyst layers) of the X-ray diffraction (XRD) patterns obtained from the as-grown Au-ZnO NWs and TNFs samples, respectively. 67
- 3.10** (a) and (c) show high-magnification SEM images of a single NW and a TNF dispersed on two different copper grids, respectively. Corresponding EDX spectra collected from two indicated regions (1, 2) of NW and TNF in panels (a) and (c) are shown in Figures (b) and (d), revealing the local compositional details at tip particle and body, respectively. 68
- 3.11** Schematic illustrations showing the possible growth model for Au capped ZnO NW (a)-(c) and a TNF (e)-(g). (d) and (h) represent the 3-dimensional geometrical configuration of a fully grown NW and TNF, respectively. 70
- 3.12** Schematic representation of Au thin film deposited on atomically cleaned silicon substrate by flashing in MBE. (b) Low magnification SEM image of 10 ML Au/Si(100) (MBE-grown) after air annealing at 800 °C for 30 min. (c) Low magnification TEM image of the corresponding sample. (d) Selected area electron diffraction (SAED) pattern from panel (c). (e) Low magnification SEM of as-grown ZnO nanowire on the 10 ML Au/Si(100) pre-annealed @ 800 °C; Inset shows magnified view of a single ZnO nanowire. (f) Low magnification XTEM micrograph of the previous sample. (g) Shows HRTEM image taken from the highlighted region of (f). 74
- 3.13** SEM image of Au nanoparticles (NPs) formed after air annealing at 800 °C of 2 nm Au/O(t)-ZnO(0001); inset represents size distribution histogram of Au NPs of the corresponding image. (b) Low magnification SEM micrograph (plan view) of as-grown vertically oriented Au-ZnO nanowires (NWs) on 2 nm Au/O(t)-ZnO(0001) pre-annealed (at 800 °C) substrate. (c) Cross-sectional

SEM image of the sample; inset shows high magnification BSE image (Z-contrast image); brighter contrast correspond Au NPs. (d) High resolution SEM image of a single Au-ZnO NW with faceted Au NP at the tip. (e) Low-magnification TEM micrograph of a single Au-ZnO NW with faceted Au particle at the tip. (f) Selected area electron diffraction (SAED) pattern from single NW. (g) HRTEM image from the highlighted region in panel (d). (h) X-ray diffraction (XRD) pattern obtained from the corresponding sample, shows epitaxial growth of Au-ZnO NWs (vertically aligned with respect to substrate).	76
<b>4.1</b> (a)-(b) show high-magnification BSE images (Z-contrast images) of as-grown Au-ZnO NWs using two different Au catalyst layer thicknesses of 1 nm and 5 nm respectively; (c)-(d) show the same of the as-grown Au-ZnO TNFs using two different Au catalyst layer thicknesses of 1 nm and 5 nm respectively. Insets of each show their corresponding BSE images of single Au-ZnO hetero-nanostructure.	84
<b>4.2</b> (a) and (b) show the comparison of room temperature PL spectra taken from as-synthesized ZnO NW array and ZnO TNF array using our two different choices of Au catalyst layer thicknesses (1 nm and 5 nm), respectively.	85
<b>4.3</b> Comparison of UV-Vis Specular reflectance spectra obtained from (a) NWs category Au-ZnO hetero-nanostructures covered Si(110) samples with 1 nm and 5 nm Au cases and (b) TNFs category Au-ZnO hetero-nanostructures covered Si(110) samples with 1 nm and 5 nm Au cases with 800 °C air-annealed 1 nm, 5 nm Au coated Si(110) substrates, bare ZnO(0002) and bare Si(110) substrates.	87
<b>4.4</b> (a) and (c) show the SERS spectra of 1 $\mu$ M concentration CV on Au-ZnO NWs (1 nm and 5 nm Au cases both) and Au-ZnO TNFs (1 nm and 5 nm Au cases both), respectively, recorded with 514 nm. (b) and (d) present reproducible SERS spectra of CV of 1 $\mu$ M concentration on NW sample with 1 nm Au case and TNF sample with 5 nm case, respectively, recorded with 514 nm.	88
<b>4.5</b> (a) and (c) show the SERS spectra of 1 $\mu$ M concentration CV on Au-ZnO NWs (1 nm and 5 nm Au cases both) and Au-ZnO TNFs (1 nm and 5 nm Au cases both), respectively, recorded with 633 nm. (b) and (d) present reproducible SERS spectra of CV of 1 $\mu$ M concentration on NW sample with 1 nm Au case and TNF sample with 5 nm case, respectively, recorded with 633 nm.	89
<b>4.6</b> Absorbance spectra from 1 $\mu$ M CV in ethanol solution.	90
<b>5.1</b> SEM micrographs of as-grown Au-ZnO hetero-nanostructures (nanowires and triangular nanoflakes) on 5 nm Au/SiO <sub>2</sub> /Si(110) pre-annealed @800 °C substrates kept at two different positions (down stream and up stream of CVD system): (a) and (c) present top view low-magnification secondary electron images of sample A (NWs) and sample B (TNFs), respectively. (b) and (d) present corresponding samples high-magnification backscattered electron images. Inset of figures (a), (c) show the SE images a single NW and TNF, respectively.	98
<b>5.2</b> (a), (b) show the room temperature (300 °K) PL spectra taken from sample A (Au-ZnO NWs) and sample B (Au-ZnO TNFs), respectively. (c), (d) show the	

PL spectra after annealing in oxygen environment of the corresponding samples at 900 °C for 90 min.	100
<b>5.3</b> (a) and (b) show typical room temperature (300 °K) CL spectra taken from the middle portions of the Au-ZnO NW and TNF body shown in the corresponding inset SEM images, respectively.	100
<b>5.4</b> (a) and (b) show XPS analysis O (1s) spectra of the sample A (NW) and sample B (TNF), respectively, indicating the presence of three types of oxygen, O <sub>L</sub> (lattice oxygen), O <sub>V</sub> (oxygen vacancy or defects) and O <sub>C</sub> (chemisorbed oxygen species).	101
<b>5.5</b> Photocurrent response of the sample A, sample B along with B-ZnO and RB-ZnO modified ITO electrode under the periodic irradiation of visible light and the (b) Nyquist plots of samples A and B under visible light illumination (Inset is the corresponding equivalent circuit).	102
<b>5.6</b> UV-Vis diffuse-reflectance spectra (DRS) from (a) two as-grown samples A and B and (b) 5 nm Au/ZnO(0001) 800 °C air annealed sample.	103
<b>5.7</b> UV-Vis absorption spectra of 5 μM RhB in presence of (a) sample A and (b) sample B under visible-light irradiation at different time interval, (c) UV-Vis spectra of RhB before and after treatment with Sample A, Sample B, B-ZnO, RB-ZnO and only with light after 3 hrs of irradiation. (d) First order kinetics plots [ln(C/C <sub>0</sub> in %) vs irradiation time (t)] of the photocatalytic activities of the photo catalysts for RhB degradation under visible light.	104
<b>5.8</b> Temporal evolution of color of RhB aqueous solution with sample B (Au-ZnO TNFs/Si(110)) under visible light illumination.	105
<b>5.9</b> UV-Vis absorbance spectra of RhB solution under visible light irradiation (a) without catalyst (Photolysis), (b) with B-ZnO and (c) RB-ZnO.	105
<b>5.10</b> Photocatalytic activities and (b) first order kinetics plots [ln(C/C <sub>0</sub> in %) vs irradiation time (t)] of the as-grown samples A and B for phenol (5×10 <sup>-6</sup> M) degradation under visible light.	106
<b>5.11</b> Five cycles for photo degradation of 5 μM RhB by sample A (black) and sample B (red) under visible light irradiation. For each cycle the duration of visible light exposure is 3 hour.	107
<b>5.12</b> (a) and (c) Show low-magnification TEM images of single Au-ZnO NW and Au-ZnO TNF respectively, after being used in RhB degradation under visible light for consecutive five cycles. (b) and (d) show SAED patterns taken from panel (a) and (c) respectively.	107
<b>5.13</b> Schematic representation of the possible mechanism behind the visible light (λ ≥ 400 nm) photocatalytic activity of as-grown samples towards degradation of rhodamine B.	108
<b>6.1</b> (a) and (b) show cross-sectional SEM micrographs of the as-grown samples A (Au-ZnO nanowires) and B (Au-ZnO triangular nanoflakes), respectively. Insets of (a) and (b) represent BSE images (Z-contrast images) of individual NW and TNF from the respective samples. (c) and (d) Histograms show the growth misalignment of the as-grown samples A and B with respect to the substrate normal, respectively.	117

<b>6.2</b>	(a), (b) show room temperature PL spectra taken from sample A (Au-ZnO NWs) and sample B (Au-ZnO TNFs), respectively; (c) and (d) show XPS analysis O (1s) spectra of the sample A and sample B, respectively, indicating the presence of three types of oxygen, $O_L$ (lattice oxygen), $O_V$ (oxygen vacancy or defects) and $O_C$ (chemisorbed oxygen species).	<b>118</b>
<b>6.3</b>	(a) Field electron emission current density as a function of applied field (J–E) curves for the as-grown Au-ZnO nanowires (sample A - black) and Au-ZnO triangular nanoflakes (sample B – red); (b) shows corresponding Fowler–Nordheim (F–N) plots.	<b>119</b>
<b>6.4</b>	Shows work function mapping of samples A and B using Kelvin probe force microscopy (KPFM). Insets are the KPFM images of the corresponding samples. Both the scale bars in the images correspond to 4 $\mu\text{m}$ .	<b>121</b>
<b>6.5</b>	Field emission current stability of the as-grown Au-ZnO hetero-nanostructures array (samples A and B) versus time indicating fairly stable emission current over a large period (4 hrs) of time.	<b>121</b>
<b>6.6</b>	(a) Presents typical room temperature PL spectra taken from sample B (Au-ZnO TNFs) after 60 min and 90 min annealing at 900 $^{\circ}\text{C}$ in oxygen ambiances, showing decrease in defect emission related to oxygen vacancy. (b) Shows field emission characteristics of the annealed samples. F-N plots of the corresponding samples are shown in the inset.	<b>124</b>
<b>6.7</b>	(a)–(d) present the relaxed structures considered for DFT calculations (VASP) of ZnO(0001), $O_{\text{vac}}$ -ZnO(0001), Au(001)/ZnO(0001) and Au(001)/ $O_{\text{vac}}$ -ZnO(0001), respectively.	<b>126</b>
<b>6.8</b>	Electrostatic potential along z-axis considering vacuum as reference energy for (a) ZnO(0001) (b) $O_{\text{vac}}$ -ZnO(0001) (c) Au(001)/ZnO(0001) and (d) Au(001)/ $O_{\text{vac}}$ -ZnO(0001). $E_F$ and $E_V$ correspond to energy of the Fermi and vacuum level, respectively. $\Phi$ denotes the work function of the defined surface.	<b>127</b>
<b>7.1</b>	(a) Cross-sectional low magnification TEM micrograph of 5 nm Au/GeO <sub>x</sub> /Ge(100) as-deposited sample. (b) HRTEM image recorded from the highlighted region of (a). (c) Low magnification SEM image of the as-grown Au-GeO <sub>x</sub> nanowires (NWs) after air annealing @ 600 $^{\circ}\text{C}$ for 30 min, showing the high-yield growth. (d-e) High magnification SEM images of Au-GeO <sub>x</sub> NWs for 30 min and 1 hr growth, respectively; two inset figures at left side are corresponding 54 $^{\circ}$ tilted SEM images and other two inset figures at right side are single Au-GeO <sub>x</sub> NW BSE images from the corresponding samples.	<b>136</b>
<b>7.2</b>	(a) The XRD pattern of the as-grown products on Ge(100) substrate, confirming the GeO <sub>2</sub> phase with hexagonal structure. (b) TEM micrograph of a single Au-GeO <sub>2</sub> NW, showing dark contrast gold (Au) at the tip and (c) shows SAED pattern taken along $[1\bar{2}13]$ zone axis of hexagonal structure from the dotted circle in figure (b).	<b>137</b>
<b>7.3</b>	(a) SEM micrograph show the growth of GeO <sub>2</sub> NWs only on the Au coated region of the Ge(100) substrate after air annealing @ 600 $^{\circ}\text{C}$ for 30 min. (b-c) Show SEM images of the etch pits formed via active oxidation (surface	

decomposition) on the Au coated and uncoated regions on the native oxide Ge substrate during growth of NWs.	138
<b>7.4</b> (a–b) show SEM images of after annealing @ 600 °C for 30 min under low vacuum and 40 sccm Ar flow conditions, respectively. (c) Shows magnified SEM image of the highlighted region in panel (b). (d) The XRD pattern of the as-grown products on Ge(100) substrate in Ar ambiance. (e) Low-mag TEM image of a Au-GeO <sub>2</sub> NW grown in Ar ambiance. (f) Typical SAED pattern from single GeO <sub>2</sub> NW recorded along [0001] zone axis of hexagonal structure. (g) Shows SEM image of the sample annealed in 40 sccm O <sub>2</sub> flow.	139
<b>7.5</b> Schematic diagram of a plausible mechanism involved in GeO <sub>2</sub> NWs growth. (a) as-deposited substrate before annealing. (b–c) show the expected processes involved in the VLS growth of Au-GeO <sub>2</sub> NWs (for the case of as-deposited substrate annealed in air ambiance).	141
<b>7.6</b> Room temperature PL spectra from GeO <sub>2</sub> NWs obtained at 600 °C annealing (a) in air atmosphere and (b) under 40 sccm Ar flow. (c) Comparative diffuse reflectance spectra. (d) Low-mag TEM image of Au NPs decorate Au-GeO <sub>2</sub> N/MWs (grown in Ar ambiance).	142
<b>7.7</b> (a) Schematic representation of photodetector device under illumination. (b) I-V characteristics of the three photodetectors made of as-grown N/MWs, Au NPs decorated similar N/MWs and without sample (i.e., Al <sub>2</sub> O <sub>3</sub> /p-type Si(100), called as control device) measured in the dark and under the illumination of 0.2 mW/cm <sup>2</sup> of visible light ( $\lambda = 540$ nm). (c) Time responses of the devices with same bias = –2.0 V, under the visible light ( $\lambda = 540$ nm, 0.2 mW/cm <sup>2</sup> ) illumination. (d–e) Show spectral responsivity and EQE spectra of the corresponding devices respectively.	144

# Chapter 1

## Introduction

The field of nanoscience and nanotechnology is a developing inter-disciplinary paradigm that encompasses diverse fields of science and engineering, where we synthesis materials and machine their properties in a useful way for device integration at nanometric regime. Any materials with characteristic length less than 100 nm at least in one direction can be defined as nanoscale materials. At this length scale, because of inherited high surface to volume ratio, almost all materials show unusual physical, chemical and mechanical properties as compared to what they exhibit in bulk or macro scale [1-5]. Eventually, target of nanotechnology is to establish a control over tailoring properties of nanomaterials for multi-disciplinary applications such as, nanoscale electronic devices, energy storage, sensors, nanomedicine and solar cells, etc. With the emerging area of nanoscience and nanotechnology, one-dimensional (1D) inorganic semiconductor nanostructures (NSs) of various morphologies (such as nanowires, nanotubes, nanoflakes, nanobelts etc.) have been considered as ideal systems, not only for fundamental importance in basic science but also to explore their potential in technological applications [2-9]. Among the inorganic semiconductor NSs, 1D oxide semiconductor NSs are the focus of current research interests both in experimentally as well as theoretically because of their largely tunable stable physical, chemical and mechanical properties along with easy large scale synthesis viability [5, 6, 9-12]. There are many typical functional oxide semiconductors (OS) nanostructures being studied over the decades, that include but not limited to ZnO [11-18], TiO<sub>2</sub> [19, 20], GeO<sub>2</sub> [21-25], CuO [26], Ga<sub>2</sub>O<sub>3</sub> [27], In<sub>2</sub>O<sub>3</sub> [28], WO<sub>3</sub> [29], SnO<sub>2</sub> [30]. Owing to their versatile properties, they have been used in many applications, such as, transparent electronics, piezoelectric transducers, photovoltaics, catalysis, sensors, optoelectronics devices [5, 10-32]. This thesis work is based on two different classes of high direct bandgap oxide semiconductors (OSs), one is group II-VI semiconductor zinc oxide (ZnO) having bandgap  $\approx 3.37$  eV and other is group IV-VI germanium oxide (GeO<sub>2</sub>) having bandgap  $\approx 5$  eV [13, 33].

From materials perspective, among all the OSs, ZnO has been considered one of the most versatile material owing to high mechanical strength, thermal stability, high oxidation resistivity, non-toxic character, abundant in reserve and low-cost large scale synthesis viability [12, 16, 17]. ZnO, generally, can have three different types of crystal structures: hexagonal wurtzite, zincblende and rocksalt phases. But, in ambient pressure and temperature ZnO found to have stable hexagonal wurtzite structure (space group  $C6mc$ ) with lattice constants,  $a = b = 0.3249$  nm and  $c = 0.5206$  nm [16, 34]. The structure of ZnO consists of tetrahedrally co-ordinated alternating planes composed of  $O^{2-}$  and  $Zn^{2+}$  ions, which are stacked along the c-axis (see Figure 1.1(a)). This tetrahedral coordination of oppositely charged ions in ZnO creates an asymmetry along hexagonal c-axis and consequently possesses a spontaneous polarization because of finite dipole moment [14, 15, 35]. Figure 1.1(b) represents a simple crystal structure of ZnO in wurtzite phase with most commonly observed low index lattice planes,  $\{0001\}$  polar surfaces and two sets of non-polar surfaces  $\{10\bar{1}0\}$  and  $\{1\bar{2}10\}$ . It has been found theoretically that surface energies of the polar planes are higher than the non-polar planes [36]. There are four major advantages of ZnO nanostructures listed below, that made them available for diversified applications.

1. It is a wide direct band gap ( $\approx 3.37$  eV at 300 °K) semiconductor with high exciton binding energy of  $\approx 60$  meV, which is larger than the thermal energy at room temperature (RT). These facts result in excitonic emission from ZnO at RT or above and make it transparent to visible light [11, 37]. In this regards ZnO is fascinating material for photonic and optoelectronic UV/blue device applications, such as, light emitting diode, photovoltaics, laser diode, transparent electrode, etc. [10, 13, 38, 39].
2. Because of inherent spontaneous polarization, ZnO is recognized as a piezoelectric material, which leading to its applications in the field of electromechanical sensors, transducers, nano-resonators and cantilevers, etc. [14, 35]. ZnO NSs are promising materials for field emission based devices owing to their mechanical strength, thermal stability, high oxidation resistivity and low electron affinity [17]. High energy polar surfaces  $\{0001\}$  of ZnO NSs show high degree of surface activity in terms of interactions with surrounding species, which render their use as various chemical and gas sensors [11, 12, 14-16].

3. ZnO is known to be very non-toxic and bio-compatible material, so they can be uses in biological and biomedical applications, widely [14-16, 35].
4. ZnO NSs of various morphologies and dimensionalities are grown very easily by means of numerous simple growth techniques. Plenty of potential applications are open to the ZnO NSs of various morphologies (such as, nanowires, nanorods, nanobelts, nanoflakes, nanoparticles etc.) along with all above qualities [14-16, 35-39].

Based on the multifunctional nature of ZnO NSs, they are used as an ingredient in many products used in our day to day life, such as, sunscreens, self-cleaning coatings, skin lotions, ointments, lubricants/paints, adhesives, tyres, etc. [40, 41].

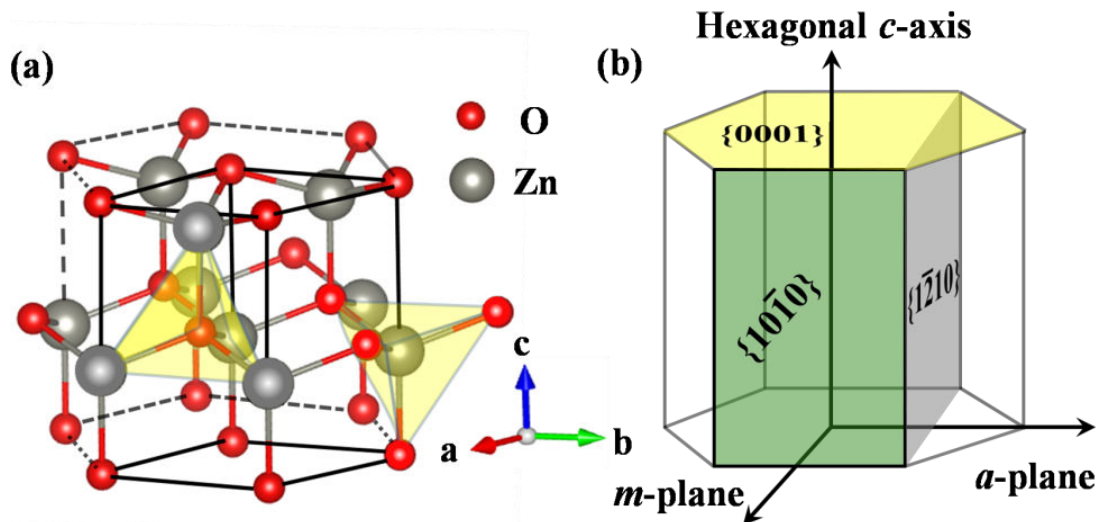


**Figure 1.1:** (a) Stick and ball representation of ZnO wurtzite structure showing tetrahedral coordination (using VESTA) [42]. (b) Hexagonal ZnO with common low index planes.

Among many OSs group IV semiconductor (especially Si and Ge) oxides, in particular  $\text{GeO}_2$  nanostructures based gadgets are very attractive for complementary metal oxide semiconductor (CMOS) integrated circuit machinery, photovoltaic and photocatalytic applications [43-45].  $\text{GeO}_2$  is another important OS (group IV-VI compound OS), last portion of this thesis work is based upon.  $\text{GeO}_2$  can be found in both crystalline (hexagonal and tetragonal phases) as well as in amorphous phase [46]. In ambient condition, they are generally found in hexagonal phase with germanium having coordination number four (4) and lattice parameters,  $a = b = 0.498 \text{ nm}$  and  $c = 0.565 \text{ nm}$  [47, 48]. Figures 1.2(a, b) show



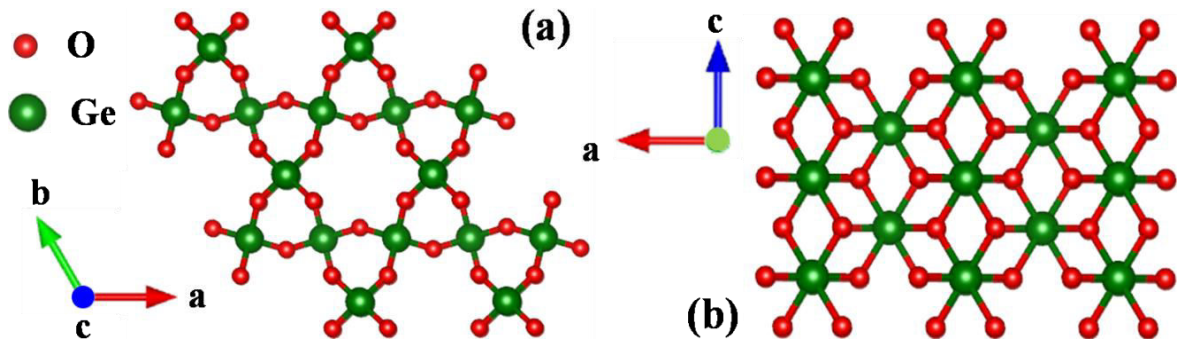


**Figure 1.2:**  $2 \times 2 \times 2$  unit cells of  $\text{GeO}_2$  crystal structures, (a) Hexagonal and (b) tetragonal rutile-like (drawn using VESTA) [46].

stick and ball representation of hexagonal and tetragonal crystal structures of  $\text{GeO}_2$ .  $\text{GeO}_2$  has got lot of attention due to its wide band gap ( $\approx 4.8 - 5.1$  eV) [33, 43, 49, 50], low optical loss [51], high thermal stability [52] as well as due its unique photonic, electronic [53] properties.  $\text{GeO}_2$  is also identified as transparent conductive oxide (TCO) having potential in optoelectronics applications. Compared to other TCO, it has higher band gap, that makes this oxide suitable candidate for developing excitation dependent UV to near infrared luminescent devices by hosting high impurity [50, 52].  $\text{GeO}_2$  NSs, especially, nanowires are highly used as nano-connections in optoelectronic communications and optical waveguide devices owing to its high refractive index  $\approx 1.7$  [48, 54, 55]. They are also useful towards photovoltaic and photocatalytic applications [43]. Significant efforts have already been devoted on studying resistive switching properties of  $\text{GeO}_2$  both experimentally and theoretically, because of its high defect density, small Ge-O bond energy and dielectric property [22, 56]. Recently, 1D  $\text{GeO}_2$  NSs and their composite with conducting materials (like CNT, graphene, RGO etc.) have drawn enough research attention for their applicability in Li-ion battery as high-performance anode material following their high theoretical reversible capacity ( $1125 \text{ mAh g}^{-1}$ ), low operating voltage ( $\leq 1.5 \text{ V}$ ), high  $\text{Li}^+$  ion diffusivity and thermal stability [23-25].

The use of these wide direct bandgap homogeneous (single material component) nanostructures ( $\text{ZnO}$  and  $\text{GeO}_2$ ) towards visible-light driven applications are hindered by some apparent drawbacks: (i) they only can absorb ultraviolet light ( $\lambda < 380 \text{ nm}$ ) and have very limited visible light response; (ii) fast radiative recombination rate of photogenerated electron-hole pairs ( $\text{e}^-$ - $\text{h}^+$  pairs) [18, 57-61]. In this regard it is now paramount to develop standard ways not only to enhance their visible-light absorption capability but also to restrain fast radiative recombination processes for their practical optoelectronic and photocatalytic device applications. Potential improvement on their visible-light activities have been

accomplished by several ways, as follows: various elemental n-type doping to engineer bandgap [57, 62, 63], hybridization with noble metal nanoparticles (like, Au, Ag) [58, 60, 61, 64, 65], creation of oxygen vacancy [18, 59, 63], coupling with other semiconductors [66, 67] and annealing in different ambiances [68]. Combining plasmonic with photonics (i.e., hybridization with noble metal) and creation of oxygen vacancies as self-doping are the two best suitable ways for the improvements in visible-light sensitivity without disturbing host oxide semiconductor matrix. Recently, hybrid semiconductor-metal nanostructures have gathered lot of attention because they provide tunable physical and chemical properties superior to their individual (single component) properties, by combining their respective photonic and plasmonic properties [58, 60, 61, 65, 69]. It is well established that metal nanoparticles (NPs), such as, Au conjugated with semiconductor, enhances visible-light absorption and also increase electron density in the conduction band of semiconductor through plasmon enhanced hot electron transfer processes utilizing their surface plasmon resonance (SPR) properties [58, 61, 70]. Besides that, Au NPs (or other noble metal NPs) also helps to restrain the recombination of photogenerated charge carriers in the semiconductor matrix by acting as passive sink, results in improved light activity [58, 60, 61, 71]. On the other hand, presence of oxygen vacancies in high band gap OSs induces visible-light absorption via decrease in bandgap, at the same time serving as electron trap centers they improve photogenerated charge separation processes, which in turn enhance visible-light driven optoelectronic, photovoltaic and photocatalytic performances [18, 59, 63]. It is also important to mention that work function of oxide semiconductor can be greatly reduced by creation of oxygen vacancy in them, which helps to improve field emission performances [59, 72, 73]. But there are no such reports where influence of Au NP along with oxygen vacancies in oxide semiconductor, on work function and corresponding field emission properties are studied systematically. From earlier reports it is clear that synthesis of such oxygen deficient or metal NPs conjugated oxide semiconductor hybrid/hetero-nanostructures usually demands at least two or multistep expensive as well as time consuming physical or chemical protocols [18, 58-65]. Therefore, it is indispensable to develop a rational, simple and inexpensive growth technique for the scalable synthesis of intrinsically self-assembled oxygen deficient various oxide semiconductor-metal hetero-nanostructures (NSs/HNs) with improved visible-light harnessing capability.

The main objective of this thesis work is to present a simple *single step* growth technique to grow intrinsically self-assembled variable oxygen deficient Au capped ZnO and

GeO<sub>2</sub> hetero-nanostructures (HNs) of various morphologies and dimensionalities. Enhanced field emission and visible-light driven properties of these as-grown samples also have been addressed with possible underlying mechanisms.

The thesis is organized as follows: The working principles and instrumentations of all the experimental techniques that have been used for the growth, characterizations and possible applications related to this thesis work are described in the chapter 2. Chapter 3 deals with the *single step* catalyzed growth of two different morphologies (nanowires → NWs and triangular nanoflakes → TNFs) Au-ZnO hetero-nanostructures (HNs) of various sizes, areal densities and oxygen vacancy concentrations on native oxide Si(100), (110), (111) and single crystalline ZnO(0001) substrates using chemical vapor deposition (CVD) technique. The role of native oxide, substrate orientation and position in side growth chamber, catalyst Au layer thickness and vapor pressure on the growth of HNs have been discussed in detail. Possible growth mechanisms for the growth of ZnO NSs with and without faceted Au at the tips depending on the growth parameters have been proposed and explained. Surface enhance Raman spectroscopy (SERS) applications towards the detection of crystal violet molecules, using these Au-ZnO HNs coated Si substrates following their lower reflectance in the visible wavelength regime have been addressed in chapter 4. Possible correlations between antireflection properties, excitation wavelength and SERS activity of these plasmonic substrates are also suggested. Chapter 5 describes the visible light driven photocatalytic applications for degradation of organic pollutants (rhodamine B and phenol) following high visible-light photoresponse of the as-grown samples. Enhanced photocatalytic performance offered by triangular morphology Au-ZnO HNs (TNFs) sample is attributed to the presence of high oxygen vacancies in them, leading to their low charge transfer resistance. A new method of reducing ZnO work function ( $\Phi$ ) via combined presence of metal Au at the tip and oxygen vacancies has been proposed and corresponding enhanced field emission properties are studied in chapter 6. To deduce the effect of Au and oxygen vacancy concentrations on effective  $\Phi$  of ZnO, Kelvin probe force microscopy (KPFM) was used and also first principle density functional theory (DFT) calculations were done to support experimental findings qualitatively. Chapter 7 deals with a novel *single step* growth of Au nanoparticles capped GeO<sub>2</sub> hybrid/hetero nano/micro-wires (N/MWs) on 5 nm Au/GeO<sub>x</sub>/Ge(100) substrates, just via annealing in different ambiances without any external supply of source vapor. Different growth parameters (such as, catalyst, ambiance and annealing time) functions on the vapor-liquid-solid (VLS) growth of Au-GeO<sub>2</sub> N/MWs have been studied. The visible-light

photodetection application of these as-grown Au-GeO<sub>2</sub> N/MWs promoted by the presence of plasmonic Au NP at the tip in combination with high oxygen vacancies in them was also investigated. Summary and conclusions of the work presented in this thesis along with future research scopes in this area are given in chapter 8.

## References

- [1] C. N. R. Rao, P. J. Thomas and G. U. Kulkarni, *Nanocrystals: Synthesis, Properties and Applications* (Springer, 2007, ISBN: 978-3-540-68751-1).
- [2] P. Moriarty, *Rep. Prog. Phys.* **64**, 297 (2001).
- [3] P. Alvisato, *Science* **271**, 933 (1996).
- [4] C. Burda, X. Chen, R. Narayanan and M. A. El-Sayed, *Chem. Rev.* **105**, 1025 (2005).
- [5] S. Zhuiykov, *Nanostructured Semiconductor Oxides for the Next Generation of Electronics and Functional Devices: Properties and Applications* (Elsevier, 2013, ISBN: 978-1-78242-220-4).
- [6] P. D. Yang et al., *Adv. Mater.* **12**, 323 (2002).
- [7] T. Y. Zhai et al., *J. Phys. Chem. C* **111**, 2980 (2007).
- [8] Y. N. Xia et al., *Adv. Mater.* **15**, 353 (2003).
- [9] R. K. Joshi and J. J. Schneider, *Chem. Soc. Rev.* **41**, 5285 (2012).
- [10] T. Zhai et al., *Sensors* **9**, 6504 (2009).
- [11] Y. W. Heo et al., *Mater. Sci. Eng. R-Rep.* **47**, 1 (2004).
- [12] M. J. S. Spencer, *Prog. Mater. Sci.* **57**, 437 (2012).
- [13] M. H. Huang et al., *Science* **292**, 1897 (2001).
- [14] Z. L. Wang, *J. Phys.: Condens. Matter* **16**, R829 (2004).
- [15] S. Xu and Z. L. Wang, *Nano Res.* **4**, 1013 (2011).
- [16] U. Ozgur et al., *J. Appl. Phys.* **98**, 041301 (2005).

- [17] Z. Zhang et al., *Sci. Rep.* **4**, 4676 (2014).
- [18] S. A. Ansari et al., *Nanoscale* **5**, 9238 (2013).
- [19] L. Francioso and P. Siciliano, *Nanotechnology* **17**, 3761 (2006).
- [20] J. Liang and G. Zhang, *ACS Appl. Mater. Interfaces* **4**, 6053 (2012).
- [21] L. Nejaty-Moghadam et al., *J. Mater. Sci. Mater. Electron.* **26**, 6386 (2015).
- [22] A. V. Shaposhnikov et al., *Appl. Phys. Lett.* **100**, 243506 (2012).
- [23] Y. Lin, K. C. Klavetter, A. Heller and C. B. Mullins, *J. Phys. Chem. Lett.* **4**, 999 (2013).
- [24] Y. Son et al., *Nano Lett.* **14**, 1005 (2014).
- [25] X. Wang et al, *J. Am. Chem. Soc.* **133**, 20692 (2011).
- [26] S. Nandy et al., *Adv. Funct. Mater.* **25**, 947 (2015).
- [27] Y. C. Choi et al., *Adv. Mater.* **12**, 746 (2000).
- [28] M. J. Zheng et al., *App. Phys. Lett.* **79**, 839 (2001).
- [29] J. Liu, Z. Zhang, Y. Zhao, X. Su, S. Liu and W. Wang, *Small* **1**, 310 (2005).
- [30] X. Fang, J. Yan, L. Hu, H. Liu and P. S. Lee, *Adv. Funct. Mater.* **22**, 1613 (2012).
- [31] J. G. Lu et al., *Mater. Sci. Eng. R* **52**, 49 (2006).
- [32] A. Kolmakov and M. Moskovits, *Annu. Rev. Mater. Res.* **34**, 151 (2004).
- [33] D. Kuzum et al., *IEEE Trans. Electron Dev.* **58**, 1 (2011).
- [34] K. Kihara and G. Donnay, *Can. Mineral.* **23**, 647 (1985).
- [35] Z. L. Wang and J. Song, *Science* **312**, 242 (2006).
- [36] B. Meyer and D. Marx, *Phys. Rev. B* **67**, 035403 (2003).
- [37] H. J. Xiang et al., *Appl. Phys. Lett.* **89**, 223 (2006).
- [38] M. Willander et al., *Nanotechnology* **20**, 332001 (2009).
- [39] N. H. Nickel et al., *Zinc Oxide – A Material for Micro- and Optoelectronic Applications* (Springer, 2005, ISBN: 978-1-4020-3473-2).

- [40] G. E. J. Poinern, A Laboratory Course in Nanoscience and Nanotechnology (CRC Press, 2014, ISBN: 978-1-4822-3103-8).
- [41] C. Klingshirn, *Phys. Status Solidi (b)* **244**, 3027 (2007).
- [42] [https://en.wikipedia.org/wiki/Zinc\\_oxide](https://en.wikipedia.org/wiki/Zinc_oxide).
- [43] L. Nejaty-Moghadam et al., *J. Mater. Sci. Mater. Electron.* **26**, 6386 (2015).
- [44] C. Soci et al., *Nano Lett.* **7**, 1003 (2007).
- [45] Y. Jiang et al., *Adv. Funct. Mater.* **17**, 1795 (2007).
- [46] R. D. Oeffner, A computational study of GeO<sub>2</sub> (University of Cambridge, 1999).
- [47] H. McMurdie et al., *Powder Diffraction* **69**, 1 (1986).
- [48] P. Hidalgo, B. Mendez and J. Piqueras, *Nanotechnology* **18**, 155203 (2007).
- [49] P. Broqvist, J. F. Binder and A. Pasquarello, *Appl. Phys. Lett.* **94**, 141911 (2009).
- [50] P. Hidalgo et al., *J. Phys. Chem. C* **113**, 17200 (2009).
- [51] C. I. Wu and T. P. Hogan, *Mater. Res. Soc. Symp. Proc.* **940**, 13 (2009).
- [52] S. L. Shinde and K. K. Nanda, *CrystEngComm* **15**, 1043 (2013).
- [53] Z. Jiang et al., *Mater. Lett.* **59**, 416 (2005).
- [54] F. Bellenger et al., *IEEE Electron Device Lett.* **31**, 402 (2010).
- [55] Y. Kamata, *Mater. Today* **11**, 30 (2008).
- [56] A. Prakash et al., *Nanoscale Res. Lett.* **8**, 220 (2013).
- [57] S. Liu, C. Li, J. Yu and Q. Xiang, *CrystEngComm* **13**, 2533 (2011).
- [58] M. D. L. Ruiz Peralta et al., *ACS Appl. Mater. Interfaces* **4**, 4807 (2012).
- [59] J. Wang et al., *ACS Appl. Mater. Interfaces* **4**, 4024 (2012).
- [60] W. He et al., *J. Am. Chem. Soc.* **136**, 750 (2014).
- [61] M. Wu et al., *ACS Appl. Mater. Interfaces* **6**, 15052 (2014).
- [62] A. Asahi, T. Morikawa, T. Ohwaki, K. Aoki, and Y. Taga, *Science* **293**, 269 (2001).

- [63] A. B. Patil et al., *J. Solid State Chem.* **184**, 3273 (2011).
- [64] C. Gu et al., *Cryst. Growth Des.* **9**, 3278 (2009).
- [65] Y. M. Chang et al., *ACS Appl. Mater. Interfaces* **4**, 6676 (2012).
- [66] H. Yin et al., *ACS Appl. Mater. Interfaces* **6**, 14851 (2014).
- [67] S. Jung and K. Yong, *Chem. Commun.* **47**, 2643 (2011).
- [68] Q. Zhao et al., *Appl. Phys. Letter.* **88**, 033102 (2006).
- [69] J. Zeng et al., *Adv. Mater.* **22**, 1936 (2010).
- [70] X. Lang, X. Chen and J. Zhao, *Chem. Soc. Rev.* **43**, 473 (2014).
- [71] C. Clavero, *Nature Photonics* **8**, 95 (2014).
- [72] D. C. Look et al., *Phys. Rev. Lett.* **95**, 225502 (2005).
- [73] K. K. Naik et al., *Appl. Phys. Lett.* **105**, 233101 (2014).

# Chapter 2

## Experimental Techniques

### 2.1 Introduction

This chapter deals with the details of experimental techniques that are employed to grow metal (Au) catalyzed oxide semiconductor nanostructures (NSs) (such as, faceted Au-ZnO and Au-GeO<sub>2</sub> hetero-nanostructures (HNs) of different morphologies), to characterize and check their performance in practical applications. In this thesis work, throughout Au nanoparticles (NPs) are used as catalyst for the growth of both Au-ZnO and Au-GeO<sub>2</sub> HN on various oriented silicon (Si) and germanium (Ge) substrates. The growth of Au thin films on silicon (Si) and germanium (Ge) substrates (with and without native oxide) using two types of physical vapor deposition (PVD) techniques (high vacuum coating method and ultra high vacuum based molecular beam epitaxy (MBE) method) is described. After deposition, we have annealed these as deposited substrates in ambient to form discrete Au NPs. Then we have used these Au NPs decorated Si and Ge substrates to grow Au-ZnO and Au-GeO<sub>2</sub> HN using chemical vapor deposition (CVD) technique. These deposition and growth techniques are followed by the description of characterization techniques viz. transmission electron microscopy (TEM), scanning electron microscopy (SEM), energy dispersive X-ray spectrometry (EDS), X-ray diffraction (XRD), photoluminescence (PL), cathodoluminescence (CL), X-ray photoelectron spectroscopy (XPS) and UV-Visible absorption/reflectance spectroscopy methods. Following these, we have highlighted the applications of aforementioned samples with the help of three major measurement techniques: surface enhanced Raman spectroscopy (SERS), electrochemistry, field emission (FE) and current voltage (I-V) measurements.

### 2.2 Thin film and nanostructures growth method

Thin film deposition is a major key to the creation of microelectronic devices. Large scale efforts are on to improve the quality of the deposited thin films, as this enhances the



efficiency of the created devices. Advancements in analytical instrumentation in the past few decades have helped in better understanding of the physics and chemistry of thin films, surfaces and interfaces of microstructures. Thin film depositions can be either purely physical-like evaporative methods, or purely chemical-like gas and liquid-phase processes [1]. Some of the other techniques that involve glow discharge and reactive sputtering can be regarded as physical-chemical methods. In this thesis, both physical viz. coating methods at high and ultra high vacuum conditions and chemical viz. CVD technique have been used.

### **2.2.1 Thermal evaporation at high vacuum (HV) (physical vapor deposition (PVD) technique)**

Thermal evaporation (physical vapor deposition (PVD)) is the vaporization of a material by heating to a temperature such that the vapor pressure becomes appreciable and atoms or molecules are lost from the surface into vacuum [2]. PVD employs the atomic vapor cloud formed by the vaporization of metal in a vacuum environment to cover all the surfaces. It involves the following sequential steps: (i) conversion of deposited material into vapor by heating, (ii) transportation of vapors from source to the target substrate, (iii) condensation of the vapor on the substrate and (iv) formation of thin film. Heating of the material in PVD can be done in several ways. The simplest one is the resistive heating: In this method a wire of tungsten or a boat of molybdenum is resistively heated, so that the metal being in thermal contact to the wire melts and evaporates. In electron beam evaporation, a focused beam of electrons is directed at the material, thus heating up and evaporating the material. A thermal evaporator uses an electric resistance heater to melt the material and raise its vapor pressure to a useful range. This is done at high vacuum (pressure of  $\approx 10^{-5}$  to  $10^{-7}$  mbar) condition to provide high mean free path and to reduce the incorporation of impurities from the residual gas in the chamber. Obviously, only materials with a vapor pressure higher than the heating element can be deposited without contamination of the film. The principal requirement for successful thin film is that the mean free path of the evaporated atoms must be much larger than the distance between the source and substrate [3]. The mean free path ( $L$ ) of a molecule in a gas is  $L = k_B T / \pi D^2 t$  where,  $D$  is the diameter of the gas molecules, and  $T$  is the temperature of the gas,  $k_B$  is the Boltzmann constant.

In this thesis work, thermal evaporation technique is employed to deposit gold (Au) film of  $\approx 1$  nm and  $\approx 5$  nm thick in high vacuum coating unit using molybdenum (Mo) boat.

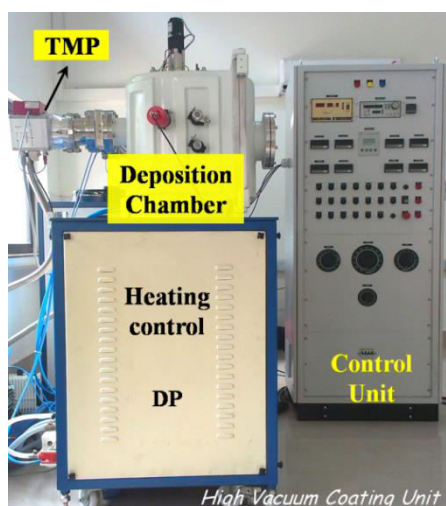


**Figure 2.1:** *High vacuum coating unit (M/s Vacuum Techniques Pvt. Ltd) installed at Institute of Physics, Bhubaneswar.*

Large current ( $\geq 120$  Amp) was passed through the boat, heated up the material to melt and evaporated for deposition (power  $\approx 130$  Watt). The coating unit consists of a cylindrical, stainless steel vacuum chamber, approximately  $\approx 50$  cm height and  $\approx 35$  cm in diameter (Figure 2.1). This chamber is connected to double stage pumping system: 250 liter per min rotary pump and either 280 liter per second oil diffusion pump or turbo molecular pump. Pirani and penning gauges are used to monitor the vacuum level during deposition. Thickness of deposited film is measured using thickness monitor (Inficon) with a quartz crystal microbalance. The quartz crystal mechanically oscillates when ac voltage is applied to it (piezoelectric effect) [4]. The resonance frequency of oscillations is dependent on the mass of the film deposited onto it. Quartz thickness monitor can measure thickness of about a single atomic layer with relatively high accuracy. To get accuracy in deposited film thickness, quartz thickness monitor is calibrated with Rutherford backscattering spectrometry (RBS) and cross-sectional TEM measurements.

### 2.2.2 Thermal evaporation using molecular beam epitaxy (MBE)

This is another thermal evaporation technique where deposition is carried out under ultra high vacuum (UHV) condition (a base pressure of  $\approx 2 \times 10^{-10}$  mbar). When we need to characterize an ultra-clean surface at an atomic level, then the fundamental demand would be that, over the duration of experiment the surface composition remains unchanged. To meet this requirement, the experimental chamber has to be at UHV. The concept of vacuum can be understood in terms of parameters such as molecular density, mean free path and the time constant to form a monolayer (ML). One ML corresponds to  $\approx 6.78 \times 10^{14}$  atoms-cm $^{-2}$  for a

Si(100) surface. Compared to low vacuum ( $\approx 10^{-2}$  mbar) in UHV conditions ( $\approx 10^{-10}$  mbar), mean free path of atoms in the growth chamber increases by factor of  $\approx 10^5$  and the time required to grow one ML increases by a factor of  $\approx 10^6$  [5]. Molecular beam epitaxy (MBE) is a sophisticated vacuum deposition system under UHV condition; where in, a very precise control over growth parameters, such as, deposition rate and uniformity are possible. The growth process is mainly governed by surface kinetics taking place during the incident atomic/molecular beam interacts with surface atoms on the substrate. Inside MBE chamber, one can observe the real time growth process by in-situ surface sensitive methods, such as, reflection high energy electron diffraction (RHEED), Auger electron spectroscopy (AES) etc.

In this thesis work, we have used a custom-designed, compact MBE system along with the capability to transfer the MBE-grown samples to a UHV STM without breaking vacuum (Omicron, GmbH). A thin Au film of thickness 10 ML ( $\approx 2$  nm) was deposited on native oxide removed cleaned Si(100) substrate under UHV (base pressure  $\approx 2 \times 10^{-10}$  mbar) condition. Native oxide removal from Si substrate was done through degassing at 600 °C for about 12 hours inside the chamber, followed by flashing for about  $\approx 2$  minutes by direct heating at a temperature of 1200 °C. After the deposition, the sample was taken out of MBE chamber for further use as template for ZnO NSs growth.

### 2.2.3 Chemical vapor deposition (CVD) technique

Chemical vapor deposition (CVD) involves the formation of a thin solid film on a substrate material by a chemical reaction of vapor phase precursors. It can thus be distinguished from PVD processes, such as, evaporation and reactive sputtering that involve the adsorption of atomic or molecular species on the substrate. The chemical reactions of precursor species occur both in the gas phase and on the substrate. Reactions can be promoted by heat (thermal CVD) or higher frequency radiations, such as, UV (Photo assisted CVD) or plasma (plasma enhanced CVD). The basic idea of this method is to evaporate source materials at high temperature in a horizontal tube furnace. The vapor is then transported in a carrier gas and subsequently deposited in a different part of the furnace to form the desired nanostructures. Figure 2.2 shows a schematic diagram of the experimental apparatus used in the studies presented here. The furnace consists of a  $\approx 100$  cm long horizontal quartz tube with an inner diameter of  $\approx 4.5$  cm, a sample holder/boat that is made of ceramic, and silicon carbide rods as heating elements. One side of the quartz tube was connected to the gas inlet

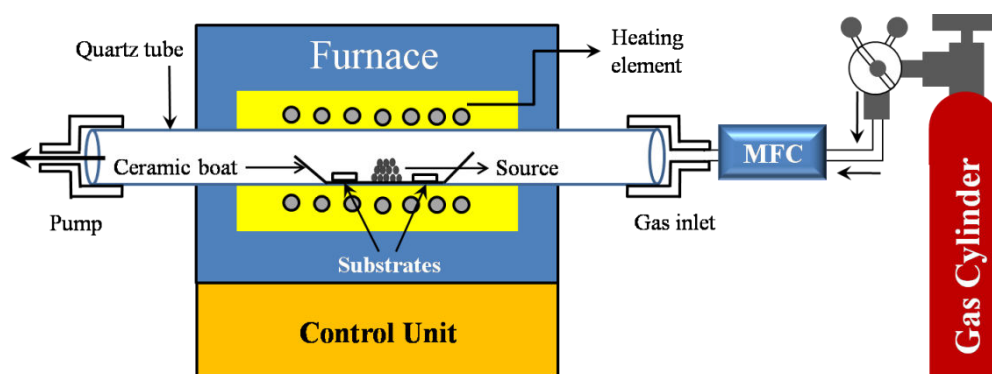


**Figure 2.2:** Schematic illustration of the single zone horizontal quartz tube furnace, that is used as Chemical Vapor Deposition (CVD) setup for the work in this thesis.

controlled by a mass flow controller (MFC) (Sevenstar D07-19B) and the other side had a gas outlet. This has a maximum temperature rating of 1400 °C and uses a PID controller (Honeywell DC1040 controller model) is used to control the temperature. Normally, source powder or mixture is placed in a ceramic boat and positioned in the middle of the furnace, which is at the highest temperature. The substrates are normally placed at down-stream or up-stream positions for collecting the produced vapor (Figure 2.2). Both ends of the tube are covered by stainless steel flanges and sealed with rubber high temperature O-rings. This quartz tube furnace can also be evacuated to low vacuum conditions ( $\approx 10^{-2}$  mbar). In the next section, various mechanisms mainly vapor-liquid-solid (VLS), vapor-solid (VS) and solid-liquid-solid (SLS) mechanisms for the growth of nanostructures with and without the use of catalysts are briefly presented below.

## 2.2.4 Growth mechanisms

### 2.2.4.1 Vapor-liquid-solid (VLS) mechanism

In 1964, Wagner and Ellis, first proposed the VLS growth mechanism for understanding Au catalyzed Si whiskers growth, having a whisker diameters of several hundred nanometers to a few micrometers [6]. Since then, this method has been employed to various material systems with diameters as thin as few nanometers, as well [7-9]. For the fabrication of compound and oxide semiconductor nanostructures, metal thin film or nanoparticles (NPs) can be used as a catalyst [10, 11]. A schematic illustration of the basic VLS mechanism for growth of ZnO nanostructures is shown in Figure 2.3 with Au as a catalyst metal. In the initial stage of VLS growth, catalyst metal is deposited on the substrate

form of a thin layer or colloidal particles. This substrate is then heated to sufficiently high temperatures and at the same time vapor phase source (for this case Zn and O produced via carbothermal reduction) material is then streamed into the reactor with the help of carrier gas. The catalyst droplet acts like a sink, collecting the growth species (Zn and O atoms/molecules) impinging on the substrate and forms eutectic alloy droplets at  $\approx 684^\circ\text{C}$  [12]. These enter the eutectic alloy droplet and adapt the liquid phase (VLS). Since the accommodation coefficient in the liquid droplet is high, this allows the droplet to supersaturate with the vapor source material. Since at the surface of the liquid droplet the vapors have high Gibbs free energy and its minimization becomes the driving force for the diffusion of vapors into the droplet. With time, the concentration of source material in the droplet rises beyond its solubility limit and the catalyst particle becomes supersaturated. As a consequence, the material starts to precipitate beneath the metal catalyst particle, nucleating the nanowire or nanotube in the solid phase. With continuous supply of source vapor, the metal catalyst particle is raised as the growing structure underneath it, gains in length [13]. Under ideal VLS growth conditions, the diameter of the grown structure corresponds to the size of the metal catalyst droplets and the structures length is directly proportional to the duration of growth process.

VLS mechanism is purely driven by energy minimization, where change in Gibbs free energy is the driving force for the growth of 1-D nanostructures [14]. For the growth kinetics, consider the growth of ZnO NSs using Au catalyst on Si substrate, Au-Zn alloy droplet is shown on the substrate (Figure 2.4) along with the formation of ZnO layer of initial thickness

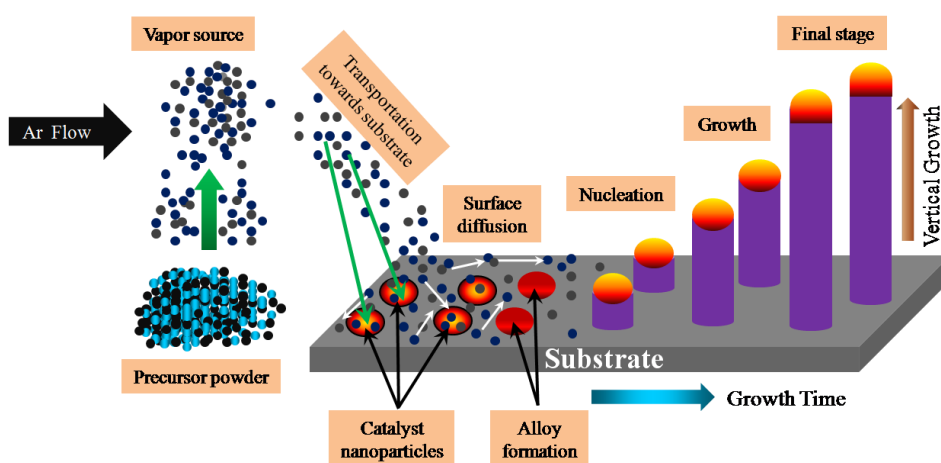


**Figure 2.3:** Schematic illustration of the VLS growth mechanism for metal-assisted nanowire; impinging of vapors, alloy formation, nucleation and formation of vertically oriented nanowires.

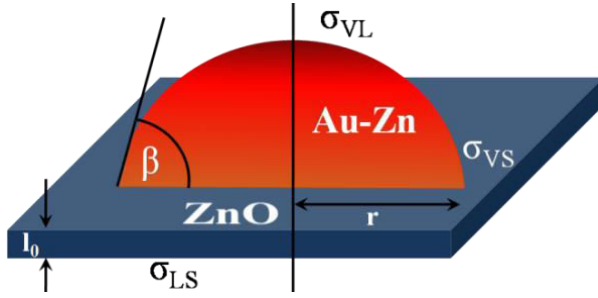


**Figure 2.4:** Schematic of the Au-Zn alloy droplet with ZnO layer on substrate.

$l_0$ . Here,  $\beta$  is contact angle,  $\sigma_{LS}$ ,  $\sigma_{VS}$  and  $\sigma_{VL}$  are the surface free energy of liquid-solid, vapor-solid and vapor-liquid interfaces, respectively. In this mechanism, during the transformation from a vapor state to a solid state, the change in Gibbs free energy ( $\Delta G$ ) is given as [14],

$$\Delta G = -\pi r^2 l_0 k_B T \ln(\eta)/\Omega + 2\pi r l_0 \sigma_{VS} \quad (2.1)$$

Here,  $P^{ZnO}$  is the vapor pressure of ZnO and  $P_{eq}^{ZnO}$  is the equilibrium vapor pressure of ZnO,  $\eta = P^{ZnO}/P_{eq}^{ZnO}$  is the vapor pressure supersaturation ratio,  $l_0$  is the thickness of ZnO layer,  $\sigma_{VS}$  is the surface tension of the vapor–solid interface,  $\Omega$  is the volume of the ZnO unit cell,  $r$  is the radius of the catalyst droplet and  $T$  is the substrate temperature. First term in the right hand side of equation 2.1 represents the reduction (due to –ve sign) in the Gibbs free energy due to crystal formation, whereas, the second term represents the increase in the surface energy due to increase in surface area. Since the change in Gibbs free energy has two components: surface tension and line tension [15], one can write the above equation in the form of effective surface tension and effective line tension;

$$\Delta G = \pi r^2 \sigma_{LS}^c + 2\pi r \tau^c \quad (2.2)$$

where,  $\sigma_{LS}^c = -l_0 k_B T \ln(\eta)/\Omega$  is called effective surface tension component, acting along the liquid-solid interface as an in-plane vector quantity and  $\tau^c = l_0 \sigma_{VS}$  is called effective line tension component, acting along the circumference of the liquid-solid interface as in-plane vector quantity. The change in Gibbs free energy can be simply written in the form of overall effective chemical tension ( $\sigma^c$ ) as;

$$\sigma^c = \sigma_{LS}^c + \tau^c/r \quad (2.3)$$

From above equation, one can conclude that the chemical tension is responsible for nanostructure shape. Final morphology of nanostructure depends on supersaturation ratio  $\eta$ , growth temperature  $T$ , and the radius of catalyst droplet  $r$ .  $\sigma^c$  depends on  $r$  which varies during the growth. For the wire to grow, the condition  $\sigma^c < 0$  must hold throughout the growth, otherwise the nanowire growth stops.

### 2.2.3.2 Vapor-solid (VS) mechanism

The second important mechanism relevant to this thesis work is the vapor-solid (VS) mechanism [16]. The growth of 1-D nanostructures (NSs) without the assistance of the metal catalyst by using thermal evaporation is referred to vapor-solid (VS) mechanism. Considering the ZnO NSs growth, Zn vapors are first produced either by carbothermal reduction method or by evaporation method and subsequently carried by carrier gas (Argon) and condensed directly onto substrate without any intermediate stage of a liquid catalytic droplet and finally oxidation occurs to form ZnO NSs as shown (Figure 2.5). Due to anisotropic properties of the different surfaces of the crystals, the atoms on the different surfaces have a tendency to minimize their surface energies to form nanostructures. In VS growth, any coverage will be quite thin and also nucleation will occur preferentially at substrate regions where there are imperfections (e.g. dislocations threading to the surface) [17]. Furthermore, surface defects, such as, impurities or etch pits would act as nucleation centers on the substrate [18]. Even the metal catalyst particles employed in VLS growth, can also aid the nucleation of VS-grown NSs at suitable growth conditions, where the catalyst particle acts only as nucleation site and remains at the bottom during growth [19]. In general, VS grown nanostructures are catalyst free. The dimensions of the nanostructures depend on the growth conditions and properties of the buffer or nucleation layer. Therefore, in the VS mechanism, the positions and densities of the grown nanostructures are very difficult to control compared to the nanostructure formation guided by a catalyst assisted VLS growth.

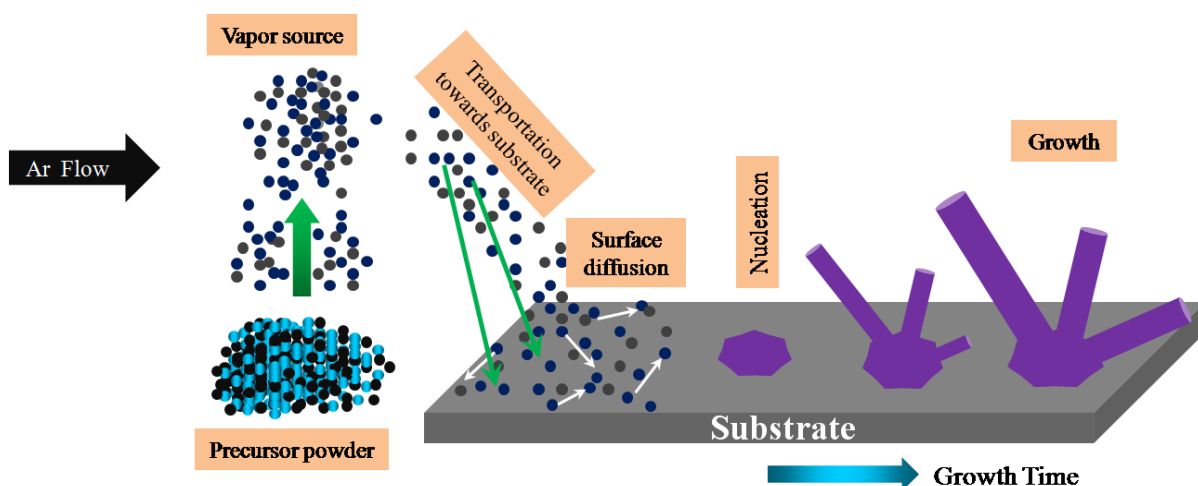


**Figure 2.5:** Schematic of VS growth mechanism, impinging of vapors, formation of seed and formation of nanowires.

### 2.2.3.3 Solid-liquid-solid (SLS) mechanism

Unlike the cases of VLS and VS, the solid-liquid-solid (SLS) growth mechanism is relatively straightforward. SLS growth mode explains the synthesis of nanowires, such as Si without any gas phase precursor like  $\text{SiH}_4$  or  $\text{SiCl}_4$ . Silicon nanowires can be grown directly on a metal layer (specifically Au and Ni) covered silicon (Si) substrate, where metal acts as catalyst and Si substrate acts as the source of silicon atoms [20]. In the SLS process a metal catalyst is first deposited on silicon substrate. Then annealing of the as-deposited Si substrate leads to formation of metal-silicon alloy droplet. To form these eutectic alloy droplets, the temperature should be beyond eutectic temperature corresponding to their binary phase diagram. If one uses Au as catalyst, then the eutectic temperature would be  $\approx 363^\circ\text{C}$ , whereas for Ni catalyst, it is  $\approx 993^\circ\text{C}$  [20, 21]. As the vaporization temperature of Si is  $\geq 1400^\circ\text{C}$ , so at those temperatures the only source of Si is the silicon substrate. Because of the relatively high solubility of Si in the eutectic alloy droplet (such as  $\text{Ni}_x\text{Si}_{1-x}$  and  $\text{Au}_x\text{Si}_{1-x}$ ), more Si atoms will diffuse through the solid substrate–liquid alloy interface into the liquid alloy phase. Now, continuous supply of silicon atoms from the substrate to the droplet at elevated temperatures causes supersaturation of silicon atoms inside the alloy droplet (such as  $\text{Ni}_x\text{Si}_{1-x}$  and  $\text{Au}_x\text{Si}_{1-x}$ ) which leads to precipitation of silicon at the interface of the droplet and the substrate. This precipitation of Si atoms via catalyst-Si alloy droplet at the solid substrate, results in formation of the Si nanowire. A schematic representation of Si NWs growth is shown in Figure 2.6 [21].

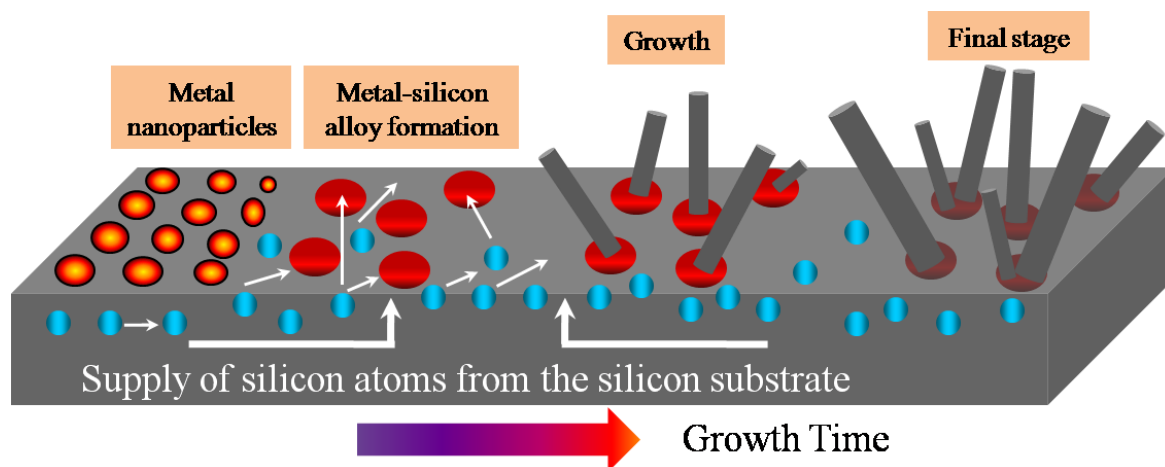


**Figure 2.6:** Schematic illustration of the SLS growth mechanism for metal assisted Si nanowires growth.



## 2.3 Characterization and application techniques

Surface morphology, shape and local compositional analysis of the as-grown samples were examined using field emission gun based scanning electron microscopy (FEG-SEM) of 20 kV electrons, equipped with back scattered electron (BSE) detector and energy dispersive X-ray (EDX) detector and high-resolution transmission electron microscopy (HRTEM) of 200 keV electrons with selected area electron diffraction (SAED) facility. X-ray diffraction (XRD) measurements were performed to check the crystallinity of samples. Optical properties were characterized by PL setup using a He–Cd laser (325 nm pump line), cathodoluminescence (CL) attached with SEM (at SINP, Kolkata) and UV–VIS–NIR spectrometer at room temperature. X-ray photoelectron spectroscopy (XPS) measurements were carried out at the base pressure of  $\leq 10^{-10}$  mbar using VG Scienta-R3000 hemispherical energy analyzer. All these facilities are present at IOP, except CL attachment to SEM.

We have employed those as-grown Au-ZnO and Au-GeO<sub>2</sub> hetero-nanostructures (HNs) towards potential applications, such as: SERS template for detection of low concentration biomolecules, harnessing visible part of the solar spectrum towards the photocatalytic degradation of organic compounds and microorganisms in water, electron field emitter, photo-detector and other plasmonic applications. Here, the working principles and instrumentations about the major techniques used for the above purposes will be discussed.

### 2.3.1 Transmission electron microscope (TEM)

Transmission electron microscopy (TEM) is a very valuable tool in materials science and is routinely used for studying the crystal structure and microstructure of materials [22–24]. Microscopy can be carried out with various probes, such as visible light, x-rays, electrons besides various scanning probe methods, such as, atomic force microscopy (AFM), scanning tunneling microscopy (STM) etc. The diffraction limited resolution constraints in studying materials at atomic scale using optical microscopy. An electron microscope is a type of microscope that uses energetic electrons (few 10 keV to few MeV) to illuminate a specimen [25]. Here, the wavelength of the electron  $\approx 0.008$ – $0.001$  nm and hence the spatial resolution improves and we get a much enlarged image than that of optical microscopy. The TEM is one class of electron microscope where electrons transmit through the sample to form an image below the specimen. During transmission, the electrons interact with the specimen,

giving rise to signals containing information about the internal structure and chemistry of the specimen. Electron diffraction patterns and lattice images are two forms of data which give crystallographic and morphological information in TEM. Lattice images are interference patterns between the direct beam and diffracted beams, viewed in direct space, and are obtained by high-resolution TEM (HRTEM) imaging. In the images, the spacing of a set of fringes represents the lattice spacing. The image or diffraction phenomena are aspects related to the scattering of incident electrons from the specimen atomic potentials. For direct information of defect structure on the atomic scale, an HRTEM is particularly useful (with low spherical aberration coefficient or aberration corrected) [23]. In selected area diffraction pattern (SAED), the sample is illuminated with a parallel electron beam to ensure the focusing of the transmitted and diffracted beam onto the back focal plane of the objective lens. A specific area of the sample is selected by an SAED aperture that is in an image plane conjugate with the sample in the electron optic system of the TEM. The inserted SAED aperture acts as a virtual aperture in the sample plane [22].

### 2.3.1.1 Instrumentation

The TEM instrumentation is easier to understand by dividing it into three sections: illumination section, sample stage, imaging section. A schematic diagram of illumination section, sample stage and imaging section is shown in Figure 2.7. An electrostatic lens in the form of Wehnelt cup is used after the filament to converge the maximum number of emitted electrons. Illumination section consists of electron source, Wehnelt cup, acceleration column and condenser lenses (Figure 2.7(a)). Usually thermionic gun (W, LaB<sub>6</sub>) or field emission gun (FEG) are used as electron sources. A high voltage is generated in a separated power supply unit using Cockcroft-Walton technique and is coupled to the acceleration column. Following the acceleration column, the energetic electron beam pass through the condenser lens system. After leaving the electron gun, electrons are accelerated towards the anode and enter the column. Since the velocity of the electrons is close to the speed of light, the wavelength of the electrons (at 200 keV) has to be corrected for relativistic effects:

$$\lambda = 2m_0eE/h^2 (1 + eE/2m_0c^2)^{0.5} \quad (2.4)$$

Using different size of condenser aperture, one can change the illuminated area on the specimen. The function of the condenser lens system is to provide a parallel or a convergent beam of electrons at the specimen surface (Figure 2.8). In practice, this is not possible and the beam always possesses a certain kind of convergence during imaging at higher magnification,

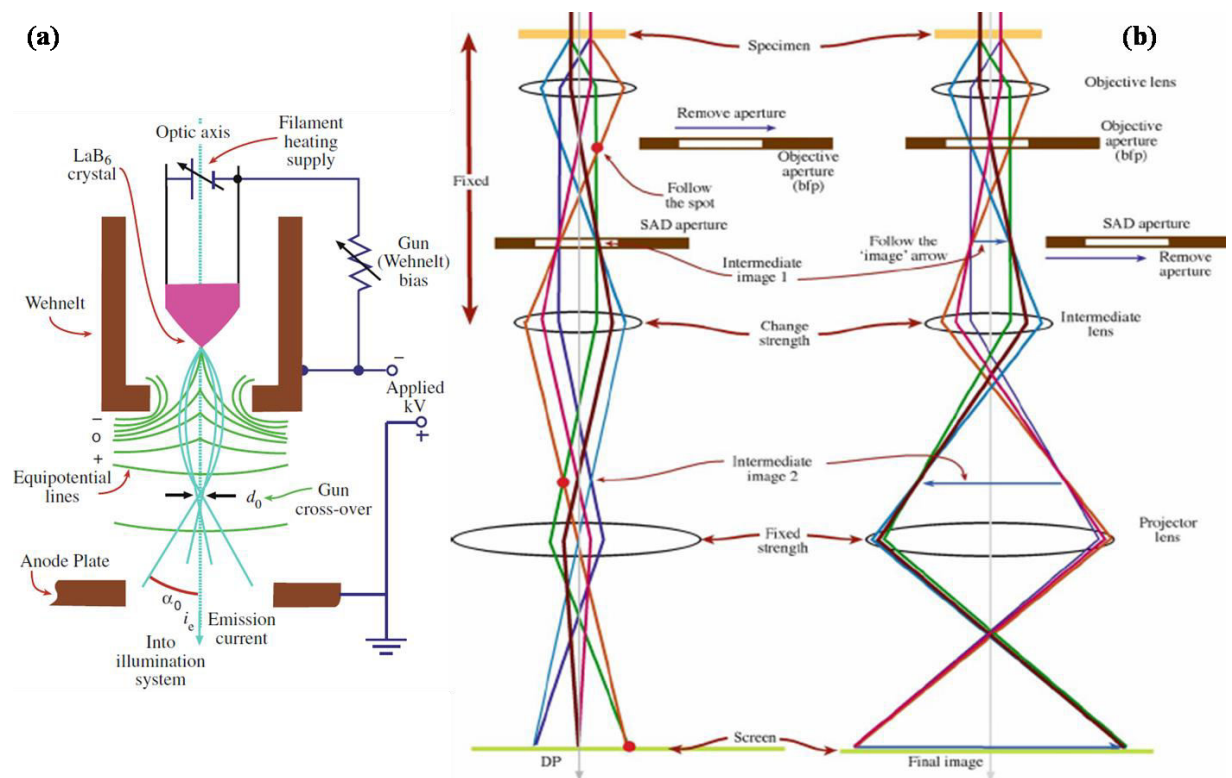


**Figure 2.7:** A schematic diagram of (a) filament and illumination part, (b) diffraction pattern formation and image formation [22].

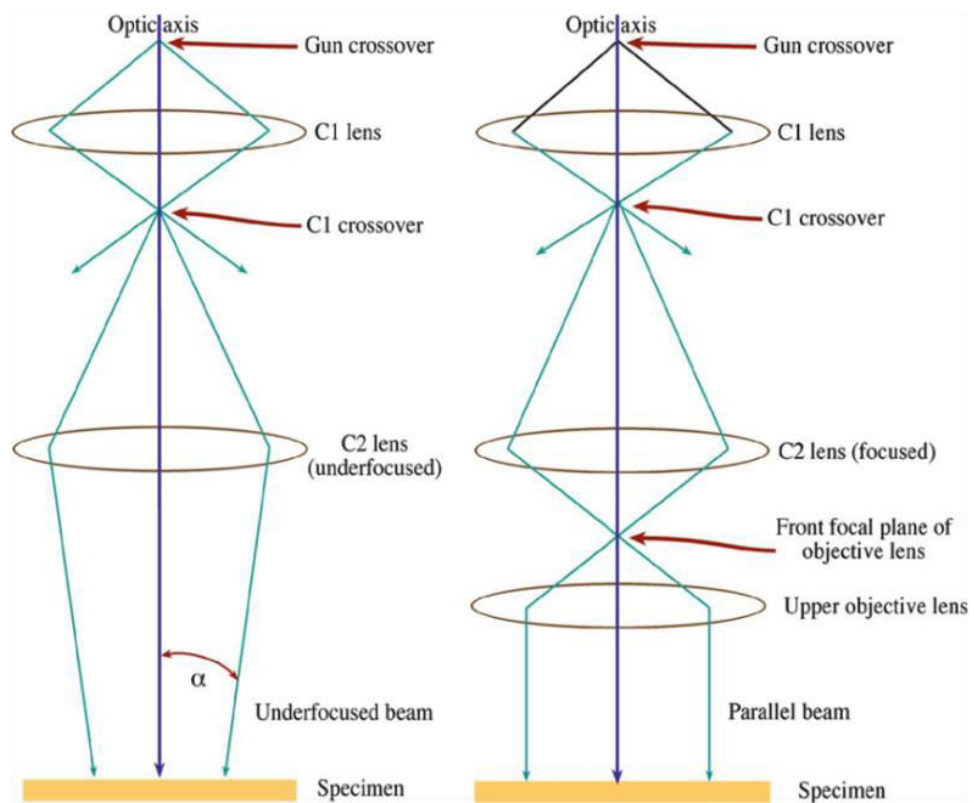


**Figure 2.8:** Parallel-beam operation in the TEM: the basic principle illustrated (left) and the practical situation in most TEMs (right) [22].

usually, in the range of  $\approx 1$  mrad for LaB<sub>6</sub> emitters (for our machine, it is  $\approx 0.68$  mrad). After this stage, specimen is inserted either from the side (our case) or from the top, which used to be at the middle of upper and lower part of the objective lens (OL). Upper part of the OS is also act as condenser lens (so called condenser mini lens). The OS is the most important part of the TEM. After the objective lens, objective aperture and selected area diffraction aperture are placed (Figure 2.7(b)). The combination of intermediate and projector lenses do the magnification. Here, the quality of the image is taken care by the OL which eventually decides the resolution of the microscope. The imaging system consists of several magnifying lenses (known as intermediate lenses), which magnify the image or SAD formed by the objective lens. Projector lens system projects the image onto the detector (CCD/TV Camera), coupled to a computer to grab images. Electrons being charged particles, TEM column is always kept at high vacuum ( $\approx 10^{-8}$  mbar) in order to get a collimated electron beam.

In this thesis, all the TEM measurements have been carried out using JEOL 2010 TEM operating at 200 keV (corresponding  $\lambda \approx 0.0025$  nm) with LaB<sub>6</sub> thermionic emission based electron source (Figure 2.9). The pole piece of objective lens (OL) is an ultra high

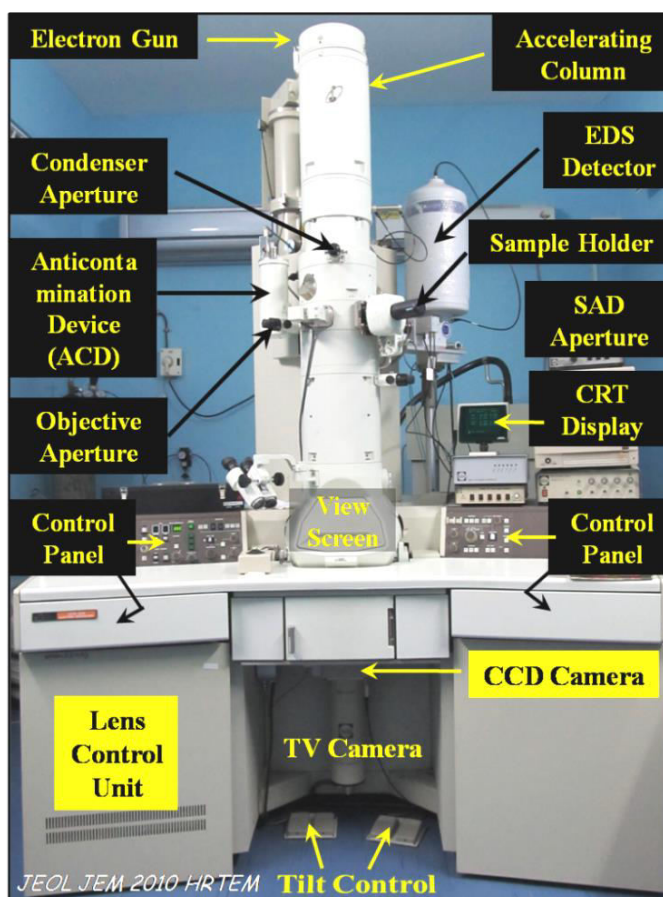


**Figure 2.9:** 200 keV JEOL HRTEM installed at Institute of Physics, Bhubaneswar.

resolution pole piece (UHR-URP22) with a spherical aberration coefficient ( $C_s$ ) of 0.5 mm which allows achieving point-to-point resolution of 0.194 nm. The images were recorded in a charge-coupled device (CCD) based detector with 40 ms time resolution and with  $4008 \times 2672$  pixels (Model 832, Orius CCD detector, Gatan).

### 2.3.1.2 Diffraction and imaging

The conventional TEM image formation for thicker specimen is very similar to the projector principle. In this case, an incoherent particle model can describe the interaction of the electrons with the specimen. Specimen contains variation in thickness and density. So, the electrons will lose more energy when they transmit through the thicker and denser region and hence it will appear as darker object. Same way, the thinner region will appear as brighter object. This contrast in imaging mode arises due to variation of thickness and is referred as mass-thickness contrast. In diffraction contrast, contrast depends up on the crystallinity of the specimen. However, for thin specimen at high resolution, the wave nature of the electrons has to be invoked to understand the contrast formation mechanism. If the specimen is thin enough and crystalline, then elastic scattering is usually coherent and these scattered/transmitted electrons are contribute to the image formation. After the exit of electrons (elastically transmitted coherent electron beams), the diffraction spots and image are used to form at back-focal plane and image plane of objective lens (OL), respectively. The diffraction pattern can be understood by taking the fast Fourier transform (FFT) of the wave function of electron at the back focal plane of OL (Figure 2.7(b)). The lattice image will form due to interference between the direct and diffracted beams depending on the phase difference between these two. So the highly diffracted beams are used to cut down by the objective aperture. The resolution and the details of image formation are governed by the contrast transfer function (CTF). The CTF depends on microscope parameters such as  $\lambda$ ,  $C_s$ , chromatic aberration coefficient ( $C_c$ ), defocus, width of defocus, stabilities in high voltage, OL lens current etc. To retrieve structural information of the specimen from the micrographs it is necessary to calculate the trajectory of the electron wave through the specimen. In the kinematical approximation, multiple scattering of the electrons in the sample is ignored resulting in an undisturbed central beam. This approach already fails at smaller thickness. In dynamical calculations, all the scattered beams and their mutual exchange of intensity during the course of multiple scattering in the specimen are taken into account. It is possible to do full dynamical calculations but these are made difficult by the available computing power. Using

the fact that the vast majority of the electrons are scattered in a forward direction with small diffraction angles, Cowley and Moodie devised the multi-slice approximation [26]. In order to understand the geometry of electron diffraction, we can ignore the lens system, which merely magnifies the DP. A schematic diagram showing the geometry of diffraction pattern formation and may consider the much simpler ray diagram shown in Figure 2.10. This is necessary to get the crystallographic information about the specimen. Consider, a beam of electrons impinges on a crystalline specimen. Some of the electrons will pass through the specimen without interaction (direct beam) and hit the phosphor screen which is at a distance  $L$  (camera length) from specimen. Other electrons are diffracted through an angle  $2\theta$  by the crystal planes of spacing “ $d$ ” and hit the phosphor screen at a distance “ $R$ ” from the direct beam. According to Bragg's law of diffraction, the diffracted beam follows the relation  $2d\sin\theta = \lambda$ , which can be simplified for the small angle diffraction as  $\lambda/d = 2\theta$ . From the trigonometric relation (again for the small angle approximation) we can write  $R/L = 2\theta$ . Combining these two, we find

$$d = \lambda L/R \quad (2.5)$$

As the  $\lambda$  and  $L$  are constant for the instrument, the quantity “ $\lambda L$ ” is called camera constant. If we know the camera constant, then we can determine “ $d$ ” simply by measuring  $R$  on the pattern. It is to be noted that  $L$  is not a physical distance between the specimen and screen, but is a notional distance which can be changed by the operator.

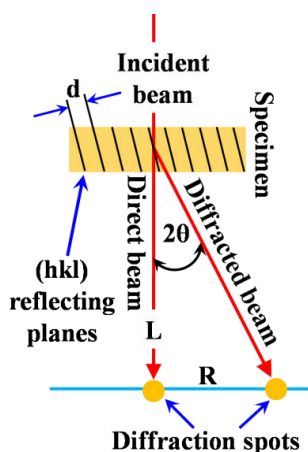


**Figure 2.10:** A schematic diagram showing the geometry of diffraction pattern formation [22].

### 2.3.1.3 Beam (electrons)-specimen interaction

It is well known that our eye cannot see anything unless it interacts with visible light through reflection or refraction, which are basically two forms of scattering. Similarly, in electron microscopy, we have the interactions (scattering) of electrons with specimen.

Electron scattering can be broadly divided in two groups: elastic (no energy loss) and inelastic (loss of energy) scattering. The all possible interactions of electrons with solid have schematically shown in Figure 2.11. After entering into the specimen, most of the electrons are elastically scattered by the nuclei of the specimen atoms. Some electrons are inelastically scattered by the electrons in the specimen. Compared to X-ray or neutron diffraction the interaction of electrons with the specimen is huge and multiple scattering events are common. For thick specimens at lower resolutions an incoherent particle model can describe the interaction of the electrons with the specimen. However, for thin specimens at high resolution, this description fails because the wave character of the electrons is then predominant. The electrons, passing the specimen near the nuclei are accelerated towards the nuclei causing small, local reductions in wavelength, resulting in a small phase change of the electrons. Information about the specimen structure is therefore transferred to the phase of the electrons. For the formation of high resolution images, only the elastically scattered electrons are of importance. The inelastic scattered electrons contribute mostly to the background of the image. Electron energy loss spectrum (EELS) of the inelastic scattered electrons contains valuable information of the chemical composition of the specimen. The inelastic scattered electrons also produce Kikuchi lines in the electron diffraction pattern that is helpful for accurate crystallographic alignment of the crystals in the specimen.

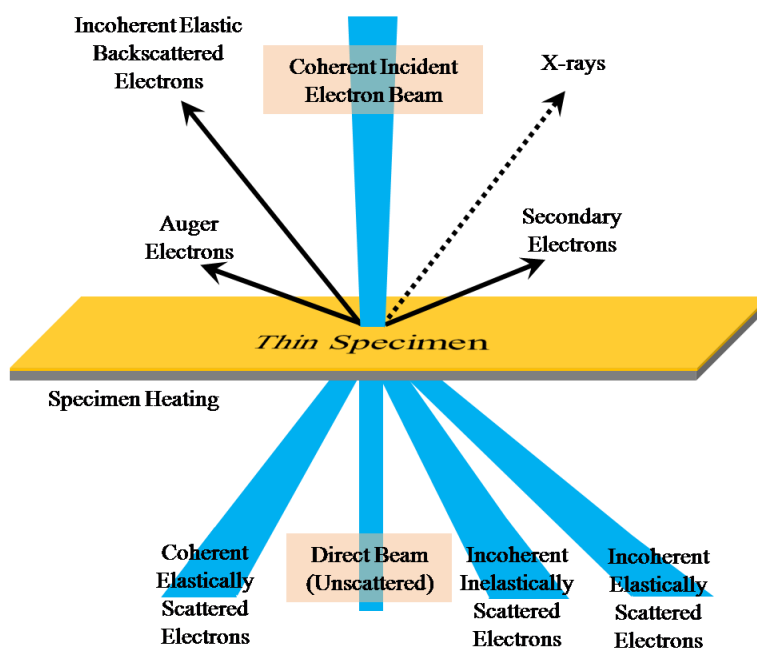


**Figure 2.11:** Schematic presentation of various signals generated when a high-energy beam of electrons interacts with a thin specimen. Most of these signals can be detected in different types of TEM.



### 2.3.1.4 Sample preparation (mechanical process)

Sample preparation is the most important part of the TEM characterization. As the electrons transmit through the specimen, the specimen has to thin down to the electron transparency ( $< 100$  nm) for conventional TEM and even lesser ( $< 10$  nm) for HRTEM. There are two types of samples to be prepared depending on the interest of study. Cross-sectional TEM (XTEM) sample is required to probe the interface and/or bulk solid, while planar TEM specimen preparation is required to probe the surface morphology. Figures 2.12 and 2.13 schematically present the methods of planar and XTEM sample preparations respectively.

#### Planar specimen preparation:

For Planar TEM sample preparation, we cut the sample into 3 mm disc using ultrasonic disc cutter and thin down to  $\approx 100$   $\mu\text{m}$  from rare side using lapping and polishing (LP) system (South Bay Technology (SBT), Model 910). Here, the mechanical thinning starts with a rough emery paper with larger grit size and ends with an emery paper with finer grit size. Then the specimen is again thinned ( $\approx 20$   $\mu\text{m}$ ) and polished by diamond paste and alumina suspension in dimple grinder (DG) system (Gatan, Model 656). In this process, the edge remains thicker but center part becomes dimpled. The final electron transparency is achieved by ion milling with precision ion polishing system (PIPS) (Gatan, Model 691).

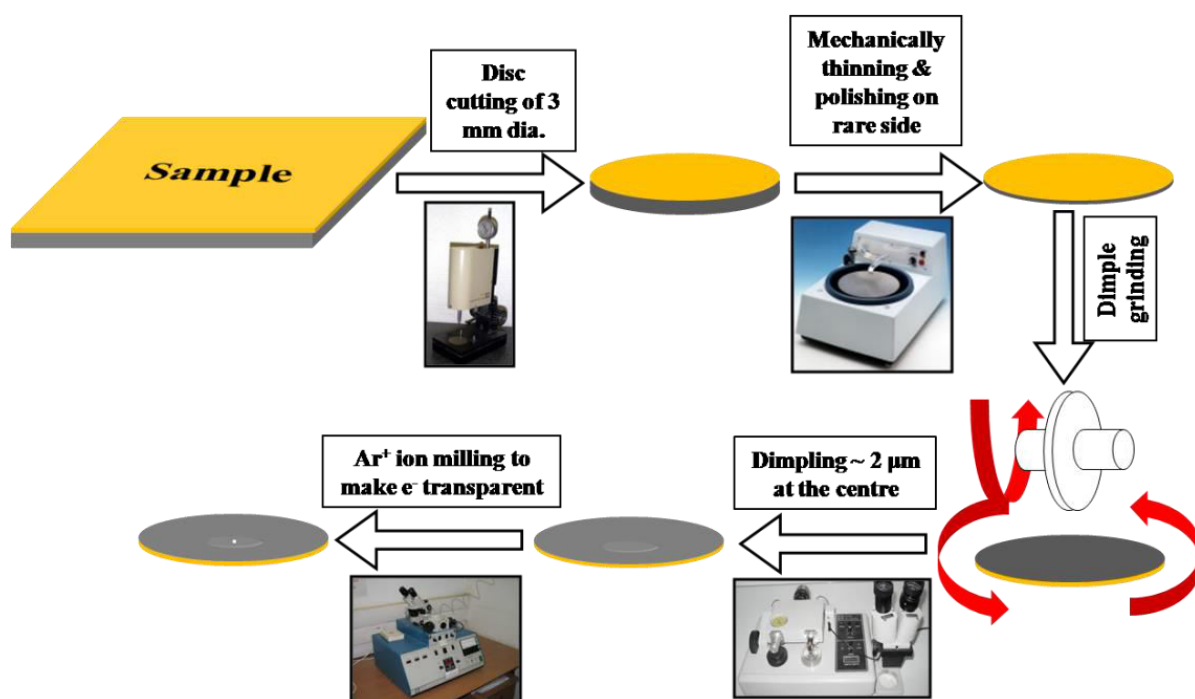


**Figure 2.12:** A schematic diagram of procedure to prepare a typical planar TEM specimen.



During PIPS,  $\approx 3$  keV Ar ion beam is used to sputter the material out from the specimen in grazing incidence ( $5^\circ - 7^\circ$ ) (Figure 2.12).

### Cross-sectional specimen preparation:

For cross-sectional TEM sample preparation, we cut the as deposited sample into two rectangular pieces of size  $(2.5 \times 5)$  mm<sup>2</sup> each using abrasive slurry saw (SBT, Model 850). Then the pieces are glued face to face using Gatan G1 epoxy as thin as possible. This assembly is then glued with two silicon dummy pieces with similar dimensions. Next, it was put in a stainless steel (SS) tube having inner and outer diameters 2.9 mm and 3.1 mm, respectively. Then we make  $\leq 500$   $\mu$ m slice out of it using low speed diamond wheel saw (Gatan, Model 650). After that, mechanical thinning is done from both sides (using LP) and then one side (using DG). Finally, electron transparency is achieved by  $\approx 3$  keV Argon ion milling in PIPS. Complete XTEM sample preparation is depicted pictorially in Figure 2.13.

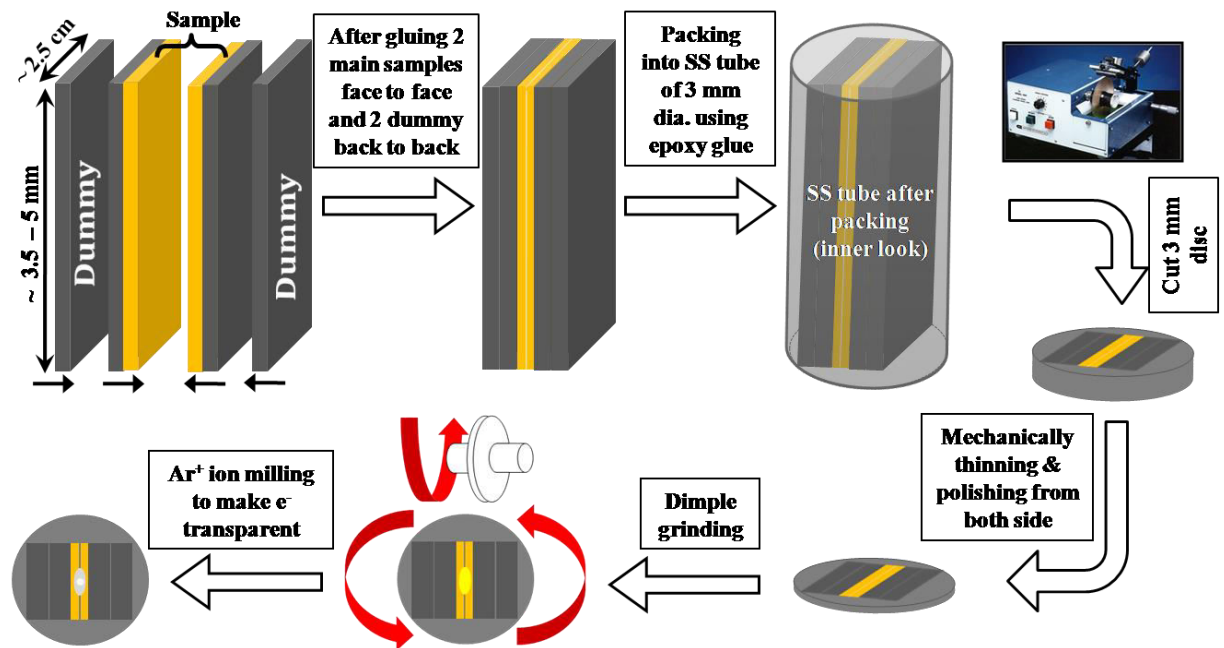


**Figure 2.13:** A schematic diagram of procedure to prepare a typical XTEM specimen.

### 2.3.2 Focused ion beam – scanning electron microscope (FIB–SEM) cross beam system

The combination of field emission scanning electron microscopy (FESEM) and focused ion beam (FIB) is a future key technology for semiconductor and material science

related applications. A scanning electron microscope (SEM) is a microscope that uses electrons instead of light to form an image. Since their development in the early 1950's, scanning electron microscopes have developed new areas of study in the medical and physical science communities. The focused ion beam (FIB) technique was mainly developed during the late 1970s and the early 1980s. Modern FIB systems are becoming widely available in semiconductor research and processing environments, as well as in failure analysis and chip-design centers. The technology enables localized milling and deposition of conductors and insulators with high precision, hence its success in device modification, mask repair, process control and failure analysis and also the preparation of specimens for TEM. The experimental setup used for this thesis work is a cross-beam system coupling a Carl Zeiss, Neon 40 scanning electron microscope (SEM, Gemini Column) and a Canion 31 focused ion beam (FIB, Orsay Physics), equipped with gas injection system (GIS, Orsay Physics), STEM detector, Four Quadrant Back scattered electron detector (Carl Zeiss ) and EDS detector (INCA, Oxford) (Figure 2.14). The two beams are focused on the same point of the sample and coincide at a crossover point 5 mm below the objective lens of the SEM. The working distance (WD) for the FIB in this coincidence point is 12 mm. The geometrical layout and arrangement of the two columns enables perpendicular tilt of the sample to the ion beam in the coincidence point. To provide full eucentric tilt at all operating conditions a 6-axis motorized eucentric specimen stage is used. This allows real time simultaneous FIB machining and non-destructive non-contaminating SEM imaging at high resolution. The sample may be tilted between  $0^\circ$  to  $54^\circ$  to face perpendicularly the ion or the electron beam.

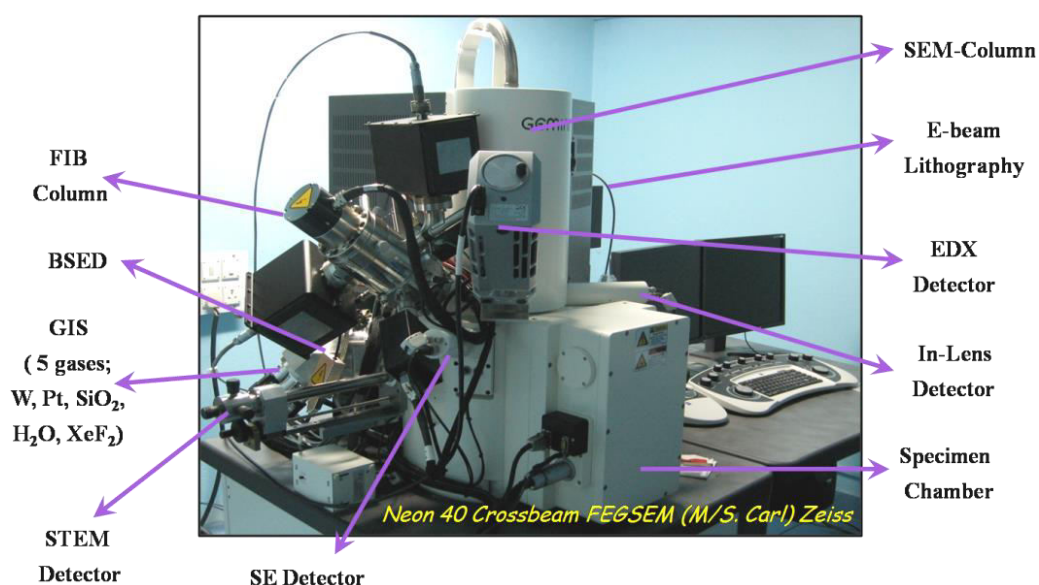


**Figure 2.14:** FIB-SEM crossbeam system installed at Institute of Physics, Bhubaneswar.

At 0° tilt, imaging at normal incidence with the electron beam is possible while at 54°, imaging and machining with the FIB is performed. The FIB column operates at an accelerating voltage of Ga<sup>+</sup> ions ranging from 2 to 30 kV with a minimal Gaussian beam diameter around 7 nm. The beam current can be varied from 1 pA for the lowest current to 50 nA. Our FIB system can be used for imaging, milling and deposition. One Kleindiek micromanipulator (MM3A-EM) is attached inside the specimen chamber for TEM lamella preparation (for lift out). The system is fitted with a computer controlled GIS that can handle up to five different gases for metal and insulator deposition or enhanced and selective etching. Gas flows from a reservoir through a capillary. Temperature of reservoirs and capillaries are independently controlled. The needles at the end of the capillaries are mounted on a micro stage table. Thus they can be precisely positioned close to the working area (< 100 μm) in order to create a local high gas pressure. A turbo molecular pump ensures a dynamic pumping and the base pressure in the chamber is  $\approx 10^{-6}$  mbar. The working principles of SEM and FIB are separately discussed below.

### **2.3.2.1 Scanning electron microscope (SEM)**

The microscope used in this work is a Zeiss Neon 40. This microscope is equipped with a field emission gun, GEMINI electron-optics, a lateral secondary electron (SE) detector (Everhart-Thornley), a backscatter detector, an in-lens detector. The main characteristic of the GEMINI optics is the use of a beam booster and an objective lens which acts as a combined electrostatic/electromagnetic lens. The electrons generated at the gun tip are accelerated to the set acceleration voltage as they approach towards the anode. However, the beam booster, which is installed directly after anode, is always at a potential of an extra 8 kV when the set acceleration voltage is  $\leq 20$  kV. When low voltages are used, this arrangement will ensure that the energy of the electrons in the beam path will always be 8 kV higher than the set acceleration voltage and will reduce the influence of magnetic stray fields on the electron beam. Before the electron beam exits the objective lens, the electrostatic lens reduces the potential by an opposite applied 8 kV. The main advantage of this technique is that a stable beam is obtained even at low acceleration voltages. In addition to acting as a retardant towards the electrons ejected from the electron column, the electrostatic lens will act as a collector for the electrons generated at the sample surface. The sample electrons are accelerated and focused back up the beam path, where the in-lens detector is positioned

(annular detector). The combination of the electrostatic lens and the in-lens detector results in a very high detection efficiency even at low ( $< 1$  kV) acceleration voltages [27].

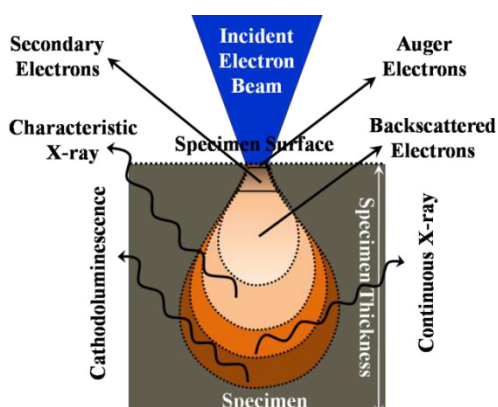
### **Image formation:**

Image formation in the SEM is dependent on the acquisition of signals produced from the electron beam and specimen interactions. These interactions can be divided into two major categories: elastic interactions and inelastic interactions. Elastic scattering results from the deflection of the incident electron by the specimen atomic nuclei or by outer shell electrons of similar energy. This kind of interaction is characterized by negligible energy loss and by a wide-angle directional change of the scattered electrons. Incident electrons that are elastically scattered through an angle of more than  $90^\circ$  are called backscattered electrons (BSE), and yield a useful signal for Z-contrast imaging. Inelastic scattering occurs through a variety of interactions between the incident electrons and the electrons and atoms of the sample, and results in the primary beam transferring substantial energy to them. The amount of energy loss depends on whether the specimen electrons are excited singly or collectively and on the binding energy of the electron to the atom. As a result, the excitation of the specimen electrons during the ionization of specimen atoms leads to the generation of secondary electrons (SE). In addition to those signals that are utilized to form an image, a number of other signals are produced when an electron beam strikes a sample, including the emission of characteristic X-rays, Auger electrons and cathodoluminescence (Figure 2.15). Impingement of primary beam of electrons on sample, cause emission of either secondary electrons (SE's) due to the inelastic interaction or backscattered electrons (BSE's) due to the elastic interactions, which are mainly used for image formation. As a result of inelastic interactions of the primary electrons with the sample, the secondary electrons are emitted from the sample with energy less than 50 eV [28]. Whereas energy distribution of the backscattered electrons generated via elastic interactions has a peak just below the primary electron energy and a tail towards zero. As the secondary electrons are lower in energy than the backscattered electrons, they can be separated easily from the high energy backscattered electrons via application of electric field. As the secondary electrons have very less energy, so there emission takes place very shallow level from the sample surface. Secondary electron image thus gives information about the topography of the sample.

Back scattered electrons (BSE) are basically primary electrons which have been reflected back from a specimen via elastic collision events in one of two ways: (1) under the

strong Coulomb field of an atomic nucleus (i.e. Rutherford scattering) and (2) incident beam of electrons can undergo multiple low-angle deflections/scattering which together comprise a deflection of  $> 90^\circ$ . Elastic interactions in both the ways result in emission of BSE with energies somewhat less than the incident beam and hence some minor inelastic scattering must be involved (usually due to the emission of white X-ray). The shape of the interaction volume between incident electrons and target specimen was qualitatively predicted by Duncumb and Shields (1963). According to them the same energy electrons penetrate more deeply into sample materials having low atomic number (Z). Number of backscattered electrons emission will have dependency on the atomic number (Z) of the target atom. If samples/specimens contain elements of different atomic number Z (polyphase specimens) then the BSE image will give different intensities and contrasts, where higher Z area will appear as brighter than smaller Z area. So, Atomic number or Z-contrast is can be seen easily in the BSE detector images. Whereas SE images of the same area contain less detail because SE emission is largely independent of atomic number Z [29].

Most commonly an Everhart-Thornley detector (E-T detector) is used to detect the electron signals in the scanning electron microscope (SEM). The E-T detector consists of a Faraday cage covering a scintillator, an optical guide and a photomultiplier tube. The Faraday cage is placed outside the detector and either a negative or a positive bias voltage can be applied to it. When a negative bias voltage is applied, all secondary electrons are rejected and hence only the backscatter signal is detected. When a positive bias voltage is applied to the Faraday cage, the secondary electrons are attracted to the detector. The positive bias voltage causes the trajectory of electrons emitted from the sample over a large solid angle to be directed towards the detector. In the detector the electrons are accelerated to the scintillator where they induce light emission. The light is guided to the photomultiplier tube amplifying the signal and converting it into an electric current which can be read out on a screen.



**Figure 2.15:** Schematic representation of various signals generated as a result of the electron-specimen interaction in a SEM.

### **Energy dispersive X-ray spectrometry (EDS)**

Energy dispersive x-ray spectrometry (EDS) is an analytical technique used for the elemental or chemical compositional characterization of material [30, 31]. EDS characterization includes detection of X-rays are emitted from sample due its interactions with energetic electron beam being irradiated, which are used to identify the elements present in the sample and their relative amounts. When an incident electron is scattered inelastically, it knocks out a core electron and then an electron from a higher orbital fills the empty state (hole) in lower (core) orbital. The energy difference between these two orbitals is released in the form of photons (their energy used to be in the X-ray regime when a core level electron is knocked out), whose energy is characterized for the transition in the respective target atom by Mosley's law. The emitted characteristics X-rays are detected by spectrally resolved (typically few eV/channel) with an appropriate energy dispersive detector, like Si(Li) or SDD (Si drifted detector). When X-ray emitted from specimen falls on the detector crystal its energy is absorbed by electrons in the valence band of the semiconductor and goes to the conduction band, leaving behind holes in the valence band. A high bias voltage applied at the back and front faces of the detector sweeps these electrons and holes, producing a charge signal. And the size of the produced charge signal is proportionally related to the energy of the incident X-ray. Then the field effect transistor (FET) circuit attached to the backside of the detector converts charge signal to a voltage signal. An EDX spectrum displays peaks corresponding to the energy levels for which the most X-rays had been received. Each of these peaks is sensitive to an atom, and therefore, corresponds to a single element. The higher intensity peak in a spectrum corresponding to an element corroborates its more presence in the sample. An EDX spectrum not only recognizes the element corresponding to each of its peaks, but also inform about type of X-ray it corresponds.

#### **2.3.2.2 Focused ion beam (FIB)**

The structure of the ion column is similar to that of the electron column, the major difference is instead of an electron beam the gallium ion ( $\text{Ga}^+$ ) beam is used. A vacuum of about  $10^{-10}$  mbar is maintained inside the ion column. The basic components of a FIB system are normally an ion source, an ion optics column (for acceleration), a beam deflector and a substrate stage. The ion beam is generated from a liquid metal ion source (LMIS) by the application of a strong electric field. In a Liquid metal ion source (LMIS), a metal ( $\text{Ga}^+$ ) is

heated to the liquid state and provided at the end of a capillary or a needle. Then a Taylor cone is formed under the application of a strong electric field at the tip of a tungsten needle. As the cone's tip gets sharper, the electric field becomes stronger, until ions are produced by field evaporation. A typical extraction voltage 7 kV is applied to the tungsten needle. The extraction current under normal operating conditions is  $\leq 2.1 \mu\text{A}$ . After a first refinement through the aperture, the ion beam is condensed in the first electrostatic lens. The beam stigmatism is adjusted by the use of upper octopole deflector coil. The ion beam energy is typically between 2 and 30 keV, with beam currents varying between 1 pA and 50 nA. With the use of motor controlled aperture assembly of different sizes, the beam current can be tuned, allowing both a fine beam for high-resolution imaging on sensitive samples and a heavy beam for fast and rough milling. Blanking of the beam is accomplished by the blanking deflector and aperture, while the lower octopole is used for raster scanning the beam over the sample in a operator specified pattern. In the second electrostatic lens, the beam is focused to a fine spot, enabling a best resolution of  $\approx 10 \text{ nm}$ . All operations such as stage movement, controlling valves for gas injection system (GIS), turning on and off pumps and manipulating the ion beam are done using a Zeiss provided inbuilt software. A system of vacuum pumps is needed to maintain the vacuum inside the column and the work chamber. An oil free rotary pump is used in combination with a turbo pump for pumping the work chamber.

### **TEM lamella preparation by FIB:**

TEM lamella preparation using FIB is illustrated in Figure 2.16. At first, region of interest is selected and then it is imperative to coat the specimen surface with platinum (Pt) film of  $\approx 1 \mu\text{m}$  thick in order to protect the surface during ion milling. Now, with 30 keV ion beam energy, machining begins under normal incidence. Starting from the external faces, two trenches are dug, one on each side of the area of interest, digging closer until a nanometer thick slice remains at the desired location. The width and depth of these trenches are almost  $16 \mu\text{m}$  and  $10 \mu\text{m}$  respectively. Next job is to transfer lamella to TEM grid. Now, this lamella is welded to a micro manipulator (Kleindiek, MM3A-EM) for lifting out from the bulk material. This manipulator has three axis freedom in movement (up/down, azimuthal and in/out) and completely robotically controlled. Manipulator has sub-nanometer resolution in movement with  $\approx 100 \text{ cm}^3$  working range. Then, it is placed on a carbon coated support microscope grid and welded and micro manipulator is taken out with the ion beam to release the slice. Next, the specimen on grid is tilted by  $\pm 1.5^\circ$  about normal incidence of ion beam in

order to thinning and thin slice 100 nm thick is routinely obtained. To eliminate the amorphous layer generated by high energy ions, the final thinning is performed at low ion beam energy (5 keV). Thinned specimen is now ready for observation. Additional FIB thinning/low energy  $\text{Ar}^+$  milling of the lamella may be done after TEM observation if needed.

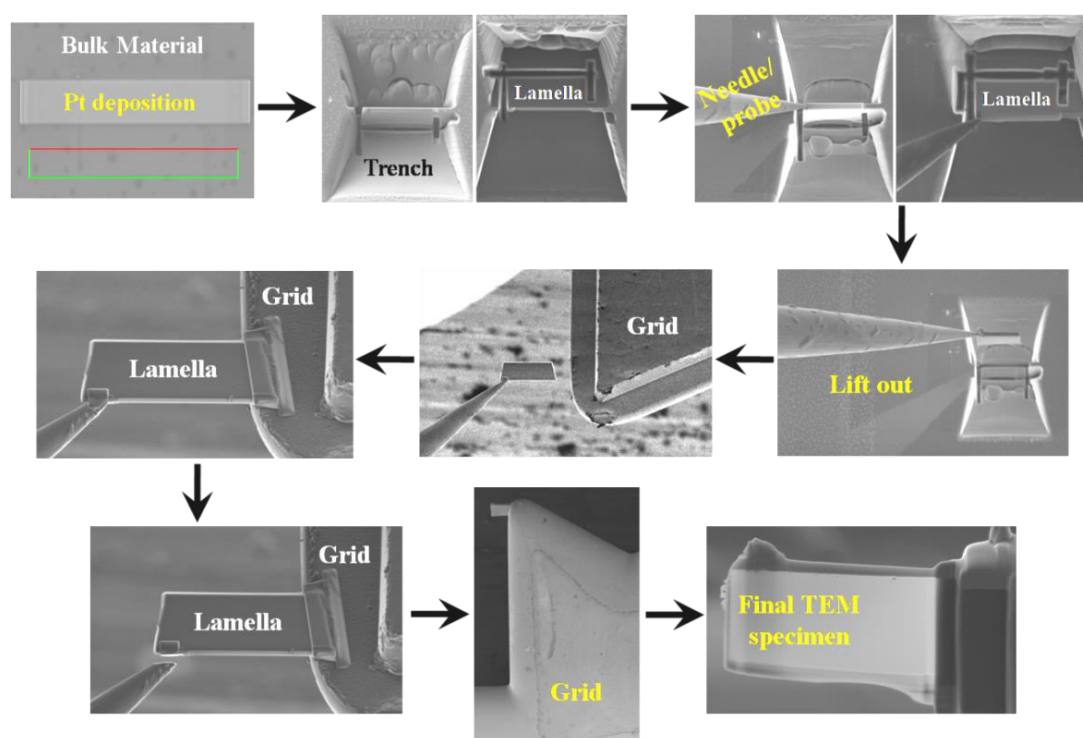


**Figure 2.16:** Illustration of TEM lamella preparation utilizing FIB.

### 2.3.3 X-ray diffraction (XRD)

X-ray diffraction is a technique used for determining the crystal structures, such as lattice parameters and strain in the system. Crystal consists of regularly arranged array of atoms, and X-rays are electromagnetic waves. X-rays striking an electron produces secondary spherical waves emanating from the electron. This phenomenon is called elastic scattering and the electron is called scatterer. Regular array of scatterers produce regular array of spherical waves which can interfere constructively or destructively. Incident X-rays falls on a sample and reflected with the same angle as incident angle and these reflected beams undergo interference and this interfered beam is collected by scintillation detector which is converted into a voltage pulse which will be fed to a computer to display the spectrum of intensity vs. angle of incidence. Instrumentation of XRD system broadly consists of X-ray source, goniometer for mounting the sample and the detector in the reflection geometry. When the



sample stage moves in the  $\theta$  plane the detector will move in the corresponding  $2\theta$  plane to collect the data. Using XRD technique growth directions, alloy formation and material compositions of crystalline samples can be determined. The diffraction of monochromatic X-rays takes place at those particular angles of incidence which satisfy the Bragg law,  $2d\sin\theta = n\lambda$ . Here  $d$  is the inter-planar spacing of the diffracted planes,  $\theta$  is the incident angle,  $n$  is an integer and  $\lambda$  is the wavelength of the incident X-ray beam (Figure 2.17). For this thesis work we have used synchrotron X-rays at Photon Factory, KEK, Japan (Indian Beam line 18B) with a wavelength of  $1.089 \text{ \AA}$ . The energy tunability of synchrotron radiation allows working with an appropriate wavelength for specific experiments. Some of the XRD measurements were performed by a Philips Xpert PRO MRD Cradle using  $\text{Cu K}\alpha$  ( $\lambda = 1.54 \text{ \AA}$ ) radiation.

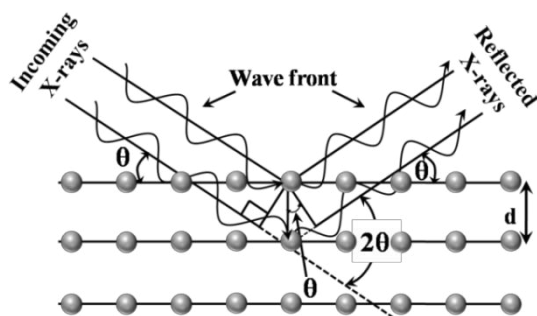


**Figure 2.17:** Schematic representation of X-ray diffraction occurring in a crystal with spacing  $d$ .

### 2.3.4 Photoluminescence (PL)

Photoluminescence (PL) is the spontaneous emission of light from a material under optical excitation [32]. PL measurement is a kind of powerful and nondestructive technique, which has been carried out on most of semiconductors. To date, there are many different type lasers have been widely used in the PL setup, for example, He-Cd laser with  $325 \text{ nm}$ ,  $\text{Ar}^+$  laser with  $316 \text{ nm}/514 \text{ nm}/488 \text{ nm}$ , Nd:YAG pulsed laser with  $266 \text{ nm}$ , tunable solid state lasers and so on. Photoluminescence (PL) is a process in which a photon of energy  $h\nu$  is absorbed by the valence electrons and is excited to the higher energy states in the conduction band leaving holes in the valence band. The radiative recombination of electrons from the minimum of conduction band to the top of valence band holes emits a photon, as shown in Figure 2.18. Figure 2.18 shows the photoluminescence process in direct band gap materials. When photon of energy  $h\nu_{\text{excitation}}$  greater than the band gap ( $E_g$ ) is incident, then injection of electron from the valence band to conduction band takes place. This process will cause the formation of hole in the valence band and free electron in the conduction band, and electron hole pair may be created at some higher energy state and will lose energy through

longitudinal optical phonon excitation (intra-band relaxation is caused by energy transfer to the crystal lattice) during rapid thermal decay. After that non-equilibrium electrons and holes tend to relax back to the ground state via radiative transition and emission of photon takes place, which is known as photoluminescence (PL). However, only the energy of photons is equal to or higher than the band gap, the absorption can happen in materials. Therefore, we have to choose different excitation source to do the measurements according to different material with different electronic band structure. The PL peak positions reveal transition energies and the PL intensity implicates the relative rates of radiative and non-radiative recombination processes. We also can change other external parameters during the PL measurement, such as temperature, excitation power and applied external perturbation such as magnetic and/or electrical field, which can improve our understanding about electronic band structure of the samples. Using PL measurement technique, we can obtain a variety of information about the material being studied as follows [32].

(1) **Band gap information:** Band gap of a semiconductor can be determined when a radiative transition takes place between band to band corresponding to band gap. PL measurements not only informative about the band gap of a semiconductor or compound semiconductor, but also help us to understand the controlled tailoring of band gap for practical necessity.

(2) **Impurity and defect states determination:** As the PL signal originates near the surface of a material, so PL analysis is sensitive to the surface characterization. Generally, even in pure semiconductors there are always some impurities and native defects, which are responsible for creation of some localized defect states inside the band gaps. These extra defect states forms bands and also take part in the radiation recombination processes. The PL peak position in energy/wavelength scale corresponding to those states can be used to identify specific defects, and the PL peak intensities qualitatively can be used to determine relative information concerning their concentrations.

(3) **Recombination mechanisms:** It is well understood that the “recombination” process after photo-excitation in PL includes both radiative and non-radiative processes due to the presence of the defect levels and surface states inside the band gap. The PL intensity depends on several parameters such as power of photo-excitation, defect density and temperature, which are determined by the dominant recombination processes. Thus, studying excitation power/temperature/time dependent PL spectra will definitely enable us to understand the underlying physics behind the recombination mechanisms.

(4) **Optical quality of material:** The evidence for the existence of the defects in a material can be concluded if there is any non-radiative recombination processes happening. Sometimes these defects are harmful for device performance and also for some case they are considered to be important. Through PL measurement, we can qualitatively quantify the integral proportion of non-radiative recombination in the PL emission processes, which will help us to recognize that material as a good or bad optical material.

PL is simple, versatile, and nondestructive technique. The instrumentation that is required for ordinary PL work is modest: an optical source and an optical power meter or spectrophotometer. Indeed, the technique requires very little sample manipulation or environmental control. Because the sample is excited optically, electrical contacts and junctions are unnecessary and high-resistivity materials pose no practical difficulty. The photoluminescence (PL) characteristics of all the samples were recorded at room temperature using a He-Cd laser (325 nm pump line) with an output power of  $1.3 \text{ W/cm}^2$ . PL signals were analyzed using a TRIAX-320 monochromator with a standard lock-in technique.

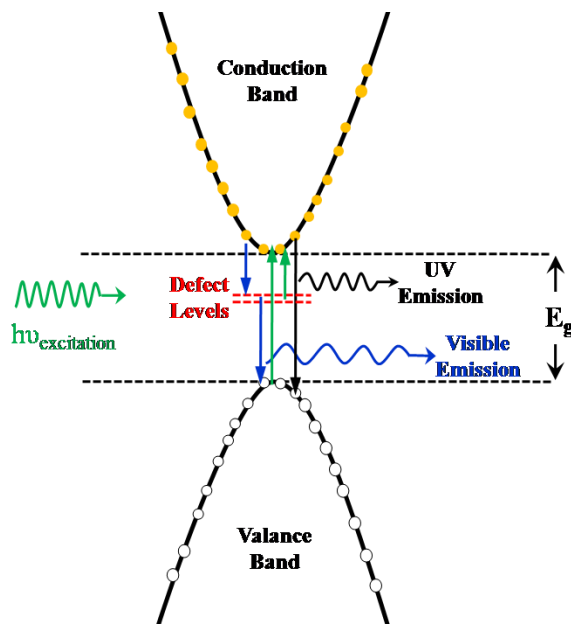


**Figure 2.18:** Schematic of the process occurring during photoluminescence in a direct band gap semiconductor after excitation at frequency  $\nu_{excitation}$ .

### 2.3.5 Cathodoluminescence (CL)

It is discussed previously, that when a beam of high energy electrons (order of keV) interacts with matter, variety of signal produces, which includes secondary electrons (SE), back scattered electrons (BSE), auger electrons, X-rays, and photons in the wavelength range from UV to near-infra-red (SEM section see Figure 2.15). Emission of photons induced by

electrons after interactions with semiconductor material (i.e., luminescent material) is known as cathodoluminescence (CL). This is analogous to the photoluminescence process where instead of electron beam; photon is used as excitation source. Cathodoluminescence (CL) or electron beam induced radiation emission (EIRE) spectroscopy and imaging measurements on our as-synthesized samples were performed in a ZEISS SUPRA40 SEM equipped with the Gatan MonoCL3 cathodoluminescence system (at SINP, Kolkata). In the present study, data were recorded with an electron acceleration voltage of 5 keV and beam current of about 300 pA with a beam diameter (spot size) of  $\approx 10$  nm at room temperature (RT). Electron beam was directed on the samples through a hole of diameter 1 mm in the retractable paraboloidal light collection mirror [33].

### 2.3.6 Reflectance

Reflectance is the amount of incident light that is reflected by a surface. Optical reflectance measurements were obtained using a Shimadzu UV 3101PC UV-visible-NIR spectrophotometer equipped with a specular reflectance measurement accessory. The spectral range that can be studied with this instrument is 200 to 3200 nm. However, in the present thesis, most of the spectra were collected over a wavelength range of 250–1000 nm using 1 nm increment. The reflectance mode works in a specular reflection geometry arrangement with  $45^\circ$  incidence angle of light.

### 2.3.7 X-ray photoelectron spectroscopy (XPS)

Photoelectron spectroscopy (PS) is based on the photoelectric effect [34, 35] in which electrons are emitted from the sample via interaction with electromagnetic radiation. In X-ray photoelectron spectroscopy (XPS), as the name states, X-ray is used for the emission of photoelectrons. Compared to ultraviolet photoelectron spectroscopy (UPS) where the energy of the impinging radiation is order of few tens of eV, the energy of X-ray is in the order of a few thousand of eV. Therefore, electron from outer and inner core shells of atoms/molecules can be excited in XPS, whereas UPS can only knockout electrons those are in valance band. X-ray photoelectron spectroscopy (XPS) is a spectroscopic technique which quantitatively gives the elemental composition, chemical state and charge state of the elements which are there in the material. XPS is a surface sensitive technique that can be used to analyze the

surface chemistry of a material in its as-synthesized state, or after some post treatment. Since the discovery of photoelectric effect by Heinrich Rudolf Hertz in 1887, it has become the most interesting light-matter phenomenon which was successfully explained later in 1905 by Albert Einstein. Kai Siegbahn and his group in 1954 from Uppsala University (Sweden) developed and first XPS spectrum was recorded with high-energy-resolution from cleaved sodium chloride (NaCl) material [36]. When x-ray photons interact with a sample it leads to ionization and the emission of a core shell electron from the atoms of the sample. As we know the energy of the incoming x-ray photon, the binding energy ( $E_B$ ) of the emitted electrons can be evaluated by following equation

$$E_B = E_{\text{photon}} - (E_{\text{kinetic}} + \Phi) \quad (2.6)$$

where  $E_{\text{photon}}$  is the energy of the x-ray photon,  $E_{\text{kinetic}}$  the kinetic energy of the emitted electron, measured by an electron analyzer;  $\Phi$  is the work function of the material. Mg  $K_\alpha$  and Al  $K_\alpha$  are the two most widely used sources because of their high energy and narrow width. So, XPS spectra are generated by irradiating a material with a beam of X-rays, during this process basically we measure (through software attached to the system) simultaneously the kinetic energy and number of electrons that escape from the 1 to 10 nm deep from the top surface of the material being analyzed. The XPS system consists of an ultra high vacuum (UHV) chamber that contains an X-ray source, an electron analyzer, and a sample holder.

In this thesis work, XPS characterization was carried out by employing the model S/N-10001 (Project No. 251, Prevac, Poland) with a VG Scienta-R3000 hemispherical energy analyzer. Spectra were taken by using 1253.6 eV for Mg- $K_\alpha$  and 1486.6 eV for the Al- $K_\alpha$  lines as the X-ray source operating at 200 W (10 kV and 20 mA). XPS system base pressure of  $6 \times 10^{-10}$  mbar was maintained during all data acquisition. The spectrometer is well calibrated with respect to Ag standard and referring to the  $E_B$  of the Ag 3d<sub>5/2</sub> (368.2 eV).

### 2.3.8 Surface enhanced Raman spectroscopy/scattering (SERS)

In 1928, the Indian physicist C. V. Raman discovered that for visible wavelength of a small fraction of the radiation scattered by certain molecules differs from that of the incident beam and furthermore that the shifts in wavelength depend upon the chemical structure of the molecules responsible for the scattering [37]. The Raman effect is based on molecular deformations caused by oscillating electric field  $\vec{E}$  associated with incident electromagnetic radiation (usually laser) determined by molecular polarizability  $\alpha$ . This electric field  $\vec{E}$

interacts with the electron cloud of the bonds of that molecule and excites one of the phonons into a virtual state. Upon interaction with the sample molecule, it induces electric dipole moment  $\vec{P} = \alpha\vec{E}$ , which is responsible for molecular deformation. Periodical deformation molecules begin vibrating with characteristic frequency  $\nu_m$ . The amplitude of vibration of the molecule is known as nuclear displacement. For the spontaneous Raman effect, the molecule will be excited from the ground state to a virtual energy state, and relax into a vibrational excited state, which gives Stokes Raman scattering line and if the molecule is already in vibrational excited state then it generates anti-Stokes Raman scattering line (Figure 2.19(a)).

Raman spectroscopy technique is based on Raman effect, where monochromatic light usually from a laser source inelastic scattered from molecule, which involves excitation of molecules by using an intense light source and measuring the scattered radiation by the molecules. Because of the low probability of light being scattered (approximately 1 in 10 million), the Raman intensity is inherently very weak. Therefore, a lot of effort has been devoted in order to improve the Raman scattering intensity. One approach that has been developed and applied successfully beside other approaches (such as stimulated Raman, coherent anti-Stokes Raman spectroscopy and resonance Raman), to improve the intensity is known as Surface enhanced Raman Spectroscopy/scattering (SERS). This technique was first described by Fleischmann et al. in 1974 [38]. Since then, a lot of work has been done to understand the reason for the enhancement. Besides Fleischmann's group, the research groups of Van Duyne and Jeanmaire, and Albrecht and Creighton, independently reported the significant enhancement of the Raman scattering when molecules are adsorbed on a metal surface [39, 40]. Van Duyne and Jeanmaire explained this enhancement in Raman signal in terms of change of the electric field experienced by the molecules, and this phenomenon is known as electromagnetic enhancement (EM). At the same time, Albrecht and Creighton also reported that Raman scattering was enhanced by charge (electron) transfer or chemical bond formation between the molecules and the metal substrate, which cause change in polarizability  $\alpha$ . This enhancement mechanism named as chemical enhancement. Although the mechanisms leading to the enhancement are still not completely understood, it is generally accepted that both electromagnetic enhancement and chemical enhancement mechanisms contribute together to the enhanced SERS signals. The electromagnetic enhancement results from the amplification of light by the excitation of localized surface plasmon resonances, in which the light concentration occurs preferentially in the gaps, crevices or sharp/nanoscale features of plasmonic materials [41-43]. Chemical enhancement

primarily depends on charge transfer processes, where the excitation wavelength is in resonance with metal-molecule charge transfer electronic states [44]. With the development of SERS in recent years, research interests have shifted to practical applications [45-48]. To better understand the SERS behavior, some fundamentals, including the two main enhancement pathways, electromagnetic enhancement, and chemical enhancement will be discussed in the following sections.

### 2.3.8.1 Mechanisms

#### Electromagnetic enhancement mechanism:

Surface plasmon in conduction materials (noble metal) is formed due to rapid oscillation of their free electron density induced by incident light. The particle resulting from the quantization of the oscillation of the free electrons is known as “plasmon.” When plasmon is restricted to surfaces and interacts strongly with electric field of incident light, a polariton is formed, also known as non-radiative evanescent wave. The plasmon wave resides at the interface of the materials with positive dielectric constant and those with negative dielectric constant. The plasmon can either be localized or propagating on the conducting surface. When the metallic nanostructure dimensions (such as Au, Ag, Cu nanoparticles are generally used) are smaller or order of the wavelength of the excitation light, then the formed evanescent wave is known as localized surface plasmon resonance (LSPR). The most widely accepted model of the LSPR phenomenon on metal nanoparticles (NPs) surface is illustrated in Figure 2.19(b) [47]. When the metal NPs are exposed to the incident light of proper

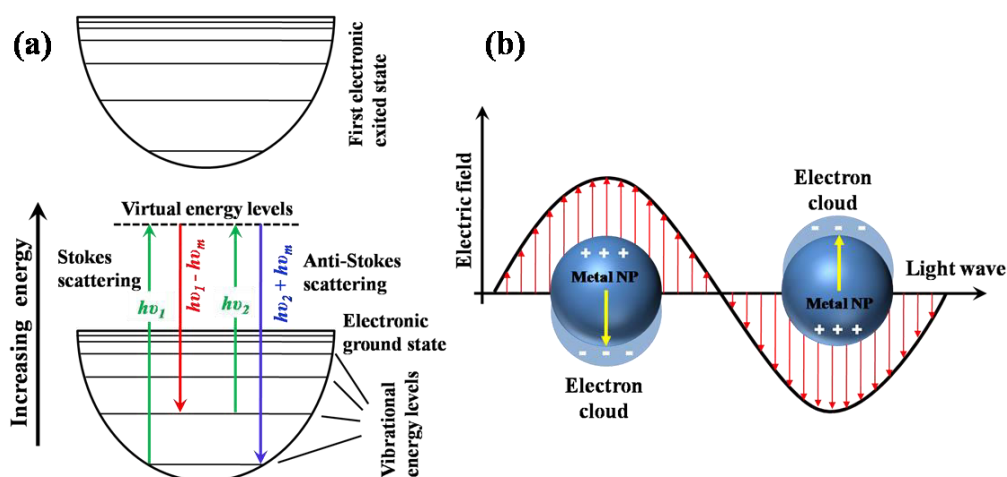


**Figure 2.19:** (a) Energy level diagram showing the states involved in Raman signal. (b) Model of LSPRs at the spherical nanoparticle surface [47].

wavelength, the oscillating electric field localized on the surface can cause the free electrons in the metal NPs to oscillate coherently. When the charged cloud of conduction electrons is oscillated away from the nuclear frame work of the NP, strong columbic attraction arises and forces the oscillation of the conduction electrons cloud back to the nuclear framework. This back and forth oscillation results in a large enhancement of electromagnetic field of the light at the surface of metal NP. The magnification of both the incident EM field and the Raman scattering field composes the SERS EM enhancement mechanism [42]. This enhancement is possible, when the wavelength of the incident light and the Raman signal wavelength are nearly matches with the plasmon wavelength of metal NP then only resonance will occur and the enhancement will be maximized [43]. In case of significantly smaller NP with respect to the wavelength of the incident light, the electric field due to plasmon on the surface of the metal sphere and the electric field of the incident light can be correlated by the equation

$$E \text{ (induced)} = (\epsilon_1 - 2\epsilon_2)/(\epsilon_1 + 2\epsilon_2) E \text{ (light)} \quad (2.7)$$

where,  $E \text{ (induced)}$  and  $E \text{ (light)}$  represent for the electric or electromagnetic (EM) field induced on the surface and electric field of the excitation light. There,  $\epsilon_1$  and  $\epsilon_2$  are the complex dielectric function and relative permittivity of the surrounding media respectively. Theoretically, from the equation, when  $\epsilon_1$  equals  $2\epsilon_2$ , an infinite EM is achieved on the surface which is an ideal LSPR condition. The electromagnetic enhancement is thought to be the main contribution towards the SERS signal enhancement by a factor of  $10^6$  to  $10^{10}$ .

#### **Chemical enhancement mechanism:**

This mechanism includes any enhancement of the Raman intensity of surface species/molecules via charge transfer process or via formation of a chemical bond with the metal surface. The mechanism is correlated to the charge transfer between the probed molecule and the surface, because charge transfer between the interacting species is one of the most significant characteristics of chemical reactions [49]. The chemical enhancement usually contributes only a factor of  $10^2$  to the enhancement which is almost negligible with respect to electromagnetic enhancement.

#### **2.3.8.2 Distance dependence**

The intensity of the Raman scattered light is proportional to the square of the magnitude of any electric fields irradiated on the analyte molecule on the surface. The



magnitude of EM field includes two electric fields i.e., electric fields induced on the analyte molecule without nanostructure on the surface and with nanostructure feature on the surface. Since the EM enhancement primarily contributes in SERS and electric field strength decrease with space from the excitation source, an analyte molecule can be benefited from the enhancement even if it is away from the enhancing nanostructure surface by a certain distance. Theoretically, in a sphere model, SERS enhancement ( $G$ ) is related to the radius of the spherical nanostructure ( $r$ ) and the distance between the molecule and spherical metal nanostructure ( $d$ ) via equation  $G = [r / (r + d)]^{10}$ . The enhanced intensity dependency on the distance between the analyte and the spherical metal roughness feature were experimentally studied by Duyne's group in 2004 [50]. Experimentally, it has been observed that the Raman enhancement intensity drops by a factor of 10 with an increasing distance of 2 to 3 nm.

In this thesis, The surface enhanced Raman scattering (SERS) measurements were carried out using micro-Raman spectrometer having  $2\text{ cm}^{-1}$  spectral resolution using 514 nm (green laser) and 633 nm (red laser) excitations, at University of Hyderabad, Hyderabad and some experiments were done at Institute of Material and Minerals Technology (IMMT), Bhubaneswar. All SERS measurements were carried out in a backscattering geometry, using a 50X microscope objective lens for focusing with a numerical aperture of 0.7. Typical laser power at the sample surface was  $\approx 1\text{ mW}$  with a spot size of  $\approx 2\text{ }\mu\text{m}$ .

### 2.3.9 Electrochemistry

Photo-electrochemical measurements were performed using two-compartment three-electrode cell with ITO coated quartz substrate (area  $\approx 1\text{ cm}^2$ ) modified by our samples (via drop-casting liquid samples) as working electrode, a Pt wire as auxiliary electrode and Ag/AgCl (3M NaCl) as reference electrode in 0.01 M  $\text{Na}_2\text{SO}_4$  supporting electrolyte solution. Here, the photo-response and impedance spectra (Nyquist plots) were obtained by illuminating  $\approx 1\text{ cm}^2$  area of the working electrode at zero bias voltage against Ag/AgCl with a 100 Watt lamp (with a luminous irradiance of  $10\text{ mW/cm}^2$  at the sample) switch ON and OFF conditions and the generated photocurrent signals were measured by the computer controlled CHI 660C electrochemical work station. The impedance data analyses were done using the program EQUIVALENT CIRCUIT written by B.A. Boukamp (University of Twente). All the electrochemical experiments were performed in inert argon atmosphere at IMMT, Bhubaneswar.

### 2.3.10 Field emission (FE)

Electron emission can be understood as the emission of electrons from the surface of a material by applying external energy to the electrons in the material. This phenomenon is most frequently observed in metals as there are more free electrons and in some semiconductors also. The minimum energy (usually measured in electron volts) required to remove an electron from the Fermi level in a metal to a point an infinite distance away from the surface is known as the work function of that surface [51]. There are various ways through which an electron can be extracted out from a material. Based on the external source of energy (EE) for the emitted electron, the mechanisms are classified as photo emission (light as EE), thermionic emission (heat as EE), secondary electron emission (energetic electron as EE) and field emission (electric field as EE). The mechanism relevant to this research work is of course based on the electron emission due to the application of electric field. A relevant electron emission mechanism theory will be discussed in detail below, where emission is taking place solely under the influence of an electric field.

#### **Fowler-Nordheim Model:**

The mechanism of field emission has no correlation with the other electron emission mechanisms since it is based on the phenomenon of quantum mechanical tunneling. It was 1<sup>st</sup> observed in 1897 by Wood [52] but was first explained correctly by R. Fowler and L. Nordheim [53] in 1928. Fowler-Nordheim (F-N) explained that electrons are emitted as they tunnel through a potential barrier that is lowered and narrowed because of the presence of intense electric fields and they derived the emission current density. The Fowler-Nordheim Model [54] described the electron emission from metals into a region of high electric field in vacuum is framed based on the following assumptions:

- (1) The temperature of the metal is 0 °K.
- (2) The free-electron approximation applies inside the metal.
- (3) The surface is considered to be smooth (compared to width of the potential barrier small roughens were neglected) and
- (4) The effective potential barrier close to the surface in the vacuum region is combination of image charge potential and potential due to external electric field.

Especially for metal, the electrons are assumed to have a constant effective potential energy -  $W_a$ . Then, in presence of an electric field ( $E$ ), the potential barrier is described by [55]

$$V(x) = -W_a \quad \text{where } x < 0 \quad (2.8)$$

$$= -e^2/4x - eFx \quad \text{where } x > 0 \quad (2.9)$$

Figure 2.20(a) shows the one-dimensional potential energy barrier faced by an electron inside the metal, near the surface. Generally, field emission (FE) behavior is determined by the Fowler-Nordheim (FN) equation which is defined as

$$J = A\beta^2 E^2 / \Phi \exp(-B\Phi^{3/2} / \beta E) \quad (2.10)$$

where,  $J$  is FE current density ( $\mu\text{A}/\text{cm}^2$ ),  $E$  is applied electric field ( $\text{V}/\mu\text{m}$ ),  $A$  and  $B$  are constants with  $A = 1.54 \times 10^{-6} \text{ A}\cdot\text{eV}/\text{V}^2$  and  $B = 6.83 \times 10^3 \text{ eV}^{-3/2} \text{ V}/\mu\text{m}$ , The enhancement factor,  $\Phi$  work function (eV) of the emitter and  $\beta$  is field enhancement factor (FEF) which depends on several parameters like, geometry of the emitter (such as dimension and shape, aspect ratio etc.), emitters surroundings and also shape and distance of the counter electrode. Field emission from semiconductors is a much more complicated process due to its low carrier concentration in bulk emitter compare to metal emitter. In the presence of external electric field, low carrier concentrations allow the field penetrating into the semiconductor, causing band bending and nonlinearity in the current-voltage characteristics in F-N plot. The  $\beta$  value can be figured out from the slopes of the F-N plot (which is  $\ln(J/E^2)$  Vs  $(1/E)$ ) by using the equation

$$\beta = -6.83 \times 10^3 \times (\Phi)^{3/2} / \text{slope} \quad (2.11)$$

Schematic representation of FE phenomena from a sample is shown in Figure 2.20(b).

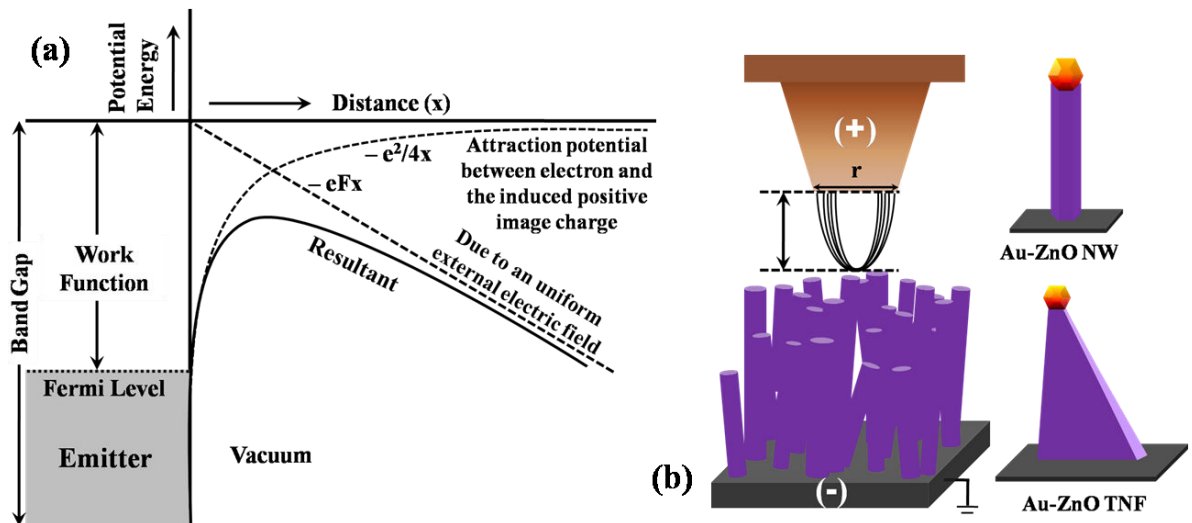


**Figure 2.20:** (a) 1D potential energy barrier for an electron near a metal surface [55]. (b) A schematic illustration of field emission phenomenon, showing the emission from the tip of an emitter. The emitters can have different tip geometry such as, Au-ZnO NW, Au-ZnO TNF.

In this thesis, FE measurements were performed using a simple diode configuration in a high vacuum chamber ( $\approx 5 \times 10^{-7}$  mbar) equipped with a high voltage source meter (Keithley, Model 2410) at room temperature. A micro-gauge variable stepper has been employed with anode plate to precisely keep the separation between emitter surfaces to anode plate. A copper plate of tip diameter 2.5 mm (area  $\approx 0.05 \text{ cm}^2$ ) was used as anode and the Au-ZnO HNs grown silicon substrates were attached to the cathode plate with conductive copper tape (sheet resistance  $\approx 0.004 \Omega$ ) for FE characterizations. For all the measurements anode to cathode separation was kept at  $\approx 100 \mu\text{m}$ . To check the reproducibility of our as-grown samples, we have done same measurements on different locations of the samples.

### 2.3.11 Visible light photodetector (I-V) characteristics

The room temperature current-voltage (I-V) characteristics of our device (made of Au-GeO<sub>2</sub> nanowires as main material) were studied using a Keithley semiconductor parameter analyzer (model no. 4200-SCS) under dark condition and upon illumination of monochromatic light ( $\lambda = 540 \text{ nm}$ , power density  $0.2 \text{ mW/cm}^2$ ). The spectral photocurrent response (responsivity) and external quantum efficiency (EQE) was measured using a setup consisting of a broadband light source, a monochromator, a mechanical chopper (set to 187 Hz), and a lock-in amplifier (Stanford Research, SR 530).

## 2.4 References

- [1] K. Seshan, Handbook of thin-film deposition processes and techniques (Noyes Publications, New York, 2<sup>nd</sup> Ed. 2002, ISBN: 978-0-8155-1442-8).
- [2] R. Glang, "Vacuum evaporation" Ch I in Thin film technology (McGraw-Hill Book Co., 1970).
- [3] D. M. Mattox, "Vacuum Evaporation and Vacuum Deposition" Ch V in Hand book of PVD processing (Noyes Publications, 1998, ISBN: 978-0-8155-2037-5).
- [4] M. Ohring, Materials Science of Thin Films. Deposition and Structure (Elsevier, Academic Press, 2002, ISBN: 978-0-12-524975-1).

- [5] K. Oura, V. G. Lifshits, A. A. Saranin, A. V. Zotov and M. Katayama, *Surface Science - An Introduction* (Springer-Verlag, 2003, ISBN: 978-3-662-05179-5).
- [6] R. S. Wagner and W. C. Ellis, *Appl. Phys. Lett.* **4**, 89 (1964).
- [7] M. Yazawa, M. Koguchi, A. Muto and K. Hiruma, *Appl. Phys. Lett.* **61**, 2051 (1992).
- [8] K. Hiruma et al., *J. Appl. Phys.* **77**, 447 (1995).
- [9] A. M. Morales and C. M. Lieber, *Science* **279**, 208 (1998).
- [10] X. Duan and C. M. Lieber, *Adv. Mater.* **12**, 298 (2000).
- [11] P. Nguyen, H. Ng and M. Meyyappan, *Adv. Mater.* **17**, 1773 (2005).
- [12] H. S. Liu, K. Ishida, Z. P. Jin and Y. Du, *Intermetallics* **11**, 987 (2003).
- [13] C. C. Weigand et al., *Cryst. Growth Des.* **11**, 5298 (2011).
- [14] Ji-Tao Wang, *Nonequilibrium Nondissipative Thermodynamics: With Application to Low-pressure Diamond Synthesis* (Springer-Verlag, 2002, p. 65. ISBN 978-3-540-42802-2).
- [15] P. Blecua, R. Lipowsky and J. Kierfeld, *Langmuir* **22**, 11041 (2006).
- [16] A. P. Levitt, *Whisker Technology* (Wiley-interscience, 1970).
- [17] W. K. Burton, N. Cabrera and F. C. Frank, *Nature* **163**, 398 (1949).
- [18] P. L. Edwards and S. Huang, *J. Am. Ceram. Soc.* **49**, 122 (1966).
- [19] D. S. Kim, R. Scholz, U. Gösele and M. Zacharias, *Small* **4**, 1615 (2008).
- [20] M. Paulose, O. K. Varghese and C. A. Grimes, *J. Nanosci. Nanotech.* **3**, 341 (2003).
- [21] H. F. Yan et al., *Chem. Phys. Lett.* **323**, 224 (2000).
- [22] D. B. Williams and C. Barry Carter, *Transmission Electron Microscopy: A Textbook for Materials Science* (Springer, 2<sup>nd</sup> Ed. 2009, ISBN: 978-0-387-76500-6).
- [23] John C. H. Spence, *High-resolution Electron Microscopy* (Oxford Science Publications, 2013, ISBN: 978-0-199-66863-2).
- [24] B. Fultz and J. Howe, *Transmission Electron Microscopy and Diffractometry of Materials* (Springer, 2nd Ed. 2005, ISBN: 978-3-642-29761-8).

- [25] M. Knoll and E Ruska, *Z. Physik.* **78**, 318 (1932).
- [26] J. M. Cowley and A. F. Moodie, *Acta Crystallogr.* **10**, 609 (1957).
- [27] J. Ackermann, Manual for the SUPRA (VP) and ULTRA Scanning Electron Microscopes. Smart SEM V. 05.00. Carl Zeiss SMT Ltd. (2005).
- [28] J. Goldstein, et al., Scanning Electron Microscopy and X-ray Microanalysis (Springer, 3rd Ed. 2003, ISBN: 978-1-4615-0215-9).
- [29] G. Lloyd, *Mineral. Mag.* **51**, 3 (1987).
- [30] D. K. Schroder, Semiconductor material and device characterization (Wiley-IEEE press, 2006, ISBN: 978-0-471-73906-7).
- [31] P. E. J. Flewit and R. K. Wild, Physical methods for material characterization (IOP publishing, 2nd Ed. 2003, ISBN: 978-0-750-30808-3).
- [32] J. E. Toney, Photoluminescence Spectroscopy. Characterization of Materials (John Wiley & Sons, 2002, DOI: 10.1002/0471266965.com058).
- [33] P. Das and T. K. Chini, *Curr. Sci.* **101**, 849 (2011).
- [34] B. V. Crist, Handbook of Monochromatic XPS Spectra, The Elements of Native Oxides (Wiley, 2000, ISBN: 978-0-471-49265-8).
- [35] J. F. Watts and J. Wolstenholme, An Introduction to Surface Analysis by XPS and AES (Wiley & Sons, 2005, ISBN: 978-0-470-86793-8).
- [36] K. Siegbahn and K. I. Al. Edvarson, *Nuclear Physics* **1**, 137 (1956).
- [37] C. V. Raman and K. S. Krishna, *Nature* **121**, 501 (1928).
- [38] M. Fleischmann, P. J. Hendra and A. J. McQuillan, *Chem. Phys. Lett.* **26**, 163 (1974).
- [39] D. L. Jeanmaire and R. P. Van Duyne, *J. Electroanal. Chem.* **84**, 1 (1977).
- [40] M. G. Albrecht and J. A. Creighton, *J. Am. Chem. Soc.* **99**, 5215 (1977).
- [41] E. Hao and G. C. Schatz, *J. Chem. Phys.* **120**, 357 (2004).
- [42] B. J. Marquis, A. D. McFarland and C. L. Haynes, *Anal. Chem.* **80**, 3431 (2008).
- [43] A. Campion and P. Kambhampati, *Chem. Soc. Rev.* **27**, 241 (1998).

- [44] P. Kambhampati and A. Campion, *J. Chem. Soc. Faraday Trans.* **92**, 4775 (1996).
- [45] J. D. Driskell et al., *Anal. Chem.* **77**, 6147 (2005).
- [46] G. Braun et al., *J. Am. Chem. Soc.* **129**, 6378 (2007).
- [47] C. L. Haynes, A. D. McFarland and R. P. Van Duyne, *Anal. Chem.* **77**, 338A (2005).
- [48] A. J. Haes et al., *MRS Bull.* **30**, 368 (2005).
- [49] P. L. Stiles, J. Dieringer and R. P. Van Duyne, *Annu. Rev. Anal. Chem.* **1**, 601 (2008).
- [50] C. L. Haynes and R. P. Van Duyne, *J. Phys. Chem. B* **105**, 5599 (2001).
- [51] J. I. Gersten and F. W. Smith, *The Physics and Chemistry of Materials* (Wiley, illustrated Ed. 2001, ISBN: 978-0-471-05794-9).
- [52] R. W. Wood, *Phys. Rev. (Series I)* **5**, 1 (1897).
- [53] R. H. Fowler and L. Nordheim, *Proc. R. Soc. London, Ser A*, **119**, 173 (1928).
- [54] A. G. J. V. Oostrom, *Validity of the Fowler-Nordheim Model for Field Electron Emission* (Netherland Philips Research Laboratories, 1966).
- [55] E. L. Murphy and R. H. Good, *Phys. Rev.* **102**, 1464 (1956).

# Chapter 3

## **Au Catalyzed Vapor-Liquid-Solid (VLS) Growth of Faceted Au-ZnO Hetero- Nanostructures on Low Index Silicon Surfaces: Role of Native Oxide at the Interface**

### **3.1 Introduction**

In this chapter, we will be focused on the Au catalyzed growth of faceted Au capped ZnO hetero-nanostructures (HNs) of different morphologies and dimensionalities, on Au/SiO<sub>2</sub>/Si(100), (110) and (111) @ 800 °C pre-annealed substrates. The Au-ZnO HNs, of two significantly different morphologies (Au-ZnO Nanowires (NWs) and Triangular nanoflakes (TNFs)) have been grown simultaneously on two substrates, kept at two different positions in the growth chamber with respect to the source and gas flow direction. The thickness of the catalyst layer (we have used  $\approx 1$  nm and  $\approx 5$  nm Au as catalyst layer) is found to be an important factor governing areal density (no of HNs per unit area) and aspect ratio (i.e., length and diameter) of the as-grown Au-ZnO HNs on both the substrates (downstream and upstream). Here, we have established a *single step* growth technique, where integration of one faceted Au NPs on top of every single ZnO NSs to form semiconductor-metal, Au-ZnO hetero-nanostructures (HNs) is achieved, without any post-growth multistep processes. In this work, we have addressed the role of native oxide on Si substrate, on the Au catalyzed growth of ZnO HNs via combined VLS and VS growth modes. Interestingly, we have not found any Au-ZnO HNs growth in case of Au deposited on atomically cleaned Si substrates (without native oxide SiO<sub>2</sub>), only very less density ZnO nanowires were found. At the end of this chapter we will describe the vertically aligned faceted Au NP capped ZnO HNs on lattice matched single crystalline oxygen terminated ZnO(0001) substrate. Consistent reproducibility of these two types of HNs morphology, nanowire (NW) and triangular nanoflake (TNF) have been investigated.



One-dimensional (1D) oxide semiconductor materials have gathered great attention not only due to their fundamental importance but also due to the technological necessity. There are several 1D semiconductors including oxide semiconductors have attracted large community of research community, which includes GaN, InN, TiO<sub>2</sub>, SnO<sub>2</sub>, GeO<sub>2</sub>, ZnO, CuO, CeO, CdO, MgO etc [1-5]. In comparison with other oxide semiconductors, ZnO has been actively worked upon from variety of research communities due to their high photosensitivity, large direct bandgap (3.37 eV), relatively high exciton binding energy (60 meV), non-toxic character, abundant in reserve and low-cost large scale synthesis viability [6-9,10-12]. In recent decades various 1D ZnO nanostructures have been studied extensively due to their interesting physical properties different than their bulk form [13]. For future applications of one-dimensional (1D) ZnO nanostructures it is very important to be able control their alignment, shape, size (diameter and length), and their distribution. As the size, shape and morphology of the NSs have key importance on their applications, various 1-D ZnO NSs with different morphologies, such as nanowires (NWs), nanorods (NRs), nanotubes (NTs), nanobelts, nanonails, nanoflakes (NFs), nanowalls, nanotetrapods and nanosheets have been synthesized [14-16]. ZnO nanostructures with different morphologies finds different applications: rods (UV photonic devices: light emitting diodes, optical switching etc), needle (field emission plasma displays), wire (various gas, chemical and biological sensors, interconnects for nano circuits), belts (piezoelectric nano-mechanical devices), films (solar cells) and so on [6-10, 17-21]. The detailed morphology is very sensitive to the growth conditions. To get such variations, several growth/synthesis protocols have been established, such as solution based synthesis, pulsed laser deposition and vapor phase transport (VPT) depositions (like CVD, MOCVD, thermal evaporation etc.) with and without catalyst and so forth [14, 16, 22-24]. To control precisely the size, shape, morphology and orientation of the metal nanoparticle (NP) conjugated ZnO hetero-nanostructures (HNs) via metal (such as gold, palladium, platinum, copper etc.) catalyzed chemical vapor phase transport (VPT) method we have to properly focus on various growth parameters like: growth temperature, types of substrate (such as substrate material and crystallographic orientation) and catalyst layer thickness. Further VPT growth method can be classified into three different growth modes, those are vapor-liquid-solid (VLS), vapor-solid (VS) and solid-liquid-solid (SLS). Among various methods of source vaporization used in VPT including thermal evaporation (by heat), laser ablation (by photons), sputtering (by positive ions) and electron beam evaporation, thermal evaporation is widely used for 1D nanostructure growth. There are several processing parameters such as substrate type and orientation, carrier gas flow rate,

source composition and purity, substrate temperatures, growth time, which can be controlled and need to be selected carefully before and during the vaporization [16, 25]. A well accepted and understood mechanism of 1D HNs growth via gas phase reaction of relevance to this thesis work is called the vapor liquid solid (VLS) growth mode which offers flexibility in control over size, shape and growth position [22, 26, 27]. In this work, we also have explored the growth of ZnO NSs/HNs via vapor solid (VS) growth mode along with VLS mode. In 1965 Wagner and Ellis first proposed this VLS mechanism during studies of large single crystalline Si whisker growth [27]. It is well documented in the literature that the morphology and degree of alignment of ZnO NSs depends crucially on the type of substrate and its orientation among several other factors [25]. To grow oriented/aligned ZnO NSs/HNs preferred substrate is the top priority. Many research groups all over the world have been using various substrate including Si, sapphire ( $\text{Al}_2\text{O}_3$ ), GaN, ZnO buffer layered Si (among others) substrate to study role of substrate and its orientation for ZnO NSs growth [25, 28-33]. Among those substrates, native oxide coated Si is very common for growth of ZnO NSs, because Si is easily available, stable at high temperature and of relatively low cost. It is observed that with native oxide ( $\text{SiO}_2$ ) on Si substrate, well aligned growth of ZnO NSs is not possible via either catalyzed or uncatalyzed growth. But it's possible to grow aligned ZnO NSs up to some extent by depositing thin buffer layer on  $\text{SiO}_2/\text{Si}$  substrate which will minimize the lattice mismatch between the substrates and ZnO NSs [31, 33]. It is paramount to mention that for VLS growth mode, most important requirement is the selection of proper metal catalyst with respect to the growth conditions (like type of substrate, growth temperature etc.). Metal catalyst islands on the surface of the substrates are used to act as nucleation sites and control the position of the NSs/HNs grown via VLS mode of growth. In the VLS mechanism various metals as catalyst have been used extensively for different semiconductor NSs, which includes gold, platinum, nickel, silver, palladium or copper [27]. The selection of the catalyst depends on various factors like reaction temperature, VLS interfacial energies and type of substrate. Most important things behind choosing catalyst are, metal NPs should melt and form alloy with transported vapor and not react with substrate at the growth temperature. Particularly for the growth of ZnO NSs/HNs on various low index Si substrates and single crystalline ZnO(0001) substrate by VPT method, we have found that Au is the most suitable catalyst. However, it has never been reported in the literature that how VLS growth mode gets affected during Au catalyzed growth of ZnO NSs/HNs on atomically cleaned Si substrates (native oxide  $\text{SiO}_2$  was removed by flashing in UHV-MBE chamber).

### 3.2 Experimental

Large-scale single-crystalline nanostructures of Au-ZnO system (Nanowires and Triangular nanoflakes) were grown by keeping the substrates at two different positions (downstream and upstream) in a single zone, side entry quartz tube furnace as depicted in Figure 3.1. The furnace consists of a  $\approx 100$  cm long horizontal quartz tube with an inner diameter of  $\approx 4.5$  cm, a sample holder/boat that is made of ceramic, and silicon carbide rods as heating elements. One side of the quartz tube was connected to the gas inlet controlled by mass flow controller and other side had gas outlet. Details about the CVD system used for all the growths we have carried out for this thesis work is presented in the previous chapter (Chapter 2). Initially, commercially available silicon wafers with three different orientations like Si(100), Si(110) and Si(111) (having  $\approx 2-3$  nm SiO<sub>2</sub> (native oxide)) were cleaned through ultrasonication in acetone and methanol for 5 minutes each and then two different thicknesses  $\approx 1$  nm and 5 nm Au films were deposited (using high vacuum coating methods) on these three kinds of substrates Si(100), Si(110) and Si(111). These substrates were annealed at 800 °C for 30 min in air prior to growth of Au-ZnO hetero-nanostructures (HNs) arrays. Two different thickness of catalyst Au layer were deposited to study the effect of thickness of Au

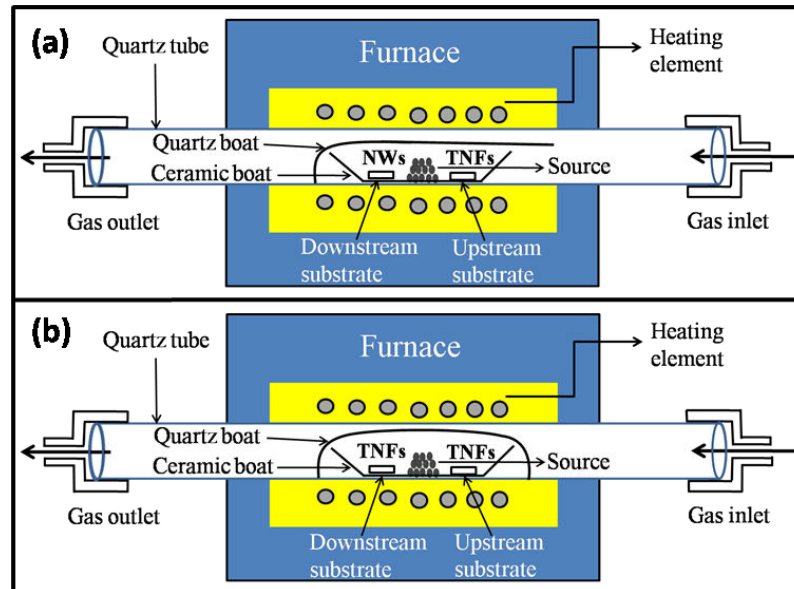


**Figure 3.1:** Schematic of growth setup (a) with one side open quartz boat (used for all growth carried out for this thesis work) and (b) with both side closed quartz boat. Except quartz boat geometry else are exactly same for both the setup (to show more growth species availability leads to triangular nanoflakes (TNFs) growth. So, for nanowires growth optimized growth species supply is required.

on the growth product [34]. Annealing of Au films on native oxide covered silicon substrates yielded well oriented and dispersed gold nanoparticles on silicon substrates and such procedure is known as solid state dewetting (schematically shown in Figure 3.2) [34]. All these six types of substrates have been used for the growth of Au-ZnO hetero-nanostructures (HNs) at growth temperature of 900 °C for 90 min growth time. In this growth process, mixture of ZnO (99.999%) and graphite powders (99.999%) at a 1:1 molar ratio were taken as the evaporating source. Growth species (Zn and O) were produced through carbothermal reduction reactions, which happen around 850 °C. That's why we have chosen our optimized

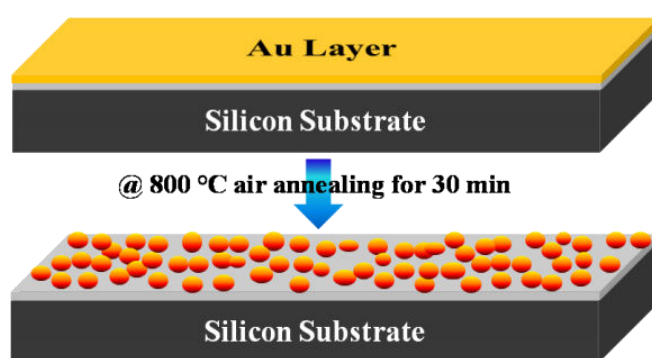


**Figure 3.2:** Schematic representations of Au thin film deposited on commercially available silicon substrate with  $\approx 2 - 3$  nm native oxide (above) and Au nanoparticles (NPs) formed after air annealing at 800 °C for 30 min (below).

growth temperature 900 °C. The source was put at the centre of a ceramic boat (diameter 1.5 cm and length 9 cm) and Au NPs decorated two substrates were placed  $\approx 2.5$  cm away either side of the source and covered by a quartz boat of diameter 2.2 cm and length 10 cm. Argon gas has been used as carrier gas with 30 sccm (standard cubic centimeter mass) flow. At the very beginning before switching on the furnace, we purge the chamber by Ar gas to ensure the removal of reactive species inside the quartz tube. The temperature at the tube centre, where quartz boat covered ceramic boat was placed, increased at a constant ramping rate 7 °C/min from room temperature to growth temperature 900 °C and the system was held at the peak temperature for 90 min under a constant 30 sccm Ar flow. During the growth experiments, 30 sccm Ar was introduced as soon as furnace temperature reached 750 °C. During that growth period Zn and CO/CO<sub>2</sub> vapor were produced and transported towards the substrates through Ar gas flow. Gold catalyst nanoparticles present on the Si substrates, causes alloying of the catalyst with Zn vapor at temperature  $\geq 700$  °C (Au-Zn alloy eutectic temperature 684 °C) [34-36] until the super saturation of Zn is reached. As pure zinc forms at

the surface of the alloyed catalyst, it is then oxidized by the low concentration of oxidizing gas, CO/CO<sub>2</sub>, and seeded crystal growth of ZnO nanostructures takes place [22, 26, 27, 35, 37]. The as-grown samples were removed from the furnace after the system cooled down to room temperature.

A thin Au film of thickness 10 ML was deposited on n-type Si(100) of resistivity 10 – 20 cm, by the molecular beam epitaxy (MBE) method under UHV (base pressure  $2 \times 10^{-10}$  mbar) conditions [38]. Only Si(100) oriented substrate was loaded into the MBE chamber and degassed at 600 °C for about 12 hours inside the chamber, followed by flashing for about 3 minutes by direct heating at a temperature of 1200 °C. In this process, native oxide was removed and a clean Si(100) surface was obtained. On such ultra clean surface, 10 ML thick gold film was grown epitaxially by evaporating Au from a Knudsen cell. Deposition rate was kept constant at 0.14 nm-min<sup>-1</sup>. During the growth, the chamber vacuum was  $6.2 \times 10^{-10}$  mbar. This 10 ML Au/Si(100) substrate was first annealed in air at 800 °C for 30 min and used for ZnO nanowires growth by following the same process as mentioned earlier (substrate kept at upstream position).

Apart from silicon substrates (with and without native oxide), we have used lattice matched single crystalline oxygen terminated ZnO(0001) substrate to grow epitaxial and vertically aligned Au-ZnO HNs. For this case, we have deposited a  $\approx 2$  nm Au thin film on ZnO(0001) and then annealed in air at same 800 °C for 30 min as earlier cases. For the growth of Au-ZnO nanowires on this substrate we have followed exactly similar steps as earlier (here substrate was kept at downstream position) except growth duration (30 min).

Surface morphology, shape and size of the as-grown Au-ZnO NWs and TNFs arrays were examined using field emission gun based scanning electron microscopy (FEG-SEM) equipped with BSE detector (Z contrast imaging), with 20 kV electrons (Neon 40 cross-beam system, M/S Carl Zeiss GmbH) and high resolution transmission electron microscopy (HRTEM) with 200 keV electrons (2010, JEOL HRTEM). Detailed structural analysis was performed using HRTEM with selected area electron diffraction (SAED) pattern capabilities. For HRTEM investigations, the Au-ZnO NWs and TNFs first mechanically scratched from respective samples and then dispersed on two different carbon coated Cu grids by drop-casting. The local compositional analyses of HNs were done by energy dispersive X-ray (EDX) spectrum that is coupled with SEM. X-ray diffraction (XRD) measurements were performed by a Philips Xpert PRO MRD Cradle using CuK $\alpha$  ( $\lambda=1.54$  Å) radiation.

## 3.3 Results and discussion

### 3.3.1 Growth of Au-ZnO HNs (Nanowires and Triangular nanoflakes) on native oxide coated Si substrates

In this section we will focus on the growth of two types of faceted Au nanoparticle (NP) capped ZnO hetero-nanostructures (HNs) of two kinds (NWs and TNFs) on native oxide ( $\approx 2 - 3$  nm) coated three low index Si substrates (Si (100), (110) and (111)) depending on the substrates position (downstream or upstream). As we are interested in VLS growth of Au-ZnO HNs, so first we have deposited  $\approx 1$  nm Au thin film on these substrates and subsequently annealed @  $800^\circ\text{C}$  in air to form Au NP decorate native oxide coated Si substrates. Figure 3.3(a) and its inset figure show SEM micrograph of the 1 nm Au/SiO<sub>2</sub>/Si(100) after  $800^\circ\text{C}$  in air annealing and corresponding size distribution histogram respectively. From this figure, it is evident that average diameter of the Au nanoparticles formed on Si(100) is  $21 \pm 4$  nm. Similarly for other two substrates (i.e., Si(110) and Si(111)) average diameter of the Au NPs are  $22 \pm 4$  nm and  $20 \pm 3$  nm respectively as shown in Figures 3.4(a) and 3.5(a). Here we can conclude that size distributions of the Au NPs formed on these three oriented Si substrates are almost same with coverage of  $\approx 25\%$ . Then we have used these Au NP decorate/SiO<sub>2</sub>/Si substrates as templates for the growth of Au-ZnO HNs using CVD technique via combined VLS and VS mechanism.

The morphological studies were carried out with FE-SEM (both secondary electron (SE) and backscattered electron (BSE) images) for all the samples. At first we will describe the results on Si(100) substrate. Figure 3.3(b) depicts low-magnification SEM image of the as-grown Au-ZnO NWs sample on substrate kept at downstream position, it shows abundance of Au-ZnO NWs. Cross-sectional view of this same sample has been presented in Figure 3.3(c), showing random alignment of the Au-ZnO NWs with respect to the substrate normal. Inset of Figures 3.3(b and c) present high-magnification SEM and backscattered electrons (BSE) image of a single faceted Au NP capped ZnO NW respectively. BSE image clearly shows brighter contrast faceted Au NP situated at the apex of the uniform diameter NW, which is also complimented by high-magnification SEM micrograph. In contrast, low-magnification SEM image of the Au-ZnO HNs grown on substrate kept at upstream position is shown in Figure 3.3(g). Cross-sectional view of this sample is given in Figure 3.3(h), showing randomly aligned triangular nanoflakes (TNFs) structure. Inset of Figures 3.3(g and

h) show high-magnification SEM and BSE (Z-contrast) micrographs of a single Au-ZnO TNF from the corresponding sample respectively. From these inset figures we can conclude that these types of HNs are tapered triangular in geometry with faceted Au at the growth front. Brighter contrast in the BSE images shown as insets of Figures 3.3(c and h)

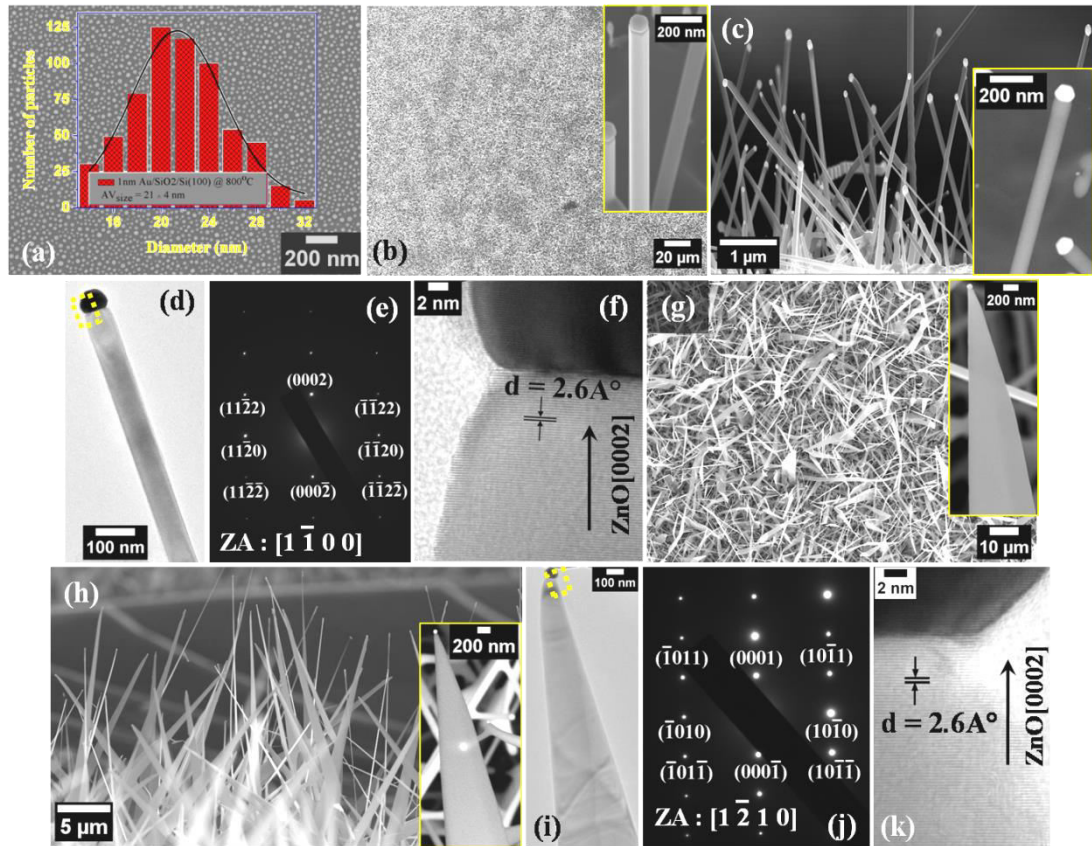


**Figure 3.3:** (a) SEM image of Au nanoparticles (NPs) formed after air annealing at 800 °C of 1 nm Au/SiO<sub>2</sub>/Si(100); inset represents corresponding size distribution histogram of Au NPs. (b and g) show low-magnification SEM micrographs of as-grown Au-ZnO nanowires (NWs) and triangular nanoflakes (TNFs) on the previous substrate, respectively; corresponding inset figures show high resolution SE images of a single NW and TNF with faceted Au NP at the tip. (c and h) present cross-sectional SEM images of the corresponding NWs and TNFs samples, respectively; corresponding insets show high resolution BSE images (Z-contrast images) of individual Au-ZnO NW and TNF. (d and i) depict low-magnification TEM micrographs of a single Au-ZnO NW and TNF with faceted Au particle at the tip of each, respectively. (e and j) are the selected area electron diffraction (SAED) pattern from individual NW and TNF, respectively. (f and k) present HRTEM images taken from the highlighted regions of Au-ZnO NW in panel (d) and Au-ZnO TNF in panel (i), respectively.



correspond Au NP which is present at the tip of both types of HNs (NWs and TNFs). From typical SEM results it is clear that sample at the downstream position consists of Au-ZnO NWs with uniform diameter with hexagonal cross-sections whereas sample at the upstream position contains Au-ZnO tapered TNFs having rectangular cross-sections with very little amount of NWs.

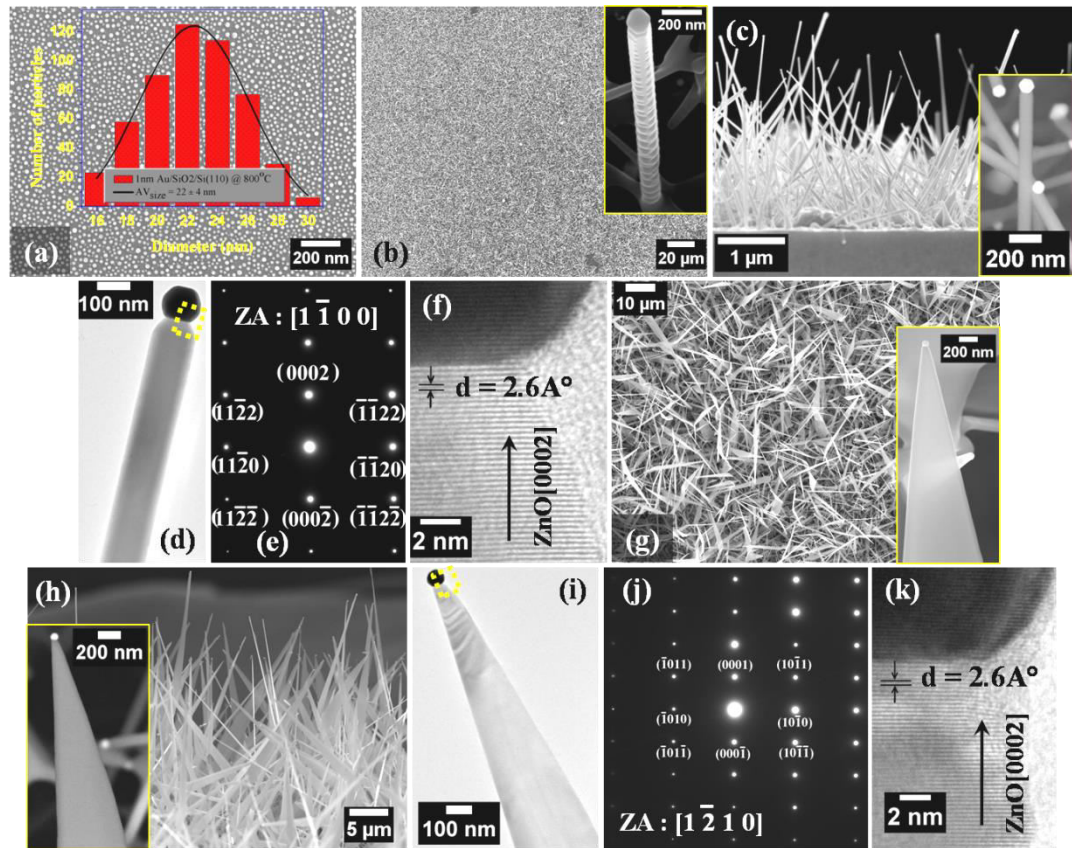


**Figure 3.4:** (a) SEM image of Au nanoparticles (NPs) formed after air annealing at 800 °C of 1 nm Au/SiO<sub>2</sub>/Si(110); inset represents corresponding size distribution histogram of Au NPs. (b and g) show low-magnification SEM micrographs of as-grown Au-ZnO nanowires (NWs) and triangular nanoflakes (TNFs) on the previous substrate, respectively; corresponding inset figures show high resolution SE images of a single NW and TNF with faceted Au NP at the tip. (c and h) present cross-sectional SEM images of the corresponding NWs and TNFs samples, respectively; corresponding insets show high resolution BSE images (Z-contrast images) of individual Au-ZnO NW and TNF. (d and i) depict low-magnification TEM micrographs of a single Au-ZnO NW and TNF with faceted Au particle at the tip of each, respectively. (e and j) are the selected area electron diffraction (SAED) pattern from individual NW and TNF, respectively. (f and k) present HRTEM images taken from the highlighted regions of Au-ZnO NW in panel (d) and Au-ZnO TNF in panel (i), respectively.



Detailed structural studies on Au-ZnO NWs and TNFs were further carried out using TEM with selected area electron diffraction (SAED) and HRTEM. Figures 3.3(d and i) show the low-magnification TEM micrographs of a single Au-ZnO NW and TNF respectively, reveal a faceted Au NP at the apex of each of them. The corresponding HRTEM images are shown in Figures 3.3(f and k) from the highlighted regions of Figures 3.3(d and i) suggest that Au-ZnO

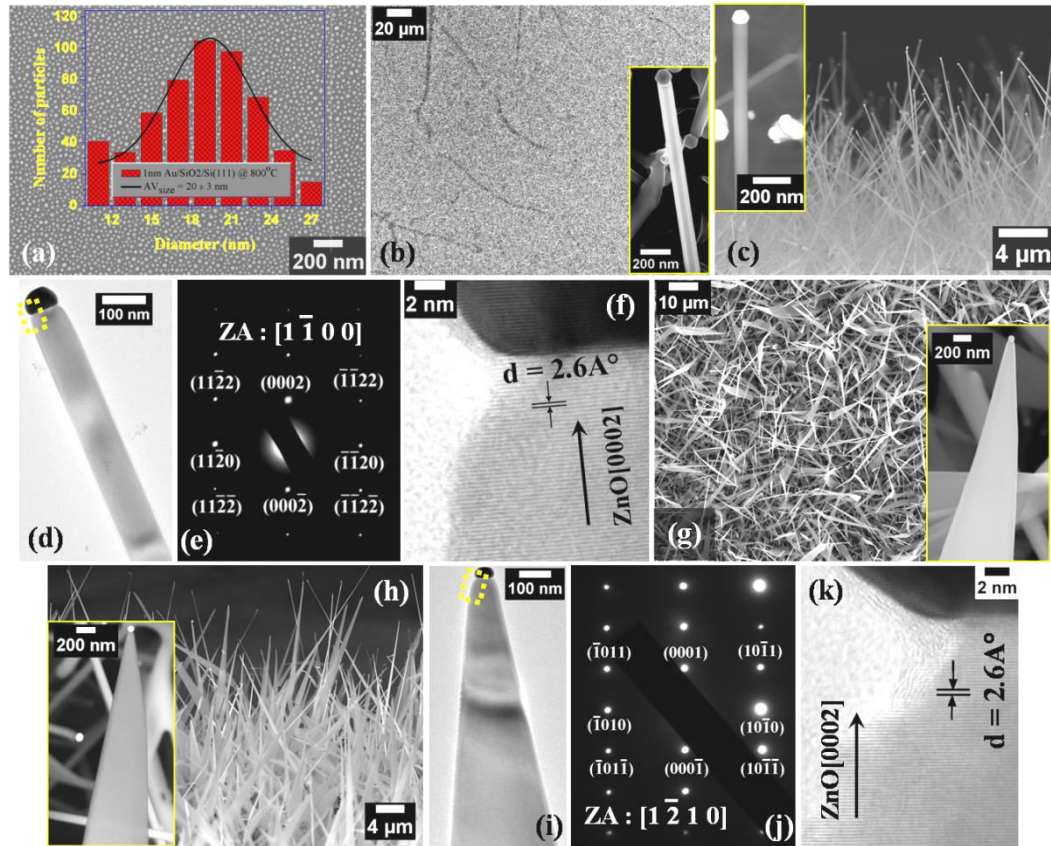


**Figure 3.5:** (a) SEM image of Au nanoparticles (NPs) formed after air annealing at 800 °C of 1 nm Au/SiO<sub>2</sub>/Si(111); inset represents corresponding size distribution histogram of Au NPs. (b and g) show low-magnification SEM micrographs of as-grown Au-ZnO nanowires (NWs) and triangular nanoflakes (TNFs) on the previous substrate, respectively; corresponding inset figures show high resolution SE images of a single NW and TNF with faceted Au NP at the tip. (c and h) present cross-sectional SEM images of the corresponding NWs and TNFs samples, respectively; corresponding insets show high resolution BSE images (Z-contrast images) of individual Au-ZnO NW and TNF. (d and i) depict low-magnification TEM micrographs of a single Au-ZnO NW and TNF with faceted Au particle at the tip of each, respectively. (e and j) are the selected area electron diffraction (SAED) pattern from individual NW and TNF, respectively. (f and k) present HRTEM images taken from the highlighted regions of Au-ZnO NW in panel (d) and Au-ZnO TNF in panel (i), respectively.

HNs are grown along common [0001] crystal direction (c-axis oriented). SAED patterns from Au-ZnO NWs and TNFs body were taken along  $[1\bar{1}00]$  and  $[1\bar{2}10]$  zone axes and are shown in Figures 3.3(e and j) respectively. These show single crystalline nature with hexagonal wurtzite phase of the HNs grown along common [0001] direction. We have also analyzed the results on other two substrates Si(110) and Si(111) in a similar fashion, shown in Figure 3.4 and Figure 3.5 respectively. From detailed electron microscopy analysis we have not found any significant differences between the Au-ZnO HNs (for both types NWs and TNFs) grown on three oriented substrates, with respect to their size, shape, morphology, density and alignment. This observation is in agreement with the previous reports on growth of ZnO NSs on native oxide coated Si substrates [39]. Statistical observations on respective samples for shape, size and dimensional details have been summarized in Table 3.1 below.

We have also done XRD analysis (shown later) on both the samples to check the large scale crystalline information. The growth fronts of each of the NW and TNF terminated with faceted catalyst Au NPs, confirmed by TEM, HR-SEM and EDX (shown later), suggest that both are catalyst assisted growth [22-24, 40, 41]. The growth of faceted NWs is in uniform diameter. But a gradual shrinking of diameter towards the growth direction of faceted TNFs was observed. The presence of catalyst NP at the tip and the faceted side-wall of HNs suggest that the growth mechanism is a mixture of VLS and VS processes [23,24,41,42]. The influences of substrate position over differences in Au-ZnO HNs morphology will be discussed thoroughly in the proposed growth models section later of this chapter. In the next section we will concentrate on the role of catalyst layer thickness on the aspect ratio and density of the as-grown Au-ZnO HNs on the same substrates.

### 3.3.2 Role of catalyst layer thickness on the dimensionality of Au-ZnO hetero-nanostructures

To check the role of initially deposited Au layer (catalyst) thickness on the growth product we have carried out similar growth with  $\approx 5$  nm Au thick film on same native oxide ( $\approx 2 - 3$  nm) coated three low index Si(100), (110) and (111) substrates. So, this time instead of  $\approx 1$  nm Au (as done earlier) we have deposited  $\approx 5$  nm Au on these substrates and followed exactly same previously adopted steps to grow Au-ZnO HNs. Figure 3.6(a) and its inset figure show SEM micrograph of the 5 nm Au/SiO<sub>2</sub>/Si(100) after 800 °C in air annealing and corresponding size distribution histogram respectively. From this figure, it is evident that

average diameter of the Au nanoparticles formed on Si(100) is  $46 \pm 8$  nm. Similarly for other two substrates (i.e., Si(110) and Si(111)) average diameter of the Au NPs are  $48 \pm 6$  nm and  $44 \pm 8$  nm respectively as shown in Figures 3.4(a) and 3.5(a). Here we can conclude that for 5 nm Au catalyst layer, size distributions of the Au NPs formed on these three oriented Si substrates are almost same with coverage of  $\approx 38$  %, but compared to 1 nm Au catalyst

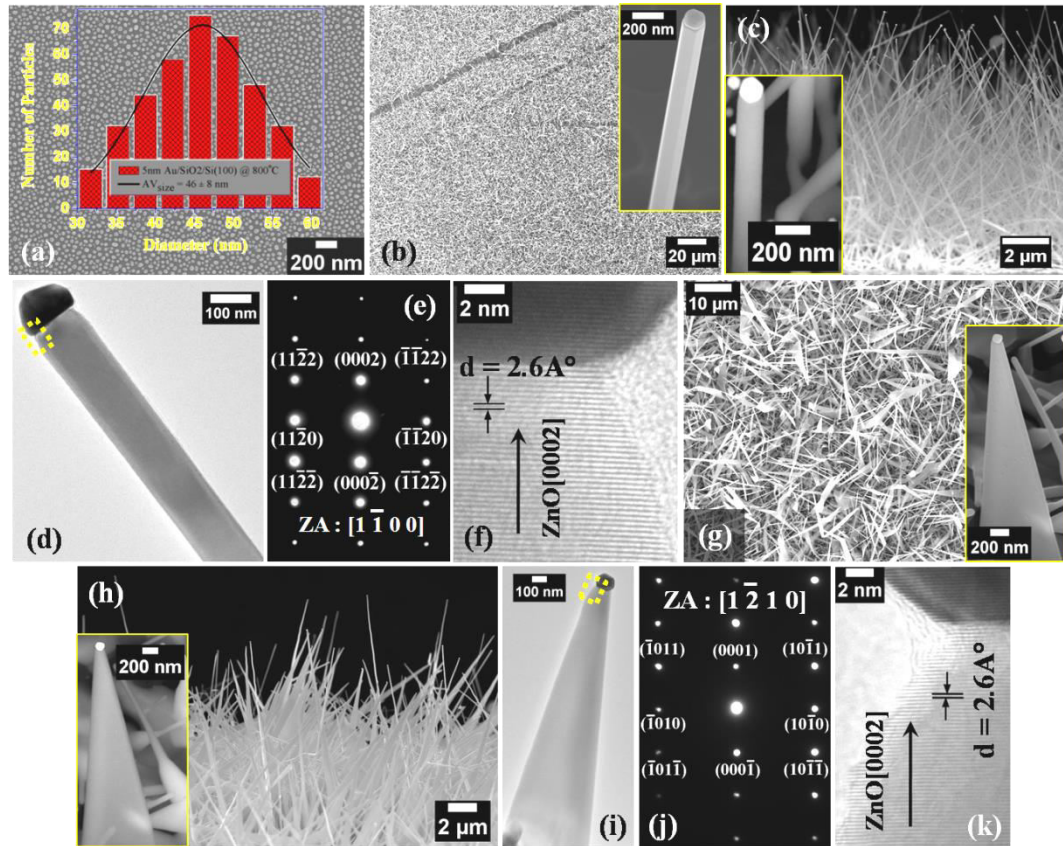


**Figure 3.6:** (a) SEM image of Au nanoparticles (NPs) formed after air annealing at 800 °C of 5 nm Au/SiO<sub>2</sub>/Si(100); inset represents corresponding size distribution histogram of Au NPs. (b and g) show low-magnification SEM micrographs of as-grown Au-ZnO nanowires (NWs) and triangular nanoflakes (TNFs) on the previous substrate, respectively; corresponding inset figures show high resolution SE images of a single NW and TNF with faceted Au NP at the tip. (c and h) present cross-sectional SEM images of the corresponding NWs and TNFs samples, respectively; corresponding insets show high resolution BSE images (Z-contrast images) of individual Au-ZnO NW and TNF. (d and i) depict low-magnification TEM micrographs of a single Au-ZnO NW and TNF with faceted Au particle at the tip of each, respectively. (e and j) are the selected area electron diffraction (SAED) pattern from individual NW and TNF, respectively. (f and k) present HRTEM images taken from the highlighted regions of Au-ZnO NW in panel (d) and Au-ZnO TNF in panel (i), respectively.

thickness cases the average diameter of the Au NPs and coverage are  $\approx 2$  times and  $\approx 1.5$  times higher respectively. Then we have used these Au NP decorate/SiO<sub>2</sub>/Si substrates as templates for the growth of Au-ZnO HNs using CVD technique via combined VLS and VS mechanisms as we have done for earlier 1 nm Au cases. For this 5 nm Au cases also we have employed FE-SEM for morphological studies for all the as-grown samples. At first we will describe the results on Si(100) substrate in a similar way as we did for 1 nm Au cases. Figures 3.6(b and g) portray low-magnification SEM images of the Au-ZnO HNs samples grown on substrate kept at downstream (NWs) and upstream (TNFs) positions respectively, which reveal abundance of HNs growth. Cross-sectional view of the corresponding samples have been shown in Figures 3.6(c and h) respectively, showing random alignment of the Au-ZnO NWs and TNFs with respect to the substrate normal. Inset of Figures 3.6(b and g) present high-magnification SEM images of single faceted Au NP capped ZnO NW and TNF respectively. As a complementary observation, Inset in the Figures 3.6(c and h) show high magnification BSE (Z-contrast) images of single Au-ZnO NW and TNF respectively, where brighter contrast corresponds faceted Au NP at the apex of both types of HN (NW and TNF). From both SEM and BSE high-magnification images confirm that NWs are uniform in diameter with hexagonal cross-section and TNFs are gradually tapered (shrinking in diameter towards growth front) with rectangular cross-section; and all of them contain a faceted Au NP at the growth front. From all the above SEM results it's clear that morphology wise both types of HNs (NWs and TNFs) are exactly similar for two different catalyst layers ( $\approx 5$  nm and  $\approx 1$  nm Au), but there are significant differences in the areal density (number of HNs per unit area) and dimensionality. Variations in the dimensionality for all the samples are shown in the Table 3.1 below.

Further structural studies on Au-ZnO NWs and TNFs were further carried out using TEM with selected area electron diffraction (SAED) and high resolution lattice imaging (HRTEM). Figures 3.6(d and i) show the low-magnification TEM micrographs of a single Au-ZnO NW and TNF respectively, reveal a faceted Au NP at the apex of each of them. The corresponding HRTEM images are shown in Figures 3.6(f and k) from the highlighted regions of Figures 3.6(d and i) suggest that Au-ZnO HNs are grown along common [0001] crystal direction (c-axis oriented). SAED patterns from Au-ZnO NWs and TNFs body were taken along  $[1\bar{1}00]$  and  $[1\bar{2}10]$  zone axes and are shown in Figures 3.6(e and j) respectively. These show single crystalline nature with hexagonal wurtzite phase of the HNs grown along common [0001] direction. We have also described the results on other two substrates Si(110)



and Si(111) in a similar was, shown in Figure 3.7 and Figure 3.8 respectively. What we have observed in cases of 1 nm Au, here also for 5 nm Au cases rigorous microscopy analysis concluded that Au-ZnO HNs (for both types NWs and TNFs) grown on three oriented substrates have no significant differences, with respect to their size, shape, morphology, density and alignment. This observation is in agreement with the earlier reports on growth of

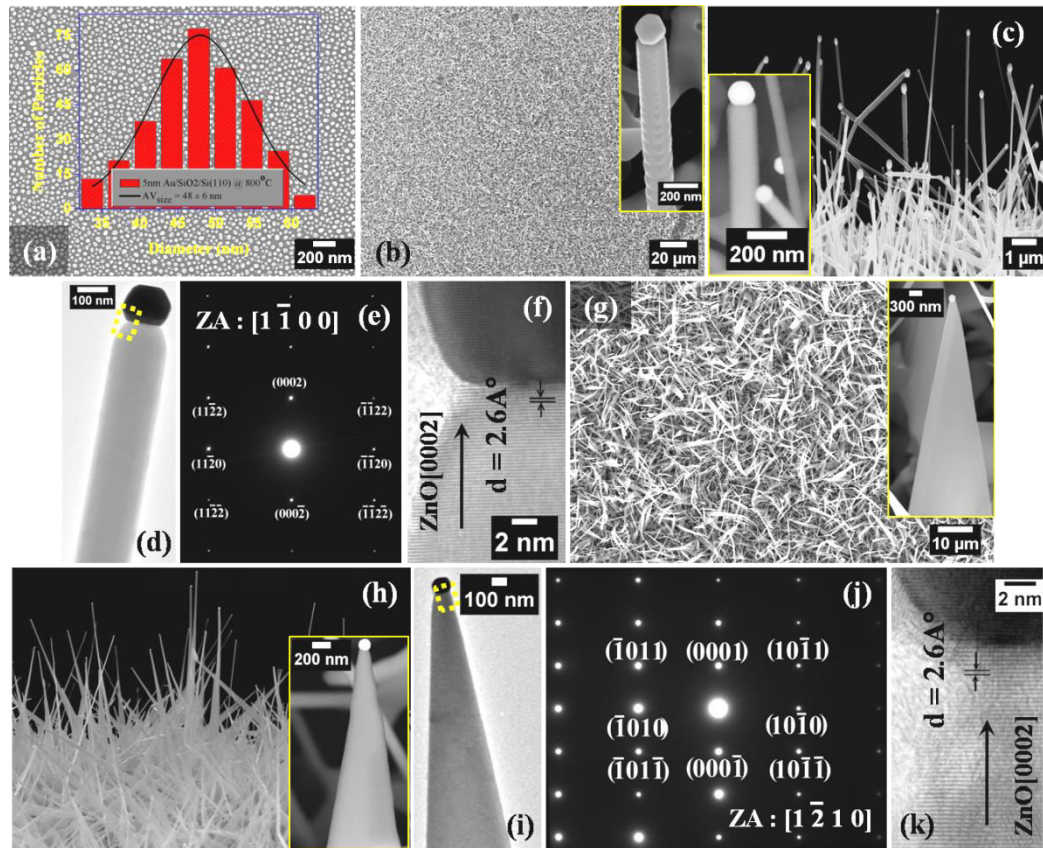


**Figure 3.7:** (a) SEM image of Au nanoparticles (NPs) formed after air annealing at 800 °C of 5 nm Au/SiO<sub>2</sub>/Si(110); inset represents corresponding size distribution histogram of Au NPs. (b and g) show low-magnification SEM micrographs of as-grown Au-ZnO nanowires (NWs) and triangular nanoflakes (TNFs) on the previous substrate, respectively; corresponding inset figures show high resolution SE images of a single NW and TNF with faceted Au NP at the tip. (c and h) present cross-sectional SEM images of the corresponding NWs and TNFs samples, respectively; corresponding insets show high resolution BSE images (Z-contrast images) of individual Au-ZnO NW and TNF. (d and i) depict low-magnification TEM micrographs of a single Au-ZnO NW and TNF with faceted Au particle at the tip of each, respectively. (e and j) are the selected area electron diffraction (SAED) pattern from individual NW and TNF, respectively. (f and k) present HRTEM images taken from the highlighted regions of Au-ZnO NW in panel (d) and Au-ZnO TNF in panel (i), respectively.

ZnO NSs on native oxide coated Si substrates [39]. Details structural information about the Au-ZnO NWs (grown on downstream substrate) and Au-ZnO TNFs (grown on upstream substrate) grown using 1 nm Au and 5 nm Au as catalyst layer, have been tabulated in Table 3.1. Now it is paramount to emphasize that using 5 nm Au as catalyst layer, as-grown HNs (NWs and TNFs) areal density and diameter have been increased by  $\approx 1.6 - 1.8$  times,

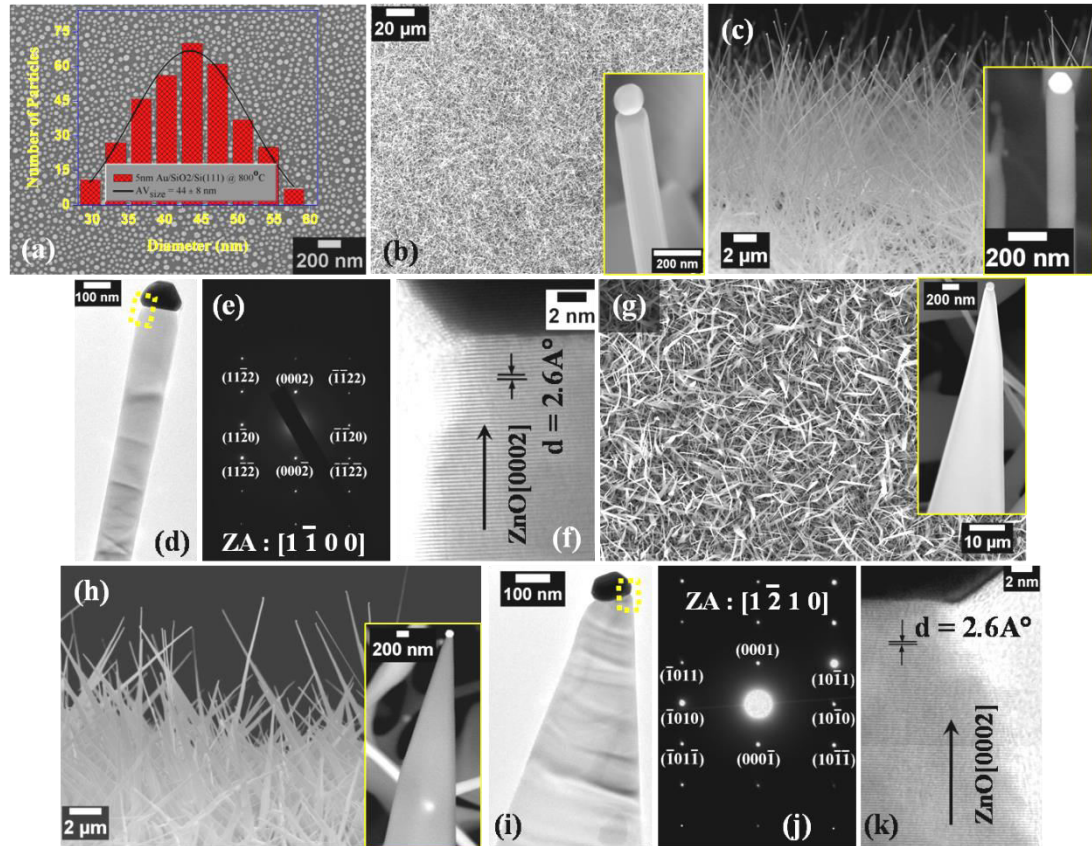


**Figure 3.8:** (a) SEM image of Au nanoparticles (NPs) formed after air annealing at 800 °C of 5 nm Au/SiO<sub>2</sub>/Si(111); inset represents corresponding size distribution histogram of Au NPs. (b and g) show low-magnification SEM micrographs of as-grown Au-ZnO nanowires (NWs) and triangular nanoflakes (TNFs) on the previous substrate, respectively; corresponding inset figures show high resolution SE images of a single NW and TNF with faceted Au NP at the tip. (c and h) present cross-sectional SEM images of the corresponding NWs and TNFs samples, respectively; corresponding insets show high resolution BSE images (Z-contrast images) of individual Au-ZnO NW and TNF. (d and i) depict low-magnification TEM micrographs of a single Au-ZnO NW and TNF with faceted Au particle at the tip of each, respectively. (e and j) are the selected area electron diffraction (SAED) pattern from individual NW and TNF, respectively. (f and k) present HRTEM images taken from the highlighted regions of Au-ZnO NW in panel (d) and Au-ZnO TNF in panel (i), respectively.

**Table 3.1:** Detail about the dimensions and areal densities of the as-grown samples.

Details	Au–ZnO NWs		Au–ZnO TNFs	
	1 nm case	5 nm case	1 nm case	5 nm case
<b>Tip diameter (nm)</b>	75±24	130±40	64±26	112±49
<b>Length (μm)</b>	13±8	6±5	17.5±13	8±6
<b>Base (nm)</b>	75±24	130±40	1200±650	1500 ±700
<b>Areal density (/cm<sup>2</sup>)</b>	$2.6 \times 10^8$	$4.27 \times 10^8$	$2.25 \times 10^8$	$4.0 \times 10^8$
<b>Cross-section</b>	Uniform hexagonal with {10 $\bar{1}$ 0} exposed six side facets		Gradually tapered rectangular with {1 $\bar{2}$ 10} and {10 $\bar{1}$ 0} exposed four side facets	

whereas length and aspect ratio have been reduced by < 50 % (i.e.,  $\approx 0.5$  times) in comparison with the same category of samples grown using 1 nm Au as catalyst layer.

We have also done XRD analysis on both kinds of HNs samples grown on all three low index Si substrates (grown using 5 nm thick Au as catalyst) to check the large scale crystalline information. We have presented two comparison spectra for two category of samples (NWs on downstream substrate, and TNFs on upstream substrate) grown on three Si(100), (110) and (111) substrates, shown in Figures 3.9(a, b). Figure 3.9(a) shows almost similar spectra recorder for Au-ZnO NWs category samples on three different Si substrates, with all visible reflections corresponding to ZnO hexagonal wurtzite structure (JCPDS No. 36 -1451). Similarly Figure 3.9(b) shows practically identical spectra for Au-ZnO TNFs category samples on three different Si substrates, with all visible reflections corresponding to ZnO hexagonal wurtzite structure (JCPDS No. 36 - 1451). From XRD data also we can conclude that HNs are single crystalline in nature and there are no significant differences between the samples grown on three different orientations native oxide coated silicon substrates, which are in agreement with electron microscopy (EM) results. The XRD peak intensity of (002) is higher than other peaks for all the samples shown in Figures 3.9(a, b), indicate that majority of the Au-ZnO NWs and TNFs are indeed oriented along c-axis direction, which support our EM findings. At the same time we have checked how XRD patterns evolve for both category of samples (Au-ZnO NWs and TNFs) using 1 nm and 5 nm Au catalyst layers on Si(110) substrates. Figures 3.9(c, d) represent XRD comparison patterns

taken from NWs and TNFs category samples grown using two different Au layers (1 nm and 5 nm) on Si(110). It is worthy to notice that XRD peak intensities are higher for both Au-ZnO NWs and TNFs samples grown using 5 nm Au compared to 1 nm Au, which suggest that higher density of HNs were grown with higher catalyst layer thickness (i.e., 5 nm). After analyzing all HRTEM, SAED and XRD, it is clear that as-grown NWs and TNFs are predominantly grown along [0002] direction.

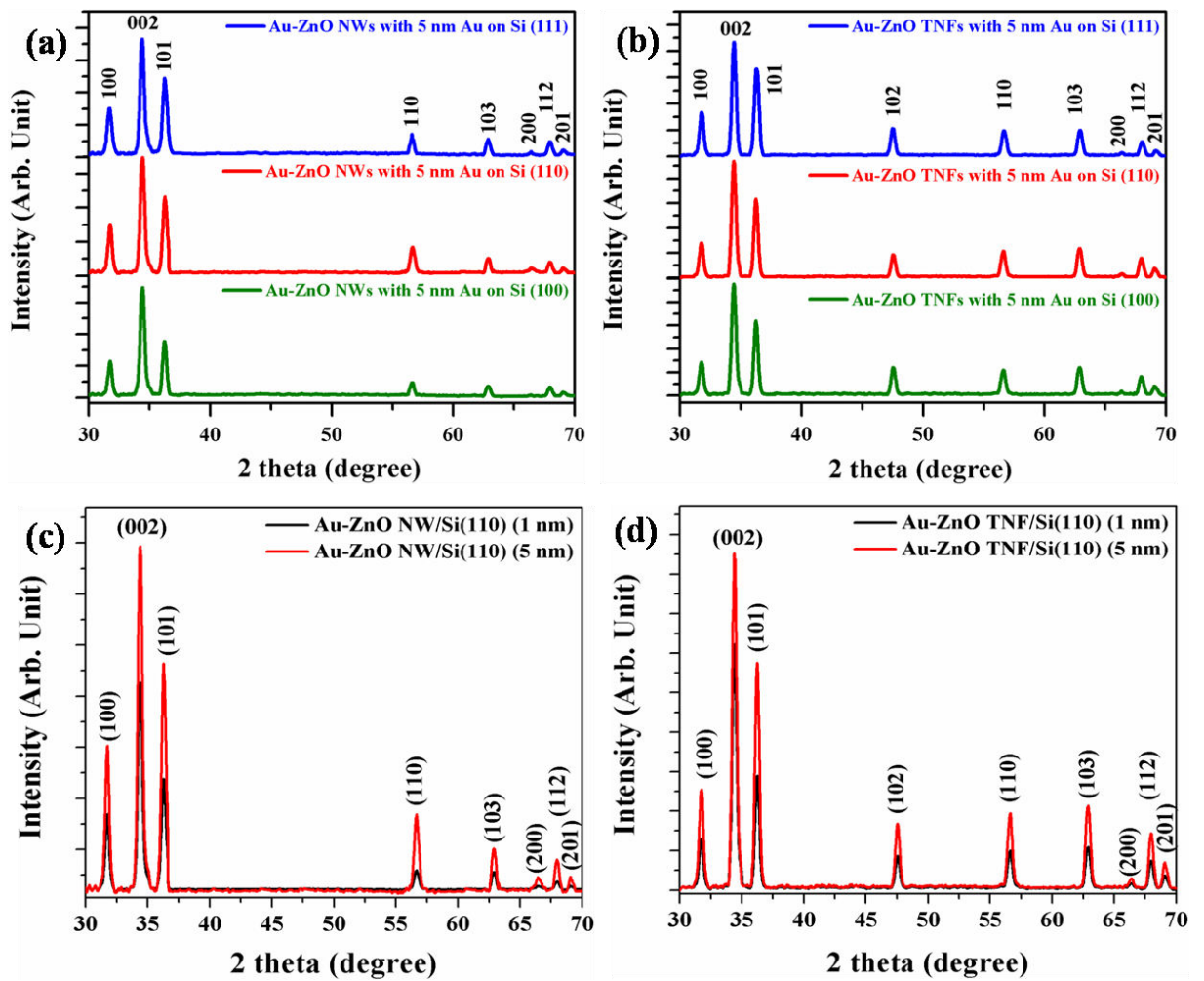


**Figure 3.9:** (a) Shows comparison of the XRD patterns obtained from the as-grown ZnO NWs samples grown on 5 nm Au coated (pre-annealed) three different oriented silicon substrates as Si(100), Si(110) and Si(111). (b) Shows comparison of the XRD patterns obtained from the as-grown ZnO TNFs samples grown on 5 nm Au coated (pre-annealed) three different oriented silicon substrates as Si(100), Si(110) and Si(111). (c) and (d) show comparison (1 nm and 5 nm Au as catalyst layers) of the X-ray diffraction (XRD) patterns obtained from the as-grown Au-ZnO NWs and TNFs samples, respectively.



Now, it is essential to elucidate the growth mechanisms involved in the simultaneous growth of two different morphology HNs (NWs and TNFs), just by placing substrate templates at two different positions in the CVD chamber, keeping all other growth parameter remain unchanged. Elemental analysis of the as-grown samples were done using energy dispersive spectrometry (EDS) equipped with FE-SEM and are shown in Figure 3.10. The EDS spectra from both the HNs indicate that faceted NPs at their tip are having Au as a major contribution with a smaller amount of Zn, whereas their body part show only O and Zn signals. The growth fronts of each of the NW and TNF terminated with faceted catalyst Au NPs, confirmed by TEM, HR-SEM and EDS, suggest that both are catalyst assisted growth [22-24, 34, 40, 41,43]. The as-grown faceted NWs are in uniform diameter. But a gradual shrinking of diameter towards the growth direction of faceted TNFs was observed. The presence of catalyst NP at the tip and the faceted side-wall of HNs suggest that the growth mechanism is a mixture of VLS and VS processes [23, 24, 41-43]. The influences of substrate position over differences in Au-ZnO HNs morphology will be discussed thoroughly in the proposed growth models in the next section of this chapter.

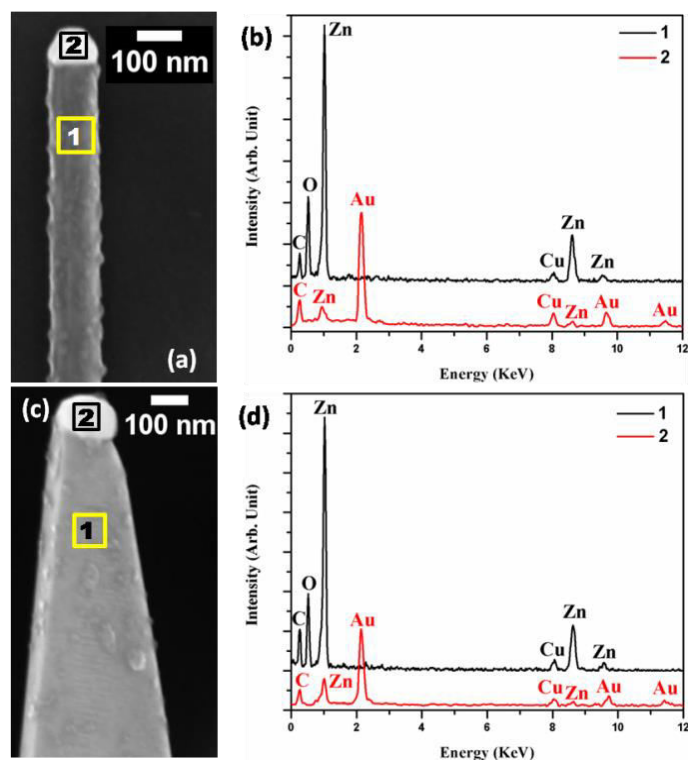
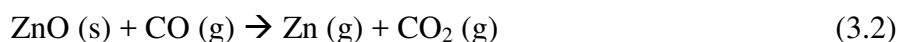
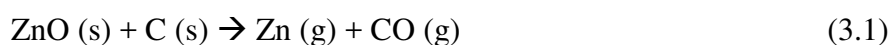


**Figure 3.10:** (a) and (c) show high-magnification SEM images of a single NW and a TNF dispersed on two different copper grids, respectively. Corresponding EDX spectra collected from two indicated regions (1, 2) of NW and TNF in panels (a) and (c) are shown in Figures (b) and (d), revealing the local compositional details at tip particle and body, respectively.

### 3.3.3 Proposed growth models

In all the previous cases (growth on three orientation Si with two different catalyst layer thicknesses), we have found the presence of faceted Au NP at the apex/tip of every Au-ZnO HNs, confirming the VLS growth mode and is also supported by other experimental observations which is quite consistent with previous reports [22-24, 26, 40, 41]. There are at least four different stages involved in the formation of Au-ZnO HNs via VLS growth mode on Au NPs decorate SiO<sub>2</sub>/Si substrates at  $\approx 900^\circ\text{C}$  with the 30 sccm Ar flow as carrier gas:

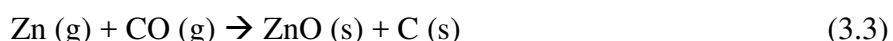
(i) production of Zn vapor via carbothermal reduction reactions given below



(ii) transportation of Zn vapor and preferential reaction with the molten Au nanoparticles deposited on silicon substrates to form Au-Zn alloy droplet,

(iii) when the Au-Zn alloy reaches beyond solubility limits of Zn, then Zn metal start precipitating (i.e., after supersaturation is reached) at the interface of Au-Zn alloy droplet and SiO<sub>2</sub>/Si substrate. Further oxidation by the residual oxygen present in the growth chamber led to the formation of ZnO ledges at the interface of alloy droplet and substrate.

(iv) further diffusion of Zn and oxygen (i.e., oxidation) to inner regions of the hetero-interface (catalyst droplet – ZnO) promoting the growth of crystalline Au capped ZnO HNs through the carbo-thermal reaction



without any external supply of oxygen [26, 34, 44]. Oxygen is also sometimes intentionally introduced with Ar in the chamber, but for our growth no external O supply was there. This ultimately leads to growth of Au-ZnO HNs (with a faceted Au NP cap at the tip) on the substrate whose diameter, length and growth position can be controlled by choosing catalyst layer thickness and deposition area on the substrate. However, owing to faceted sidewalls with uniform hexagonal cross-section of Au-ZnO NWs and triangular morphology of the Au-ZnO TNFs with rectangular cross-section, it is not conventional VLS process which alone is responsible for these growths. Rather this growth is a combination of two processes: (1) catalyst assisted VLS growth responsible for faster axial growth and (2) catalyst free VS growth which govern the radial growth of side-walls [23, 24, 41-43]. It is obvious that catalyst-driven axial growth rate beneath the catalyst droplet and interface of Au-ZnO will be

much faster compared to catalyst free side-wall growth of non-polar faces, due to polar nature of ZnO as well as a strong binding affinity of Au atoms to its polar faces [24, 41, 42, 45]. The growth mechanism of Au-ZnO NWs in this case is somewhat similar to the reported by Weigand et al. where nucleation is initiated by catalyst droplet through VLS mechanism along with simultaneous side wall deposition via VS mechanism [24]. Details about these VLS and VS growth modes have been described in the experimental technique chapter (Chapter 2). Even though growth rate is higher at the interface of catalyst-NW but still specific growth environments can facilitate significant side-wall growth via VS mechanism with growth rate governed by availability of growth species and surface-free-energy of the exposed surfaces [24, 46]. Radial growth rate will be isotropic for NWs as the side-walls are enclosed by six identical  $\{10\bar{1}0\}$  facets with equal surface free energies and i.e., VS growth rates, lead to the formation of uniform diameter of hexagonal cross-section NWs. Proposed growth model for Au-ZnO NWs growth at the downstream substrate has been illustrated schematically in Figures 3.11(a-d). On the other hand, substrate kept at the upstream location (Au-ZnO TNFs), majority of the NSs consists of nanoflakes with triangular like morphology (TNFs) with faceted Au NPs at the tip headed upward. In the past, several ways have been adopted to explain the origin of tapered morphology of the NSs, which includes catalyst droplet instability (due to the high growth temperature and high gas flow rate and pressure)

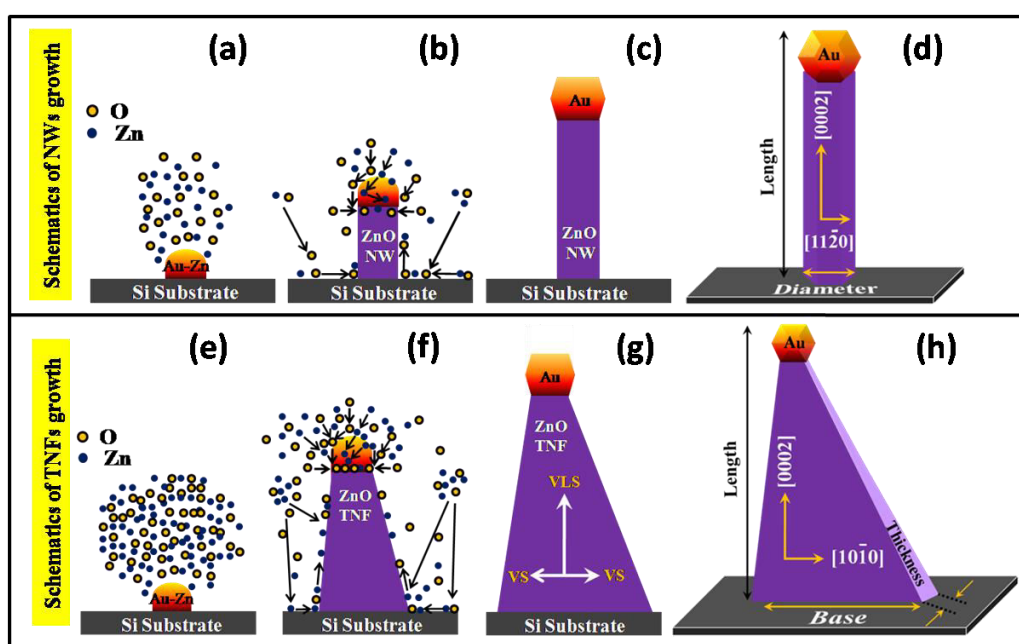


**Figure 3.11:** Schematic illustrations showing the possible growth model for Au capped ZnO nanowire (NW) (a) - (c) and a triangular nanoflakes (TNF) (e) - (g). (d) and (h) represent the 3-dimensional geometrical configuration of a fully grown NW and TNF, respectively.

and/or oversupply of growth species to the catalyst droplets serve as active consumption sites [43, 47, 48]. In our experiment, at the same time we have grown Au-ZnO HNs (NWs and TNFs) of two different morphologies on the two similar substrates kept at two different positions. The substrates position appears to be the major reason for these growths of two kinds of HNs. As upstream substrate (TNFs growth) was placed near to the open end ("gas inlet end" side) of the assembly (Figure 3.1(a)), more supply of growth species (carbothermal reaction produced Zn and O atom) must be there compared to downstream substrate (NWs growth) throughout the growth process. Now we will try to clarify previous statement about the differences in growth species availability depending on the substrates position inside the growth chamber. It is also important to mention that in this growth Ar flow rate was very small (30 sccm) which is basically supplied not only as a carrier gas but also to keep the growth environment as inert as possible (minimizing the presence of any residual gases like  $O_2$ ,  $N_2$ ) during the growth. As growth species production will be enormous and it is impossible that whole amount will be utilized to grow HNs (NWs and TNFs) in the respective samples. So it is obvious a significant amount of growth species produced has to come out side of CVD chamber, in that case it has to follow the path through open end ("gas inlet end" side) of the source-substrate assembly (i.e., through upstream position) and finally will be drain out through the gas outlet (see Figure 3.1(a)). Therefore supply of growth species will be always high on the substrate kept near to the open end (i.e., upstream substrate) of the assembly compare to the substrate kept at the closed end ("gas outlet end" side) of the assembly. As the growth species availability will be more on the up-stream substrate which allow significant catalyst free lateral growth along with dominating catalyst assisted axial growth. What we are claiming is that more supply of growth species will be required to grow Au-ZnO TNF. To support this point, we have carried out the similar growth with a quartz boat of two sides closed geometry (with same dimensions as one side opened) shown in Figure 3.1(b). As both sides of quartz boat are closed, it is obvious that availability of growth species will be more on both the downstream and upstream substrates. Interestingly we have observed that both side samples in this case contain Au-ZnO TNFs. So we can conclude that supply of more growth species is the key of getting triangular nanoflake (TNF) structures. With this it is now clear that more or over supply of growth species was there on the upstream substrate, which lead to the formation of triangular morphology nanoflakes. To visualize this explanation we have provided two schematics of our growth setup: one with one side closed quartz boat (Figure 3.1(a)) and another with both (i.e., two) sides closed (Figure 3.1(b)). Figure 3.1(a) is the main growth setup assembly, which we have used in this

whole thesis work for the growth of Au-ZnO NWs and TNFs simultaneously on two substrates kept at two different positions. The average surface area (ASA) of TNFs is  $\approx 8$  times higher than NWs ( $TNF_{ASA}/NW_{ASA} \approx 8$ ). As the TNFs become narrow along the growth direction from a wider base, most probably the VLS model controls the axial growth, while the VS growth process controls the radial growth. Here also nucleation started at the catalyst-TNF interface, similar to that of NWs case with predominant catalyst assisted axial growth rate. However, in this case particularly due to the oversupply of growth species, VS growth rate is higher and highly anisotropic compared to NWs growth case leading to the growth of triangular morphology NSs. Wider base with sharp tip end morphology may be arise due to the fact that VS growth rate is increasing away from the catalyst Au NP present at the tip of the HNs which promotes faster VLS growth rate. Even though ZnO  $\{10\bar{1}0\}$  facets are the most stable surfaces from surface energy point of view [16, 49], still we are getting significant catalyst free radial growth via VS process along these facets for TNFs sample (upstream sample). This experimental observation can be attributed to preferred VS growth along higher Miller indices and lower specific surface energy planes  $\{10\bar{1}0\}$  promoted by our specific growth environments. It has been previously observed that Au-ZnO HNs growth direction and radial growth rate via VS mechanism can be greatly influenced by growth conditions and atmosphere (like temperature,  $O_2$  partial pressure, gas flow rate, substrate, choice of catalyst etc.) [15, 16, 24]. Based on these experimental evidences, growth of TNFs at the upstream substrate has been illustrated schematically in Figure 3.11(e-h). However, detailed understanding behind this growth of ZnO TNFs is not very clear to us at this stage. Since the nucleation of the HNs (NWs and TNFs) were initiated by the catalyst Au NPs on respective Si substrates and diameter of the NSs are comparable to the size of Au NP, there is a choice of controlling their dimension as well as growth positions using our growth technique. The reproducible control over the size, shape and morphology would be very challenging for their potential applications. In the next section we will highlight the role of native oxide on Si substrate, towards the Au catalyzed VLS growth of Au-ZnO NWs.

### 3.3.4 Role of native oxide at the interface of catalyst Au layer and Si substrate

In this section focus will be made to realize the importance of native oxide on Si substrates, for the Au catalyst VLS growth of Au-ZnO HNs, which was not addressed before

by any other groups. So, in this case first we have cleaned native oxide ( $\text{SiO}_2$ ) coated Si(100) substrate by using ultra-high-vacuum (UHV) molecular beam epitaxy (MBE) chamber, to get atomically clean Si(100) substrate. To remove native oxide from Si substrate, we need to provide energy to break bonding between Si and  $\text{SiO}_2$ , and this has to be done in UHV such that further oxidation of Si will not be there (or will be very less). Cleaning of Si substrate by flashing in UHV-MBE chamber is already being reported in detail by our group seniors in their thesis work [38, 50]. After removing native oxide we have deposited 10 ML of Au ( $\approx 2$  nm) on atomically cleaned Si(100) inside MBE chamber. Then we have taken out this as-deposited 10 ML Au/Si(100) substrate to the ambience from UHV chamber and then annealed in air @ 800 °C, as we have done for with oxide cases. Schematic representation of the as-deposited MBE sample is shown in Figure 3.12(a). Low-magnification SEM image of the 10 ML Au/Si(100) substrate after 800 °C air annealing does not show formation of any faceted Au NPs as we have seen in case of native oxide Si substrates, rather some buried structures are seen (Figure 3.12(b)). Figure 3.12(c) shows low-magnification TEM image of the nano-square/rectangle NSs formed following the symmetry of the atomically cleaned Si(100) substrate (Si(100) has four fold symmetry). To get the crystalline information SAED was taken on these four-fold symmetric nano-square/rectangle NSs, shown in Figure 3.12(d). It would be great if we could take diffraction pattern from single such NSs, but minimum size of the SAD aperture available with our system is bigger than a single NS/island. From the SAED pattern shown in Figure 3.12(d), with visible spot corresponding to Au and Si phase there are some reflections identified as 1, 2, 3 and 4 on the pattern are also available. These extra spots which are not matching with either pure Au or pure Si phases, identified as 1, 2, 3 and 4 correspond to “d” spacings of 0.188 nm, 0.469 nm, 0.448 nm and 0.401 nm. When compared with the reported phases of gold silicides these lattice spacings matched with several phases such as  $\text{Au}_2\text{Si}$ ,  $\text{Au}_5\text{Si}_2$  and  $\text{Au}_3\text{Si}$  [38, 51]. So we can conclude here that after air annealing of 10 ML Au/Si(100) 800 °C various phases of gold silicides substrate symmetric structures has formed. These nano squares/rectangles are not pure Au. Now we have used these silicide squares/rectangles decorate Si(100) to grow ZnO HN/NSs following exactly similar earlier CVD growth conditions. Figure 3.12(e) presents low- magnification SEM image of the ZnO NSs sample grown on the silicide decorate Si(100), showing very low density ZnO NSs on the substrate. High-magnification SEM image of a single ZnO nanowire (inset of Figure 3.12(e)) reveals that there is no catalyst either at the tip or at the bottom, which confirms unambiguously that they were not grown via VLS growth mode [52]. These

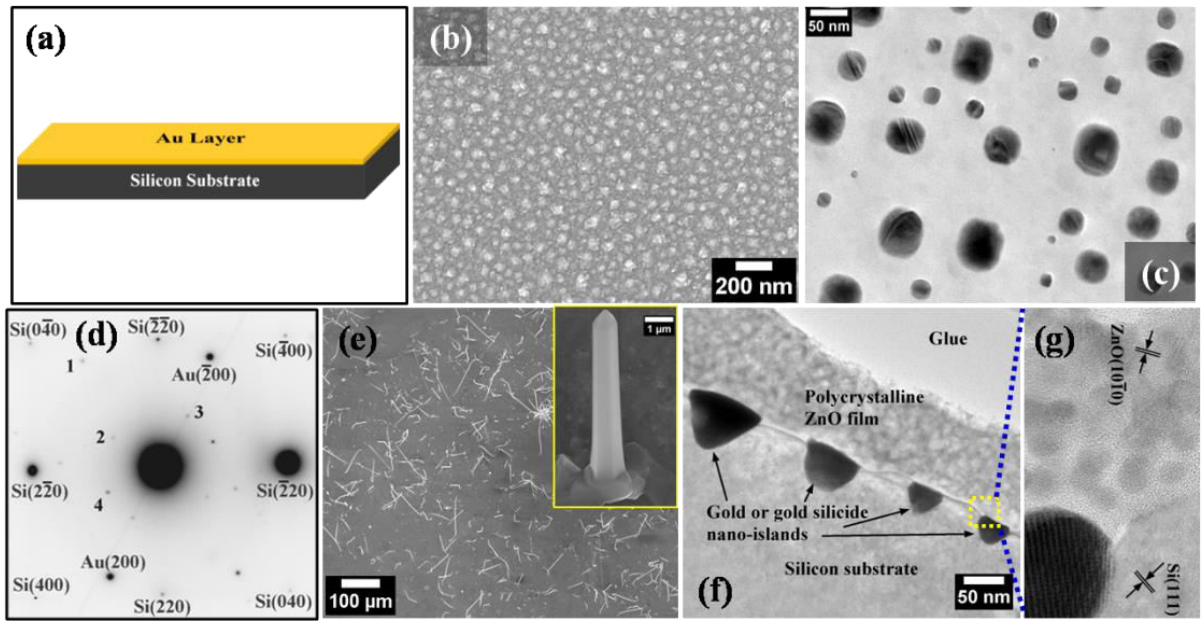


**Figure 3.12:** (a) Schematic representation of Au thin film deposited on atomically cleaned silicon substrate by flashing in MBE. (b) Low magnification SEM image of 10 ML Au/Si(100) (MBE-grown) after air annealing at 800 °C for 30 min. (c) Low magnification TEM image of the corresponding sample. (d) Selected area electron diffraction (SAED) pattern from panel (c). (e) Low magnification SEM of as-grown ZnO nanowire on the 10 ML Au/Si(100) pre-annealed @ 800 °C; Inset shows magnified view of a single ZnO nanowire. (f) Low magnification XTEM micrograph of the previous sample. (g) Shows HRTEM image taken from the highlighted region of (f).

nicely faceted ZnO NWs must have grown via vapor solid mechanism (VS). This is another important growth mode besides VLS growth mode used in this whole thesis work, which is presented elaborately in Chapter 2. To enucleate this growth behavior in more details we have prepared X-TEM (cross-sectional TEM) sample from this as-grown sample. Figure 3.12(f) shows low-magnification X-TEM image of the corresponding sample. Low-magnification XTEM image reveals that gold silicide NSs are buried inside Si substrate and covered by ZnO polycrystalline film, which further confirmed by HRTEM image shown in Figure 3.12(g). Unfortunately we have not found any ZnO NSs in the relatively small transparency region of this XTEM sample (because in TEM we see a very small transparent region of  $\approx 20 \mu\text{m}$ ). From the above electron microscopy observations of this section we now can reach to a conclusion that without native oxide at the interface of metal catalyst layer and Si substrate, VLS growth of Au-ZnO HN is just not possible. That is mainly because as there is no barrier between Au and Si, they form their alloy NSs/islands (silicide) at temperature

greater than their eutectic temperature  $\geq 363$  °C. Then these Au silicide NSs/Si(100) are not able to intake other foreign growth species (here for our case Zn and O vapor) to promote VLS growth, as they are already saturated with Si atoms and also trapped inside Si matrix. So, for Au catalyzed growth Au-ZnO HNns via VLS protocol on Si substrates, it is mandatory to have native oxide coated Si substrates.

As we have not found any aligned and substrate dependent Au-ZnO HNns on high lattice mismatch without or with native oxide coated Si substrate of three orientations (with two different thicknesses of catalyst Au layers  $\approx 1$  nm and  $\approx 5$  nm), in the next section we will focus on growth of vertically aligned/oriented Au-ZnO NWs on completely lattice matched single crystalline oxygen terminated ZnO(0001) substrate.

### 3.3.5 Growth of vertically oriented Au-ZnO nanowires

In this section we will discuss the growth of aligned/oriented Au-ZnO nanowires (NWs) on oxygen terminated ZnO(0001) substrate (with 0 % lattice mismatch). For this case we have first deposited  $\approx 2$  nm Au thin film on O(t)-ZnO(0001) substrate and then subsequently annealed in atmospheric condition at 800 °C. Figure 3.13(a) shows low-magnification SEM micrograph of the 2 nm Au/O(t)-ZnO(0001) annealed @ 800 °C sample, and inset of this figure depicts size distribution histogram of the Au NPs formed on O(t)-ZnO(0001) substrate by air annealing. Then we have used this Au NPs decorated ZnO substrate to grow Au-ZnO nanowires (NWs) via similar chemical vapor transport conditions and growth arrangements except the growth duration (30 min instead of 90 min). In this case we focus on the Au-ZnO NWs growth; therefore we have put the template only at the downstream position inside the growth chamber. Figure 3.13(b) represents low-magnification SEM image (planar view) of the as-grown Au-ZnO NWs. In this figure we only can see the tips of the products; therefore Au-ZnO NWs are grown perfectly vertically on the c-axis oriented ZnO(0001) substrate. Low-magnification cross-sectional SEM and corresponding high-magnification BSE images of the as-grown Au-ZnO NWs/ZnO(0001) are shown in Figure 3.13(c) and its inset respectively. Z-contrast BSE image in the inset of Figure 3.13(c) clearly tells that NWs are uniform in diameter and each of them holding brighter contrast faceted Au NPs at the tip, which is further confirmed by high-magnification SEM and low-



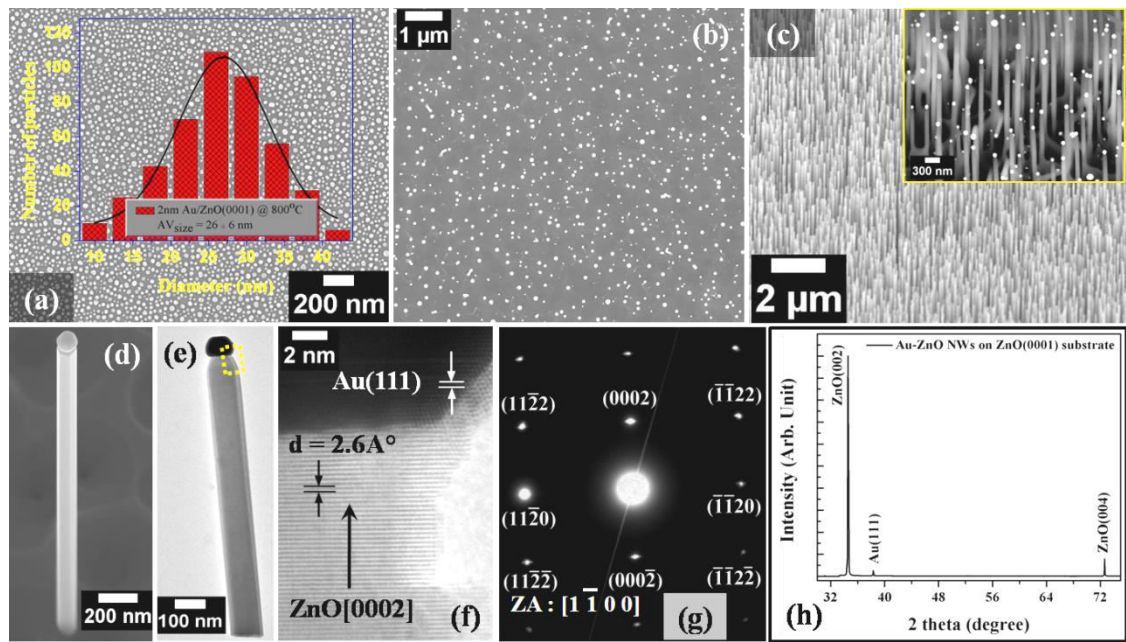


**Figure 3.13:** (a) SEM image of Au nanoparticles (NPs) formed after air annealing at 800 °C of 2 nm Au/O(t)-ZnO(0001); inset represents size distribution histogram of Au NPs of the corresponding image. (b) Low magnification SEM micrograph (plan view) of as-grown vertically oriented Au-ZnO nanowires (NWs) on 2 nm Au/O(t)-ZnO(0001) pre-annealed (at 800 °C) substrate. (c) Cross-sectional SEM image of the sample; inset shows high magnification BSE image (Z-contrast image); brighter contrasts correspond Au NPs. (d) High resolution SEM image of a single Au-ZnO NW with faceted Au NP at the tip. (e) Low-magnification TEM micrograph of a single Au-ZnO NW with faceted Au particle at the tip. (f) Selected area electron diffraction (SAED) pattern from single NW. (g) HRTEM image from the highlighted region in panel (d). (h) X-ray diffraction (XRD) pattern obtained from the corresponding sample, shows epitaxial growth of Au-ZnO NWs (vertically aligned with respect to substrate).

magnification TEM images as shown in Figures 3.13(d and e) respectively. Figure 3.13(f) shows HRTEM micrograph taken from the highlighted region of panel (e), reveals that NWs are grown along c-axis of hexagonal wurtzite structure (inter planar spacing  $d_{0002} = 2.6 \pm 0.05$  Å) with (111) oriented faceted Au NP at the growth front. From the above electron microscopy study it is clear that in this case also Au-ZnO NWs were grown via combined VLS and VS growth modes; where VLS mode is responsible for dominant axial growth of NWs and faceting of exposed side walls governed by catalyst free VS mechanism [23, 24, 44-46]. SAED pattern taken along  $[1\bar{1}00]$  zone axis confirming the growth of single crystalline ZnO NW along  $[0002]$  direction (i.e., along c-axis) is shown in Figure 3.13(g).

Complete dimensional details about the Au NPs formed on ZnO(0001) via air annealing and as-grown Au-ZnO NWs are listed in Table 3.2. To know the long range crystalline information about the as-grown Au-ZnO NWs/ZnO(0001) sample, we have done XRD measurement. Figure 3.13(h) represents XRD pattern from the as-grown sample, where two strong reflections (002), (004) corresponding to c-axis oriented ZnO NWs and one very small intensity (111) corresponding to tip grafted Au NPs were obtained. So, XRD result corroborates that almost all the ZnO NWs are oriented along [0002] i.e., along c-axis of the hexagonal wurtzite structure with [111] oriented Au NPs at the tip, which strongly compliments HRTEM result (Figure 3.13(f)).

**Table 3.2:** Structural characterization of Au NPs/O(t)-ZnO(0001) and as-grown Au-ZnO NWs

Sample Name	Nanowires parameters			Au NPs Coverage (%)	Au NP size (nm)
	Diameter (nm)	Length ( $\mu\text{m}$ )	Areal Density (NWs/cm <sup>2</sup> )		
2 nm Au on ZnO(0001)	85 $\pm$ 19	2 $\pm$ 1	$1.05 \times 10^9$	$\approx 34$	27 $\pm$ 6

From this section we can conclude that for the growth of vertically oriented Au-ZnO NSs, one of the most important criterion is the selection of substrate material and its orientation. Here we have been able to get perfectly vertically oriented Au-ZnO NWs, because we have chosen lattice matched ZnO(0001) substrate for this growth.

### 3.4 Summary

In this chapter, we have explicitly discussed the growth of faceted Au NPs conjugated ZnO HNs of various shapes, size and morphology via *single step* Au catalyzed chemical vapor transport processes (particularly VLS and VS modes) on native oxide Si substrates. We have shown the substrates position dependency on the morphology and dimensionality of the as-grown Au-ZnO HNs. We have proposed growth mechanisms involved in the formation of two different morphology HNs (NWs and TNFs) simultaneously depending on the substrates position (i.e, availability of the growth species), keeping all other growth parameter remain same. Here, we have demonstrated the role of catalyst layer thickness on the areal density and

aspect ratio of the HNs. To the best of our knowledge, for the first time, we are highlighting the role of native oxide at the interface of catalyst and Si substrate, on the Au catalyzed VLS growth of Au-ZnO HNs using detailed electron microscopy analysis. Interestingly, without native oxide (i.e., Au on atomically cleaned Si) cases only low density ZnO NSs/Si were found because VLS growth was barred by formation of buried gold silicide NSs in Si, unlikely for the native oxide (Au/SiO<sub>2</sub>/Si) cases, where high density Au-ZnO HNs/Si were observed. This observation corroborates that gold silicide is not good catalyst for VLS growth of Au-ZnO HNs. So, we can control the growth modes, as well as, type of structures (NSs or HNs), by controlling the interfacial oxide between the catalyst layer and Si substrate. At the end of this chapter we have showed the growth of aligned Au-ZnO NWs on lattice matched oxygen terminated ZnO(0001) substrate. To, grow aligned and epitaxial HNs of any material; substrate with minimum lattice mismatch (which depends on substrate material and its orientation) is one of the most important requirements. Application of plasmonic Au NP conjugated ZnO HNs/Si samples (as-grown samples), towards trace amount detection of crystal violet (CV) molecules via Surface Enhanced Raman Spectroscopy (SERS) will be discussed in the next chapter.

### 3.5 References

- [1] T. Zhai, X. Fang, M. Liao, H. Zeng, B. Yoshio and D. Golberg, *Sensors* **9**, 6504 (2009).
- [2] S. J. Pearton et al., *IEEE J. Sel. Topics Quantum Electron.* **17**, 1092 (2011).
- [3] S. M. Gupta and M. Tripathi, *Chinese Sci. Bull.* **56**, 1639 (2011).
- [4] Y. Son et al., *Nano Lett.* **14**, 1005 (2014).
- [5] Ü. Özgür et al., *J. Appl. Phys.* **98**, 041301 (2005).
- [6] S. A. Ansari, M. M. Khan, S. Kalathil, J. Lee and M. H. Cho, *Nanoscale* **5**, 9238 (2013).
- [7] J. Wang et al., *ACS Appl. Mater. Interfaces* **4**, 4024 (2012).
- [8] N. Daneshvar, D. Salari and A. R. Khataee, *J. Photochem. Photobiol. A* **162**, 317 (2004).
- [9] S. Sakthivel et al., *Sol. Energy Mater. Sol. Cells* **77**, 65 (2003).
- [10] J. L. Yang, S. J. An, W. I. Park, G. C. Yi and W. Choi, *Adv. Mater.* **16**, 1661 (2004).

- [11] W. He et al., *J. Am. Chem. Soc.* **136**, 750 (2014).
- [12] W. He et al., *ACS Appl. Mater. Interfaces* **6**, 15527 (2014).
- [13] B. Chen, H. T. Ng and C. L. Chen, *J. Exp. Nanosci.* **2**, 50 (2007).
- [14] Z. L. Wang, *Mater. Today* **7**, 26 (2004).
- [15] P. X. Gao and Z. L. Wang, *J. Appl. Phys.* **97**, 044304 (2005).
- [16] Z. L. Wang, *J. Phys.: Condens. Matter* **16**, R829 (2004).
- [17] Z. Zheng et al., *J. Mater. Chem.* **21**, 9079 (2011).
- [18] M. R. Hoffmann, S. Martin, W. Choi and D. W. Bahnemann, *Chem. Rev.* **95**, 69 (1995).
- [19] M. N. Chong, B. Jin, C. W. K. Chow and C. Saint, *Water Res.* **44**, 2997 (2010).
- [20] J. G. Yu, Y. R. Su and B. Cheng, *Adv. Funct. Mater.* **17**, 1984 (2007).
- [21] M. Pal, U. Pal, R. S. Gonzalez and P. Santiago, *J. Nano Res.* **5**, 193 (2009).
- [22] P. Yang et al., *Adv. Funct. Mater.* **12**, 323 (2002).
- [23] V. Sallet, C. Sartl, C. Vilar and P. Galtier, *Appl. Phys. Lett.* **102**, 182103 (2013).
- [24] C. C. Weigand et al., *Cryst. Growth Des.* **11**, 5298 (2011).
- [25] J. Grabowska et al., *Surf. Coat. Tech.* **200**, 1093 (2005).
- [26] M. H. Huang, Y. Wu, H. Feick, N. Tran and P. Yang, *Adv. Mater.* **13**, 113 (2001).
- [27] R. S. Wagner and W. C. Ellis, *Appl. Phys. Lett.* **4**, 89 (1964).
- [28] H.-M. Cheng et al., *Nanotechnology* **16**, 2882 (2005).
- [29] Y. Li et al., *J. Appl. Phys.* **99**, 054307 (2006).
- [30] R. T. R. Kumar et al., *Nanotechnology* **18**, 215704 (2007).
- [31] F. Fang et al., *Nanotechnology* **18**, 235604 (2007).
- [32] S. Zhang, Y. Shen, H. Fang, J. Song and Z. L. Wang, *J. Mater. Chem.* **20**, 10606 (2010).
- [33] W. J. Shen, J. Wang, Y. Duan and Y. P. Zeng, *J. Phys. D: Appl. Phys.* **39**, 269 (2006).

- [34] A. Ghosh, R. R. Juluri, P. Guha, R. Sathyavathi, A. Dash, B. K. Jena and P. V. Satyam, *J. Phys. D: Appl. Phys.* **48**, 055303 (2015).
- [35] M. Kirkham, X. D. Wang and R. L. Snyder, *Nanotechnology* **18**, 365304 (2007).
- [36] H. S. Liu, K. Ishida, Z. P. Jin and Y. Du, *Intermetallics* **11**, 987 (2003).
- [37] C. Li, G. J. Fang, Q. Fu, F. H. Su and X. Z. Zhao, *J. Cryst. Growth* **292**, 19 (2006).
- [38] A. Rath et al., *J. Phys. D: Appl. Phys.* **44**, 115301 (2011).
- [39] Z. Zhu, T. L. Chen, Y. Gu and R. M. Osgood, *Chem. Mater.* **17**, 4227 (2005).
- [40] Y. Wu and P. Yang, *J. Am. Chem. Soc.* **123**, 3165 (2001).
- [41] X. L. Chen, Y. C. Lan, J. Y. Li and M. He, *J. Cryst. Growth* **222**, 586 (2001).
- [42] T. Gao and T. Wang, *J. Phys. Chem. B* **108**, 20045 (2004).
- [43] A. Ghosh, P. Guha, A. K. Samantara, B. K. Jena, R. Bar, S. Ray and P. V. Satyam, *ACS Appl. Mater. Interfaces* **7**, 9486 (2015).
- [44] C. Y. Lee, T. Y. Tseng, S. Y. Li and P. Lin Tamkang, *J. Sci. Eng.* **6**, 127 (2003).
- [45] D. S. Kim, R. Scholz, U. Gosele and M. Zacharias, *Small* **4**, 1615 (2008).
- [46] R. A. Laudise and A. A. Ballman, *J. Phys. Chem.* **64**, 688 (1960).
- [47] A. Kar et al., *Nanoscale Res. Lett.* **6**, 1 (2011).
- [48] S. N. Mohammad, *Nano Lett.* **8**, 1532 (2008).
- [49] C. Woll, *Prog. Surf. Sci.* **82**, 55 (2007).
- [50] D. K. Goswami, K. Bhattacharjee and B. N. Dev, *Surf. Sci.* **564**, 149 (2004).
- [51] A. K. Green and E. Bauer, *J. Appl. Phys.* **47**, 1284 (1976).
- [52] A. Ghosh, P. Guha, A. Bhukta and P. V. Satyam (To be submitted, 2016).

# Chapter 4

## SERS Applications of Au-ZnO Hetero-nano structures/Si

### 4.1 Introduction

In the previous chapter we have discussed the growth of plasmonic Au NP capped ZnO hetero-nanostructures (HNs) of two types (nanowires and triangular nanoflakes) on three different oriented native oxide coated Si substrates using a single step CVD technique. Then we have explored various issues with VLS growth of those HNs, depending on the catalyst layer thickness, substrate type and its position inside the growth chamber. In this chapter, we will discuss the Surface Enhanced Raman Spectroscopy/Scattering (SERS) applications of single step CVD grown faceted Au-ZnO HNs on Si substrates of varying morphology, dimension and areal density, towards the detection of crystal violet (CV) molecule. Here, we have characterized these HNs coated Si substrates through reflectance and photoluminescence measurements, and then correlated their antireflection properties with SERS enhancement factor. These as-grown Au-ZnO HNs coated Si substrates have been used as free standing SERS substrates, to detect sub-micro molar CV molecules with their high analytical enhancement factor (AEF) and repeatability.

SERS is an accurate and unique analytical technique towards detection of molecules adsorbed on rough or nanostructured plasmonic (i.e., noble metals) substrates [1-3]. This technique was discovered in the late 1970s that has been exploited to detect low concentration analyte molecules. The detection of molecules at low concentration in solution with high sensitivity and specificity has been of great interest in fields such as biomedical research and diagnosis [4]. In the field of SERS the major challenge is to find an effective substrate which not only gives the high enhancement factor but also highly stable, robust/reusable, reproducible and easy to prepare and handle [5]. The success and the usefulness of the SERS technique depends on several important factors, including structure and surface properties of the substrate, interaction between target analyte molecules and

substrate, orientation of analyte molecules, and wavelength of light that should ideally match the surface plasmon resonance (SPR) absorption of the metal substrate [1, 6, 7]. The SERS active substrate can allow the Raman cross-section of the adsorbate molecule be enhanced by several orders of magnitude through efficient coupling of the plasmon-induced near field with the vibrational modes of molecules [8-10]. Since substrates play a key role in SERS experiments, various pathways have been adopted to grow SERS active substrates, but with limited successes [5, 11-15]. SERS substrates are generally made of pure metallic nanostructures (in particular Au, Ag and Cu as their SPR falls in the visible regime) of various size, shape and architectures [11-16]. Recently, template-based methods for SERS substrate preparation become popular because of high SERS sensitivity and robustness. In particular, one-dimensional (1D) semiconductor nanostructures (NSs) of various morphologies have been used as templates and then coupled with free-electron possessing metal nanoparticles (especially Au and Ag) for preparing SERS substrate [5, 16-21]. However, for all of the above cases coupling is achieved by following two or multi-step processes, where NSs are grown in first step and then attachment with plasmonic NPs separately in number steps. In contrast, a limited number of reports are there where plasmonic properties of the intrinsically self-assembled metal-semiconductor NSs towards SERS applications have been addressed [22]. Among all semiconductor materials, ZnO is a practically nontoxic and biosafe material, and thus of special interest for applications in the field of SERS [5, 16, 21, 23]. Au-ZnO 1D HNs have attracted intense attention for their use as SERS active substrates for trace level molecule detection [5, 6, 16, 21, 23]. Au is chosen because of its low fluorescence and excellent oxidation resistant characteristics and ZnO as a high refractive index material promotes strong light confinement, leading to a strong SERS signal. Therefore, it is important to develop a simple single step growth technique to prepare Au-ZnO hetero-nanostructures (HNs) on solid substrate for their use in SERS applications readily. We have developed a single step CVD technique to grow Au-ZnO HNs on various oriented Si substrates and then used these as-grown samples for the detection of trace amount crystal violet (CV) molecules [6, 24] using SERS technique.

## 4.2 Experimental

Growth of 4 types of Au-ZnO hetero-nanostructures (Au-ZnO NWs array with  $\approx 1$  nm and  $\approx 5$  nm Au layer thicknesses and also Au-ZnO TNFs array with the same Au layer

thicknesses) has already been discussed with growth model in the previous chapter (Chapter 3). Surface morphology, shape and size characterization of those as-grown samples were examined using back-scattered electron (BSE) detector attached to the field emission gun based scanning electron microscopy (FEG-SEM) Neon 40 cross-beam system (M/S Carl Zeiss GmbH). Optical properties of the Au-ZnO HNs were characterized by PL setup using a He-Cd laser (325 nm pump line) and UV-VIS-NIR spectrometer at room temperature (3101PC, Shimadzu, Japan).

The SERS measurements were carried out using micro-Raman spectrometer having  $2\text{ cm}^{-1}$  spectral resolution using a 514 nm (green laser) and 633 nm (red laser) excitations, focused through a 50x objective lens. 1  $\mu\text{M}$  concentration of CV was prepared by dissolving the required amount of CV in ethanol. For each test, 10  $\mu\text{l}$  of the CV solution was drop-casted onto the SERS substrates and dried at room temperature.

## 4.3 Results and discussion

### 4.3.1 Morphological properties

A straightforward and yet a very useful method has been used to grow simultaneously two different types of Au-ZnO hetero-nanostructures (HNs) (nanowires (NWs) and triangular nanoflakes (TNFs)) at two different positions in CVD chamber on pre-annealed (800 °C in air) either 1 nm Au/SiO<sub>2</sub>/Si(110) or 5 nm Au/SiO<sub>2</sub>/Si(110) substrates. Detail structural information, growth conditions and formation mechanisms are elaborately presented in chapter 3 [6, 24]. Figure 4.1(a, b) show the BSE images of the as-grown NWs category samples (Au-ZnO NWs) with 1 nm and 5 nm Au cases respectively; corresponding insets show BSE images (Z-contrast images) of single NW. Figure 4.1(c, d) show the BSE images

**Table 4.1:** Structural details about the as-grown samples

Details	Au-ZnO NWs		Au-ZnO TNFs	
	1 nm case	5 nm case	1 nm case	5 nm case
Tip diameter (nm)	75±24	130±40	64±26	112±49
Length (μm)	13±8	6±5	17.5±13	8±6
Base (nm)	75±24	130±40	1200±650	1500±700
Areal density (/cm <sup>2</sup> )	$2.6 \times 10^8$	$4.27 \times 10^8$	$2.25 \times 10^8$	$4.0 \times 10^8$
Cross-section	Uniform hexagonal		Gradually tapered rectangular	



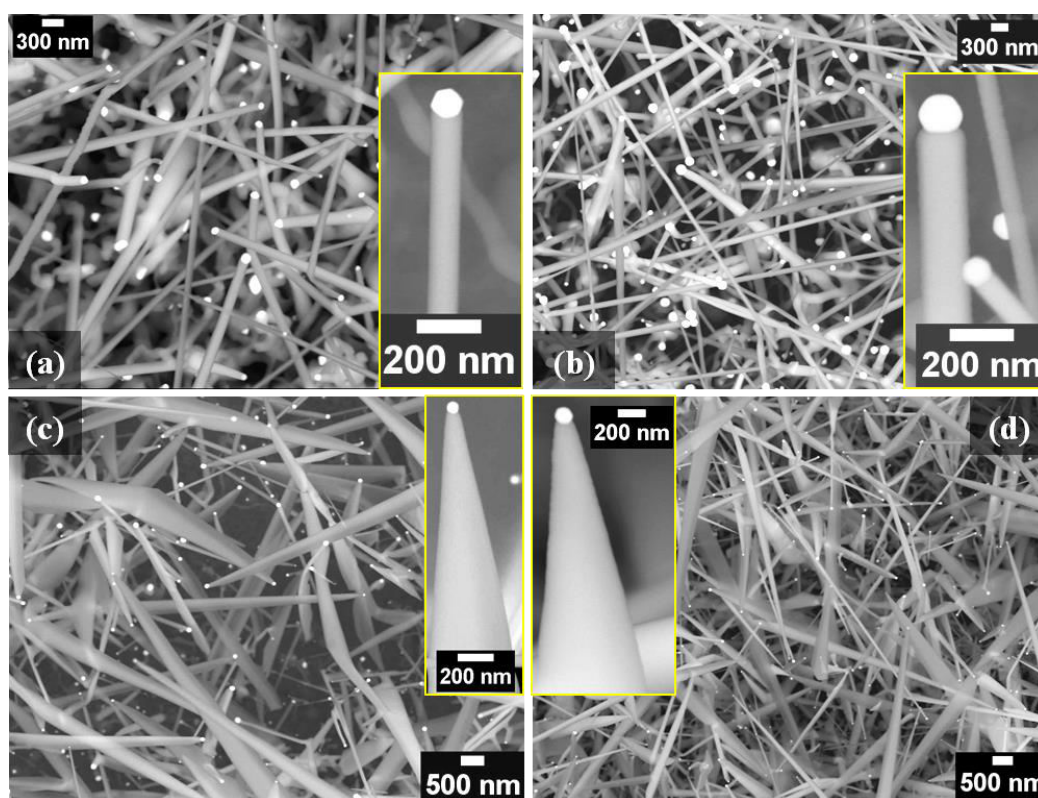


**Figure 4.1:** (a)-(b) show high-magnification BSE images (Z-contrast images) of as-grown Au-ZnO NWs using two different Au catalyst layer thicknesses of 1 nm and 5 nm respectively; (c)-(d) show the same of the as-grown Au-ZnO TNFs using two different Au catalyst layer thicknesses of 1 nm and 5 nm respectively. Insets of each show their corresponding BSE images of single Au-ZnO hetero-nanostructure.

of the as-grown TNFs category samples (Au-ZnO TNFs) with 1 nm and 5 nm Au cases respectively; respective insets show BSE images (Z-contrast images) of single TNF. Brighter contrast for each hetero-nanostructure (HNs) at the tip signifies faceted Au NP. Statistical observations about the shape, size and morphological information of total 4 as-grown samples are tabulated in Table 4.1.

### 4.3.2 Optical properties

Optical measurements of our as-grown samples were carried out using PL with a He-Cd laser of excitation wavelength 325 nm at room temperature. In general, PL spectra of ZnO nanomaterials synthesized by any (physical/chemical) route have UV and visible emissions; the intensity ratio of UV emission to visible emission is mainly influenced by the crystalline quality of ZnO. In our case, Figure 4.2 reports the PL spectra taken from all four as-grown

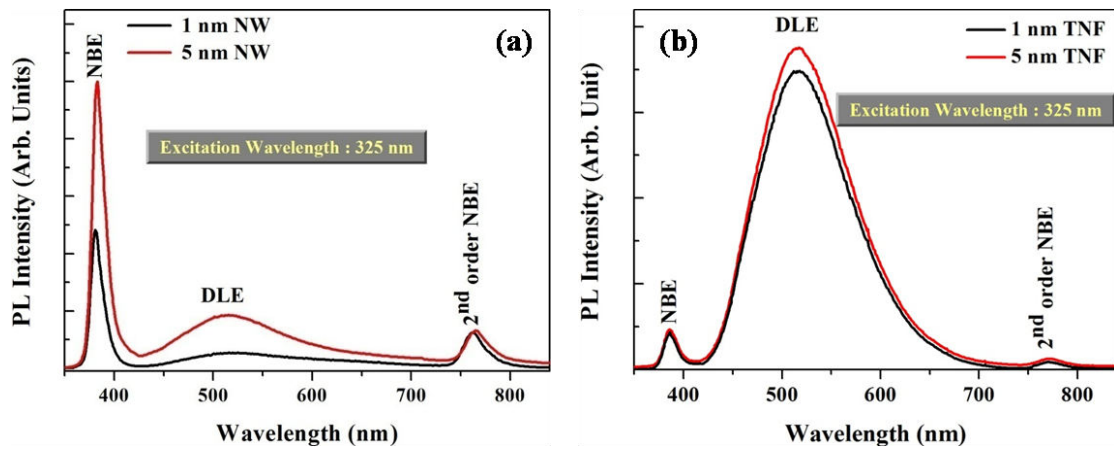


**Figure 4.2:** (a) and (b) show the comparison of room temperature PL spectra taken from as-synthesized ZnO NW array and ZnO TNF array using our two different choices of Au catalyst layer thicknesses (1 nm and 5 nm), respectively.

samples, showing three distinct regions of emission (UV, visible, and near-infrared). Despite the several reports on the visible luminescence of ZnO, its origin is still not well understood, and a number of propositions have been made to explain those emissions. Two types of NWs samples (i.e., Au-ZnO NWs with 1 nm Au and 5 nm Au) show near band-edge (NBE) emission centered at  $\approx 383$  nm and  $\approx 384$  nm respectively (Figure 4.2(a)) and the two TNFs category samples (i.e., Au-ZnO NWs with 1 nm and 5 nm Au) exhibit near band-edge (NBE) emission centered at  $\approx 385$  nm and  $\approx 386$  nm respectively (Figure 4.2(b)). This NBE emission can be understood as neutral donor bound exciton (NDBE) recombination [25, 26]. Beside these UV emissions, all the four as-grown samples show a broad deep level green emission band with an intensity maximum at  $\approx 519$  nm for both NWs (1 nm Au and 5 nm Au cases) samples (Figure 4.2(a)) and  $\approx 520$  nm for both (1 nm Au and 5 nm Au cases) TNFs samples (Figure 4.2(b)). Defect induced green emission from ZnO nanostructures/thin film is well documented in literature [27-29]. The origin of green emission from our samples can be attributed to the radiative recombination of photo-generated holes with electrons of singly ionized oxygen vacancy states or oxygen interstitial states [27-31]. The high-intensity green emission band in the PL spectra of all TNFs category samples (Figure 4.2(b)) compared to all NWs category samples (Figure 4.2(a)) attribute its higher oxygen vacancies. So, the Au-ZnO TNFs category samples contain more oxygen vacancy related defects compared to the Au-ZnO NWs samples. It is also important to emphasize that the intensity of the green emission band from TNFs category samples is almost seven times the intensity of their respective NBE whereas for NWs category samples the intensity of the green emission is

almost half of their respective NBE. So, the higher NDBE emission intensity compared to green emission for all NWs samples, contrary to all TNFs samples which may be due to the fact that the density of bound excitonic states is higher than that of the oxygen vacancy states [25]. One possible reason would be the difference in exposed average surface area (ASA) for the two types of NSs ( $TNF_{ASA}/NW_{ASA} \approx 8$ ). Interestingly, we have found that an additional sharp peak in the near-infrared (IR) region centered at  $\approx 765$  nm and  $\approx 767$  nm for Au-ZnO NWs samples with 1 nm Au and 5 nm Au respectively (Figure 4.2(a)) and  $\approx 770$  nm for both (1 nm Au and 5 nm Au) Au-ZnO TNFs samples (Figure 4.2(b)). Because the wavelengths of near-IR emission peaks are approximately twice that (or half in energy scale) of their corresponding NBE emission peaks, thus they could be attributed to the second-order diffraction of NBE emission [32-34].

Figure 4.3 (a) and (b) show the comparison of reflection spectra obtained from NWs category samples (with 1 nm and 5 nm Au) and TNFs category samples (with 1 nm and 5 nm Au) respectively with 1 nm and 5 nm Au coated Si(110) air-annealed (800° C) substrates, alongside commercially available bare ZnO(0002) and Si(110) substrates. In wavelength range of 300 - 900 nm, the average reflectance for bare Si(110) and air-annealed gold coated Si(110) substrates are observed to be 45%, 42% (with 1 nm Au) and 35% (with 5 nm Au), respectively. Gold (Au) absorbs visible light of wavelength corresponding to its surface plasmon resonance (SPR) peak. So, more Au NPs on Si substrate yield lower surface reflectance which is reflected in our data. Furthermore, ZnO NWs grown on 1 nm and 5 nm Au deposited substrates (pre-annealed at 800° C) lower the average reflectance to 4.1 % and 0.75 % respectively (Figure 4.3(a)) over a wavelength range between 300 - 900 nm. Similarly, average reflectance was scaled down to 1.05 % and 0.68 % over the same wavelength range after the growth of ZnO TNFs on 1 nm and 5 nm Au deposited substrates (pre-annealed at 800° C), respectively (Figure 4.3(b)). This antireflection nature of the Au-ZnO HNs samples compared to other four substrates over a wide range of wavelengths can be explained by scalar diffraction theory. From renowned Fresnel formulas, the reflectivity of a thin film over a substrate is determined by matching the ratios of refractive indices at the interfaces of the thin film (TF), leads to the antireflection criterion (ARC)  $n_{TF} = (n_{sub} \times n_{air})^{0.5}$ , where  $n_{TF}$ ,  $n_{sub}$  and  $n_{air}$  are the refractive index of the TF, substrate and air respectively [35, 36]. We know that the refractive indices of the ZnO, Si substrate and air are  $\approx 2.0$ ,  $\approx 3.5$  and  $\approx 1.0$  respectively. So the antireflection nature of our HNs coated Si samples are achieved as ZnO produces optical impedance match between air and Si substrate by following above

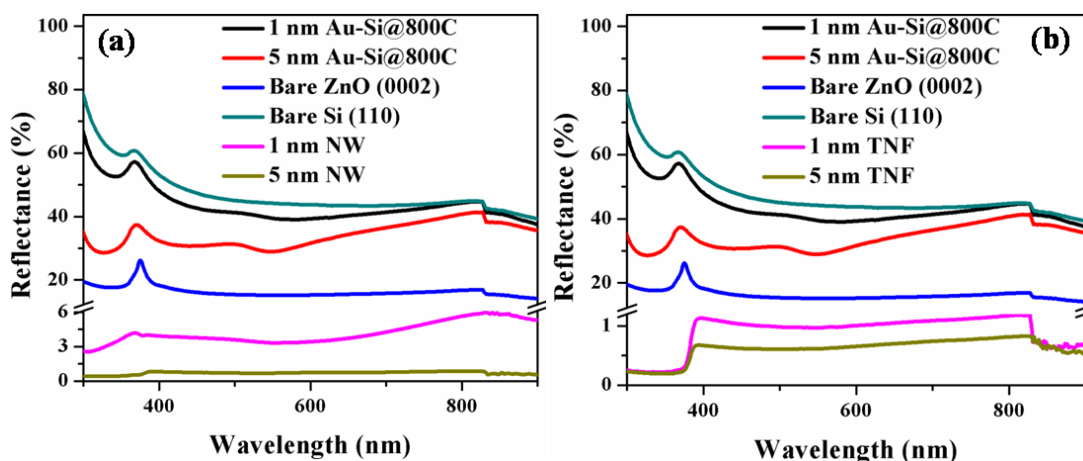


**Figure 4.3:** Comparison of UV-Vis Specular reflectance spectra obtained from (a) NWs category Au-ZnO hetero-nanostructures covered Si(110) samples with 1 nm and 5 nm Au cases and (b) TNFs category Au-ZnO hetero-nanostructures covered Si(110) samples with 1 nm and 5 nm Au cases with 800 °C air-annealed 1 nm, 5 nm Au coated Si(110) substrates, bare ZnO(0002) and bare Si(110) substrates.

ARC equation as  $(n_{\text{ZnO}} \approx (n_{\text{Si}} \times n_{\text{air}})^{0.5})$  leading to a exceptional light trapping [37, 38]. Moreover, tip diameter and areal density of both types of Au-ZnO HNs with 5 nm Au cases are larger than that with 1 nm Au cases (Table 4.1) and reflectance is lower for 5 nm cases than 1 nm cases over entire wavelength range (Figure 4.2).

### 4.3.3 SERS substrates: detection of CV (Crystal Violet) molecules

Till now we have discussed about the usefulness of the Au-ZnO NWs and TNFs array grown with faceted Au at their tip as antireflection coating. From the exceptionally lower reflectance ( $< 5\%$ ) over a wide range 300 – 900 nm wavelength shown by our all four as-grown samples, it is highly expected that these substrate would be appropriate for use as SERS-active substrates. All the 4 as-grown HNs samples (Au-ZnO NWs  $\rightarrow$  2 samples, Au-ZnO TNFs  $\rightarrow$  2 samples) have now been used to detect the crystal violet (CV) molecule of 1.0  $\mu\text{M}$  concentration (ethanol solution) with two different excitations 514 nm (green) and 633 nm (red). Figure 4.4(a) and (c) show the SERS spectra of 1  $\mu\text{M}$  concentration CV on Au-ZnO NWs and Au-ZnO TNFs (1 nm and 5 nm Au cases for both) respectively, recorded with 514 nm. Figure 4.5(a) and (c) show the SERS spectra of 1  $\mu\text{M}$  concentration CV on Au-ZnO NWs and Au-ZnO TNFs (1 nm and 5 nm Au cases for both) respectively, recorded with 633 nm. Explicit evaluation of SERS enhancement factor is almost impossible as it needs

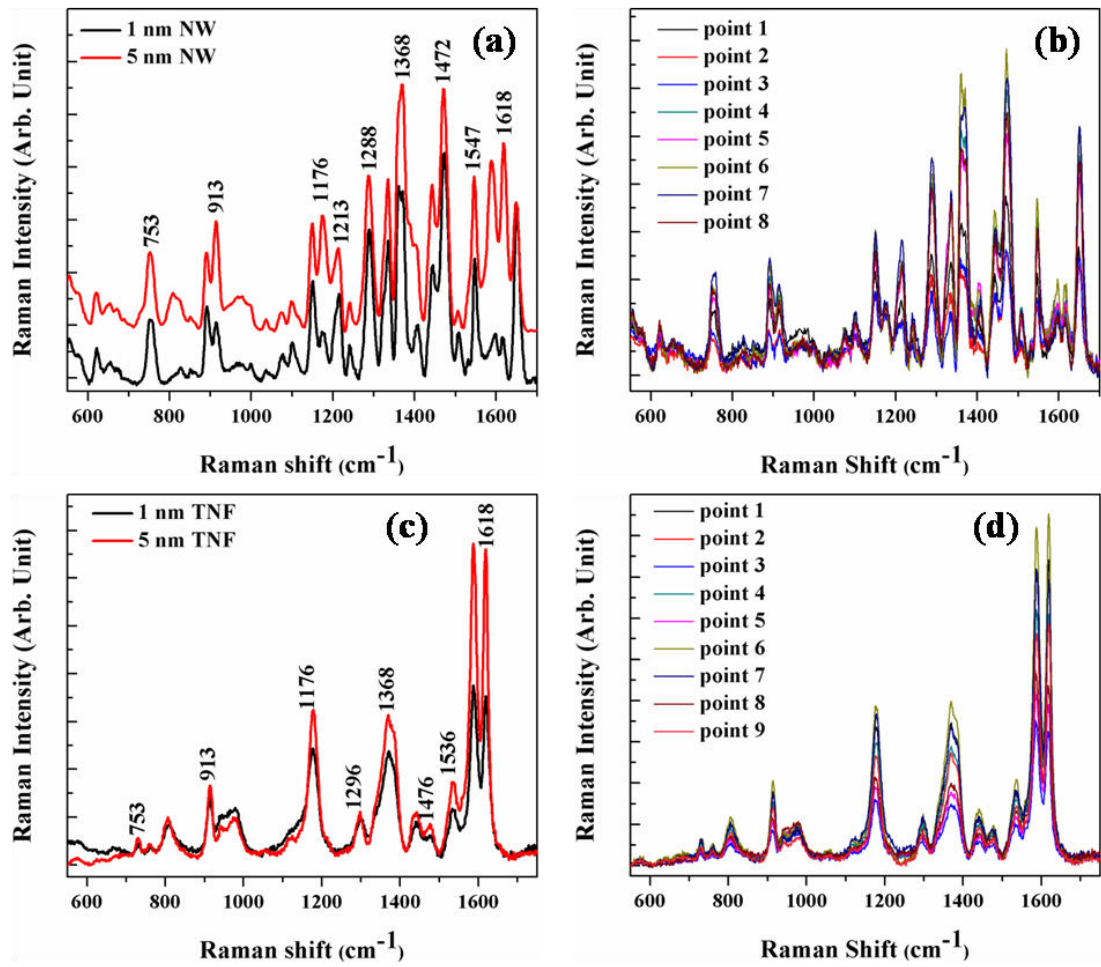


**Figure 4.4:** (a) and (c) show the SERS spectra of 1  $\mu\text{M}$  concentration CV on Au-ZnO NWs (1 nm and 5 nm Au cases both) and Au-ZnO TNFs (1 nm and 5 nm Au cases both), respectively, recorded with 514 nm. (b) and (d) present reproducible SERS spectra of CV of 1  $\mu\text{M}$  concentration on NW sample with 1 nm Au case and TNF sample with 5 nm case, respectively, recorded with 514 nm.

exact number of adsorbed molecule in the scattering volume on the SERS substrate [6]. So, analytical enhancement factors (AEF) were calculated with respect to the characteristic peak of CV (1176  $\text{cm}^{-1}$  Raman peak) for all the samples using the equation below:

$$\text{AEF} = (I_{\text{SERS}}/C_{\text{SERS}})/(I_{\text{RS}}/C_{\text{RS}})$$

where  $I_{\text{SERS}}$  and  $I_{\text{RS}}$  are the Raman signals under SERS and normal conditions, respectively;  $C_{\text{SERS}}$  and  $C_{\text{RS}}$  are the concentrations of the CV molecules in the SERS and normal samples. The calculated analytical enhancement factors (AEF) have been tabulated for all the samples with two different excitations in Table 4.2. It is evident from the table 4.2 that for both types of HNs samples grown using 5 nm Au have higher SERS enhancement factor compared to their respective HNs samples grown using 1 nm Au for both the excitations [6]. Theoretical



**Table 4.2:** Detail about calculated AEF values

Details	AEF for Au–ZnO NWs		AEF for Au–ZnO TNFs	
	1 nm case	5 nm case	1 nm case	5 nm case
1 $\mu$ M CV (514 nm)	$2.1 \times 10^4$	$3.6 \times 10^4$	$4.0 \times 10^3$	$5.3 \times 10^3$
1 $\mu$ M CV (633 nm)	$3.2 \times 10^3$	$5.2 \times 10^3$	$6.5 \times 10^2$	$9.2 \times 10^2$

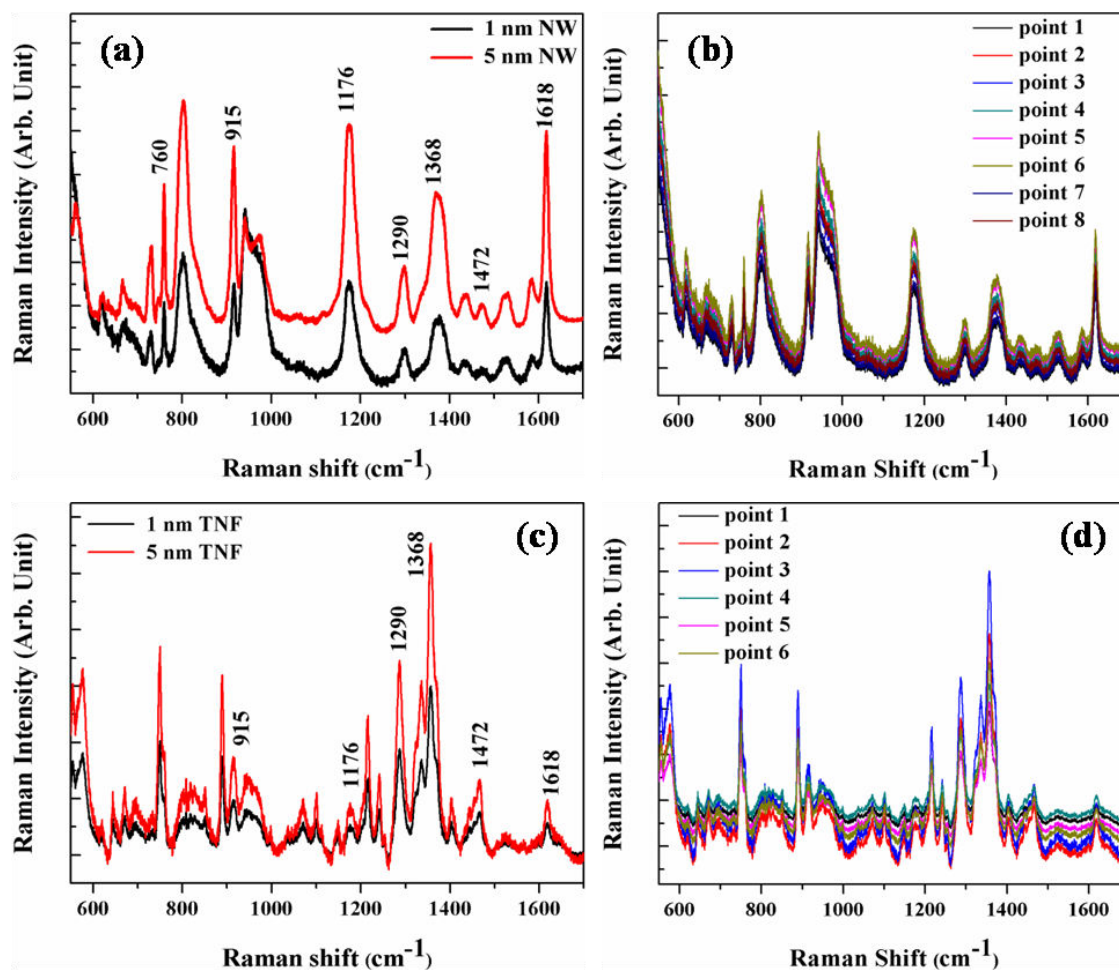


**Figure 4.5:** (a) and (c) show the SERS spectra of 1  $\mu$ M concentration CV on Au-ZnO NWs (1 nm and 5 nm Au cases both) and Au-ZnO TNFs (1 nm and 5 nm Au cases both), respectively, recorded with 633 nm. (b) and (d) present reproducible SERS spectra of CV of 1  $\mu$ M concentration on NW sample with 1 nm Au case and TNF sample with 5 nm case, respectively, recorded with 633 nm.

and experimental studies tell that, highest SERS enhancement takes place at the junction between the metal NPs, which can be increased simply by increasing areal density of metal NPs [39, 40]. As expected samples of both categories (NWs and TNFs) grown using 5 nm Au

are giving larger SERS enhancement than 1 nm Au samples of respective categories, following their higher areal densities (Table 4.2). It is also paramount to emphasize that the samples (5 nm NWs and TNFs samples) with lower reflectance exhibiting higher SERS signal enhancement, which is in agreement with earlier literatures [41-43]. Figure 4.4(b) and 4.5(b) present reproducible SERS spectra of CV of 1  $\mu\text{M}$  concentration on Au-ZnO NWs array sample with only 1 nm Au case recorded with 514 nm and 633 nm respectively. Figure 4.4(d) and 4.5(d) present reproducible SERS spectra of 1  $\mu\text{M}$  concentration CV on Au-ZnO TNFs array sample (5 nm Au case) recorded with 514 nm and 633 nm respectively. From the above experimental observations we can conclude that all four HNs/Si samples are reproducible and robust in nature, which is prerequisite for SERS applications. One can visualize from our results that 514 nm excitation offers highest AEF compared to 633 nm for all four samples. From literature, Au-ZnO (or Au-semiconductor) composite have absorption lies in the range of 505 nm to 615 nm depending on their size and substrate [44, 45]. For our all 4 samples reflectance minima corresponding to LSPR maxima occurs  $\approx 530\text{-}560$  nm (Figure 4.3). Absorption spectra of 1 $\mu\text{M}$  concentration CV solution shows absorption peak centered at  $\approx 570$  nm (Figure 4.6). According to Christy L. Haynes et al. the highest enhancement factor can be achieved when LSPR  $\lambda_{\text{max}}$  lies in between energy of the excitation wavelength and the vibrational mode of analyte molecule [46]. In consistent with L. Haynes et al. report, from the above experimental results, it is clear that the 514 nm (green laser) is most suitable for the SERS detection of CV molecule with Au-ZnO HNs system.

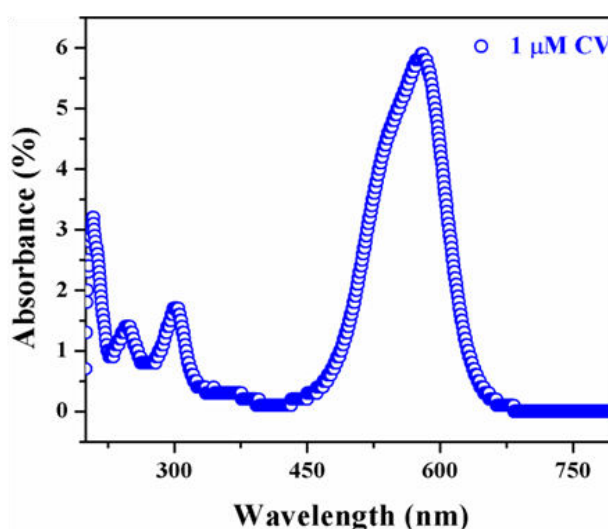


**Figure 4.6:** Absorbance spectra from 1  $\mu\text{M}$  CV in ethanol solution.

## 4.4 Summary

In this chapter, we have demonstrated SERS activity of the intrinsically self-assembled faceted Au capped ZnO HNs (NWs and TNFs) coated Si substrates which are grown using a single step CVD technique. As-grown HNs coated Si substrates are employed towards SERS detection of crystal violet (CV) molecule of 1  $\mu$ M concentration in ethanol, with two excitation lines 514 nm (green laser) and 633 nm (red laser). These substrates are highly antireflective in nature in the wavelength range of 250 to 1000 nm. This exceptional light trapping can be attributed to the optical impedance matching ZnO layer in between air and Si substrate and also surface plasmon resonance absorption from tip faceted Au NPs. It is also observed that TNFs samples from each category (1nm or 5 nm Au) have higher defect related visible emission compared to NWs samples owing to their  $\approx$  8 times higher exposed surface area. In this work we have two major conclusions: 1<sup>st</sup> one is that for a particular category of SERS substrate, activity could be increased by lowering the reflectance and the second one is higher SERS effect will be there when LSPR of the substrate lies in between the excitation wavelength and vibrational band of analyte molecule. These Au-ZnO HNs coated Si substrates yielded high SERS activity for CV, implying their potential in SERS based detection of biomolecules. In the next chapter we will show the enhanced visible light driven activities of these Au-ZnO HNs coated Si substrates, which is understood as synergetic effect of oxygen vacancies and plasmonic faceted Au NPs present in the HNs.

## 4.5 References

- [1] B. Sharma, R. R. Frontiera, A. I. Henry, E. Ringe and R.P. Van Duyne, *Mat. Today* **15**, 16 (2012).
- [2] J. Kneipp, H. Kneipp, B. Wittig and K. Kneipp, *Nanomed. Nanotech. Bio. Med.* **6**, 214 (2010).
- [3] S. E. J. Bell and N. M. S. Sirimuthu, *Chem. Soc. Rev.* **37**, 1012 (2008).
- [4] J. H. Choi, J. Lee, B. K. Oh and J. W. Choi, *J. Nanosci. Nanotechnol.* **14**, 5658 (2014).
- [5] L. Chen et al., *J. Phys. Chem. C* **114**, 93 (2010)



- [6] A. Ghosh, R. R. Juluri, P. Guha, R. Sathyavathi, A. Dash, B. K. Jena and P. V. Satyam, *J. Phys. D: Appl. Phys.* **48**, 055303 (2015).
- [7] A. Campion and P. Kambhampati, *Chem. Soc. Rev.* **27**, 241 (1998).
- [8] D. L. Jeanmaire and R. P. Van Duyne, *J. Electroanal. Chem.* **84**, 1 (1977).
- [9] M. G. Albrecht and J. A. Creighton, *J. Am. Chem. Soc.* **99**, 5215 (1977).
- [10] B. J. Marquis, A. D. McFarland and C. L. Haynes, *Anal. Chem.* **80**, 3431 (2008).
- [11] K. L. Wustholz et al., *J. Am. Chem. Soc.* **132**, 10903 (2010).
- [12] P. Mohanty et al., *J. Am. Chem. Soc.* **129**, 9576 (2007).
- [13] S. J. Lee, A. R. Morrill and M. Moskovits, *J. Am. Chem. Soc.* **128**, 2200 (2006).
- [14] M. J. Banholzer, J. E. Millstone, L. Qin and C. A. Mirkin, *Chem. Soc. Rev.* **37**, 885 (2008).
- [15] H. Ko, S. Singamaneni and V. V. Tsukruk, *Small* **4**, 1576 (2008).
- [16] G. Sinha, L. E. Depero and I. Alessandri, *ACS Appl. Mater. Interfaces* **3**, 2557 (2011).
- [17] S. K. Cha et al., *ACS Nano* **9**, 5536 (2015).
- [18] S. M. Prokes, O. J. Glembocki, R., W. Rendell and M. G. Ancona, *Appl. Phys. Lett.*, **90**, 093105 (2007).
- [19] B. Zhang, H. Wang, L. Lu, K. Ai, G. Zhang and X. Cheng, *Adv. Funct. Mater.* **18**, 2348 (2008).
- [20] S. Zhang, W. Ni, X. Kou, M. Yeung, L. Sun, J. Wang and C. A. Yan, *Adv. Funct. Mater.* **17**, 3258 (2007).
- [21] Q. Tao, S. Li, Q. Y. Zhang, D. W. Kang, J. S. Yang, W. W. Qiu and K. Liu, *Mater. Res. Bull.* **54**, 6 (2014).
- [22] D. Naumenko et al., *Nanoscale*, **6**, 13651 (2014).
- [23] C. Cheng et al., *ACS Appl. Mater. Interfaces*, **2**, 1824 (2010).
- [24] A. Ghosh, P. Guha, A. K. Samantara, B. K. Jena, R. Bar, S. Ray and P. V. Satyam, *ACS Appl. Mater. Interfaces* **7**, 9486 (2015).

- [25] Z. Zhu, T. L. Chen, Y. Gu, J. Warren and R. M. Osgood, *Chem. Mater.* **17**, 4227 (2005).
- [26] Y. C. Kong, D. Yu, B. Zhang, W. Fang and S. Q. Feng, *Appl. Phys. Lett.* **78**, 407 (2001).
- [27] B. Lin, Z. Fu and Y. Jia, *Appl. Phys. Lett.* **79**, 943 (2001).
- [28] W. M. Kwok et al., *Appl. Phys. Lett.* **89**, 183112 (2006).
- [29] C. Baratto et al., *Cryst. Eng. Commun.* **15**, 7981 (2013).
- [30] K. Vanheusden et al., *J. Appl. Phys.* **79**, 7983 (1996).
- [31] C. Li et al., *J. Cryst. Growth* **292**, 19 (2006).
- [32] T. Mahalingam et al, *Nanotechnology* **18**, 035606 (2007).
- [33] E. V. Lozada, T. V. Torchynska and J. L. Casas Espinola, *JPCS* **494**, 012011 (2014).
- [34] Y. G. Wang et al., *J. Cryst. Growth* **259**, 335 (2003).
- [35] M. Born and E. Wolf, *Cambridge University Press: Cambridge, UK* **64** (2005).
- [36] B. Paivanranta et al., *ACS Nano*, **5**, 1860 (2011).
- [37] S. H. Lee, G. E. Jellison Jr, C. E. Duty and J. Xu, *Appl. Phys. Lett.* **99**, 153113 (2011).
- [38] B. D. Choudhury, A. Abedin, A. Dev and S. Anand, *Opt. Mater. Express* **3**, 8 (2013).
- [39] Y. Wang, H. Chen, S. Dong and E. Wang, *J. Raman Spectrosc.* **38**, 515 (2007).
- [40] C. Caro, C. Lopez-Cartes and J. A. Mejias, *J. Raman Spectrosc.* **39**, 1162 (2008).
- [41] Y. J. Oh, J. J. Kim and K. H. Jeong, *Adv. Mater.* **24**, 2234 (2012).
- [42] P. R. Stoddart et al., *Nanotechnology* **17**, 680 (2006).
- [43] H. Huang, L. Liu, P. Peng, A. Hu and Y. Zhou, *J. Appl. Phys.* **112**, 123519 (2012).
- [44] Y. K. Mishra et al., *Appl. Phys. Lett.* **92**, 043107 (2008).
- [45] S. Link and M. A. El-Sayed, *J. Phys. Chem. B* **103**, 4212 (1999).
- [46] C. L. Haynes, C. R. Yonzon and R. P. Van Duyne, *J. Raman Spectrosc.* **36**, 471 (2005).

# Chapter 5

## Faceted Au-ZnO Hetero-nanostructures on Silicon Substrates (Nanowires and Triangular Nanoflakes): A Shape and Defect Driven Enhanced Photocatalytic Performance under Visible Light

### 5.1 Introduction

In this chapter, we demonstrate the use of *single step* CVD grown faceted Au-ZnO hetero-nanostructures (nanowires → NWs and triangular nanoflakes → TNFs) on crystalline Si wafers, having different morphology and oxygen defect densities, towards efficient visible light driven photocatalytic applications. The use of these HNs has been validated by their photoresponse and photocatalytic performance towards degradation of rhodamine B (RhB) and phenol under visible light illumination. The Au-ZnO TNF structures showed one order of magnitude enhancement in photocurrent density following an order of magnitude less charge-transfer resistance ( $R_{ct}$ ) compared to Au-ZnO NWs, leading to a high performance photocatalytic activity. The plausible reasons behind the better photocatalytic performance offered by Au-ZnO TNFs sample compared to NWs sample have been addressed in the light of various experimental findings. To the best of our knowledge, there are no such reports where the growth process of getting semiconductor-metal hetero-nanostructures (HNs) with significant oxygen defects in a single step process and their corresponding visible light influenced activities were systematically studied.

Highly ordered and oriented nanoscale metal oxides structures (NSs) in conjunction with plasmonic noble-metal nanoparticles (NPs) have great potential in micro/nano devices for electronic, optical and photocatalytic applications [1-5]. In last few decades, environmental problems such as air and water pollution have become a major issue for economic development and human health. Semiconductor based photocatalytic reactions

have attracted intense interest as an effective candidate for environmental treatments [6, 7]. Among several oxide semiconductor photocatalysts,  $\text{TiO}_2$  and  $\text{ZnO}$  have been most exciting materials for detoxification/purification of water/air and degradation of persistent organic pollutants (like various dyes) present in waste water through photocatalytic processes [8-17]. In comparison with  $\text{TiO}_2$ ,  $\text{ZnO}$  has been actively worked upon from variety of research communities due to their high photosensitivity, large direct bandgap (3.37 eV), relatively high exciton binding energy (60 meV), non-toxic character, abundant in reserve and low-cost large scale synthesis viability [12-15, 17-19]. Besides the photocatalytic applications of  $\text{ZnO}$  NSs, they have been extensively used in several functional devices [20-24]. As the size and shape of the NSs have key importance on their applications, various 1-D  $\text{ZnO}$  NSs with different morphologies, such as nanowires (NWs), nanorods, nanotubes, nanobelts, nanonails, nanoflakes (NFs), nanowalls and nanosheets have been synthesized [25-27]. The pure  $\text{ZnO}$  NSs show the absorption capabilities only in UV-light ( $\lambda \leq 370$  nm) due to its high bandgap (3.37 eV). This limits the use of  $\text{ZnO}$  in facile visible light driven photocatalytic applications in its pure form. So, a lot of effort has already been devoted to improve the visible light absorption capabilities (major part of solar spectrum) of  $\text{ZnO}$  material by tailoring their size, morphology, surface area, doping of non-metals and most importantly defect concentrations related to oxygen (vacancies or interstitials) [12, 13, 28-35]. Among all the pathways of boosting visible light photocatalysis, creation of oxygen vacancies is one of the convenient methods which not only increase the visible light absorption by narrowing bandgap but also restrain the recombination processes of photogenerated  $\text{e}^-$  and  $\text{h}^+$  pairs by acting as active trap centers [12, 13, 35, 36]. Though  $\text{ZnO}$  nanostructures have been studied extensively, our report *single step* CVD grown shape and defect controlled Au- $\text{ZnO}$  hetero-nanostructures (HNs like NWs and TNFs) on Si substrates with excellent visible light induced photocatalytic properties, could be one of the first such a report. The hybridization/integration of Au NPs as plasmonic noble metal on the surfaces of metal oxide NSs (like  $\text{TiO}_2$  and  $\text{ZnO}$ ) to form metal-semiconductor hetero-nanostructures (HNs) have been proposed as promising way to increase the photocatalytic efficiency [18, 19, 37-40]. In particular for Au- $\text{ZnO}$  HNs case, Au NPs act as a sink for photogenerated electrons and restrain the recombination processes. The Au NPs contribute a better charge separation process as well as facilitate electron and hole pairs production by their surface plasmon resonance (SPR) property [18, 19, 37-39, 41-44]. Now it is paramount to emphasize that all the previous reports have adopted various post-growth multistep processes to improve photocatalytic activity under visible illumination, but in our case no post-growth process is involved.

## 5.2 Experimental

### 5.2.1 Structural and optical characterization

Large-scale single-crystalline nanostructures of Au-ZnO system (Nanowires and Triangular Nanoflakes) were grown by keeping the substrates at two different positions (downstream and upstream) in a single zone, side entry quartz tube furnace. A detail about the growth and the CVD setup used has already been presented in chapter 3. For this work  $\approx$  5 nm thick Au films were deposited (using high vacuum coating methods) on native oxide Si(110) substrates and annealed at 800 °C for 30 min in air prior to the growth of Au-ZnO HNs arrays. The as-prepared Au-ZnO NWs/Si (downstream substrate) and Au-ZnO TNFs/Si (upstream substrate) samples are hereafter referred as samples A and B, respectively [45, 46].

Surface morphology, shape and size of the as-grown Au-ZnO NWs and TNFs arrays were examined using same FE-SEM and HRTEM facilities described in the previous chapters. Optical properties of the samples were characterized by photoluminescence (PL) setup under the excitation of He-Cd laser (325 nm pump line) at room temperature. Cathodoluminescence (CL) or electron beam induced radiation emission (EIRE) spectroscopy was performed in a ZEISS SUPRA40 SEM equipped with the Gatan MonoCL3 cathodoluminescence system. The X-ray photoelectron spectroscopy (XPS) measurements were carried out using VG Scienta hemispherical analyzer having resolution of 44.1 meV at 50 pass energy and Al  $K_{\alpha}$  ( $h\nu = 1486.6$  eV) source (S/N:10001, Prevac, Poland).

### 5.2.2 Photo-electrochemical measurements

For photo-electrochemical measurements, HNs from sample A and sample B were scrapped off and dispersed on ITO coated quartz substrate and dried prior use. These two types of Au-ZnO HNs (NWs and TNFs) modified ITO/Quartz were used as the working electrode. The photoelectric response measurements were carried out by illuminating 1 cm<sup>2</sup> of the working electrode at zero bias voltage against Ag/AgCl reference electrode in 0.01M Na<sub>2</sub>SO<sub>4</sub> as the supporting electrolyte. Here, the photo-response spectra were obtained with a 100 W lamp (with a Luminous irradiance of 10 mW/cm<sup>2</sup> at the sample) switch ON and OFF conditions and the generated photocurrent signals were measured by the CHI 660C electrochemical work station.

### 5.2.3 Photocatalytic activity

The photocatalytic activity of the as-grown HNs samples (samples A and B) were evaluated by degradation of rhodamine B (RhB) and phenol (as standard organic pollutant) in aqueous solution under visible light irradiation. For both the cases, NWs and TNFs coated Si substrates of area  $0.5 \text{ cm}^2$  were immersed in a 10 ml of RhB solution ( $5 \times 10^{-6} \text{ M}$ ) under the illumination of 100 Watt bulb (with a Luminous irradiance of  $10 \text{ mW/cm}^2$  at the sample) with continuous stirring in a beaker. Before the light was switched on, the beaker containing photocatalyst and RhB solution was stirred in the dark for 30 min to ensure an equilibrium adsorption of dye molecules on the catalyst (Au-ZnO NWs or TNFs on Si surfaces). Subsequently, at regular intervals from 30 min to 3 hours of exposure, 4 ml solutions were withdrawn for monitoring absorption changes using a UV-VIS absorption spectroscopy using model SHIMADZU (UV-2600). The RhB residual concentration was determined at by checking the changes in the absorbance maximized at  $\lambda_{\text{max}} = 554 \text{ nm}$  as a function of irradiation time. For phenol ( $5 \times 10^{-6} \text{ M}$ ) degradation study, all the experimental conditions were remain same as RhB case and the residual concentration was determined by following the changes in the absorbance maximized at  $\lambda_{\text{max}} = 270 \text{ nm}$  as a function of irradiation time.

## 5.3 Results and discussion

### 5.3.1 Morphological and structural characterization

The Morphological studies were carried out with FE-SEM (both secondary electron (SE) and backscattered electron (BSE) images) for both the samples A and B. Figures 5.1(a, c) depict low-magnification SE images for sample A (downstream) and sample B (upstream) respectively. Corresponding insets of these Figures 5.1(a, c) clearly show nanowire of uniform diameter (downstream substrates) and triangular nanoflake of tapered triangular shape structures (upstream substrates) with faceted Au nanoparticles at the apex. High-magnification backscattered electrons (BSE) images taken from sample A and sample B have been shown in Figures 5.1(b, d), wherein the brighter contrasts correspond Au NPs for both the samples. Comprehensive structural and compositional studies (using HREM, SAED, XRD, EDX) have been discussed thoroughly in chapter 3. Statistical observations on respective samples have been summarized in Table 5.1 [45].

**Table 5.1:** Detail about the dimensions and areal densities of the as-grown samples

Details	Sample A (Au-ZnO NWs/Si)	Sample B (Au-ZnO TNFs/Si)
Tip diameter (nm)	130±40	112±49
Length (μm)	6±5	8±6
Base (nm)	130±40	1500 ±700
Areal Density (HNs/cm <sup>2</sup> )	$4.27 \times 10^8$	$4.0 \times 10^8$
Cross-section along the growth direction	Uniform hexagonal	Gradually tapered rectangular

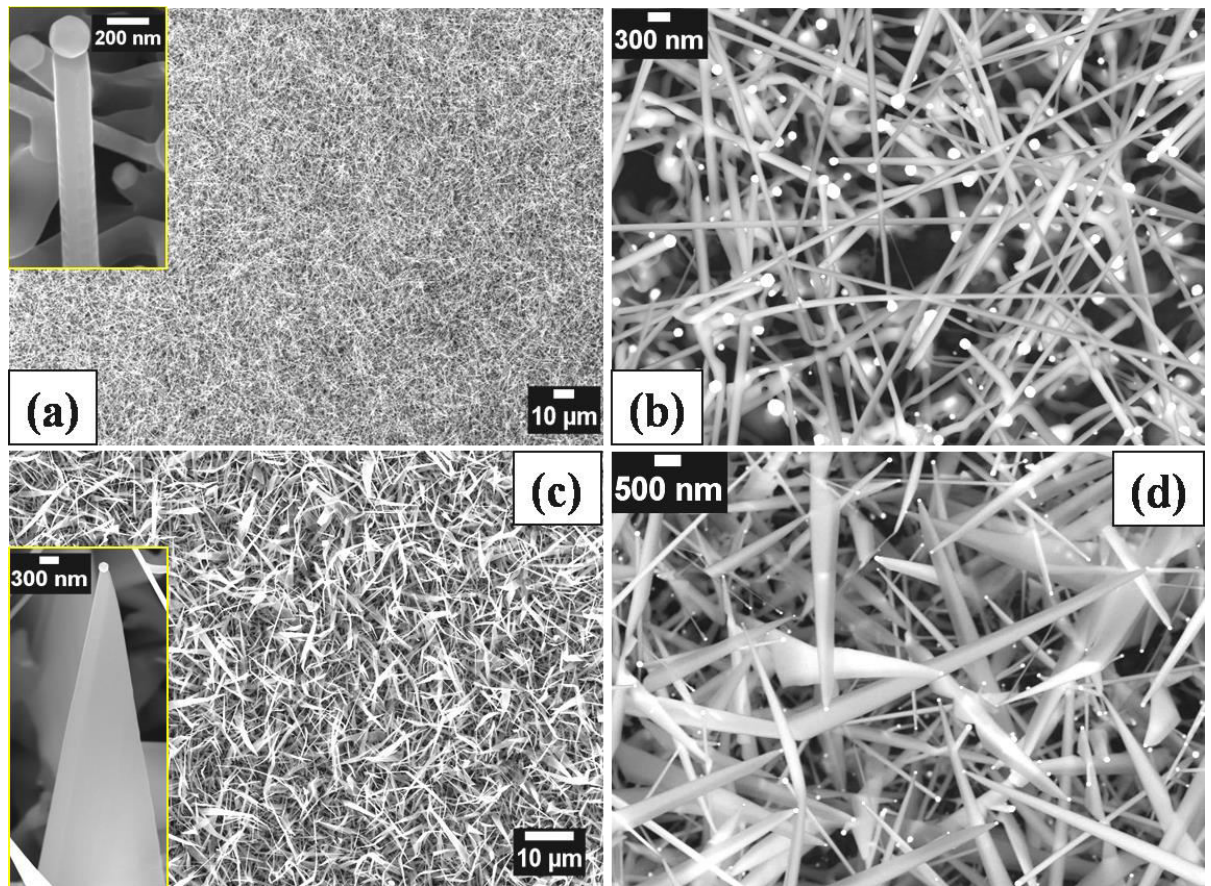


**Figure 5.1:** SEM micrographs of as-grown Au-ZnO hetero-nanostructures (nanowires and triangular nanoflakes) on 5 nm Au/SiO<sub>2</sub>/Si(110) pre-annealed @800 °C substrates kept at two different positions (down stream and up stream of CVD system): (a) and (c) present top view low-magnification secondary electron images of sample A (NWs) and sample B (TNFs), respectively. (b) and (d) present corresponding samples high-magnification backscattered electron images. Inset of figures (a), (c) show the SE images a single NW and TNF, respectively.

### 5.3.2 Optical studies

Optical measurements of our as-grown samples were carried out using PL at room temperature. Figures 5.2(a and b) report the PL spectra taken from sample A (Au-ZnO NWs/Si(110)) and sample B (Au-ZnO TNFs/Si(110)), respectively; show three distinct regions of emission (UV, visible and near-infrared) [45]. PL spectra of both the samples A and B composed of strong ultraviolet (UV) emission peaks centered at 384 nm and 386 nm, broad deep-level defect related green emissions ( $\approx 519$  nm/2.39 eV and  $\approx 520$  nm/2.38 eV) along with sharp near-infrared peaks around 767 nm and 770 nm respectively [45]. Near band edge (NBE) UV emission is attributed to the neutral donor bound exciton (NDBE) recombination [47,48]. It is important to emphasize that intensity of green emission band from sample B is almost seven times the intensity of its NBE whereas for sample A intensity of green emission is almost half of its NBE. Several reports are there explaining the various origin of the defect induced visible luminescence depending on the growth temperature, growth substrate, ambience, precursor and choices of catalyst [47, 49, 50]. To check whether oxygen related defects are causing this visible emission or not, we have performed annealing experiments under oxygen environment for both the as-grown samples at  $\approx 900$  °C for 90 min. The PL spectra of these oxygen annealed samples are shown in Figures 5.2(c, d) respectively. We have seen from the PL spectra taken on both the oxygen annealed samples, that green emissions intensity have suppressed significantly. So, the origin of green light emission can be assigned to the recombination centers created due the presence of oxygen vacancies and interstitials in the interior as well as on the surface of the ZnO NSs [45, 49-51]. The high intensity green emission band in the PL spectra of TNFs (sample B) compared to NWs (sample A) attribute its higher oxygen vacancies (Figures 5.2(a, b)). The NBE emission intensity is noticed to be lower than that of green emission from ZnO TNF (sample B) contrary to the ZnO NW (sample A) case, corroborates that the density of bound excitonic states is lesser than that of oxygen vacancy states [48, 58]. One possible reason would be the difference in exposed average surface area (ASA) for the two types of NSs ( $TNF_{ASA}/NW_{ASA} \approx 8$ ) [45]. Moreover, a little red-shift in NBE emission position ( $\approx 386$  nm) of TNF (sample B) compare to NW (sample A) case ( $\approx 384$  nm) is found. This behavior may be due to the effect of bandgap narrowing, resulting from very high amount of oxygen vacancy states in TNFs driving themselves more delocalized and overlapped with the valence band edge [12,13]. An additional peak for both types of ZnO NSs (NWs and TNFs) appears in the near-infrared (NIR) region centered at 767 nm and 770 nm respectively. As the wavelength of NIR



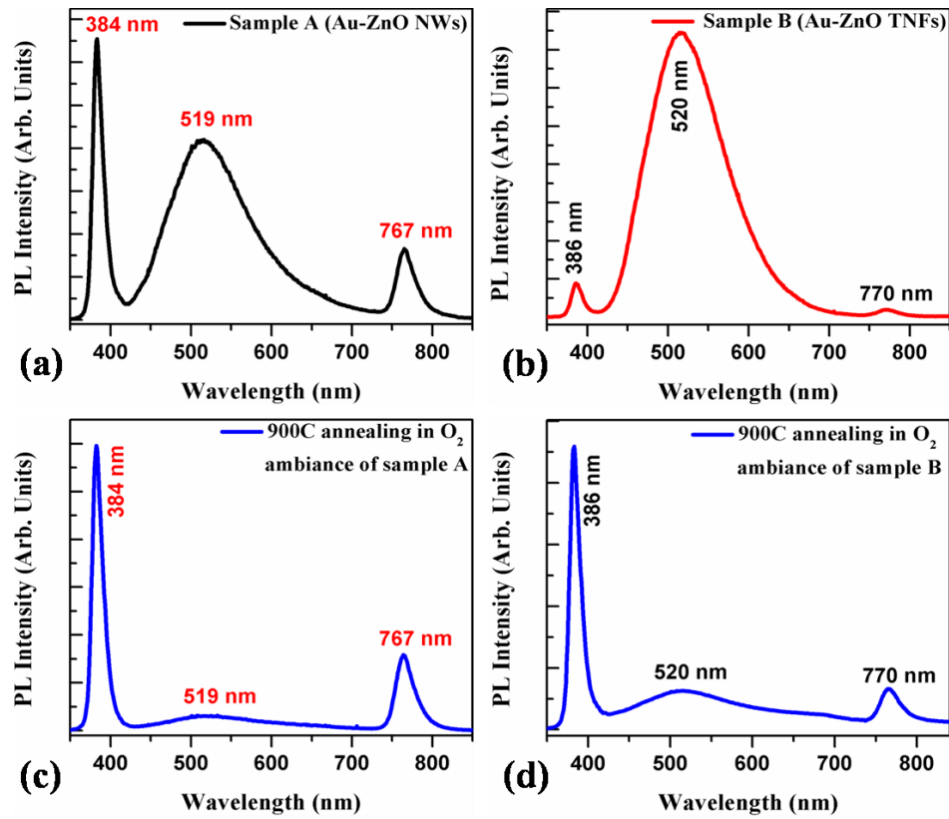


**Figure 5.2:** (a), (b) show the room temperature (300 °K) PL spectra taken from sample A (Au-ZnO NWs) and sample B (Au-ZnO TNFs), respectively. (c), (d) show the PL spectra after annealing in oxygen environment of the corresponding samples at 900 °C for 90 min.

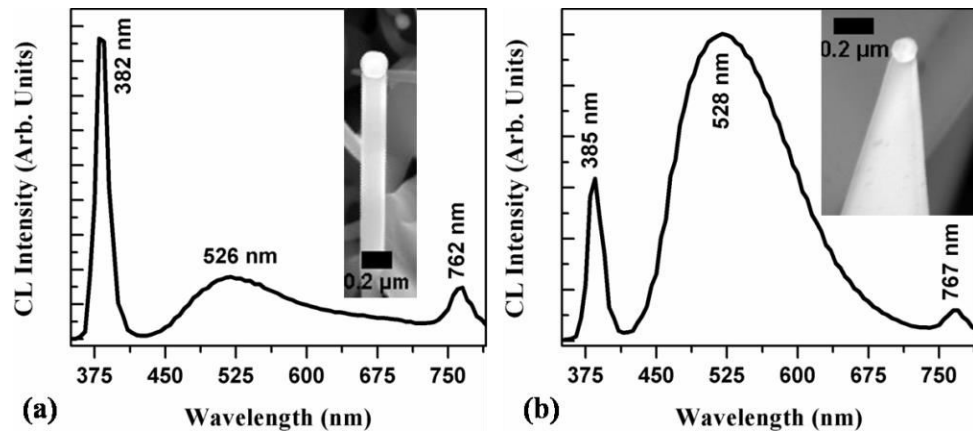


**Figure 5.3:** (a) and (b) show typical room temperature (300 °K) CL spectra taken from the middle portions of the Au-ZnO NW and TNF body shown in the corresponding inset SEM images, respectively.

emission peaks are approximately twice (or half in energy scale) of their corresponding NBE emission peaks, thus they could be attributed to the second-order diffraction of NBE emission [46, 52, 53]. It is also confirmed that luminescence characteristics of individual Au-ZnO HNs

for both the samples (NWs and TNFs) using high spatial resolution CL measurements are similar to that of PL results (Figure 5.3). To shade more light on the oxygen defect related information we have carried out XPS measurements on the same as-grown samples shown in Figures 5.4 (a, b) respectively for samples A and B. XPS results further compliment the PL and CL information, indicate that Au-ZnO TNF sample (sample B) contains more oxygen vacancy related defects compare to NW sample (sample A) [45, 54].

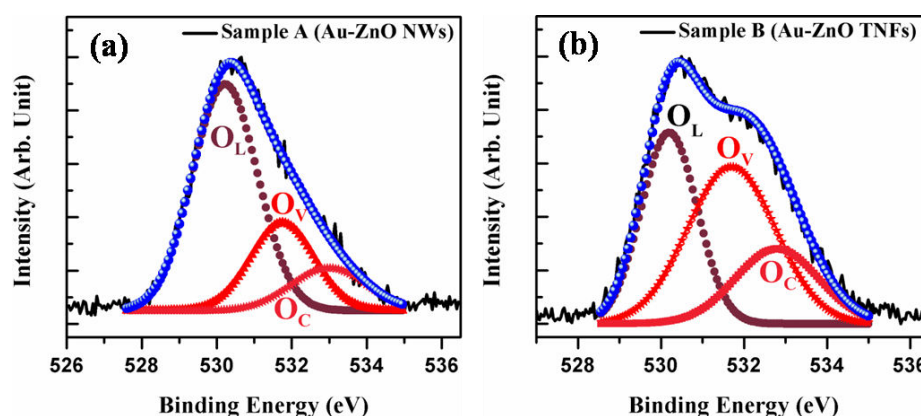


**Figure 5.4:** (a) and (b) show XPS analysis O (1s) spectra of the sample A (NW) and sample B (TNF), respectively, indicating the presence of three types of oxygen,  $O_L$  (lattice oxygen),  $O_V$  (oxygen vacancy or defects) and  $O_C$  (chemisorbed oxygen species).

### 5.3.3 Photo-electrochemical analysis

To evaluate photocatalytic properties of both the samples A and B, the photo-electrochemical measurements were performed under visible light ( $\lambda \geq 400$  nm) irradiation and compared with bulk ZnO powder (B-ZnO) and chemically synthesized ZnO nanostructures (RB-ZnO) [66] as shown in Figure 5.5(a) [45]. The photocurrent response data were collected for both the samples under on-off illumination mode. The sample B shows a very high photocurrent density compare to sample A, RB-ZnO and B-ZnO. It is worthy to point here that the ZnO has wide band gap and it should not show any photo response in visible light in its pure form. Interestingly, the photocurrent response of B-ZnO and RB-ZnO is very low compared to samples A and B suggesting their incapability for absorption of visible lights (Figure 5.5(a)). However, the enhanced photo current response reveals the significant photo absorption capabilities of samples A and B in visible light [45]. There could be two important possible reasons behind this observation; presence of (a) high mid-energy (inside bandgap) oxygen vacancy defect states and (b) visible wavelength plasmonic faceted

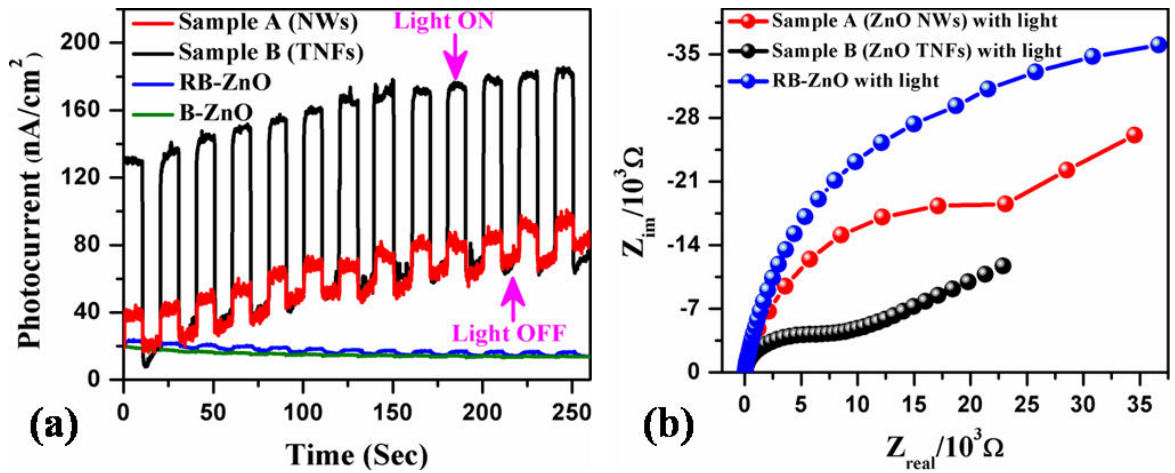


**Figure 5.5:** (a) Photocurrent response of the sample A, sample B along with B-ZnO and RB-ZnO modified ITO electrode under the periodic irradiation of visible light and the (b) Nyquist plots of samples A and B under visible light illumination (Inset is the corresponding equivalent circuit).

Au NPs at each and every tip of the NWs and TNFs [12, 13, 35, 45, 54]. The presence of oxygen vacancy in the two different samples are different, complemented by PL, CL and XPS measurements (vide supra). To support our findings we also have done diffuse-reflectance analysis. Figure 5.6(a) shows that in the visible spectrum (400 nm - 750 nm) both the samples A and B have very broad reflectance minima along with band-edge absorption in the UV regime, which are different from minima ( $\approx 550$  nm with FWHM  $\approx 159$  nm) due to SPR of Au NPs decorated on standard ZnO substrate shown in Figure 5.6(b). So, we can conclude that mid-energy defect states as well as plasmonic Au NPs present in both the samples A and B contribute together to the visible light absorption. It is also important to note that sample B (TNFs) has smaller reflectance compared to sample A (NWs), indicating the presence of more oxygen vacancy defect states in sample B (Figure 5.6(a)). Interestingly, the observed photocurrent density distinguishes their photo response and the sample B shows significantly higher than that of sample A. This can be attributed due to the enhanced transfer of photoexcited electrons from valence band (VB) of ZnO and SPR of Au NPs to the conduction band (CB) of ZnO [44]. As both samples contain almost same density of Au-ZnO HNs (NWs and TNFs), so the difference in their photo response must be coming from the variation of their O vacancy concentrations. To gain deeper insight into the electron transport behaviors in the photoanode, electron transfer process of the samples has been investigated by electrochemical impedance spectroscopy (EIS) study. Figure 5.5(b) shows the Nyquist plots for sample A, sample B and RB-ZnO in presence of visible light. The charge transfer

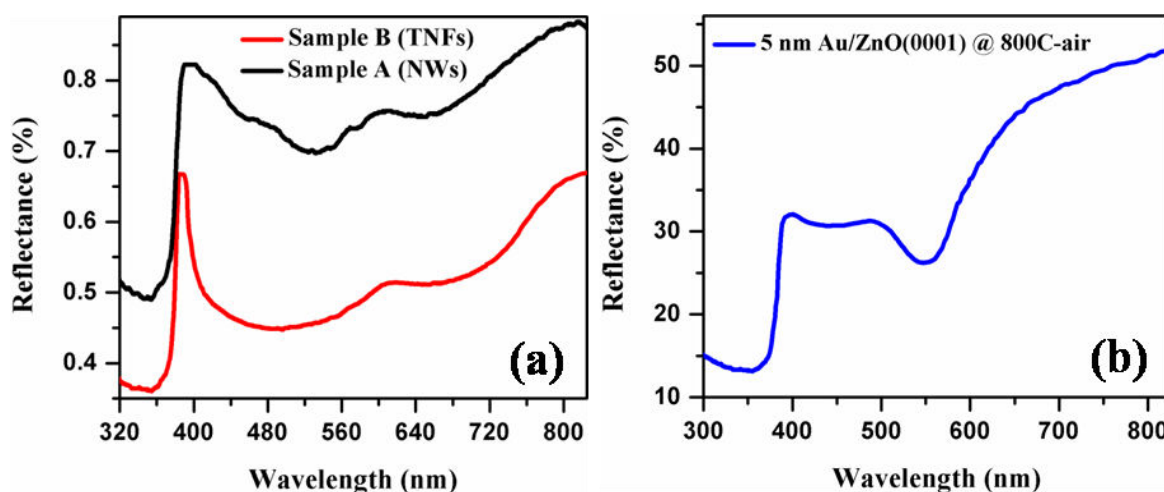


**Figure 5.6:** UV-Vis diffuse-reflectance spectra (DRS) from (a) two as-grown samples A and B and (b) 5 nm Au/ZnO(0001) 800 °C air annealed sample.

resistance ( $R_{ct}$ ) for all three cases is estimated from the diameter of the arc in the Nyquist diagram. The smaller  $R_{ct}$  value represents better charge transfer ability [56, 57]. Therefore, the electrochemical impedance spectral data are fitted using a suitable equivalent circuit diagram to calculate the  $R_{ct}$  values. It denotes that the charge transfer resistance  $R_{ct}$  of sample A ( $\approx 60$  k $\Omega$ ) is almost 10 times higher than the sample B ( $\approx 6.6$  k $\Omega$ ). This can be attributed to the presence of more oxygen vacancies in sample B compare to sample A, which actually facilitating the better electron transfer efficiency on its surfaces leading to better photoresponse performances [14, 45, 56]. In order to support the above conclusion, the EIS measurement was carried out for RB-ZnO shown as blue curve in Figure 5.5(b). It shows much bigger diameter of the arc in the Nyquist diagram suggesting very high  $R_{ct}$  value compared to samples A and B. As the photocurrent response for B-ZnO was negligible (see green curve in Figure 5.5(a)) we have not done EIS measurement for this. It is also important to highlight that the oxygen vacancy is not only one factor for visible light absorption of ZnO nanostructures but the Au nanoparticles (NPs) on every ZnO nanostructures play also a crucial role. As Au NP exhibits a surface plasmon resonance (SPR) band in the visible range about  $\lambda = 520$ -560 nm, upon irradiation of visible light electrons below the Fermi level ( $E_f$ ) will be excited to the surface plasmon (SP) states, leaving positive charges ( $h^+$ ) below  $E_f$ . At the same time  $e^-$  from VB and defect states of ZnO NSs will be excited to CB, and further transferred to the Fermi level of Au, because most of the defect levels and  $E_f$  of ZnO lies below the  $E_f$  of Au [38, 41, 43, 44, 54]. In this case, Au NPs acts as electrons trap sites for the efficient separation of photogenerated  $e^-$  and  $h^+$  pairs to increase the photocurrent, along with oxygen vacancy states.

### 5.3.4 Photocatalytic degradation of rhodamine B and phenol

Inspired by the excellent increased photoelectron transfer performance of as synthesized Au-ZnO HNs (sample A  $\rightarrow$  Au-ZnO NWs/Si(110) and sample B  $\rightarrow$  Au-ZnO TNFs/Si(110)), the photocatalytic degradation of rhodamine B (RhB) and phenol were carried out under visible light irradiation (100 Watt bulb, with irradiance  $10 \text{ mW/cm}^2$  at the sample,  $\lambda \geq 400 \text{ nm}$ ) to evaluate their photocatalytic performance [45]. Experiments showed that no significant degradation occurred in the absence of either photocatalyst (samples) or light, which confirms that degradation of RhB is a photocatalytic effect of Au-ZnO NWs and TNFs (samples A and B). The temporal evolution of absorption spectra of RhB solution after successive irradiation of light with samples A and B are shown in Figure 5.7(a, b) respectively. It was observed that the absorbance maxima of RhB ( $\lambda_{\text{max}} = 554 \text{ nm}$ ) markedly decreased with irradiation time and almost vanished after 180 min of irradiation with sample

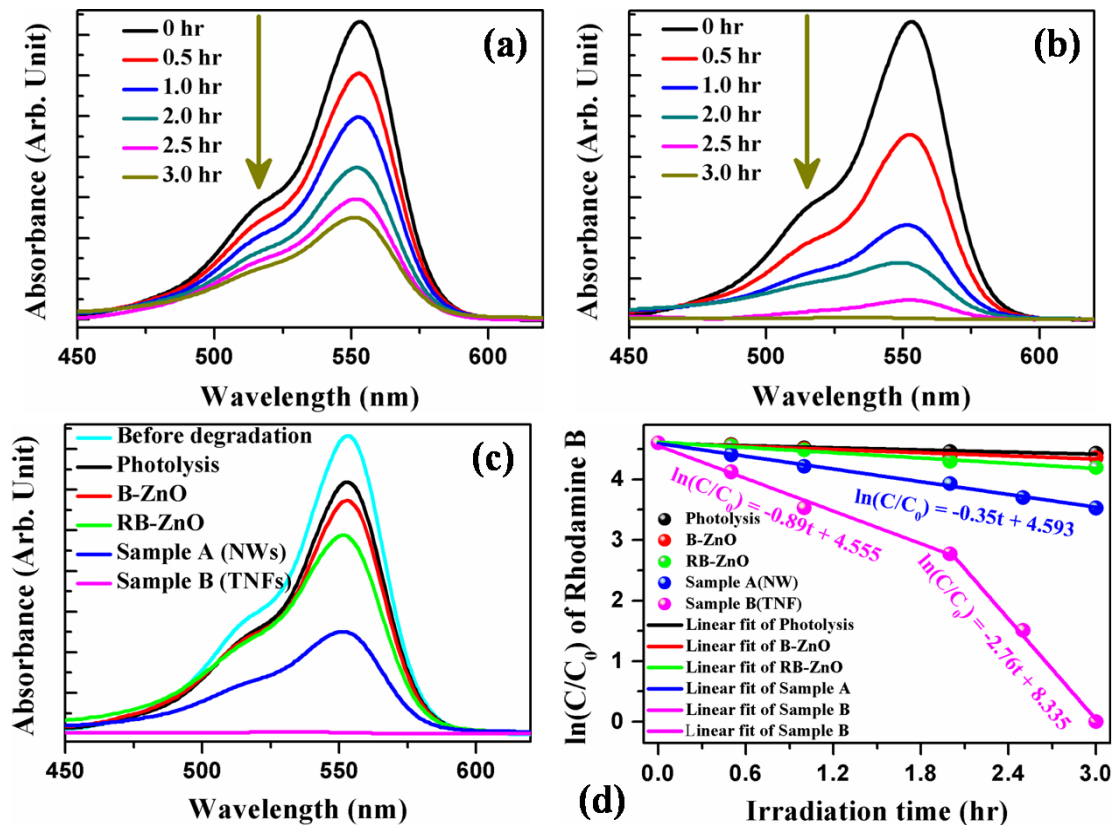


**Figure 5.7:** UV-Vis absorption spectra of 5  $\mu\text{M}$  RhB in presence of (a) sample A and (b) sample B under visible-light irradiation at different time interval, (c) UV-Vis spectra of RhB before and after treatment with Sample A, Sample B, B-ZnO, RB-ZnO and only with light after 3 hrs of irradiation. (d) First order kinetics plots [ $\ln(C/C_0)$  in %] vs irradiation time (t)] of the photocatalytic activities of the photo catalysts for RhB degradation under visible light.



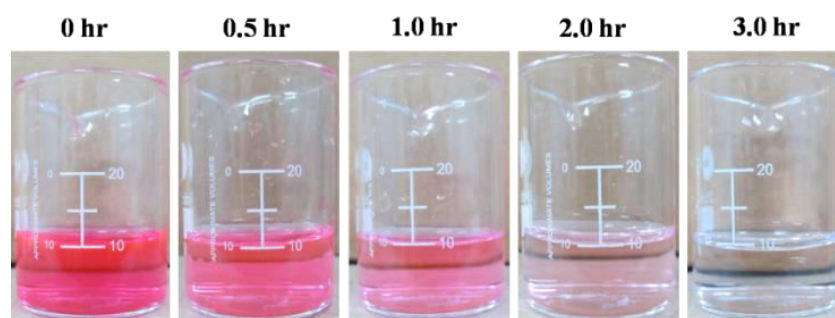


**Figure 5.8:** Temporal evolution of color of RhB aqueous solution with sample B (Au-ZnO TNFs/Si(110)) under visible light illumination.

B (Au-ZnO TNFs Si(110)). The optical photographs of the RhB solution after treatment with sample B at different interval of time were collected and presented in Figure 5.8. It is worthy to emphasize that the photocatalytic decolorization (or mineralization) of RhB is better for sample B. This can be attributed to the presence of high concentration of oxygen vacancy states which enhances or facilitate degradation processes [14, 33, 45, 56]. Further, the photocatalytic performance of B-ZnO and RB-ZnO NSs was checked to authenticate the above fact along with photolysis (without catalyst). Interestingly, these samples show very poor photocatalytic performance compared to sample A and sample B (Figure 5.9). Overall, the RhB degradation performances of all the samples (samples A and B, bulk ZnO powder, RB-ZnO) after 3 hrs of visible light irradiation are shown in Figure 5.7(c). Figure 5.7(d) shows the degradation trends of RhB solution as a function of irradiation time, which clearly shows that Au-ZnO TNFs/Si sample has higher photocatalytic activity compared to sample A, B-ZnO and RB-ZnO samples. Photocatalytic decolorization of low concentration dye followed a pseudo-first-order reaction and its kinetics can be expressed as, [10, 36, 38, 39]

$$\ln(C/C_0) = -kt \quad (5.1)$$

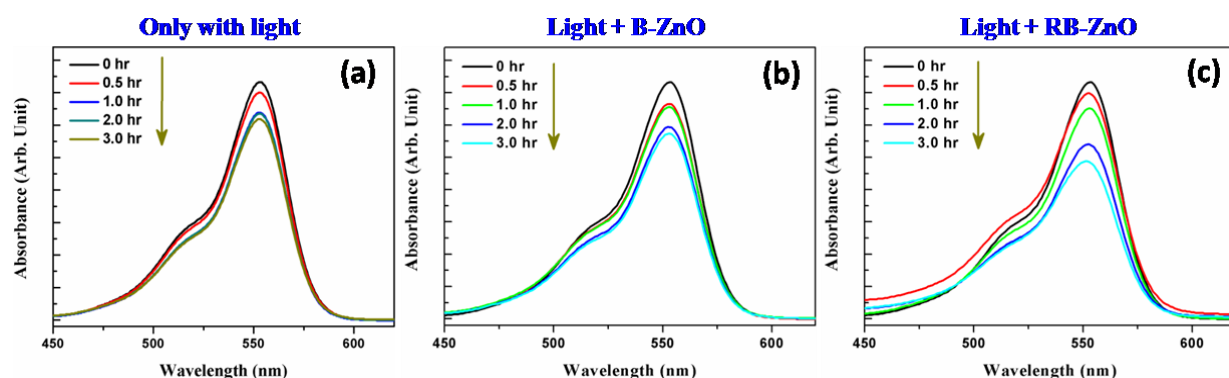


**Figure 5.9:** UV-Vis absorbance spectra of RhB solution under visible light irradiation (a) without catalyst (Photolysis), (b) with B-ZnO and (c) RB-ZnO.

where  $k$  is the apparent rate constant, and  $C_0$  and  $C$  are the initial and after irradiation concentrations of RhB solution respectively. The rate constant ( $k$ ) for RhB degradation were calculated to be  $0.0015 \text{ min}^{-1}$ ,  $0.0024 \text{ min}^{-1}$ ,  $0.0058 \text{ min}^{-1}$  and  $0.0305 \text{ min}^{-1}$  (average of two slopes in two regions 0 – 2 and 2 – 3 hr with  $k$  values 0.015 and  $0.046 \text{ min}^{-1}$ ) respectively for B-ZnO, RB-ZnO, sample A and sample B (see Figure 5.7(d)). Considering average wavelength of the visible light ( $\lambda=550 \text{ nm}$ ) we have calculated the average photonic efficiency ( $\Phi$ ) using the equation;

$$\Phi (\%) = (kC_0V/I_0A) \times 100 \quad (5.2)$$

where,  $I_0$  is the photon flux ( $\text{Einstein sec}^{-1} \text{ cm}^{-2}$ ),  $k$  is the degradation rate constant ( $\text{sec}^{-1}$ ),  $A$  is the illuminated area ( $\text{cm}^2$ ),  $C_0$  is the initial RhB concentration ( $\text{mol L}^{-1}$ ),  $\lambda$  is the average illumination wavelength of the visible light (meter) and  $V$  is the volume of RhB aqueous solution (L) [45, 58]. The average photonic efficiency ( $\Phi$ ) for B-ZnO, RB-ZnO, sample A (NWs) and sample B (TNFs) are calculated to be 0.0054 %, 0.0085 %, 0.021 % and 0.11 % respectively. Thereof sample B (TNFs) over sample A (NWs) appears to be the best photocatalyst among all, towards the degradation of RhB. To verify the enhance photocatalytic properties of the as-grown sample B (TNFs) compare to sample A (NWs), we have further carried out the degradation of standard organic pollutant phenol in aqueous ( $5 \times 10^{-6} \text{ M}$ ) solution under exactly similar experimental conditions (like RhB degradation). We found from the phenol degradation plots, indeed sample B (TNFs) has superior photocatalytic property than sample A (NWs) shown in Figure 5.10. The photocatalytic stability of as-grown samples A and B was also evaluated to check their reusability upon 3 hrs of irradiation

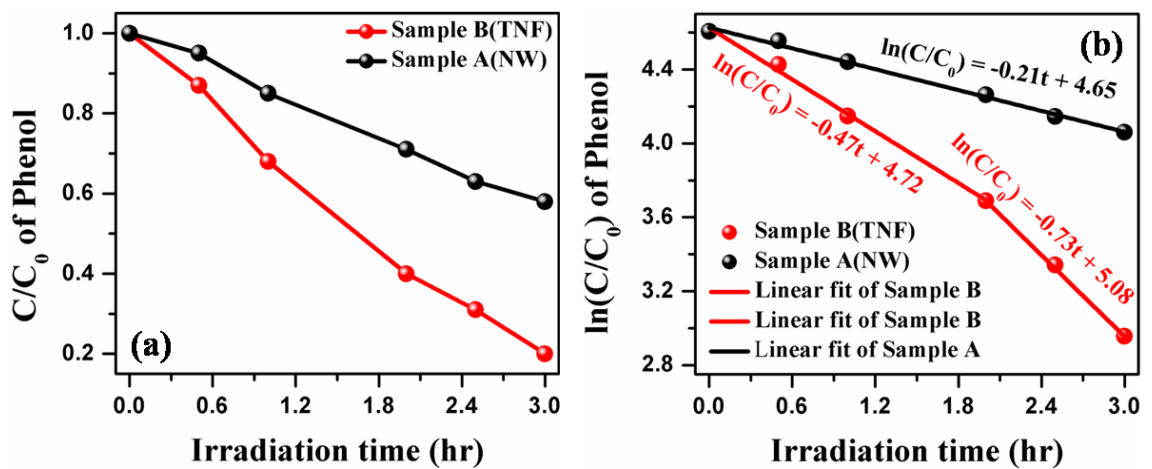


**Figure 5.10:** (a) Photocatalytic activities and (b) first order kinetics plots [ $\ln(C/C_0$  in %) vs irradiation time ( $t$ )] of the as-grown samples A and B for phenol ( $5 \times 10^{-6} \text{ M}$ ) degradation under visible light.

up to 5 consecutive cycles of photo degradation (of only RhB) experiment (Figure 5.11). Interestingly, the dye degradation capabilities for both the samples A and B remain unchanged without any further treatment even after 5 cycles of experiments.

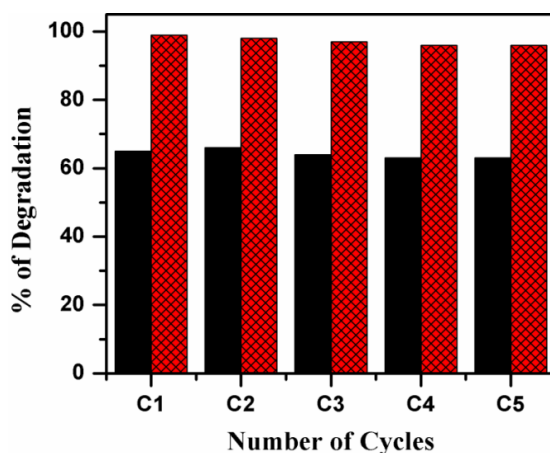


**Figure 5.11:** Five cycles for photo degradation of 5  $\mu\text{M}$  RhB by sample A (black) and sample B (red) under visible light irradiation. For each cycle the duration of visible light exposure is 3 hour.

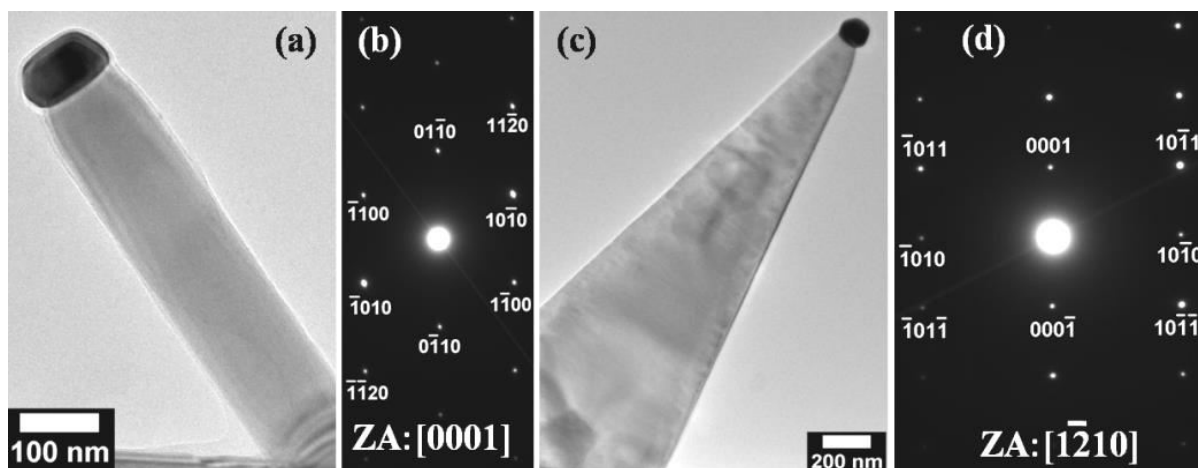


**Figure 5.12:** (a) and (c) Show low-magnification TEM images of single Au-ZnO NW and Au-ZnO TNF respectively, after being used in RhB degradation under visible light for consecutive five cycles. (b) and (d) show SAED patterns taken from panel (a) and (c) respectively.

Further TEM and SAED results from the samples A and B after being used for 5 cycles of degradation performances; indicate good stability and recyclability of the as-grown HNs (Figure 5.12). This signifies the excellent efficiency of present samples for practical applications. The point should be noted here that the present samples will attract better practical photocatalytic applications compared to the available powdered samples (B-ZnO and RB-ZnO powder). The main disadvantage of powder catalysts is the post-recovery tedious processes, which barred their commercialization. So, the advantage for the



photocatalysts grown on the solid substrate is that it can be easily removed from the reaction container, and a simple washing using distilled water will make it ready for further use.

### 5.3.5 Plausible photocatalytic degradation mechanism

The attempt has been made to discuss the plausible reaction mechanism for the photodegradation of RhB over Au nanoparticle capped oxygen deficient Au-ZnO HNs under visible light irradiation. The reaction mechanism involved during the course of photo-assisted degradation of RhB aqueous solution using Au-ZnO HNs as photocatalyst is schematically presented in Figure 5.13 [45]. The photocatalytic activity consists of three competitive processes as follows (1) generation of  $e^-$  and  $h^+$  pairs through absorption of adequate photon energy, (2) charge separation between photogenerated  $e^-$  and  $h^+$  and (3) their promotion to the surface of HNs to produce highly active oxidative species (AOS) through surface redox reactions [59]. These strong non-selective oxidants and photo-induced hole ( $h^+$ ) further reacts with organic dye RhB and degrades into non-toxic products (e.g.,  $CO_2$  and  $H_2O$ ) [38, 59]. Usually, the photocatalytic efficiency is limited by the recombination process of photogenerated charge carriers. Here the oxygen vacancy states and plasmonic metal Au NPs together prolong the lifetime of the  $e^-$  and  $h^+$  pairs by restraining recombination processes and promote the photocatalytic activity [45].

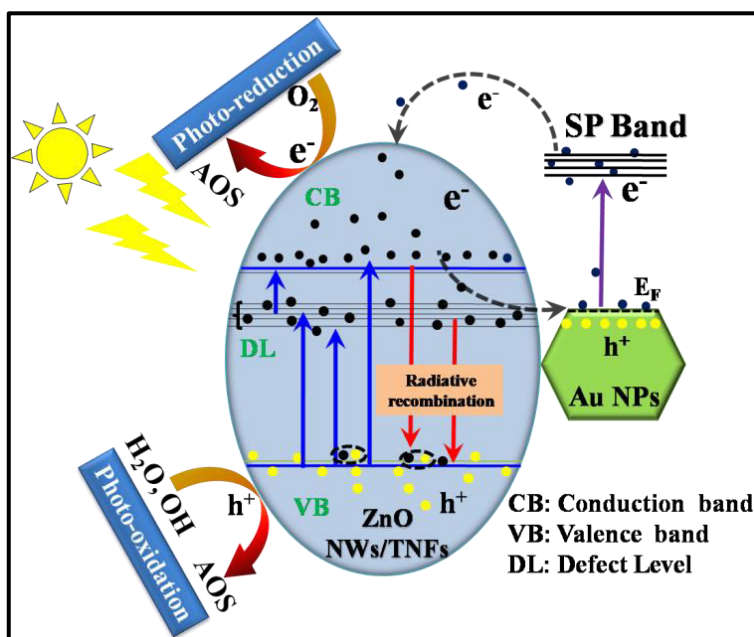


**Figure 5.13:** Schematic representation of the possible mechanism behind the visible light ( $\lambda \geq 400$  nm) photocatalytic activity of as-grown samples towards degradation of rhodamine B.

## 5.4 Summary

In summary, we have demonstrated visible light driven enhanced photocatalytic performances towards the degradation of rhodamine B and phenol, of Au-ZnO HNs grown on single crystalline Si(110) substrates. From the PL, CL and XPS measurements, Au-ZnO TNFs/Si(110) found to have more oxygen related defect states compared to Au-ZnO NWs/Si(110) which perhaps due to  $\approx 8$  times larger average surface area ( $TNF_{ASA}/NW_{ASA} \approx 8$ ). The TNFs sample has shown 10 times less charge-transfer resistance ( $R_{ct}$ ) compared to NWs sample, owing to their higher oxygen related defect states leading to enhancement in visible light induced photo-current densities ( $\approx 4$  times). Following the higher surface defects and less  $R_{ct}$  of sample B (TNFs) compared to sample A (NWs), has delivered better photocatalytic degradation of  $5 \times 10^{-6}$  Molar RhB with average degradation rate constant  $0.0305 \text{ min}^{-1}$  and photonic efficiency 0.11 %, those are  $\approx 5.3$  times higher than sample A ( $0.0058 \text{ min}^{-1}$ , 0.021 %). We have further cross-checked the enhance photocatalytic property of TNFs sample over NWs sample by studying the degradation of standard organic pollutant (phenol). Role of oxygen vacancies in conjunction with the presence of Au NPs at the apex of HNs have been discussed elaborately. Reusability of both the samples up to 5 cycles of operations were checked, showing very good stability and no further treatment is involved before using them in the next cycle. This high photocatalytic property and robustness of the Au-ZnO TNFs sample could endow its use in harnessing visible part of the solar spectrum towards the degradation of organic compounds and microorganisms in water. In the next chapter we will be discussing enhanced field emission properties of those Au-ZnO HNs as an effect of reduction in work function of ZnO HNs due to presence of metal and variable oxygen vacancies in them. We have tried to elucidate underlying physics of such phenomenon in the light of various experiments and first principle density functional calculations.

## 5.5 References

- [1] A. Kolmakov, D. O. Klenov, Y. Lilach and M. Moskovits, *Nano Lett.* **5**, 667 (2005).
- [2] Y. Xie et al., *J. Am. Chem. Soc.* **131**, 6648 (2009).
- [3] M. Fernandez-Garcia et al., *Chem. Rev.* **104**, 4063 (2004).

- [4] D. V. Talapin, J. S. Lee and E. V. Shevchenko, *Chem. Rev.* **110**, 389 (2009).
- [5] Z. Zheng et al., *J. Mater. Chem.* **21**, 9079 (2011).
- [6] M. R. Hoffmann, S. T. Martin and D. W. Bahnemann, *Chem. Rev.* **95**, 69 (1995).
- [7] M. N. Chong, B. Jin, C. W. K. Chow and C. Saint, *Water Res.* **44**, 2997 (2010).
- [8] J. G. Yu, Y. R. Su and B. Cheng, *Adv. Funct. Mater.* **17**, 1984 (2007).
- [9] T. Y. Leung, C. Y. Chan, C. Hu, J. Yu and P. K. Wong, *Water Res.* **42**, 4827 (2008).
- [10] C. W. Kim et al., *RSC Adv.* **2**, 11969 (2012).
- [11] G. Liu, L. Z. Wang, H. G. Yang and G. Q. Lu, *J. Mater. Chem.* **20**, 831 (2010).
- [12] S. A. Ansari, M. M. Khan, S. Kalathil and M. H. Cho, *Nanoscale* **5**, 9238 (2013).
- [13] J. Wang et al., *ACS Appl. Mater. Interfaces* **4**, 4024–4030 (2012).
- [14] N. Daneshvar, D. Salari and A. Khataee, *J. Photochem. Photobiol. A* **162**, 317 (2004).
- [15] S. Sakthivel et al., *Sol. Energy Mater. Sol. Cells* **77**, 65–82 (2003).
- [16] M. Pal, U. Pal, R. S. Gonzalez, E. Mora and P. Santiago, *J. Nano Res.* **5**, 193 (2009).
- [17] J. L. Yang, S. J. An, W. I. Park, G. C. Yi and W. Choi, *Adv. Mater.* **16**, 1661 (2004).
- [18] W. He et al., *J. Am. Chem. Soc.* **136**, 750 (2014).
- [19] W. He et al., *ACS Appl. Mater. Interfaces* **6**, 15527 (2014).
- [20] R. F. Service, *Science* **276**, 895 (1997).
- [21] M. H. Huang, S. Mao, H. Feick, H. Q. Yan, Y. Y. Wu, H. Kind, E. Weber, R. Russo and P. D. Yang, *Science* **292**, 1897 (2001).
- [22] C. J. Lee et al., *Appl. Phys. Lett.* **81**, 3648 (2002).
- [23] Z. L. Wang and J. H. Song, *Science* **312**, 242 (2006).
- [24] Y. Cui, Q. Wei, H. Park and C. M. Lieber, *Science* **293**, 1289 (2001).
- [25] Z. L. Wang, *Mater. Today* **7**, 26 (2004).
- [26] P. X. Gao and Z. L. Wang, *J. Appl. Phys.* **97**, 044304 (2005).

- [27] Z. L. Wang, *J. Phys.: Condens. Matter* **16**, R829 (2004).
- [28] M. Y. Guo et al., *J. Phys. Chem. C* **115**, 11095 (2011).
- [29] J. Becker et al., *J. Phys. Chem. C* **115**, 13844 (2011).
- [30] A. McLaren and S. C. Tsang, *J. Am. Chem. Soc.* **131**, 12540 (2009).
- [31] E. S. Jang, J. H. Won, S. J. Hwang, and J. H. Choy, *Adv. Mater.* **18**, 3309 (2006).
- [32] Z. R. Tian et al., *Nat. Mater.* **2**, 821 (2003).
- [33] Z. Han, L. Liao, Y. Wu, S. Shen and J. Chen, *J. Hazard. Mater.* **217**, 100 (2012).
- [34] J. C. Wang, P. Liu, X. Z. Fu, Z. H. Li and X. X. Wang, *Langmuir* **25**, 1218 (2009).
- [35] Y. Zheng et al., *Inorg. Chem.* **46**, 6675 (2007).
- [36] S. Liu, C. Li, J. Yu and Q. Xiang, *CrystEngComm* **13**, 2533 (2011)
- [37] M. Ahmad et al., *J. Mater. Chem.* **21**, 7723 (2011).
- [38] M. D. L. Ruiz Peralta et al., *ACS Appl. Mater. Interfaces* **4**, 4807 (2012).
- [39] Z. F. Bian, T. Tachikawa and T. Majima, *J. Phys. Chem. C* **116**, 25444 (2012).
- [40] N. Morales-Flores, U. Pal and E. S. Mora, *Appl. Catal., A* **394**, 269–275 (2011).
- [41] X. Lang, X. Chen and J. Zhao, *Chem. Soc. Rev.* **43**, 473 (2014).
- [42] W. L. Ong, S. Natarajan, B. Kloostrab, and G. W. Ho, *Nanoscale*, **5**, 5568 (2013).
- [43] X. Ma, Y. Dai, L. Yu and B. Huang, *ACS Appl. Mater. Interfaces* **6**, 12388 (2014).
- [44] M. Wu et al., *ACS Appl. Mater. Interfaces* **6**, 15052 (2014).
- [45] A. Ghosh, P. Guha, A. K. Samantara, B. K. Jena, R. Bar, S. Ray and P. V. Satyam, *ACS Appl. Mater. Interfaces* **7**, 9486 (2015).
- [46] A. Ghosh, R. R. Juluri, P. Guha, R. Sathyavathi, A. Dash, B. K. Jena and P. V. Satyam, *J. Phys. D: Appl. Phys.* **48**, 055303 (2015).
- [47] Z. Zhu, T. L. Chen, Y. Gu, J. Warren and R. M. Osgood, *Chem. Mater.* **17**, 4227 (2005).
- [48] Y. C. Kong et al., *Appl. Phys. Lett.* **78**, 407 (2001).

- [49] B. Lin, Z. Fu and Y. Jia, *Appl. Phys. Lett.* **79**, 943 (2001).
- [50] K. Vanheusden et al., *J. Appl. Phys.* **79**, 7983 (1996).
- [51] Y. Jiao, H. J. Zhu, M. J. Zhou and Q. Li, *J. Phys. Chem. C* **114**, 208 (2010).
- [52] T. Mahalingam et al., *Nanotechnology* **18**, 035606 (2007).
- [53] Y. G. Wang et al., *J. Cryst. Growth* **259**, 335 (2003).
- [54] A. Leelavathi and N. Ravishankar *Phys. Chem. Chem. Phys.* **15**, 10795 (2013).
- [55] A. K. Samantara, S. C. Sahu and B. K. Jena, *J. Mater. Chem. A* **2**, 12677 (2014).
- [56] W. H. Leng, Z. Zhang and C. N. Cao, *J. Phys. Chem. B* **109**, 15008 (2005).
- [57] N. J. Bell et al., *J. Phys. Chem. C* **115**, 6004 (2011).
- [58] J. Jiang, X. Zhang, P. Sun and L. Zhang, *J. Phys. Chem. C* **115**, 20555 (2011).
- [59] S. Pyne et al., *Spectrochem. Acta Mol. Biomol. Spectros.* **93**, 100 (2012).

# Chapter 6

## **Tuning Work Function of Randomly Oriented ZnO Nanostructures by Capping With Faceted Au Nanostructure and Oxygen Defects: Enhanced Field Emission Experiments and DFT Studies**

### **6.1 Introduction**

In the previous chapter, we have discussed the oxygen vacancy and plasmonic Au nanoparticles (NPs) assisted enhanced photocatalytic applications of the Au-ZnO hetero-nanostructures (HNs) on single crystalline Si(110) substrates under visible-light. Then we have proposed possible mechanism in order to clarify the role of metal Au and oxygen vacancies present in ZnO HNs towards enhanced visible-light photocatalytic effects. In this chapter, focus is made on relating the field emission properties, with experimentally determined local work function variation and comparing with model DFT calculations. We report on the local work function modulation by incorporation of faceted Au NPs on oxygen deficient ZnO HNs. We have shown the enhanced field emission (FE) properties of highly oxygen deficient Au-ZnO triangular nanoflakes (TNFs) with tapered geometry compared to nanowires (Au-ZnO NWs) of uniform diameter and less oxygen defects. DFT calculations following Kelvin probe force microscopy (KPFM) and XPS results, suggested that the enhanced FE properties of Au-ZnO TNFs compared to NWs is probably due to the presence of high oxygen vacancies in the TNFs, which facilitate easy electron tunneling via reduction in ZnO work function. To the best of our knowledge, we report the highest field enhancement factors and lowest turn-on field, in particular for non-aligned ZnO nanostructures.

Cold-cathode electron field emitters are become potentially very useful and attracted for applications in a wide range of field emission (FE) based devices such as high brightness flat-panel displays, electron microscopes, vacuum microwave amplifiers and X-ray sources

[1-4]. In field emission process, electrons emit from material through tunneling under stimulus of a high applied electric field. Among all the path ways of electron emissions, this technique has drawn much attention for its fundamental and technological necessities [5, 6]. Currently micro and nano-fabrication technologies have been developed for fabricating field emission based devices. To meet with this demand, besides carbon-nanotube (CNT) [7, 8] plenty of 1D metal oxide semiconductor nanostructures/hetero-nanostructures (NSs/HNs) of various morphologies have been developed including TiO<sub>2</sub> [9, 10], ZnO [11-16], SnO<sub>2</sub> [17], WO<sub>3</sub> [18] etc. From materials perspective, among all the oxide semiconductors ZnO has been considered one of the most promising material for field emitters owing to its mechanical strength, thermal stability, high oxidation resistivity and low electron affinity [11]. According to the Fowler-Nordheim theory [19], FE characteristics is strongly influenced by two parameters: field enhancement factor ( $\beta$ ) defined by the ratio of local to applied field, that is associated with structures (composition, tip diameter and aspect ratio) and work function ( $\Phi$ ) of emitters. One can improve FE characteristics in two ways: by tailoring the geometry (morphology, tip size and aspect ratio) and/or by reducing work function via electronic structure modification. Plethora of attempts have been made to grow various morphology ZnO NSs and study their effect in the FE performances [12-14, 20-23]. It still remains a challenge to grow NSs with uniform fine tip and high aspect ratio, which are prerequisites for device integration. Alternatively, one can improve FE performances by reducing effective work function  $\Phi_{\text{eff}}$  (i.e., tunneling barrier) via tuning the electronic structure of ZnO NSs [24]. To do so, various ways like, heavy n-type doping [25, 26], decoration/coating of noble metal nanoparticles (like, Au, Ag, Pt) on the ZnO NSs surfaces [16, 17], hydrogen plasma treatment [27], coating them with amorphous carbon and nitride films [28] and annealing in different ambiances [29] have been adopted. In addition recently there is lot of interest on tuning work function of ZnO, which is being done by following ways: (1) via attachment of dipolar self-assembled monolayers perpendicular to the surface of ZnO and/or (2) via hybridization with donor organometallic, organic or inorganic molecule/polymer, which induces charge transfer between the adsorbate molecule and substrate surface [30]. The later approach of tuning work function of ZnO was employed successfully using various molecular layers of organometallic, organic or inorganic molecule/polymer covered on different orientation ZnO surfaces [31, 32]. Modification of  $\Phi$  is taking place via formation of dipoles through the charge transfer processes between the attached molecule and ZnO the, where dipoles can appear either as electron donor or acceptor on the ZnO surface [30-32]. It is also known that, work function can be reduced by creation/generation of oxygen vacancies in the

ZnO NSs. The as-grown ZnO surface can show a high density of bulk and near-surface defects depending on the growth technique, parameters; which can tune  $\Phi$  of ZnO via modification of electronic states [33]. Among the various defects, oxygen vacancies ( $O_v$ ) which act as donor defects [34, 35], are likely to play a major role in the modification of electronic structures for controlling FE performances. In present, oxygen deficient ZnO NSs have attracted with great deal of interest towards the visible light driven photocatalytic applications [36, 37]. Recently, Naik et al. has reported the role of oxygen vacancies in the ZnO nanosheets, on the electronic properties using density functional theory (DFT) and studied their FE properties [38]. However, till date no such report is there where influence on electronic properties due to the presence of metal nanoparticle (NP) and oxygen vacancy together in ZnO NSs and their enhanced FE performances were simultaneously studied.

## 6.2 Experimental

Surface morphology, size and structural characterization of those as-grown samples were done using back-scattered electron (BSE) and secondary electron detectors attached to the field emission gun based scanning electron microscopy (FEG-SEM; Neon 40 cross-beam system). PL measurements were carried with He-Cd laser (325 nm pump line) at room temperature. The XPS measurements were carried out at the base pressure of  $6 \times 10^{-10}$  mbar using a VG Scienta-R3000 hemispherical energy analyzer. Spectra were taken using Mg  $K_\alpha$  ( $h\nu = 1253.6$  eV) radiation as the X-ray source operating at 200 W. Field emission was carried out by a diode configuration in a high vacuum chamber ( $\approx 5 \times 10^{-7}$  mbar) equipped with a high voltage source meter (Keithley, Model 2410) at room temperature. A micro-gauge variable stepper has been employed with anode plate to precisely keep the separation between emitter surfaces to anode plate. A copper plate of tip diameter 2.5 mm (area  $\approx 0.05$  cm<sup>2</sup>) was used as anode and the Au-ZnO HNs grown Si substrates were used as cathode for FE characterizations. For all the measurements anode to cathode separation was kept at  $\approx 100$   $\mu$ m. Henceforth, we will call Au-ZnO NWs/Si(110) as sample A and Au-ZnO TNFs/Si(110) as sample B. Reproducibility of our as-grown samples were checked by doing measurements on different locations of the samples. In order to find local work function of the as-grown samples, which could be very much different from the bulk ZnO as well as variations among these two samples depending on their morphology and oxygen defect densities, the Kelvin probe force microscopy (KPFM) was used. The KPFM of Au-ZnO HNs samples were



examined by ex-situ AFM (MFP-3D, Asylum Research USA) in lift modes, with a lift height of 100 nm, using conductive Pt-coated tips (AC240TM, Electric-Lever, Olympus) having  $\approx$  30 nm radius of curvature. We also have measured the change in contact potential difference ( $V_{CPD}$ ) with the lift height (up to 3  $\mu$ m), which remains unchanged with height.

Theoretical calculations were performed by Vienna Ab initio simulation package (VASP), which is based on density functional theory (DFT) calculation using the plane-wave basis set [39, 40], core electrons were described with the Projector Augmented Wave (PAW) method [41]. The Perdew, Burke and Ernzerhof (PBE) [42] generalized gradient approximation (GGA) was employed for describing the exchange-correlation potentials. The cutoff energy for the plane wave basis states equals to 500 eV is sufficient to achieve a total energy convergence of 5 meV or less. Brillouin zone sampling was made with the Monkhorst Pack scheme and a K-Point grid of  $5 \times 5 \times 1$ . The structures were optimized until force between the neighboring atoms reaches to lower than 0.001 eV/Å. To calculate the work function, we consider the ( $\sqrt{3} \times 6$ ) supercell of ZnO(0001) surface and (2 $\times$ 7) supercell of Au(001). These result in 138 atoms in total, of which 48 atoms are of Zn, 48 atoms are of O and rest 42 atoms are of Au. These supercells were considered, to minimize the lattice mismatch to 3.44%. For the DFT calculations three layers of Au(001) were built on four double-layers (DL) of ZnO(0001) surface. Then Au(001)/ZnO(0001) surface was fully relaxed for further calculations. The last layer of ZnO(0001) surface was fixed during relaxation. A vacuum thickness of more than 13 Å was used in perpendicular direction to the Au/ZnO plane to minimize the spurious interactions with its own periodic image.

## 6.3 Results and discussion

### 6.3.1 Morphological and structural properties

We have employed a simple and effective technique to grow successfully, two different types of Au-ZnO hetero-nanostructures (HNs) on pre-annealed (800 °C in air) 1 nm Au/SiO<sub>2</sub>/Si(110) substrates kept at two different positions in CVD chamber simultaneously (discussed in chapter 3). Detail growth procedures and formation mechanisms are already presented in chapter 3 [36, 43]. Figures 6.1(a, b) show the cross-sectional view of the as-grown samples A (Au-ZnO NWs/Si(110)) and B (Au-ZnO TNFs/Si(110)) respectively; corresponding insets show BSE images (Z-contrast images) of single NW and TNF, where

brighter contrast at the tip corresponds faceted Au NP. Statistical observations from a large number of SEM images yielded: NWs (sample A) are of  $13 \pm 8 \mu\text{m}$  in length and have average diameter  $75 \pm 24 \text{ nm}$ ; tapered TNFs (sample B) are of  $1200 \pm 650 \text{ nm}$  in width at the base to  $64 \pm 26 \text{ nm}$  at the tip and have length is around  $17.5 \pm 13 \mu\text{m}$ . From cross-sectional view SEM images it's quite apparent that both types of Au-ZnO HNs (NWs  $\rightarrow$  sample A and TNFs  $\rightarrow$  sample B) are not perpendicular to the Si substrate, rather they are randomly aligned with respect to substrate normal. Angular distribution histograms of the as-grown non-aligned/randomly aligned HNs are shown in the Figure 6.1(c, d) respectively.

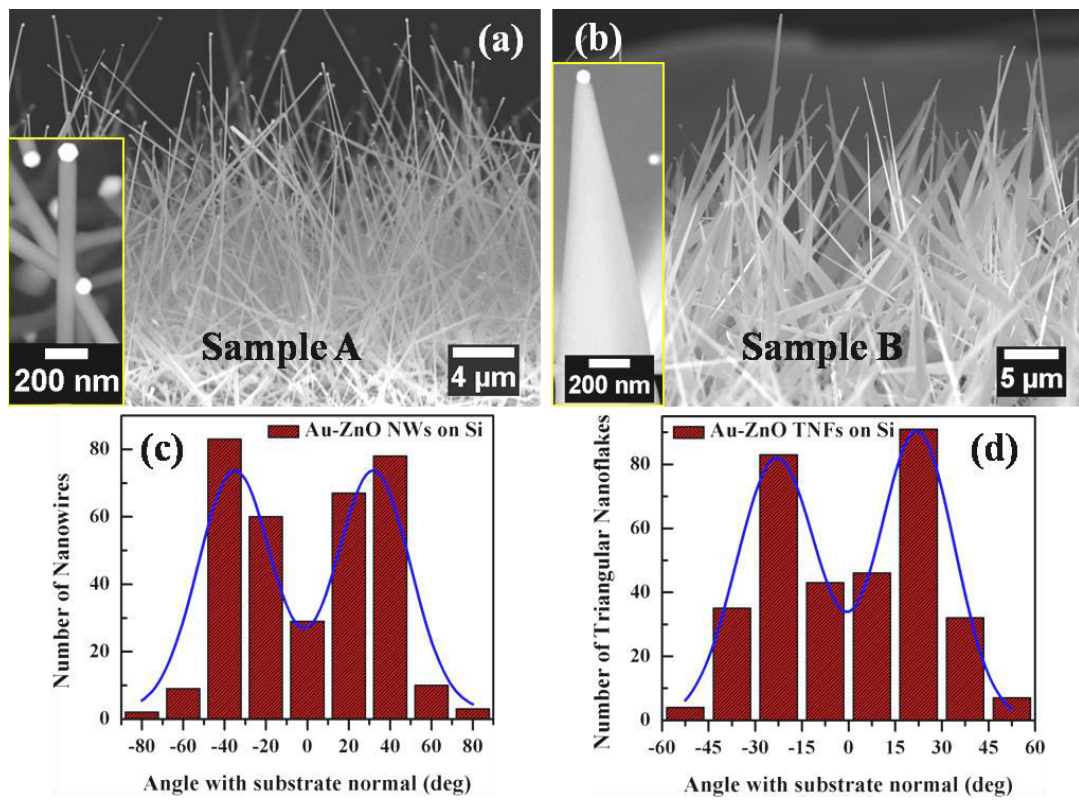


**Figure 6.1:** (a) and (b) show cross-sectional SEM micrographs of the as-grown samples A (Au-ZnO nanowires) and B (Au-ZnO triangular nanoflakes), respectively. Insets of (a) and (b) represent BSE images (Z-contrast images) of individual NW and TNF from the respective samples. (c) and (d) Histograms show the growth misalignment of the as-grown samples A and B with respect to the substrate normal, respectively.

### 6.3.2 Optical properties

The optical quality of the as-grown samples A and B were checked using room temperature photoluminescence (PL) measurements. PL spectra from sample A and sample B are shown

in Figures 6.2(a, b) respectively. PL spectra from sample B (Figure 6.2(b)) clearly shows the much higher intensity of defect related visible emission compared to near band edge (NBE) UV emission, in contrast sample A shows very weak defect induced visible emission compared to NBE emission (Figure 6.2(a)). Origin of these visible emissions is attributed to the oxygen related defects associated with the as-grown Au-ZnO HNs [36, 43]. To probe the oxygen related defects present in the samples A and B we have taken O1s core-level XPS spectra, shown in Figures 6.2(c, d) respectively. Figures 6.2(c, d) indicate that sample B (Au-ZnO TNFs/Si(110)) has much more oxygen vacancies compare to sample A (Au-ZnO NWs/Si(110)), according to the peak intensities corresponding to oxygen vacancy at binding energy of 531.5 eV [44]. So, strong visible emission in PL spectra from sample B (Au-ZnO TNFs) must be originating from the defect states created inside the band gap due to the presence of high oxygen vacancies [24].

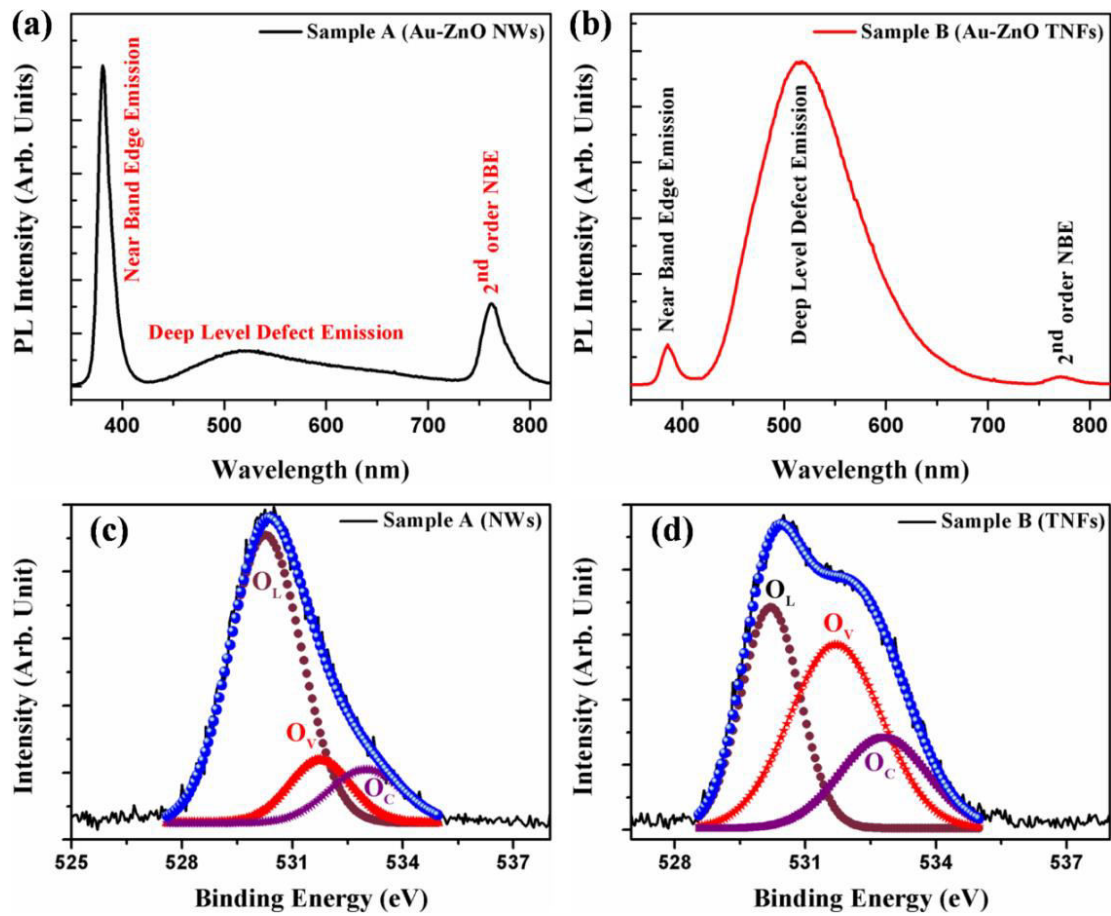


**Figure 6.2:** (a), (b) show room temperature PL spectra taken from sample A (Au-ZnO NWs) and sample B (Au-ZnO TNFs), respectively; (c) and (d) show XPS analysis O (1s) spectra of the sample A and sample B, respectively, indicating the presence of three types of oxygen,  $O_L$  (lattice oxygen),  $O_V$  (oxygen vacancy or defects) and  $O_C$  (chemisorbed oxygen species).

### 6.3.3 Field emission properties

Figure 6.3(a) plots the field emission current density ( $J$ ) of two samples A and B as a function of applied electric field ( $E$ ). Field emission  $J$  versus  $E$  behavior can be analyzed theoretically by using Fowler-Nordheim equation

$$J = (A\beta^2 E^2 / \Phi) \exp(-B \Phi^{3/2} / \beta E) \quad (6.1)$$

$$\text{Or, } \ln(J/E^2) = \ln(A\beta^2 / \Phi) - (B \Phi^{3/2} / \beta) \times (1/E) \quad (6.2)$$

where,  $J$  is FE current density ( $\mu\text{A}/\text{cm}^2$ ),  $E$  is applied electric field ( $\text{V}/\mu\text{m}$ ),  $A$  and  $B$  are constants with  $A = 1.54 \times 10^{-6} \text{ A-eV}/\text{V}^2$  and  $B = 6.83 \times 10^3 \text{ eV}^{3/2} \text{ V}/\mu\text{m}$ ,  $\beta$  is field enhancement factor (FEF) and  $\Phi$  is the work function (eV) of the emitter [46, 47]. Here, we have found turn-on ( $E_{\text{TO}}$ ) and threshold ( $E_{\text{TH}}$ ) fields are respectively to be  $0.86 \text{ V}/\mu\text{m}$  and  $1.3 \text{ V}/\mu\text{m}$  corresponding to sample A (Au-ZnO NWs) and  $0.52 \text{ V}/\mu\text{m}$  and  $1.0 \text{ V}/\mu\text{m}$  corresponding to sample B (Au-ZnO TNFs). Here,  $E_{\text{TO}}$  and  $E_{\text{TH}}$  are defined as the electric fields required to draw current densities of  $0.1 \text{ mA}/\text{cm}^2$  and  $0.9 \text{ mA}/\text{cm}^2$  respectively. The Figure 6.3(b) corresponds to the F-N plots of observed  $J$ - $E$  characteristics, displayed with  $\ln(J/E^2)$  Vs  $(1/E)$ , showing two different slopes in two different field regions. The calculated slope values for samples A and B are  $-3.41$  and  $-0.883$  at high field regimes and  $-0.619$  and  $-0.135$  at low field regimes. Hence, the  $\beta$  values can be figured out from the slopes of the F-N plot by using the equation

$$\beta = -6.83 \times 10^3 \times (\Phi)^{3/2} / \text{slope} \quad (6.3)$$

Origin of these two slopes nature in the F-N plots for ZnO as well as for other semiconductor field emitters have been explained previously by various point of views, such as on the basis

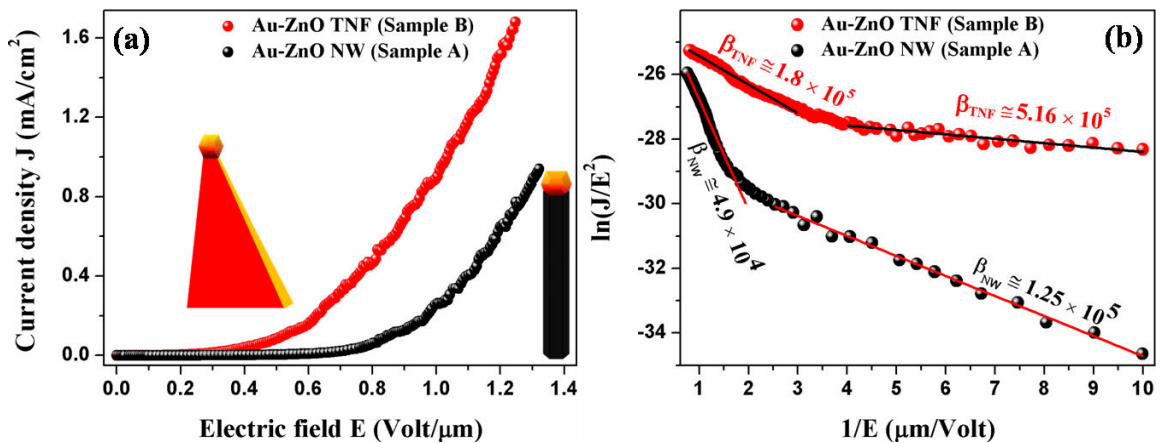


**Figure 6.3:** (a) Field electron emission current density as a function of applied field ( $J$ - $E$ ) curves for the as-grown Au-ZnO nanowires (sample A - black) and Au-ZnO triangular nanoflakes (sample B - red); (b) shows corresponding Fowler-Nordheim (F-N) plots.

of emission from the conduction band (CB) and valence bands (VB), space charge effect, adsorbents or defects in the emitters and local field variation [14, 16, 24, 48-51]. Interestingly, in the present case, larger and smaller slopes have been observed in the higher and lower field regions respectively, which is in agreement with several earlier reports [14, 24, 48, 52]. Following previous reports, we also can explain that the electron emission from both the conduction band (CB) and valence band (VB) lead to this two slope behavior of F-N Plots [14, 48, 49]. So, at the lower applied field values electrons are coming only from the CB but at higher field electrons both from the CB as well as from VB (i.e., 3.37 eV below the CB) contribute to the J Vs E plot. FE results clearly tell that samples A and B both exhibit very good electron tunneling characteristics with significant variations in their turn-on fields ( $E_{TO}$ ) and slopes in the corresponding F-N plots (both high and low field regimes). These differences in the F-N slopes (Figure 6.3(b)) for sample A and sample B eventually mean that they offer different field enhancement factors (FEF), which describe the ability of the specific emitters to intensify the applied field. From equation (6.3) one can understand that FEF is inversely proportional to the slope, so sample B has better electron FE behavior compared to sample A following its smaller slope values and lower  $E_{TO}$ . Sample B contains HNs of tapered geometry (Au-ZnO TNFs) which is favorable for good field emitter from geometrical perspective but FEF ( $\beta$ ) does not depends only on the geometry of the emitters but also average work function ( $\Phi$ ) of the emitter surface. So, we have analyzed average work function of both HNs coated sample surfaces by using Kelvin probe force microscopy (KPFM). In KPFM technique, an AC voltage is applied to the tip to induce an oscillating electrostatic force between the cantilever tip and sample surface. This technique allows to compensate the electrostatic interactions at each scan point on the sample by adjusting an external DC bias ( $V_{DC}$ ) to match the contact potential difference ( $V_{CPD}$ ) between tip and sample [53]. So, we can calculate the work function of the sample surface by knowing  $V_{DC}$  using the following equation

$$V_{DC} = V_{CPD} = (\Phi_{\text{sample}} - \Phi_{\text{tip}})/e \quad (6.4)$$

where  $\Phi_{\text{sample}}$  and  $\Phi_{\text{tip}}$  are the work functions of the sample and tip, respectively [53]. We have calibrated the tip work function ( $\Phi_{\text{tip}}$ ) with respect to a standard Au surface (taking  $\Phi_{\text{Au}} = 5.1$  eV). Using the above equation (6.4) the calculated work function values for samples A and B are determined to be  $5.04 \pm 0.05$  eV and  $4.7 \pm 0.1$  eV respectively, as shown in Figure 6.4. As we have already discussed the reason behind two slope nature in F-N plot, therefore the effective work functions for samples A and B will be  $\Phi = 5.04$  eV and 4.7 eV at lower field and  $\Phi_{\text{eff}} = \Phi + E_g = 8.41$  eV and 8.07 eV at higher field. Likewise  $\beta$  values are

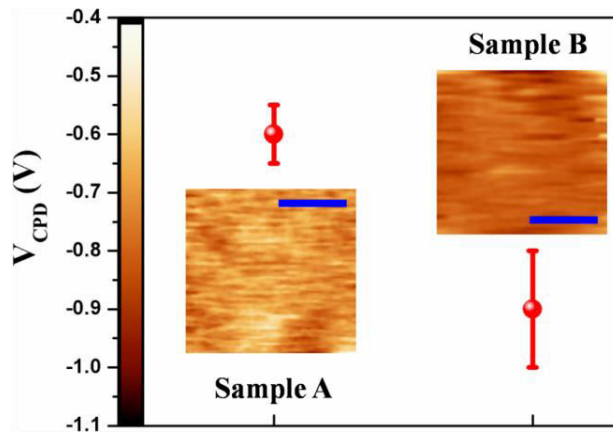


**Figure 6.4:** Shows work function mapping of samples A and B using Kelvin probe force microscopy (KPFM). Insets are the KPFM images of the corresponding samples. Both the scale bars in the images correspond to  $4\ \mu\text{m}$ .

calculated to be  $1.25 \times 10^5$  and  $4.9 \times 10^4$  for sample A and  $5.16 \times 10^5$  and  $1.8 \times 10^5$  for sample B, in the lower and higher field regions, respectively [24]. The robustness in terms of stability of emission current density ( $J$ ) as a function of time is very crucial for cold cathodes in practical FE based device applications. The FE stability of the samples A and B have been investigated over a period of 4 hrs at the applied field of  $1\ \text{V}/\mu\text{m}$ , shown in Figure 6.5. Fluctuations in  $J$  were found to be  $< 7\%$  and  $< 1\%$  of the average current values of  $0.25\ \text{mA}/\text{cm}^2$  and  $0.9\ \text{mA}/\text{cm}^2$ , for samples A and B respectively, corroborate high emission stability of both the samples [24]. A post FE operation SEM study reveals no conformational change of the emitter emphasizing that our as-grown Au-ZnO HNs have excellent structural stability against high electric fields [54]. The recent survey confirms that observed FE behavior of the sample B (TNFs) with respect to its  $E_{\text{TO}}$ ,  $\beta$  and stability in  $J$ , is significantly better than the representative results from other types of ZnO NSs reported so far, as summarized in Table 6.1. Owing to the low  $E_{\text{TO}}$ , high  $\beta$  and robust nature in terms of

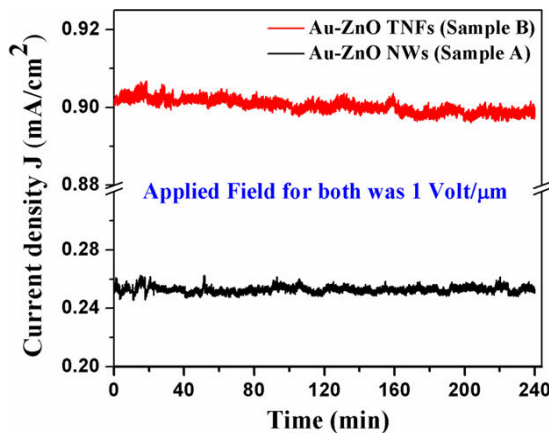


**Figure 6.5:** Field emission current stability of the as-grown Au-ZnO hetero-nanostructures array (samples A and B) versus time indicating fairly stable emission current over a large period (4 hrs) of time.



emission and structural stability, these emitters can be utilized for new generation vacuum micro-/nano-electronics applications [13, 14]. It is evident from the results that sample B

**Table 6.1:** Representative results on field emission performances of various ZnO nanostructures with and without Au.

Emitter	Turn-on field (V- $\mu\text{m}^{-1}$ ) for specific emission current density	Field enhancement factor ( $\beta$ )	Emission stability: Current density, duration and fluctuation	Ref .
Au decorated ZnO Nanopillars	2.65 for 10 $\mu\text{A}/\text{cm}^2$	3313	370 $\mu\text{A}/\text{cm}^2$ , 1 hr, $6 \pm 2\%$	16
ZnO Nanosheets arrays	2.4 for 0.1 $\mu\text{A}/\text{cm}^2$	5812	1 $\mu\text{A}$ , 3 hrs	38
ZnO Nanostructures	1.17 for 10 $\mu\text{A}$	23133	24 $\mu\text{A}$ , 160 min, $> 10\%$	48
ZnO Nanobelts	2.9 for 1 $\text{mA}/\text{cm}^2$	$1.4 \times 10^4$	-----	55
Pencil-like ZnO Nanowires	3.82 for 10 $\mu\text{A}/\text{cm}^2$	2303	-----	56
Tailored ZnO Nanorod/ Nanowire Arrays	1.8 for 0.1 $\mu\text{A}/\text{cm}^2$	5 750	-----	57
In-doped ZnO nanochips	2.5 for 0.01 $\text{mA}/\text{cm}^2$	$10640 \pm 3$	0.23 $\text{mA}/\text{cm}^2$ , 25 hrs, 4 %	58
ZnO Nanoneedles	0.85 for 0.1 $\mu\text{A}/\text{cm}^2$	8328	-----	59
Au catalyzed ZnO Nanowires	0.92 for 13.0 $\mu\text{A}/\text{cm}^2$	$4.7 \times 10^3$	-----	60
ZnO arrays	4.4 for 4 $\mu\text{A}/\text{cm}^2$	Two region emission: High field region $\beta \approx 296$ and Low field region $\beta \approx 1339$	-----	22
Au-ZnO NW (sample A)	0.86 for 0.1 $\text{mA}/\text{cm}^2$	Two region emission: High field region $\beta \approx 4.9 \times 10^4$ and Low field region $\beta \approx 1.25 \times 10^5$	0.25 $\text{mA}/\text{cm}^2$ , 4 hrs, $< 7\%$	24
Au-ZnO TNF (sample B)	0.52 for 0.1 $\text{mA}/\text{cm}^2$	Two region emission: High field region $\beta \approx 1.8 \times 10^5$ and Low field region $\beta \approx 5.16 \times 10^5$	0.90 $\text{mA}/\text{cm}^2$ , 4 hrs, $< 1\%$	24

(TNFs) exhibits better field emission property than sample A (NWs), with a lowest  $E_{TO}$  value of  $0.52 \text{ V}/\mu\text{m}$  and  $\approx 4$  times higher field enhancement factor ( $\beta$ ). It is now paramount to emphasize that both the HNs (NWs and TNFs) contain faceted Au NP at their tips, which definitely influence overall FE property through charge (electron) transfer from Au to CB of ZnO, modifying electronic band structure to equilibrate the Fermi levels [15, 16, 25, 61]. First of all it is known that work function of Au ( $\Phi_{Au} = 5.1 \text{ eV}$ ) is higher than that of intrinsic ZnO ( $\Phi_{ZnO} = 5.2 \text{ to } 5.3 \text{ eV}$ ) with respect to vacuum level [16, 61]. So, electron transfer from Au NP to ZnO surface will be directed by the contact electric field, which is generated due to the difference in Fermi level positions in Au and ZnO [15, 16, 61, 62]. These transported electrons will be gathered at the interface of Au and ZnO, causing devaluation of ZnO work function via downward band bending on the ZnO side [61], which in turn improve the FE characteristics [15, 16, 62]. Since Au NPs are present in both the samples, better FE characteristics offered by sample B (TNFs) compared to sample A is not coming from the influence of Au, for sure. However, the combined effect of special tapered geometry confirmed from electron microscopy and lowering of work function due to the presence of more oxygen vacancies probed by XPS in sample B could lead to this enhanced FE characteristics [12, 16, 38, 45, 51, 63]. To understand the exact influence of  $O_{vac}$  on enhanced FE performance of sample B (Au-ZnO TNFs), we have studied the FE behavior of sample B after changing  $O_{vac}$  concentration by annealing in oxygen ambience at  $900^\circ\text{C}$  for 60 min and 90 min. From Figure 6.6(a) it is found that after annealing in oxygen ambiances,  $O_{vac}$  related defect emission (centered  $\approx 520 \text{ nm}$ ) has been decreased significantly compared to as-grown sample B (Figure 6.2(b)). It is also observed that intensity of the defect emission is decreasing with increasing annealing time, with lowest intensity achieved for 90 min of annealing. We have now two Au-ZnO TNFs samples (60 and 90 min annealed) with different  $O_{vac}$  concentrations but much less compared to as-grown Au-ZnO TNFs sample (sample B). At the same time it is interesting to emphasize that the intensity ratio of near band edge emission  $I_{NBE}$  (centered  $\approx 386 \text{ nm}$ ) to defect emission  $I_{DE}$  (centered  $\approx 520 \text{ nm}$ ) of 90 min oxygen annealed sample B is almost similar to that of as-grown sample A (see Figure 6.2(a) and Figure 6.6(a)). Then we have performed FE measurements with these two 60 min and 90 min oxygen annealed samples and compared with FE results obtained from as-grown samples A and B, to deduce the effect of  $O_{vac}$  concentrations on FE behavior. Figure 6.6(b) and its inset represent the FE and F-N behavior from the corresponding samples. Table 6.2 depicts comparative FE properties of these two 60 min and 90 min annealed samples along with pristine as-grown samples B and A. From Table 6.2 it is visible that FE performance of



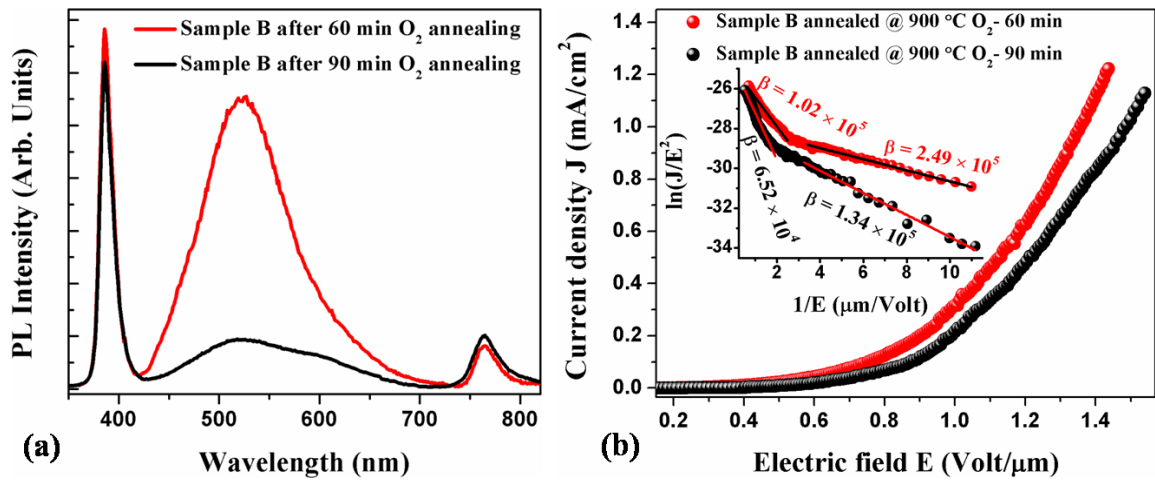


**Figure 6.6:** (a) Presents typical room temperature PL spectra taken from sample B (Au-ZnO TNFs) after 60 min and 90 min annealing at 900 °C in oxygen ambiances, showing decrease in defect emission related to oxygen vacancy. (b) Shows field emission characteristics of the annealed samples. F-N plots of the corresponding samples are shown in the inset.

sample B (Au-ZnO TNFs) in terms of turn-on field ( $E_{TO}$ ) and field enhancement factor (FEF) is getting deteriorated with decreasing  $O_{vac}$  concentration upon annealing in oxygen ambiances and 90 min annealed sample B becomes comparable with as-grown sample A.

**Table 6.2:** FE properties of as-grown sample A, sample B and sample B after annealing in oxygen ambiances for 60 min and 90 min

Emitter	Turn-on field ( $V\cdot\mu m^{-1}$ ) for specific emission current density	Field enhancement factor ( $\beta$ )
As-grown sample B (Au-ZnO TNFs)	0.52 for $0.1 mA/cm^2$	High field region $\beta \approx 1.8 \times 10^5$ and Low field region $\beta \approx 5.16 \times 10^5$
Sample B after annealed in oxygen for 60 min	0.75 for $0.1 mA/cm^2$	High field region $\beta \approx 1.02 \times 10^5$ and Low field region $\beta \approx 2.49 \times 10^5$
Sample B after annealed in oxygen for 90 min	0.84 for $0.1 mA/cm^2$	High field region $\beta \approx 6.52 \times 10^4$ and Low field region $\beta \approx 1.34 \times 10^5$
As-grown sample A (Au-ZnO NWs)	0.86 for $0.1 mA/cm^2$	High field region $\beta \approx 4.90 \times 10^4$ and Low field region $\beta \approx 1.25 \times 10^5$

From these observations we now can conclude that enhanced FE behavior shown by sample B compared to sample A is primarily due to the presence of higher  $O_{vac}$  in TNFs. Nevertheless, FE characterises of sample B, even after 90 min of annealing in oxygen ambience is slightly better than that of sample A as seen from the Table 6.2, despite the fact

that  $I_{\text{NBE}}/I_{\text{DE}}$  in PL for these two samples are almost similar. This confirms that morphology variation has influence on the FE property but not significant for our cases.

It has already been reported that presence of oxygen vacancies in ZnO can improve the FE characteristics via lowering tunneling barrier i.e., reducing work function by shifting Fermi level towards vacuum [38]. To understand the underlying reason of such enhanced FE behavior delivered by oxygen deficient Au-ZnO HNs, we have studied the influence of Au (metal) along with oxygen vacancy in the ZnO NSs on the modulation of work function, using first principle density functional theory (DFT). In the next section we have systematically described how pinning of work function further can take place due to presence of Au in the ZnO NSs with oxygen vacancy.

### 6.3.4 DFT results

Here, we discuss about the density functional theory (DFT) based studies to find the work function ( $\Phi$ ) of mainly four different surfaces: with and without oxygen vacancies ( $\text{O}_{\text{vac}}$ ) in 4 DL of ZnO, 0001 surface, named as ZnO(0001) and  $\text{O}_{\text{vac}}$ -ZnO(0001) respectively and Au(001) on top of previous two surfaces named as Au(001)/ZnO(0001) and Au(001)/ $\text{O}_{\text{vac}}$ -ZnO(0001). In our calculations with oxygen vacancy, one O atom has been removed out of 48 atoms from arbitrary lattice site, so the calculations have been done with an oxygen vacancy of 2.08%. The relaxed structures considered for the DFT calculations are shown in Figure 6.7. The deep valence band of ZnO is mainly dominated by the O 2s orbital, whereas, shallow valence band is composed of Zn 3d, 4s orbitals with major contribution from O 2p orbital [64]. The conduction band lower part is composed of Zn 4s, 4p and O 2p. So, in both the bands of ZnO there is hybridization between the orbitals [65]. The Zn–O bond is partially ionic with covalent character due to the hybridization of O 2p and Zn 3d states. Now as a result of oxygen vacancies in the ZnO, four Zn atoms (neighbor of  $\text{O}_{\text{vac}}$  site) have less positive charge estimated using the bader charge analysis. So some amount of d electrons are unshared and retain in the vicinity of Zn atoms, which will deploy Zn 3d states towards the conduction band, attributing to formation of donor states known to be impurity/defect states inside the bandgap. We have observed the stretching of bond distances between Zn atoms with other O atoms after deoxygenating these surfaces (as seen from the images of relaxed structures in Figures 6.7(b, d)). Consequently, metal cluster of the unsaturated Zn atoms are trying to form (interaction increases) in the place of point defect due to vacancy,

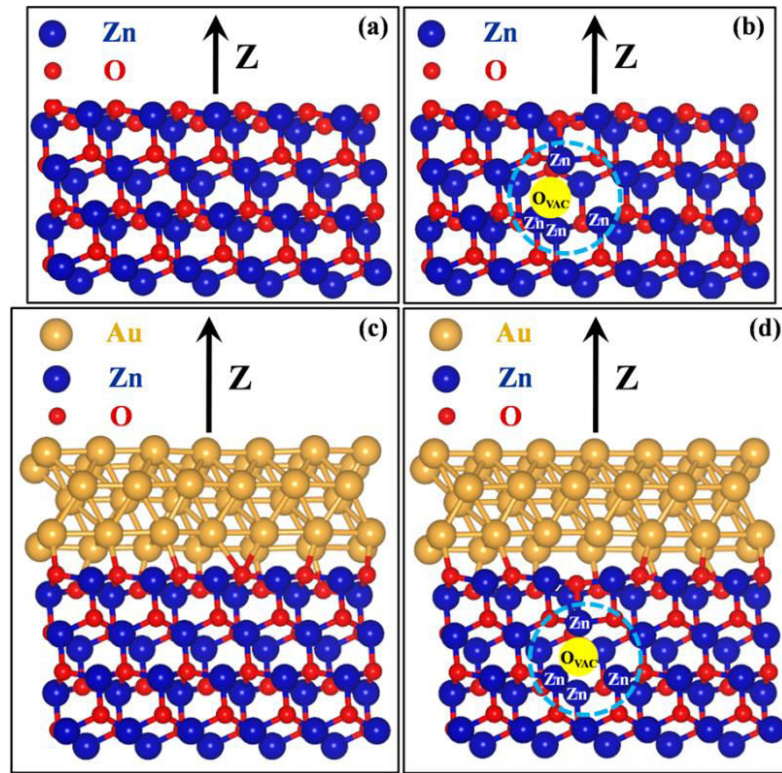


**Figure 6.7:** (a)–(d) present the relaxed structures considered for DFT calculations (VASP) of ZnO(0001),  $O_{vac}$ -ZnO(0001), Au(001)/ZnO(0001) and Au(001)/ $O_{vac}$ -ZnO(0001), respectively.

which lead to an increase in electron density around that vacancy site. These unshared d electrons induce shifting of Fermi level towards the vacuum, which lead to reduction in ZnO work function.

It is more interesting when Au (metal) is present on the ZnO surface along with  $O_{vac}$ . The Au atoms interact strongly with the surface O atoms of ZnO surface. This leads to the hybridization of Au 5d and O 2p orbitals, stimulates charge transfer from Au to O atom and further reduces work function of ZnO on top of the effect of  $O_{vac}$ . Figure 6.8 demonstrates the estimated work function of four different structures from DFT calculations. The difference between potential energy of one electron between Fermi level ( $E_F$ ) and vacuum level ( $E_V$ ) is defined as the work function ( $\Phi$ ). Figures 6.8(a and b) demonstrate the electrostatic potential as a function of interlayer separation along Z-direction for ZnO and  $O_{vac}$ -ZnO surfaces respectively. The estimated  $\Phi$  is about 4.91 eV for  $O_{vac}$ -ZnO(0001) surface, which is about 0.07 eV lesser than pure ZnO(0001) surface ( $\Phi = 4.98$  eV) [38], whereas the  $\Phi$  for Au(001)/ZnO(0001) and Au(001)/ $O_{vac}$ -ZnO(0001) are about 4.17 eV and 3.91 eV (Figures 6.8(c and d)) respectively [24]. This indicates that the barrier height for the tunneling electron is further decreased by 0.26 eV due to the presence of oxygen vacancy in the case of

Au(001)/O<sub>vac</sub>-ZnO(0001) surface, compared to without O<sub>vac</sub> case (i.e., Au(001)/ZnO(0001)). So, here we are getting following trend in the  $\Phi$ , viz.,  $\Phi_{\text{ZnO}} > \Phi_{\text{O}_{\text{vac}}\text{-ZnO}} > \Phi_{\text{Au/ZnO}} > \Phi_{\text{Au/O}_{\text{vac}}\text{-ZnO}}$  [24]. These DFT results qualitatively supports our experimental findings, where sample B (Au-ZnO TNFs) with more oxygen vacancies shows lower  $\Phi$  than sample A (Au-ZnO NWs). In conclusion, apart from the geometrical enhancement factor, presence of O<sub>vac</sub> in metal NPs capped ZnO NSs additionally increase emission current via reduction in tunneling barrier  $\Phi$ , leading to an excellent field emission (FE) characteristics [24].

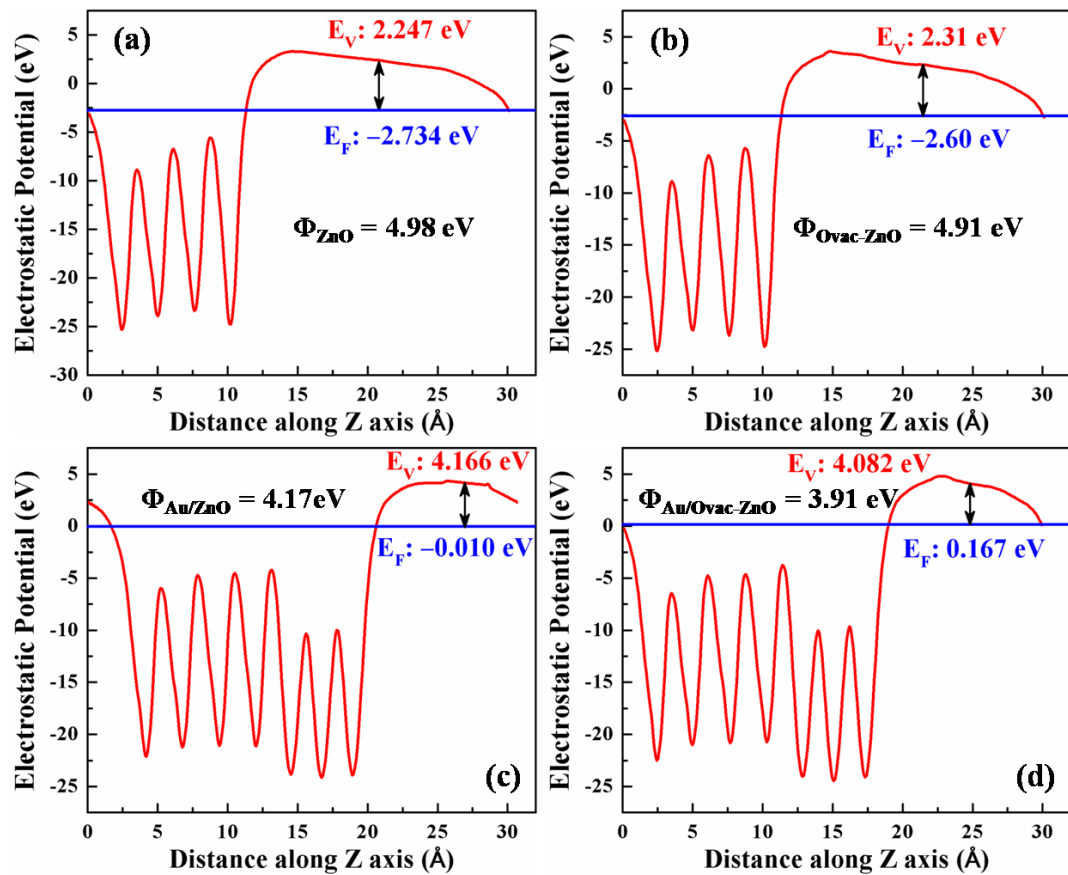


**Figure 6.8:** Electrostatic potential along z-axis considering vacuum as reference energy for (a) ZnO(0001) (b) O<sub>vac</sub>-ZnO(0001) (c) Au(001)/ZnO(0001) and (d) Au(001)/O<sub>vac</sub>-ZnO(0001).  $E_F$  and  $E_V$  correspond to energy of the Fermi and vacuum level, respectively.  $\Phi$  denotes the work function of the defined surface.

## 6.4 Summary

In summary, we report the local work function ( $\Phi$ ) modulation of ZnO HNs by the combined effect of metal Au NPs at the tip and varying oxygen vacancies (O<sub>vac</sub>) in them,

probed by experiments and also qualitatively supported by DFT calculations. We have investigated the FE properties of non-aligned/randomly oriented Au-ZnO HNs having two different morphologies and oxygen defect densities. Here we have found TNFs with tapered geometry and more  $O_{vac}$  exhibits enhanced FE performances with lower turn-on field and  $\approx 4$  times higher field enhancement factor  $\beta \approx 5.16 \times 10^5$  compared to NWs with less  $O_{vac}$ . Using KPFM technique we have probed local  $\Phi$  of TNFs sample with high  $O_{vac}$  is found out to be  $4.7 \pm 0.1$  eV, which is  $\approx 0.34$  eV less in comparison with NWs sample. DFT calculations suggested that Au-ZnO HNs with oxygen vacancies will have lower effective  $\Phi$  (tunneling barrier) because of excess unshared d-electrons of Zn atoms (nearest of O vacancy site) and charge transfer induced electronic band structure modification, which lead to increase in electron donating capability i.e., improvement in field emission behavior. Therefore, we can conclude that Au-ZnO HNs with higher  $O_{vac}$ , must show better FE characteristics. Excellent FE properties including very high  $\beta$ , low turn-on field of 0.52 Volt/ $\mu\text{m}$  and emission stability for 4 hrs (at current density of 0.9 mA/cm<sup>2</sup>), offered by high oxygen deficient Au-ZnO TNFs sample could be useful for FE based device applications. In the next chapter, we will cogitate on Au catalyzed growth of Au-GeO<sub>2</sub> nanowires with various dimension and oxygen defects, on 5 nm Au/GeO<sub>x</sub>/Ge(100) in various ambiances without external supply of growth species, followed by visible-light photodetection application.

## 6.5 References

- [1] I. Brodie and C. A. Spindt, *Adv. Electron. Electron Phys.* **83**, 1 (1992).
- [2] C. Hernandez-Garcia, M. L. Stutzman and P. G. O'Shea, *Phys. Today* **61**, 44 (2008).
- [3] Q. H. Wang et al., *Appl. Phys. Lett.* **72**, 2912 (1998).
- [4] L. Wei et al., *IEEE Electron Device Lett.* **29**, 452 (2008).
- [5] E. L. Murphy and R. H. Good Jr., *Phys. Rev.* **102**, 1464 (1956).
- [6] J. M. Bonard et al., *Appl. Phys. A Mater. Sci. Process.* **69**, 245 (1999).
- [7] W. A. de Heer, A. Chatelain and D. Ugarte, *Science* **270**, 1179 (1995).
- [8] Y. Saito and S. Uemura, *Carbon* **38**, 169 (2000).
- [9] B. Xiang et al., *J. Phys. D. Appl. Phys.* **38**, 1152 (2005).

- [10] J. Liang and G. Zhang, *ACS Appl. Mater. Interfaces* **4**, 6053 (2012).
- [11] Z. Zhang et al., *Sci. Rep.* **4**, 4676 (2014).
- [12] Q. Zhao et al., *Appl. Phys. Lett.* **86**, 203115 (2005).
- [13] C. J. Lee et al., *Appl. Phys. Lett.* **81**, 3648 (2002).
- [14] T. Premkumar, Y. S. Zhou and K. Baskar, *ACS Appl. Mater. Interfaces* **2**, 2863 (2010).
- [15] C. Ye, Y. Bando, X. Fang, G. Shen and D. Golberg, *J. Phys. Chem. C* **111**, 12673 (2007).
- [16] Y. M. Chang et al., *ACS Appl. Mater. Interfaces* **4**, 6676 (2012).
- [17] X. Fang, J. Yan, L. Hu, H. Liu and P. S. Lee, *Adv. Funct. Mater.* **22**, 1613 (2012).
- [18] J. Liu, Z. Zhang, Y. Zhao, X. Su, S. Liu and E. Wang, *Small* **1**, 310 (2005).
- [19] R. H. Fowler and L. Nordheim, *Proc. Royal Soc. London. Ser. A* **119**, 173 (1928).
- [20] F. Xu, K. Yu, G. D. Li, Q. Li and Z. Q. Zhu, *Nanotechnology* **17**, 2855 (2006).
- [21] C. X. Xu and X. W. Sun, *Appl. Phys. Lett.* **83**, 3806 (2003).
- [22] C. X. Xu et al., *Appl. Phys. Lett.* **88**, 161921 (2006).
- [23] Y. B. Li, Y. Bando and D. Golberg, *Appl. Phys. Lett.* **84**, 3603 (2004).
- [24] A. Ghosh, P. Guha, R. Thapa, S. Selvaraj, M. Kumar, B. Rakshit, T. Dash, R. Bar, S. K. Ray and P. V. Satyam, *Nanotechnology* **27**, 125701 (2016).
- [25] C. X. Xu, X. W. Sun and B. J. Chen, *Appl. Phys. Lett.* **84**, 1540 (2004).
- [26] X. Y. Xue et al., *Appl. Phys. Lett.* **89**, 043118 (2006).
- [27] J. B. You et al., *Appl. Phys. Lett.* **94**, 262105 (2009).
- [28] L. Liao, J. C. Li, D. F. Wang, C. Liu, Q. Fu and L. X. Fan, *Nanotechnology* **16**, 985 (2005).
- [29] Q. Zhao et al., *Appl. Phys. Lett.* **88**, 033102 (2006).
- [30] N. Kedem et al., *Phys. Chem. Chem. Phys.* **16**, 8310 (2014).

- [31] R. Schlesinger et al., *Nat. Commun.* **6**, 6754 (2015).
- [32] R. Schlesinger et al., *Phys. Rev. B* **87**, 155311 (2013).
- [33] H. Li et al., *Chem. Mater.* **24**, 3044 (2012).
- [34] J. Wang et al., *ACS Appl. Mater. Interfaces* **4**, 4024 (2012).
- [35] D. C. Look et al., *Phys. Rev. Lett.* **95**, 225502 (2005).
- [36] A. Ghosh, P. Guha, A. K. Samantara, B. K. Jena, R. Bar, S. Ray and P. V. Satyam, *ACS Appl. Mater. Interfaces* **7**, 9486 (2015).
- [37] J. Wang, P. Liu, X. Fu, Z. Li, W. Han and X. Wang, *Langmuir* **25**, 1218 (2009).
- [38] K. K. Naik et al., *Appl. Phys. Lett.* **105**, 233101 (2014).
- [39] G. Kresse and J. Furthmüller, *Phys. Rev. B* **54**, 11169 (1996).
- [40] G. Kresse and J. Furthmüller, *Comput. Mater. Sci.* **6**, 15 (1996).
- [41] P. E. Blöchl, *Phys. Rev. B* **50**, 17953 (1994).
- [42] J. P. Perdew, K. Burke and M. Ernzerhof, *Phys. Rev. Lett.* **77**, 3865 (1996).
- [43] A. Ghosh, R. R. Juluri, P. Guha, R. Sathyavathi, A. Dash, B. K. Jena and P. V. Satyam, *J. Phys. D: Appl. Phys.* **48**, 055303 (2015).
- [44] X. G. Han et al., *J. Phys. Chem. C* **113**, 584 (2009).
- [45] Y. W. Zhu et al., *Appl. Phys. Lett.* **83**, 144 (2003).
- [46] C. H. Hung and W. T. Whang, *J. Cryst. Growth* **268**, 242 (2004).
- [47] N. S. Ramgir et al., *Nanotechnology* **17**, 2730 (2006).
- [48] D. Yuvaraj, R. Kaushik and K. Narasimha, *ACS Appl. Mater. Interfaces* **2**, 1019 (2010).
- [49] N. Liu, G. Fang, W. Zeng, H. Long and X. Zhao, *J. Phys. Chem. C* **115**, 14377 (2011).
- [50] Y. L. Chueh et al., *Appl. Phys. Lett.* **86**, 133112 (2005).
- [51] Y. Huang et al., *J. Phys. Chem. C* **111**, 9039 (2007).
- [52] M. Bielecki et al., *Phys. Chem. Chem. Phys.* **12**, 3203 (2010).

- [53] W. Melitz, J. Shen, A. C. Kummel and S. Lee, *Surf. Sci. Rep.* **66**, 1 (2011).
- [54] N. Rihon, *Surf. Sci.* **70**, 92 (1978).
- [55] W. Wang, B. Zeng, J. Yang, B. Poudel, J. Huang and Z. Ren, *Adv. Mater.* **18**, 3275 (2006).
- [56] F. H. Chu et al., *Nanoscale* **4**, 1471 (2012).
- [57] H. Zeng et al., *Adv. Funct. Mater.* **19**, 3165 (2009).
- [58] K. Mahmood, P. S. Bin and H. J. Sung, *J. Mater. Chem. C* **1**, 3138 (2013).
- [59] C. J. Park, D. K. Choi, J. Yoo, G. C. Yi and C. J. Lee, *Appl. Phys. Lett.* **90**, 083107 (2007).
- [60] S. Y. Li, P. Lin, C. Y. Lee and T. Y. Tseng, *J. Appl. Phys.* **95**, 3711 (2004).
- [61] X. Wang, X. Kong, Y. Yu and H. Zhang, *J. Phys. Chem. C* **111**, 3836 (2007).
- [62] Y. Ling-min and Z. Chang-chun, *Appl. Surf. Sci.* **255**, 8359 (2009).
- [63] Y. H. Yang, B. Wang, N. S. Xu and G. W. Yang, *Appl. Phys. Lett.* **89**, 043108 (2006).
- [64] Y. Imai, A. Watanabe and I. Shimono, *J. Mater. Sci. Mater. Electron.* **14**, 149 (2003).
- [65] Y. Dong and L. J. Brillson, *J. Electron. Mater.* **37**, 743 (2008).



# Chapter 7

## Novel Large Scale Growth of Au-GeO<sub>2</sub> Nano/Micro-wires: Surface-plasmons and Oxygen-defects Mediated Visible-light Photodetection

### 7.1 Introduction

The main focus of the previous chapter was relating the enhanced field emission properties of oxygen deficient Au-ZnO hetero-nanostructures with experimentally determined local work function variation and comparing with model DFT calculations. In this chapter, we report on the high throughput growth of Au capped oxygen deficient GeO<sub>2</sub> nano/micro-wires (N/MWs) on  $\approx 5$  nm Au coated native oxide Ge(100) substrate by means of a simple *single step* annealing method. We have shown Au catalyzed vapor–liquid–solid (VLS) growth of Au-GeO<sub>2</sub> N/MWs via generation of growth species through metal induced surface decomposition (active oxidation) without any supply of source from outside. The growth of N/MWs as well as the formation of etch pits on the substrate surface via annealing in various ambiances (in atmospheric, low-vacuum, 40 sccm oxygen and argon flow) are addressed with plausible growth mechanisms. In spite of having high bandgap of GeO<sub>2</sub>, we have shown the visible-light photodetection application of Au-GeO<sub>2</sub> N/MWs grown in Ar ambiance. We have attributed this visible-light detection using Au-GeO<sub>2</sub> N/MWs, to the visible-light absorption, induced by SPR of plasmonic Au nanoparticles (NPs) and high oxygen vacancies in them. To clarify the role of tip plasmonic Au NPs present in the N/MWs, we have showed  $\approx 4$  times enhancement in the photodetection performance in terms of photoresponse, responsivity and external quantum efficiency (EQE) just by further Au NPs decoration on the as-grown N/MWs surfaces.

Nanoscale oxide semiconducting materials are the interesting and attractive area in the field of nano-materials research because of their interesting physical, chemical and mechanical properties as well as their technological wide range of nanoscale electronic, optoelectronic and photovoltaic applications [1-5]. Among all the nanoscale devices, photon

sensors or photodetectors are become important for their usages as binary switch in imaging techniques and light-wave communications, as well as in future optoelectronic nano-circuits [5-9]. For efficient photodetector applications one dimensional (1D) oxide semiconductor nanostructures (NSs), particularly nanowires (NWs) are the highly appreciated candidates due to their large surface-to-volume ratio and direct charge transport pathway, which leads to short transport time and superior sensitivity [6, 10-13]. Among many oxide semiconductor NSs, group IV semiconductor (especially Si and Ge) oxides, in particular GeO<sub>2</sub> has got lot of importance due to its wide band gap ( $\approx 4.8 - 5.1$  eV) [5, 14, 15], high refractive index [16, 17], low optical loss [18], high thermal stability [17] along with unique photonic, electronic [19] properties. 1D GeO<sub>2</sub> NSs individually could be used for wide range of future device applications, such as, in electronics, nano-connections in optoelectronic communications and optical devices, photovoltaic and photocatalytic applications [2, 5, 20-22]. In particular GeO<sub>2</sub>, as a dielectric oxide, show resistive switching property because of its high defect density, low Ge-O bond formation energy and feasibility of oxygen vacancy formation at low temperature [21, 23]. Due to the resistive switching behavior of GeO<sub>2</sub>, it has been chosen as a promising material besides SiO<sub>2</sub>, HfO<sub>2</sub>, Ta<sub>2</sub>O<sub>5</sub>, Nb<sub>2</sub>O<sub>5</sub> for resistive random access memory (RRAM) for future memory device applications [22]. Recently, 1D GeO<sub>2</sub> nano-micro structures and their various composites have been considered as promising candidate as active anode material in Li-ion batteries because of high theoretical specific reversible capacity ( $1125 \text{ mAh g}^{-1}$ ), high volumetric capacity of  $4653 \text{ mAh cm}^{-3}$ , high Li<sup>+</sup> diffusivity, low operation voltage and higher thermal stability [24-26]. Over the year's lot of efforts have been put towards photodetection, especially concerned about the detection of visible zone of the solar spectrum due to the importance in various environmental and biological research, sensing, launching missile etc [10, 27, 28]. However, the intrinsic wide bandgap (in the UV light range) properties of almost all oxide semiconductor NSs including GeO<sub>2</sub> NSs, limits their practical visible light driven sensing, photovoltaic, photocatalytic etc. applications. Till date several post-growth multi-step strategies have been adopted to enhance the visible light absorption capability and also improve efficiencies of visible light driven activities of those oxide semiconductor NSs. These strategies include incorporation of plasmonic noble metal nanoparticles (NPs), various doping, creation of oxygen vacancies, dye sensitization, coupling with other semiconductors etc [29-31]. So, it is extremely important to develop a simple growth technique for large scale growth of NSs with inherent enhanced visible light absorption capabilities [32]. 1D GeO<sub>2</sub> NSs (such as nanowires and nanotubes) have been grown via various physical and chemical methods, including thermal oxidation, self-catalytic, metal-catalyzed, physical evaporation

and carbothermal reduction reaction [2, 18, 19, 32-37]. It is reported that volatilization of semiconductors surfaces occurs through decomposition of substrate surface via active oxidation resulting in the formation of monoxide vapor and etch pits on the surface [32, 38, 39]. It is also reported that presence of metal NPs (like Au) on the substrate can influence the decomposition processes significantly [32, 39, 40]. This monoxide vapor production and its use as source for catalyzed growth of nanowires via vapor-liquid-solid (VLS) mechanism on the same metal NPs decorated substrate can happen simultaneously [32].

## 7.2 Experimental

Samples were grown in a horizontal ceramic tube (length  $\approx$  85 cm and inner diameter 4.8 cm) furnace with single zone side entry at atmospheric condition. Ge(100) wafers with native oxide ( $\text{GeO}_x \approx 4 - 5$  nm) were used as the substrates for the growth [32]. First, Ge(100) wafers were cleaned in acetone for 5 min and then in methanol for 5 min in ultrasonic bath. A  $\approx$  5 nm thick Au film was deposited on the cleaned substrates by high vacuum physical vapor deposition (PVD) technique. Following this, Au deposited substrates were put at the centre of a ceramic boat of diameter 1.5 cm and 9 cm long, and then loaded into the both sides opened tube furnace at its central position. The temperature of the furnace was increased to 600 °C at a rate of 7 °C min<sup>-1</sup> and kept there until growth ends. The furnace was then switched off and allowed to cool to room temperature.

To check the ambience dependence, annealing experiments for 5 nm Au/GeO<sub>x</sub>/Ge(100) substrates in argon (Ar), oxygen (O<sub>2</sub>) ambiances (with 40 sccm flow) and low-vacuum ( $\leq 10^{-3}$  mbar) condition were carried out, keeping all other parameters same. To understand the role of Au layer for growth process, a mask was used during the  $\approx$  5 nm thick Au film deposition that enabled to have the same Ge(100) sample with and without Au layer [32].

Morphology and structural characterization of the as-grown specimens were studied using field emission gun based scanning electron microscope (FEG-SEM) with 20 kV electrons and high resolution transmission electron microscope (HRTEM) with 200 keV electrons. X-ray diffractometer (Philips X'pert Pro MRD cradle) was used to obtain large scale crystalline information, in grazing incidence mode (at  $\approx$  1.5 degree). Optical properties of the as-grown samples were characterized by photoluminescence (PL) measurements using

a He-Cd laser and reflectance measurements using UV-Vis spectrometer (Shimadzu-3101PC, Japan) at room temperature. The I-V characteristics of the devices were studied using a Keithley semiconductor parameter analyzer (model no. 4200-SCS) under dark and upon illumination of monochromatic light. The spectral photocurrent response (responsivity) and external quantum efficiency (EQE) was measured using a setup consisting of a broadband light source, a monochromator, a mechanical chopper (set to 187 Hz), and a lock-in amplifier (Stanford Research, SR 530) done at IIT, Kharagpur.

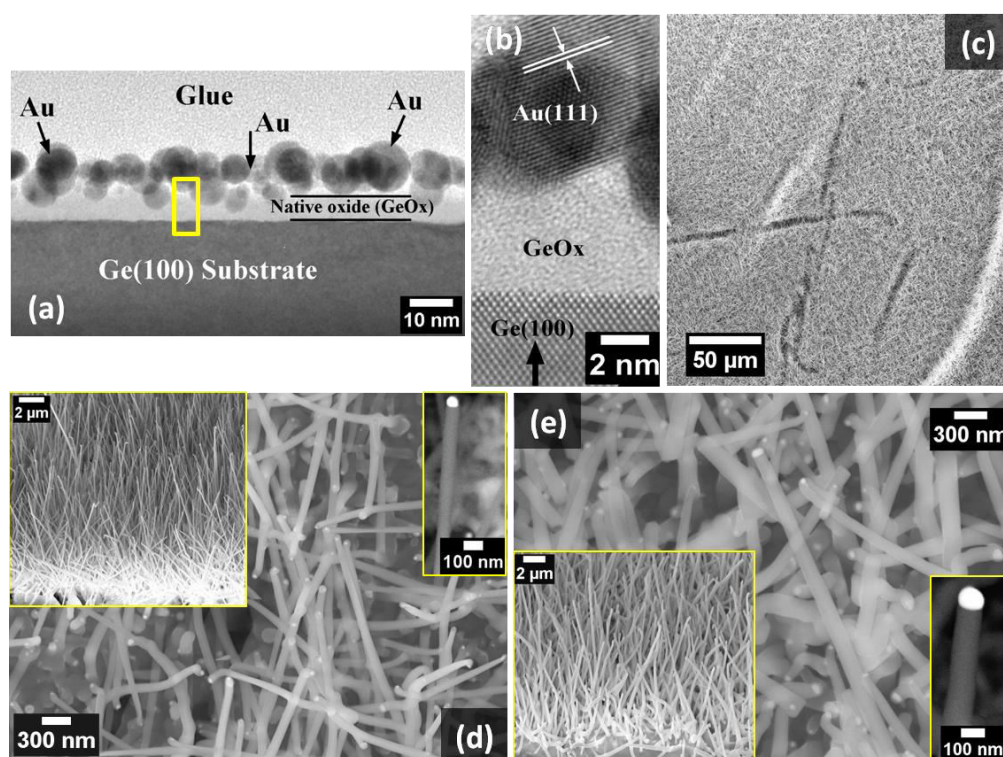
Photodetection properties of as-grown sample (Au-GeO<sub>2</sub> N/MWs) with higher oxygen vacancies (grown in 40 sccm Ar ambiance) was studied by fabricating an Al<sub>2</sub>O<sub>3</sub>/Au-GeO<sub>2</sub> N/MWs/p-type Si(100) device structure with top and bottom aluminum (Al) contact, as shown in Figure 7.7(a). To make this device, 1st we have scratched as-grown Au-GeO<sub>2</sub> N/MWs from the Ge substrate and dispersed in methanol followed by ultrasonication for 10 min and then spin coated on freshly prepared p-type Si(100) substrate (Si substrates were cleaned in piranha solution followed by etching in 2% HF aqueous solution for 2-3 min at room temperature to obtain H-passivated fresh Si surfaces). After that high bandgap Al<sub>2</sub>O<sub>3</sub> of  $\approx 4$ -5 nm was deposited on dispersed Au-GeO<sub>2</sub> N/MWs/Si(100) substrate, using radio frequency (RF) magnetron sputtering system. Following this, top and bottom Al contacts were taken using thermal evaporation system. We also have studied photodetection performance by making similar device structures after decoration of Au NPs on the same category as-grown Au-GeO<sub>2</sub> N/MWs sample. Au NPs decoration was done by depositing  $\approx 4$  nm Au layer on the as-grown samples followed by annealing at 400 °C [32].

## 7.3 Results and discussion

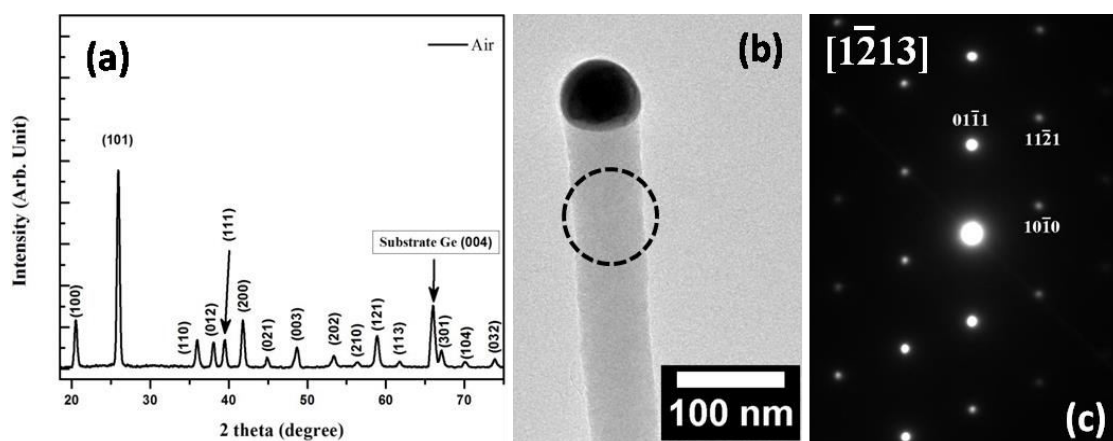
### 7.3.1 Morphological and structural properties

Figure 7.1(a) shows the cross-sectional low magnification TEM micrograph of the 5 nm Au/GeO<sub>x</sub>/Ge(100) as-deposited sample. Figure 7.1(b) presents HRTEM image taken from the highlighted region in Figure 7.1(a), showing the crystalline Au film grown on crystalline Ge substrate separated by  $\approx 5$  nm sub-stoichiometric native oxide (GeO<sub>x</sub>). Figures 7.1(c-d) show the low and high-magnification SEM images of the sample after 30 min of annealing in air, showing high-yield growth of GeO<sub>x</sub> NWs with brighter contrast Au NPs at the tip. The average diameter and length of NWs are calculated to be  $67 \pm 10$  nm and  $5 \pm 2$   $\mu$ m respectively,

with highest aspect ratio  $\approx 100$ . To check role of annealing time over the dimension of the NWs, we have carried out the same experiment for one hr and the corresponding SEM image is shown in Figure 7.1(e) [32]. The average diameter and length of these NWs (1 hr sample) comes out to be  $129 \pm 17$  nm and  $7 \pm 3$  nm, respectively, with highest aspect ratio  $\approx 80$ , which is less than the 30 min case. Insets at the left side in the Figures 7.1(d-e) are SEM images (tilted view), correspond out-of-plane growth of the Au-GeO<sub>x</sub> NWs of 30 min and 1 hr air annealing samples respectively. BSE images shown in the insets (right side) of Figures 7.1(d-e) conform the presence of Au the tip of each NW (as brighter contrast) for both the cases [32]. Hereafter, we will discuss only about the Au-GeO<sub>x</sub> NWs grown by 30 min of annealing. To get the large scale crystalline information, XRD was done on the as-grown sample. Figure 7.2(a) shows the XRD spectrum, reveals the overall crystallinity of the as-synthesized product. All the visible reflections can be indexed to the hexagonal structure of



**Figure 7.1:** (a) Cross-sectional low magnification TEM micrograph of 5 nm Au/GeO<sub>x</sub>/Ge(100) as-deposited sample. (b) HRTEM image recorded from the highlighted region of (a). (c) Low magnification SEM image of the as-grown Au-GeO<sub>x</sub> nanowires (NWs) after air annealing @ 600 °C for 30 min, showing the high-yield growth. (d-e) High magnification SEM images of Au-GeO<sub>x</sub> NWs for 30 min and 1 hr growth, respectively; two inset figures at left side are corresponding 54° tilted SEM images and other two inset figures at right side are single Au-GeO<sub>x</sub> NW BSE images from the corresponding samples.



**Figure 7.2:** (a) The XRD pattern of the as-grown products on Ge(100) substrate, confirming the GeO<sub>2</sub> phase with hexagonal structure. (b) TEM micrograph of a single Au-GeO<sub>2</sub> NW, showing dark contrast gold (Au) at the tip and (c) shows SAED pattern taken along [1 $\bar{2}$ 13] zone axis of hexagonal structure from the dotted circle in figure (b).

germanium oxide (GeO<sub>2</sub>) with lattice constants of  $a=4.985 \text{ \AA}$  and  $c= 5.648 \text{ \AA}$  (JCPDS card, 36-1463) with one extra peak coming from the Ge substrate [32]. Further observation using TEM (Figure 7.2(b)) on a single Au-GeO<sub>2</sub> NW reveals that NWs are uniform in diameter ( $\approx 65 \text{ nm}$ ), which is consistent with the SEM result. At the same time a dark contrast Au nanoparticle was found at the tip of the NW, as we have already seen in SEM-BSE images. Interestingly, GeO<sub>2</sub> NWs undergo a quick phase transformation from crystalline to amorphous phase within 1-2 seconds of exposure owing to their high electron beam sensitivity. Due this instability we could not able perform further micro-nano structural study using high resolution TEM, which is consistent with previous studies on GeO<sub>2</sub> NWs [2, 32, 33, 37]. But, we could able to record SAED pattern from a single NW. Figure 7.2(c) shows the SAED pattern from the highlighted region taken along [1 $\bar{2}$ 13] zone axis of hexagonal structure, reveals that NWs are single crystalline in nature and preferably grown along  $\langle 01\bar{1}1 \rangle$  direction [32].

To know the selectivity of the growth and role of Au on the growth of Au-GeO<sub>2</sub> NWs, we have carried out air annealing experiment on a single substrate with two regions (Au coated and uncoated) keeping all other growth parameters same. Figure 7.3(a) shows that the NWs were only grown at the location where Au film was present on the substrate and in contrast no such growth was observed on the other region (where Au was absent). Figures 7.3(b-c) show that etch pits formed on the two regions are different and it is clear that presence of Au NPs have enhanced the surface decomposition via active oxidation [32, 39] of the Ge(100)

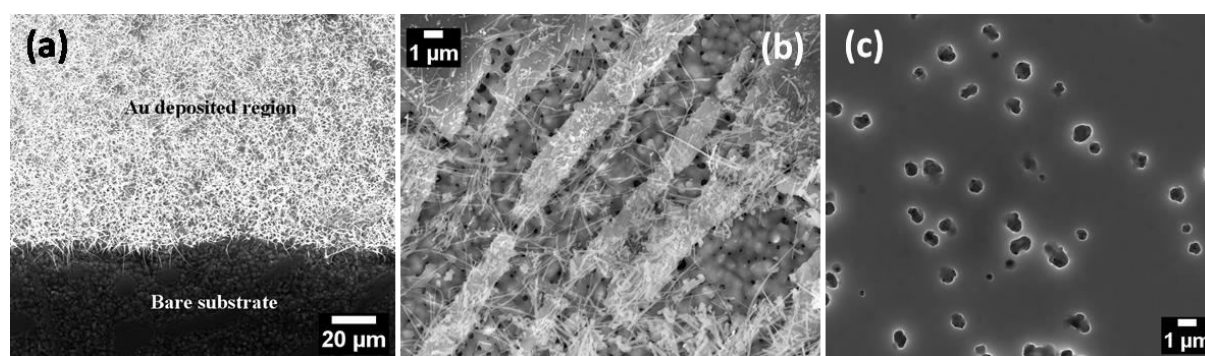


**Figure 7.3:** (a) SEM micrograph show the growth of GeO<sub>2</sub> NWs only on the Au coated region of the Ge(100) substrate after air annealing @ 600 °C for 30 min. (b-c) Show SEM images of the etch pits formed via active oxidation (surface decomposition) on the Au coated and uncoated regions on the native oxide Ge substrate during growth of NWs.

substrate. From this observation, we can conclude that NWs growth to take place catalyst Au on the native oxide Ge substrate is necessary [32].

Further, we have studied the role of growth environment by carrying out three separate annealing experiments at 600 °C for 30 min on three similar as-deposited samples (5 nm Au/GeO<sub>x</sub>/Ge(100)) but in three different ambiances (in low vacuum ( $\leq 10^{-3}$  mbar), under 40 sccm Ar and 40 sccm O<sub>2</sub> flow) [32]. SEM image of the sample after annealing in low vacuum condition is shown in Figure 7.4(a), displaying the formation of nano square or rectangular etch pits on the Ge(100) substrate following its 4 fold symmetry [32, 41, 42]. No Au-GeO<sub>2</sub> NWs growth was observed on the substrate in this case. Significant efforts have already been devoted to pattern substrates with desirable nanostructures on Si, GaN, Ge, ZnO etc by various means of expensive and time consuming techniques, such as e-beam/ion-beam lithography with and without masking, chemical etching, vapor phase etching, various plasma reactive ion etching, sublimation etc [41, 43-46]. Figures 7.4(b-c) show the low and high magnification SEM images, respectively of the as-grown Au-GeO<sub>2</sub> nano/micro-wires (N/MWs) having very high aspect ratio, after similar annealing under 40 sccm Ar flow. In particular, the wires obtained under Ar flow are of diameter in the range of  $100 \pm 10$  nm and lengths that reach tens of microns, so that the wires have aspect ratio 200 – 300 or higher. In comparison with air annealing case, significantly higher diameter, length and aspect ratios Au-GeO<sub>2</sub> N/MWs were observed for Ar annealing case [32]. XRD pattern collected from this sample (Figure 7.4(d)) giving the similar reflections as the air annealing sample, suggests that the products (N/MWs) are GeO<sub>2</sub> with hexagonal crystal structure (JCPDS card, 36-1463).



TEM image of a single Au-GeO<sub>2</sub> N/MWs (Figure 7.4(e)) shows uniform diameter of  $\approx 90$  nm with Au NP as dark contrast at the tip. Figure 7.4(f) shows the SAED pattern from a single GeO<sub>2</sub> N/MWs taken along [0001] zone axis of hexagonal crystal system revealing its single crystalline nature. Interestingly, annealing under O<sub>2</sub> flow (40 sccm) we have not found any such growth of Au-GeO<sub>2</sub> N/MWs or substrate symmetric etch pits on the Ge substrate surface (Figure 7.4(g)). With these observations we can conclude that oxygen presence is necessary for growth of N/MWs but there is an upper limit of O<sub>2</sub> partial pressure beyond which growth cannot take place [32, 39]. In our growth process no external growth species were supplied, substrate itself decomposed in presence of Au NPs and produce monoxide vapor (GeO) through active oxidation that feeds the growth [32, 39]. So, Au layer on the Ge substrate and optimum O<sub>2</sub> pressure in the annealing chamber are the crucial parameters for the growth of Au-GeO<sub>2</sub> N/MWs. In the next section we will discuss the possible growth mechanism of Au-GeO<sub>2</sub> NWs grown in atmospheric condition.

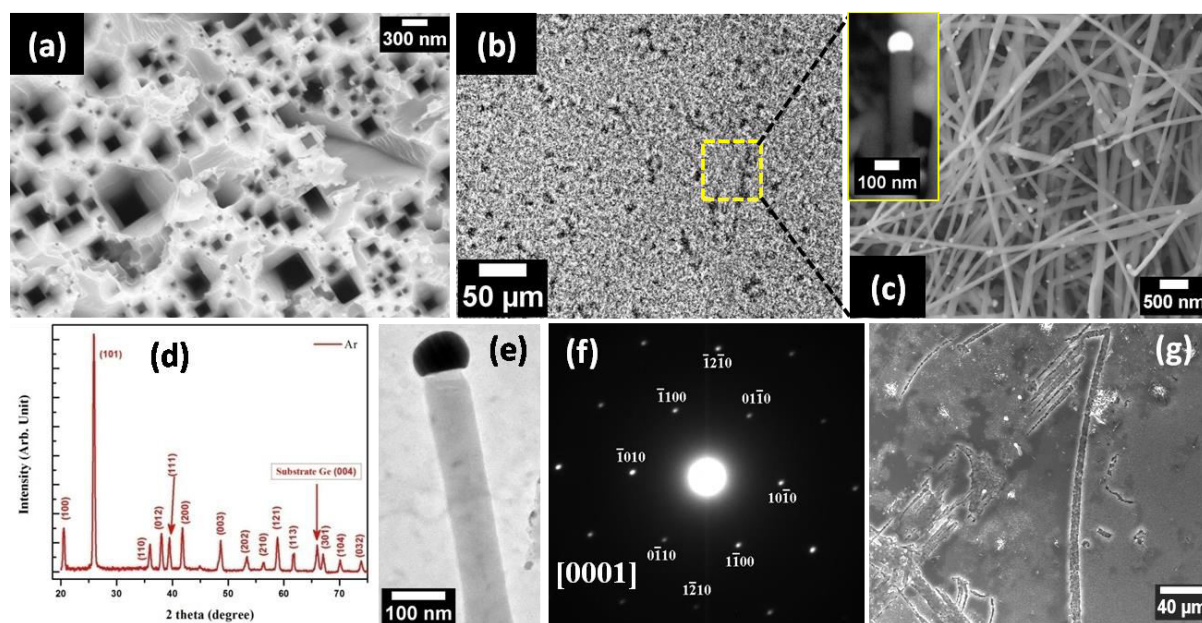


**Figure 7.4:** (a–b) show SEM images of after annealing @ 600 °C for 30 min under low vacuum and 40 sccm Ar flow conditions, respectively. (c) Shows magnified SEM image of the highlighted region in panel (b). (d) The XRD pattern of the as-grown products on Ge(100) substrate in Ar ambiance. (e) Low-mag TEM image of a Au-GeO<sub>2</sub> NW grown in Ar ambiance. (f) Typical SAED pattern from single GeO<sub>2</sub> NW recorded along [0001] zone axis of hexagonal structure. (g) Shows SEM image of the sample annealed in 40 sccm O<sub>2</sub> flow.



### 7.3.1.1 Growth mechanism

There are two well established growth mechanisms for understanding the growth of 1-D nanowires, one is vapor-liquid-solid (VLS) and second is vapor-solid (VS) mechanism. The most prominent characteristics of VLS growth is the presence of metal nanoparticle at the tips of the NWs, which serve as active adsorption site of the growth species and forms liquid alloy droplet during growth [32, 33, 36, 39, 47]. In the present case, we have observed the presence of dark contrast Au NP at the tips of NWs in SEM as well as in TEM images (Figures 7.1(e) and 7.2(b)) and also no growth was observed without catalyst layer. Hence the VLS mechanism is the most likely process through which the growth of this Au-GeO<sub>2</sub> NWs can be understood. Schematic representation of the growth processes of Au-GeO<sub>2</sub> NWs have been shown in Figure 7.5. We propose the growth mechanism for the growth of Au-GeO<sub>2</sub> NWs as follows (schematically presented in Figure 7.5):

1) 1<sup>st</sup> step of growth is the production of growth species which is monoxide vapor (GeO) via catalyst mediated active oxidation of the 5 nm Au/GeO<sub>x</sub>/Ge(100) substrate surface through the following reactions [19, 32, 39, 40] at 600 °C ( $\approx$  sublimation temperature of GeO).



where, “s” and “g” stand for solid phase and gaseous phase, respectively.

2) In the 2<sup>nd</sup> step these volatile GeO could get absorbed by the nearby Au NPs in their molten state and forms Au-Ge-O alloy droplet at 600 °C (> the eutectic temperature 361 °C) [48]. These dissolved GeO further react with residual O<sub>2</sub> and forms GeO<sub>2</sub> (equation (7.3)). When the alloy droplets get saturated with GeO<sub>2</sub>, the crystalline Au-GeO<sub>2</sub> NWs begin to grow from the droplets.



3) A fraction of metastable GeO vapor undergoes a disproportionation (or reduction-oxidation) reaction, producing GeO<sub>2</sub> and Ge mixture (equation (7.4)) during at that annealing process (at 600 °C) [49, 50]. The Ge(s) thus formed, again interacts with GeO<sub>2</sub> (s) (as shown in equation (7.1)) and the growth process continues to form Au NP capped GeO<sub>2</sub> NWs.



Figures 7.5(b-c) schematically present the growth species formation via active oxidation,

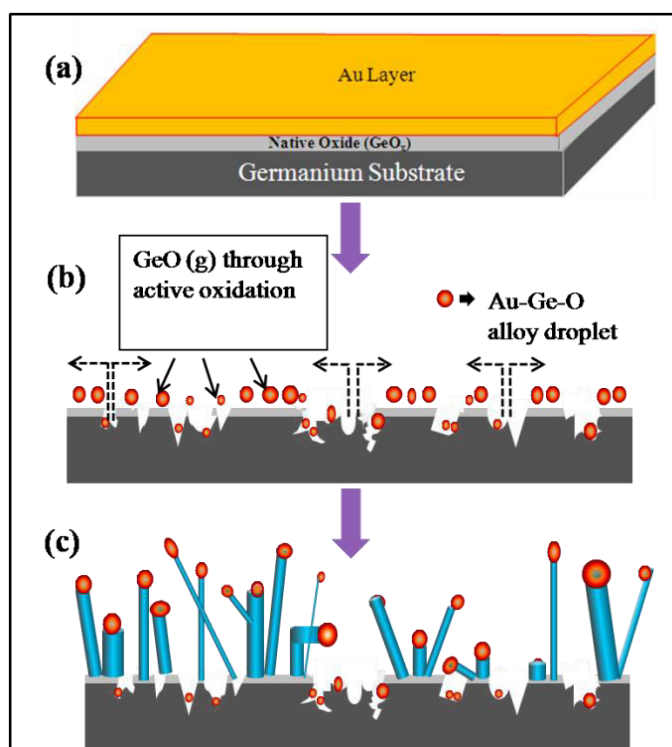


**Figure 7.5:** Schematic diagram of a plausible mechanism involved in GeO<sub>2</sub> NWs growth. (a) as-deposited substrate before annealing. (b-c) show the expected processes involved in the VLS growth of Au-GeO<sub>2</sub> NWs (for the case of as-deposited substrate annealed in air ambience).

nucleation and growth of GeO<sub>2</sub> NWs, which occur simultaneously on the 5 nm Au/GeO<sub>x</sub>/Ge(100) substrate upon air annealing [32].

### 7.3.2 Optical properties

Figures 7.6(a, b) show the typical PL spectra taken from the samples grown in air and Ar (40 sccm) ambiances, that depict broad emission bands ranging from 360 to 490 nm and 370 nm to 560 nm, respectively [32]. To know more about the origin of such broad emissions we have fitted these spectra with Gaussian functions. For Au-GeO<sub>2</sub> NWs (grown in air) best fit is obtained with three Gaussian peaks: two in violet region centered around 390 nm, 412 nm and one in the blue region centered  $\approx$  442 nm. For Au-GeO<sub>2</sub> N/MWs (grown in Ar) best fit is obtained with three different Gaussian peaks: centered at 405 nm (in violet region), 443 nm (in blue region) and 496 nm (in blue-green region) [32]. Origin of both blue and green emission can be attributed to the radiative recombination of the electrons in the oxygen

vacancy induced donor states ( $V_O^-$ ) with holes on the oxygen-germanium vacancy pairs induced acceptor states ( $V_{Ge}, V_O^+$ ) [32, 51]. But origin of violet emission is very difficult to assign: possible reasons could be either oxygen or germanium deficient luminescence centers [36, 51]. It is now paramount to emphasize that green emission is only observed in case of sample grown in Ar environment. As we have discussed in the growth model that volatile growth species (GeO) were supplied from the substrate itself through active oxidation reactions, no external supply of Ge was present. So, it is expected to have oxygen/or germanium deficiencies in those as-synthesized samples for both the ambiances

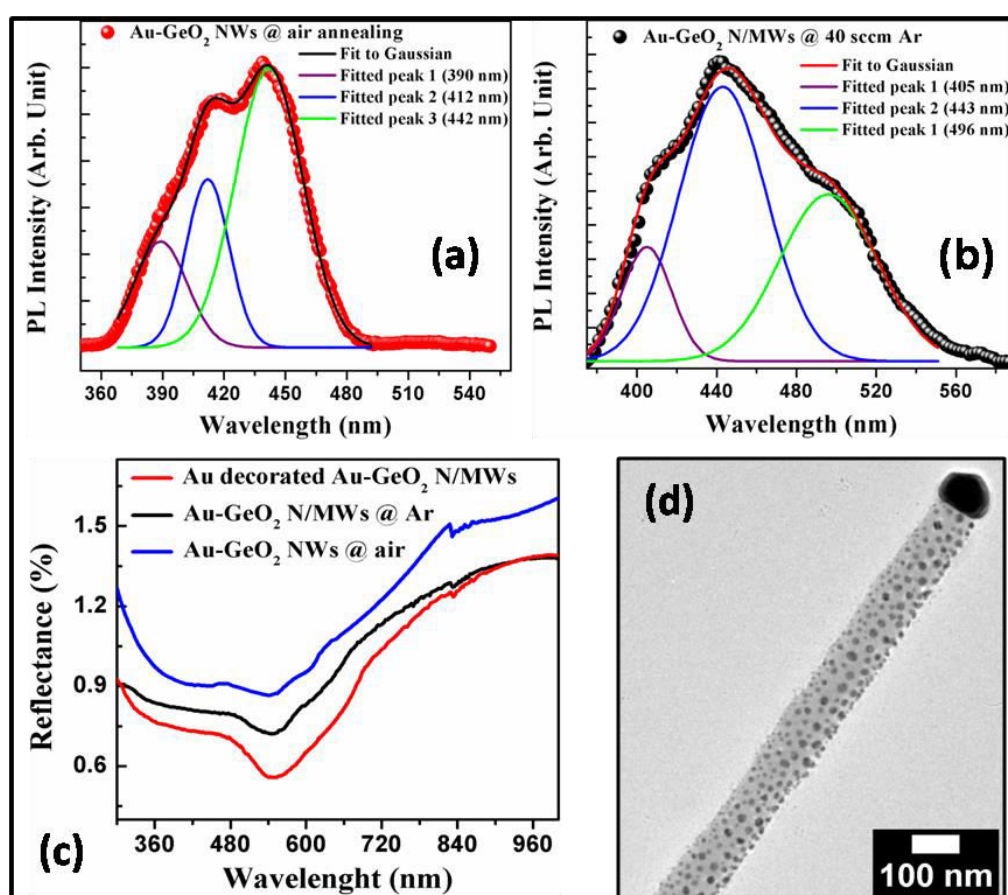


**Figure 7.6:** Room temperature PL spectra from GeO<sub>2</sub> NWs obtained at 600 °C annealing (a) in air atmosphere and (b) under 40 sccm Ar flow. (c) Comparative diffuse reflectance spectra. (d) Low-mag TEM image of Au NPs decorated Au-GeO<sub>2</sub> N/MWs (grown in Ar ambiance).

(Au-GeO<sub>2</sub> NWs or N/MWs) [32]. But probability of having oxygen deficiencies is more than the Ge deficiencies because Ge atom can diffuse from the beneath substrate at high temperature. Now for the growth in Ar ambiance, external oxygen supply should be less

compare to growth in air atmosphere, this could result in Au-GeO<sub>2</sub> N/MWs grown to have more oxygen vacancies compare to air grown sample, thus leading to extra green emission in PL spectra. Presence of oxygen vacancies in conjunction with plasmonic Au NPs at the tip of as-grown N/MWs may influence their visible light activity [32].

Figure 7.6(c) presents the UV–Vis diffuse reflectance spectra taken from both the as-grown Au-GeO<sub>2</sub> NWs and N/MWs samples (in air and Ar ambiances) in the wavelength range from 300 nm to 1000 nm. It can be clearly observed from the reflectance spectra that, in the visible spectral range, (400 nm to 700 nm) both the samples show very low reflectance (< 1 %) with a minima at  $\approx 545$  nm, which can be attributed to the surface plasmon resonance (SPR) absorption of Au NPs that are present at the tip of the NSs [52, 53]. A relatively less reflectance is observed for the Au-GeO<sub>2</sub> N/MWs (i.e., Ar case) compared to air annealing sample (Au-GeO<sub>2</sub> NWs), which can be due to the high roughness of the sample. To study the response from Au NPs in the visible light absorption, further Au NPs were decorated on the surfaces of Au-GeO<sub>2</sub> N/MWs (grown in Ar) as discussed in the experimental section. Figure 7.6(d) represents low-mag TEM micrograph of a single N/MW after Au NPs decoration. As expected further reduction in reflectance (i.e., increase in absorption) is observed for the Au NPs decorated Au-GeO<sub>2</sub> N/MWs (red curve in Figure 7.6(c)). Following these studies, visible-light sensing application of the sample grown in Ar ambience and after Au decoration (Au-GeO<sub>2</sub> N/MWs) are carried out and presented in the section (section 7.3.3) below [32].

### 7.3.3 Visible-light photodetector applications

We have analyzed visible light detection properties of Au capped GeO<sub>2</sub> N/MWs which are grown in Ar ambience and then compared with the performance of similar sample after Au NPs decoration to highlight the role of plasmonic Au NPs at the tip of the N/MWs. So, for complete study we have prepared three devices: first one with as-grown Au-GeO<sub>2</sub> N/MWs sample, second one with similar category Au-GeO<sub>2</sub> N/MWs sample after decorating Au NPs on their surfaces and the last one without N/MWs sample (called as control device). The schematic diagram of the fabricated photodetector with Au capped GeO<sub>2</sub> N/MWs is shown in Figure 7.7(a).

Figure 7.7(b) shows the room temperature current density vs. applied voltage (I-V) characteristics of three devices under the dark and with illumination of fixed wavelength of

540 nm and optical power density of 0.2 mW/cm<sup>2</sup> [32]. From, the control device, I-V curve does not show significant variation in the current densities before (dark condition) and after illumination, in contrast to the devices made of Au-GeO<sub>2</sub> N/MWs before and after Au decoration. Asymmetric nature of the I-V curves confirms the formation of p-n junction between p-type Si and n-type Au-GeO<sub>2</sub> N/MWs. From I-V characteristics, significant increase in reverse current is seen under the illumination due to the photogenerated minority carriers in the depletion region of the p-n junction devices [32]. It is seen from Figure 7.7(b) that beyond applied reverse bias of -2.0 V, there is not much change in the photoresponse (ratio of photocurrent ( $I_{ph}$ ) to dark-current ( $I_d$ )) for both the devices. For the Au-GeO<sub>2</sub> N/MWs device, dark current at -2.0 V is measured to be  $I_d = 1.07 \times 10^{-8}$  A/cm<sup>2</sup>,

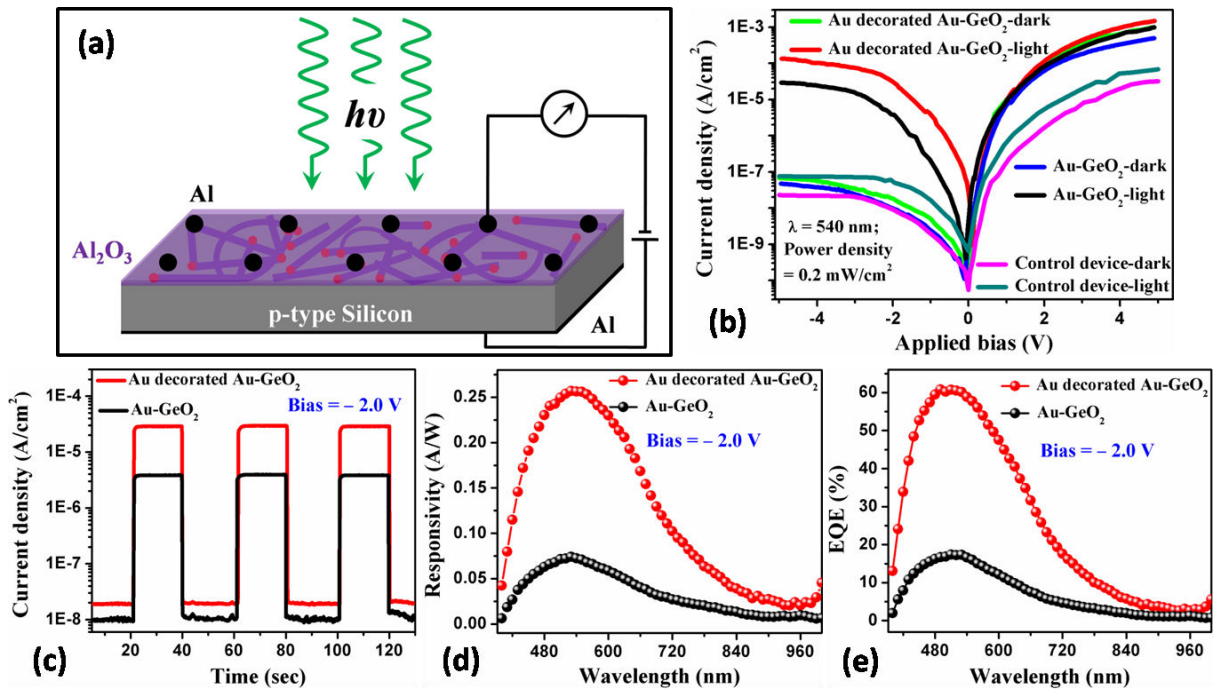


**Figure 7.7:** (a) Schematic representation of photodetector device under illumination. (b) I-V characteristics of the three photodetectors made of as-grown N/MWs, Au NPs decorated similar N/MWs and without sample (i.e., Al<sub>2</sub>O<sub>3</sub>/p-type Si(100), called as control device) measured in the dark and under the illumination of 0.2 mW/cm<sup>2</sup> of visible light ( $\lambda = 540$  nm). (c) Time responses of the devices with same bias = -2.0 V, under the visible light ( $\lambda = 540$  nm, 0.2 mW/cm<sup>2</sup>) illumination. (d-e) Show spectral responsivity and EQE spectra of the corresponding devices respectively.

that has been increased by  $\approx 360$  (photoresponse) times upon illumination and reaches a photocurrent value of  $I_{ph} = 3.86 \times 10^{-6}$  A/cm<sup>2</sup>. Whereas, under the same experimental

conditions the Au decorated Au-GeO<sub>2</sub> N/MWs device is showing  $I_d = 1.93 \times 10^{-8}$  A/cm<sup>2</sup> and  $I_{ph} = 2.87 \times 10^{-5}$  A/cm<sup>2</sup>, therefore photoresponse of  $\approx 1487$  times. So, from this observation, photoresponse from the device after decoration of Au NPs has been increased about 4 times [32]. This increment in the photoresponse can be understood as more absorption of visible light (540 nm) due to the surface plasmon of Au NPs and subsequent transfer of photogenerated hot electrons from Au NPs to the conduction band of GeO<sub>2</sub> [31, 54, 55]. The typical pulsed photocurrent time response of both the devices were measured at same bias – 2.0 V under  $\lambda = 540$  nm illumination with power density of 0.2 mW/cm<sup>2</sup> and is shown in Figure 7.7(c). Time response measurements were done for three repeated cycles with an ON/OFF interval of 20 sec, for both the devices. Inspiringly we have found to have almost same current values with light ON and OFF conditions for consecutive cycles from the respective samples [32]. The performance of a photodetector is generally evaluated by calculating its peak responsivity (R) and external quantum efficiency (EQE) or photoconductive gain (G) of the device. The responsivity (R) of a photodetector is written as the ratio of photocurrent density ( $I_{ph}$ ) to the incident power density ( $P_{opt}$ ) corresponding to a particular wavelength ( $\lambda$ ), i.e.,  $R(\lambda) = I_{ph}/P_{opt}$ . Spectral photoresponse of those devices were characterized by calculating responsivity in the spectral range from 400 to 1000 nm using a broadband source with a fixed applied bias = –2.0 V, shown in Figure 7.7(d). The peak responsivity (R) from the Au decorated Au-GeO<sub>2</sub> device is found to be 0.25 A/W, which is  $\approx 4$  times higher than that of Au-GeO<sub>2</sub> device (0.07 A/W). We also have evaluated EQE from the spectral responsivity results using the following equation [56],

$$EQE (\%) = (100 \times 1240 \times I_{ph})/(\lambda \times P_{opt}) = (100 \times 1240) \times R(\lambda)/\lambda \quad (7.5)$$

EQE spectra obtained by applying equation (7.5) from the corresponding photodetector devices have been shown in Figure 7.7(e). Figure 7.7(e) shows that peak EQE of the Au decorated Au-GeO<sub>2</sub> device is  $\approx 60$  % which is almost 4 times higher than that of the device made with as-grown Au-GeO<sub>2</sub> N/MWs ( $\approx 17$  %) corresponding to the visible light of  $\lambda = 510$  nm. From above all photodetector measurements we can conclude that Au-GeO<sub>2</sub> N/MWs are quite sensitive towards visible light photodetection and their performance further can be improved by decorating plasmonic Au NPs on the surfaces [32].

## 7.4 Summary

In summary, we report a novel *single step* method for the growth of plasmonic Au NPs capped oxygen deficient GeO<sub>2</sub> nano/micro-wires (N/MWs) of variable dimensionality, via annealing of  $\approx 5$  nm Au/GeO<sub>x</sub>/Ge(100) substrates in different ambiances using a simple horizontal tube furnace at 600 °C. We have demonstrated the role of catalyst Au and the ambiances on the growth of Au-GeO<sub>2</sub> N/MWs, by carrying out growth experiments with and without Au layer on Ge substrates under different ambiances (atmospheric condition, low vacuum and 40 sccm Ar and O<sub>2</sub> ambiances). We have proposed and discussed a plausible growth scheme of Au-GeO<sub>2</sub> N/MWs following the metal catalyzed surface decomposition and active oxidation processes, without any external supply of Ge. We report the details of successfully grown highly oxygen deficient Au-GeO<sub>2</sub> N/MWs and their use in visible light photodetection. These GeO<sub>2</sub> N/MWs show low reflectance and PL in the visible spectral regime. The Au-GeO<sub>2</sub> N/MWs photodetector exhibited a good photoresponse ( $\geq 10^2$ ) and significant responsivity of  $\approx 0.07$  A/W with EQE of 17 % at  $-2.0$  V applied bias upon illumination ( $\lambda = 540$  nm,  $0.2$  mW/cm<sup>2</sup>). This phenomenon is attributed to the oxygen vacancy related defect states in the bandgap and plasmonically generated hot electron injection from Au to conduction band of GeO<sub>2</sub>. Influence of plasmonic Au NPs at the tip of the as-grown N/MWs on visible-light photodetection was complimented by studying photodetection characteristics after decoration of Au NPs on the as-grown N/MWs surfaces. It is found that Au decorated Au-GeO<sub>2</sub> N/MWs device shows a photoresponse of  $\approx 10^3$ , responsivity of  $0.25$  A/W, EQE of  $\approx 60$  % and typically about 4 times better performance in photoresponse compared to Au-GeO<sub>2</sub> N/MWs without decoration.

## 7.5 References

- [1] Z. G. Yan and C. H. Yan, *J. Mater. Chem.* **18**, 5046 (2008).
- [2] P. Hidalgo, B. Mendez and J. Piqueras, *Nanotechnology* **18**, 155203 (2007).
- [3] X. Fang et al., *J. Mater. Chem.* **18**, 509 (2008).
- [4] A. K. Chandiran, M. Jalebi, M. Nazeeruddin and M. Gratzel, *ACS Nano* **8**, 2261 (2014).
- [5] L. Nejaty-Moghadam et al., *J. Mater. Sci. Mater. Electron.* **26**, 6386 (2015).



- [6] T. Zhai, X. Fang, M. Liao, X. Xu, B. Yoshio and D. Golberg, *Sensors* **9**, 6504-(2009).
- [7] C. Soci et al., *Nano Lett.* **7**, 1003 (2007).
- [8] Y. Jiang et al., *Adv. Funct. Mater.* **17**, 1795 (2007).
- [9] T. Zhai et al., *Chem. Soc. Rev.* **40**, 2986 (2011).
- [10] L. Zhu et al., *Chem. C* **3**, 2231 (2015).
- [11] T. Zhai, X. Fang, L. Li, Y. Bando and D. Golberg, *Nanoscale* **2**, 168 (2010).
- [12] F. Zhang, S. Niu, W. Guo, G. Zhu, X. Zhang and Z. L. Wang, *ACS Nano* **7**, 4537 (2013).
- [13] J. Jie, W. Zhang, I. Bello, C.-S. Lee and S.-T. Lee, *Nano Today* **5**, 313 (2010).
- [14] P. Broqvist, J. F. Binder and A. Pasquarello, *Appl. Phys. Lett.* **94**, 141911 (2009).
- [15] D. Kuzum et al., *IEEE Trans. Electron Dev.* **58**, 59 (2011).
- [16] P. Hidalgo, E. Liberti, B. Mendez and J. Piqueras, *J. Phys. Chem. C* **113**, 17200 (2009).
- [17] S. L. Shinde and K. K. Nanda, *CrystEngComm* **15**, 1043 (2013).
- [18] C. I. Wu and T. P. Hogan, *Mater. Res. Soc. Symp. Proc.* **940**, 13-04 (2009).
- [19] Z. Jiang et al., *Mater. Lett.* **59**, 416 (2005).
- [20] F. Bellenger et al., *IEEE Electron Device Lett.* **31**, 402 (2010).
- [21] A. Prakash et al., *Nanoscale Res. Lett.* **8**, 220 (2013).
- [22] Y. Kamata, *Mater. Today* **11**, 30 (2008).
- [23] A. V. Shaposhnikov et al., *Appl. Phys. Lett.* **100**, 243506 (2012).
- [24] Y. M. Lin, K. C. K, A. Heller and C. B. Mullins, *J. Phys. Chem. Lett.* **4**, 999 (2013).
- [25] Y. Son, M. Park, Y. Son, J. S. Lee, Y. Kim and J. Cho, *Nano Lett.* **14**, 1005 (2014)
- [26] X. Wang et al., *J. Am. Chem. Soc.* **133**, 20692 (2011).
- [27] Z. Zhan, L. Zheng, Y. Pan, G. Sun and L. Li, *J. Mater. Chem.* **22**, 2589 (2012).
- [28] S. W. Shin, K. Lee, J. Park and S. J. Kang, *ACS Appl. Mater. Interfaces* **7**, 19666 (2015).
- [29] M. Pelaez et al., *Appl. Catal. B Environ.* **125**, 331 (2012).



- [30] N. Zhou et al., *RSC Adv.* **5**, 29076 (2015).
- [31] A. Ghosh et al., *ACS Appl. Mater. Interfaces* **7**, 9486 (2015).
- [32] A. Ghosh, P. Guha, S. Mukherjee, R. Bar, S. K. Ray and P. V. Satyam (To be submitted, 2016).
- [33] Z. G. Bai et al., *Chem. Phys. Lett.* **303**, 311 (1999).
- [34] Y. Zhang, J. Zhu, Q. Zhang, Y. Yan and X. Zhang, *Chem. Phys. Lett.* **317**, 504 (2000).
- [35] Y. Su et al., *Mater. Lett.* **62**, 1010 (2008).
- [36] Z. Gu, F. Liu, M. P. Paranthaman and Z. Pan, *Cryst. Growth Des.* **9**, 35 (2009).
- [37] J. Q. Hu, Q. Li, X. M. Meng, C. S. Lee and S. T. Lee, *Adv. Mater.* **14**, 1396 (2002).
- [38] S. K. Wang et al., *J. Appl. Phys.* **108**, 054104 (2010).
- [39] A. Shalav, G. H. Collin, T. Kim and R. G. Elliman, *J. Mater. Res.* **26**, 2240 (2011).
- [40] K. Prabhakaran, F. Maeda Y. Watanabe and T. Ogino, *Appl. Phys. Lett.* **76**, 2244 (2000).
- [41] H. Wang and T. Wu, *Nanoscale Res. Lett.* **7**, 110 (2012).
- [42] T. Kawase et al., *Nanoscale Res. Lett.* **8**, 151 (2013).
- [43] T. Hino et al., *Appl. Phys. Lett.* **76**, 3421 (2000).
- [44] Y. Tian et al., *CrystEngComm.* **16**, 2317 (2014).
- [45] A. Ghosh et al., *J. Appl. Phys.* **110**, 033528 (2011).
- [46] C. Vieu et al., *Appl. Surf. Sci.* **164**, 111-117 (2000).
- [47] R. S. Wagner and W. C. Ellis, *Appl. Phys. Lett.* **4**, 89 (1964).
- [48] R. Shi et al., *J. Cryst. Growth.* **336**, 6-13 (2011).
- [49] Y. F. Zhang et al., *Phys. Rev. B* **61**, 4518 (2000).
- [50] S. K. Wang, H. G. Liu and A. Toriumi, *Appl. Phys. Lett.* **101**, 061907 (2012).
- [51] X. C. Wu, W. H. Song, Y. P. Sun and J. J. Du, *Chem. Phys. Lett.* **349**, 210 (2001).
- [52] M. C. Daniel and D. Astruc, *Chem. Rev.* **104**, 293 (2004).

- [53] A. Ghosh, R. R. Juluri, P. Guha, R. Sathyavathi, A. Dash, B. K. Jena and P. V. Satyam *J. Phys. D. Appl. Phys.* **48**, 055303 (2015).
- [54] M. Wu et al., *ACS Appl. Mater. Interfaces* **6**, 15052 (2014).
- [55] X. Lang, X. Chen and J. Zhao, *Chem. Soc. Rev.* **43**, 473 (2014).
- [56] S. Manna, S. Das, S. P. Mondal, R. Singha and S. K. Ray, *J. Phys. Chem. C* **116**, 7126 (2012).

# Chapter 8

## Summary and Conclusions

This thesis work is focused on the growth of two different wide direct band gap oxide semiconductor-metal (Au-ZnO and Au-GeO<sub>2</sub>) hetero-nanostructures (HNs) of various morphologies and oxygen defect densities, and their enhanced visible-light driven applications with modified properties. Because of high band gap (generally in the UV range) nature of these oxide semiconductor (OS) nanostructures (NSs), they don't respond well in the visible-light. In recent past, significant efforts have been devoted to improve visible-light driven activities of wide band gap OS NSs, through a time consuming and multistep chemical or physical processes and hence an expensive processes. In contrast, this thesis work demonstrate a novel *single step* Au catalyzed chemical vapor deposition (CVD) technique to grow various oxygen deficient Au capped ZnO and GeO<sub>2</sub> HN having efficient visible-light harnessing capabilities as well as prolonged lifetime of photogenerated electron-hole pairs. Possible mechanisms behind the growth of these Au-ZnO and Au-GeO<sub>2</sub> HN have been proposed and discussed in detail. In addition, several issues, which actively influence the growth of these HN, (via VLS and/or VS growth mode) such as, role of catalyst and its thickness, substrates type and orientations, native oxide on Si substrate, growth ambience and vapor pressure have been well addressed. These intrinsically self-assembled Au-ZnO and Au-GeO<sub>2</sub> HN are further utilized towards multifaceted applications, such as, robust SERS detection of CV molecule, photocatalytic degradation of hazardous organic pollutant under visible-light, electron field emission (FE) with tailored work function and visible-light photodetection. Visible-light driven activities towards above mentioned applications are documented with a detailed mechanism. Enhanced FE properties offered by Au-ZnO HN has been attributed to the reduction in work function due to the combined presence of oxygen vacancy and Au in them, probed by experiments and qualitatively supported by DFT calculations.

In this thesis, in the introduction, intrinsic properties of these two wide band gap oxide semiconductors (ZnO and GeO<sub>2</sub>) and their possible applications have been described. Introduction chapter also includes the motivation of the work being carried out for this thesis.

The working principles and instrumentations of all the major experimental techniques that have been used for the materials growth, characterization and their viable applications related to this thesis work were described in the next chapter.

A novel *single step* CVD technique has been discussed in chapter 3, towards the growth of Au-ZnO hetero-nanostructures (HNs) and only ZnO NSs of various morphologies, dimensions, alignment (randomly or vertically) and areal densities on Si and ZnO substrates. The effects of catalyst layer thickness, substrate type and orientation, position of the substrate and also native oxide on Si substrate on the Au-ZnO HNs growth has been discussed. Using detailed electron microscopy study, mechanisms involved in the formation of two different morphology HNs (nanowires  $\rightarrow$  NWs and triangular nanoflakes  $\rightarrow$  TNFs) grown simultaneously on native oxide Si substrates, have been proposed and discussed. NWs are uniform in diameter with six exposed surfaces, while TNFs are gradually tapered having triangular morphology with four exposed surfaces surrounded by  $\{1\bar{2}10\}$  and  $\{10\bar{1}0\}$ ; both the NW and TNF are grown along c-axis of wurtzite structure (i.e.,  $[0001]$ ). Similarly, vapor-solid (VS) mechanism is proposed for the growth of ZnO NSs on substrates where Au was deposited in MBE conditions on atomically cleaned Si surfaces (in UHV). So, controlling the interfacial oxide between catalyst layer and Si substrates, growth modes can be altered from VLS to VS or vice versa. It is also concluded that to grow vertically aligned Au-ZnO HNs using *single step* catalyzed CVD technique, minimum lattice miss-match substrate is the paramount requirement.

SERS activity of the intrinsically self-assembled faceted Au capped ZnO HNs (NWs and TNFs) coated Si substrates have been presented in chapter 4. As-grown HNs coated Si substrates are employed towards SERS detection of crystal violet (CV) molecule of  $1\ \mu\text{M}$  concentration in ethanol, with two excitation lines 514 nm (green laser) and 633 nm (red laser). These substrates are highly antireflective in nature in the wavelength range of 250 to 1000 nm. This exceptional light trapping can be attributed to the optical impedance matching ZnO layer in between air and Si substrate and also surface plasmon resonance absorption from tip faceted Au NPs. It is also observed that TNFs samples from each category (1 nm or 5 nm Au) have higher defect related visible emission compared to NWs samples owing to their higher exposed surface area (eight times higher surface area). A possible correlation between the antireflection property of the as-grown samples and their corresponding SERS enhancement factor has been suggested. These Au-ZnO HNs coated Si substrates yielded

high SERS activity for CV, implying their potential in SERS based detection of biomolecules.

The optical properties of Au-ZnO HNs of two morphologies NWs and TNFs have been studied using room temperature photoluminescence (PL), cathodoluminescence (CL) and XPS. From all optical studies, it has been found that Au-ZnO TNFs have much more oxygen vacancy related visible emission ( $\approx 520$  nm) compared to Au-ZnO NWs sample, along with sharp narrow FWHM near band edge (NBE,  $\approx 384$  nm). This higher amount of oxygen vacancy present in TNFs sample has been attributed to the larger average surface area (ASA) of TNF compared to NW ( $\text{TNF}_{\text{ASA}}/\text{NW}_{\text{ASA}} \approx 8$ ). These as-grown HNs/Si(110) substrates have been employed as photocatalyst for degradation of priority organic pollutants (rhodamine B and phenol) under visible-light illumination (100 Watt bulb,  $10 \text{ mW/cm}^2$ ). The Au-ZnO TNFs sample has showed one order of magnitude enhancement in photocurrent density following its one order less charge-transfer resistance ( $R_{\text{ct}}$ ) compared to NWs, resulting in  $\approx 5.3$  times higher photocatalytic degradation efficiency. Role of oxygen vacancies in conjunction with the presence of plasmonic Au NPs at the apex of HNs, towards visible-light driven activities have been proposed and discussed. This high photocatalytic property and robustness of the oxygen deficient Au-ZnO TNFs sample could endow its use in harnessing visible part of the solar spectrum towards the multidisciplinary applications.

Furthermore, electron field emission properties of these non-aligned Au-ZnO NWs and TNFs grown on Si(110) substrates have been demonstrated in chapter 6. Enhanced field emission properties with lower turn-on field ( $0.52 \text{ V}/\mu\text{m}$ ) and higher field enhancement factor ( $\approx 5.16 \times 10^5$ ) has been exhibited by TNFs sample compared to NWs sample having turn-on field ( $0.86 \text{ V}/\mu\text{m}$ ) and lower field enhancement factor ( $\approx 1.25 \times 10^5$ ). Here, focus is made on relating the field emission properties with experimentally determined local work function variation and comparing with the model DFT calculations. The DFT calculations along with the Kelvin probe force microscopy (KPFM), PL and XPS results, suggested that the enhanced field emission properties of Au-ZnO TNFs compared to NWs is probably due to the presence of very high oxygen vacancies in the TNFs, that facilitate easy electron tunneling via reduction in work function of ZnO. To the best of our knowledge, we report the highest field enhancement factors and lowest turn-on field, in particular for non-aligned ZnO nanostructures.

As a last part of this thesis, Au capped OS GeO<sub>2</sub> nano/micro-wires (N/MWs) has been grown on  $\approx 5$  nm Au coated native oxide Ge(100) substrate using a novel *single step* annealing method (Chapter 7). The role of ambience and the necessity of catalyst Au layer, as well as, optimum oxygen presence for the growth of Au-GeO<sub>2</sub> N/MWs have been studied via organized experiments. Plausible growth mechanism for the Au catalyzed growth of Au-GeO<sub>2</sub> N/MWs on Ge substrate without any supply of source from outside is proposed and discussed. In spite of having high bandgap of GeO<sub>2</sub>, the visible-light photodetection application of Au-GeO<sub>2</sub> N/MWs (first such applications) grown in Ar ambience following their lower reflectance and photoluminescence in the visible regime, has been explored. As-grown sample has offered a good photoresponse ( $\geq 10^2$ ) and significant responsivity (R) of  $\approx 0.07$  A/W with 17 % external quantum efficiency (EQE) at  $-2.0$  V applied bias upon visible-light illumination ( $\lambda = 540$  nm,  $0.2$  mW/cm<sup>2</sup>). Visible-light sensing of Au-GeO<sub>2</sub> N/MWs, has been understood by considering absorption of visible-light, induced by SPR of plasmonic Au nanoparticles (NPs) and high oxygen vacancies in GeO<sub>2</sub> N/MWs. Influence of plasmonic NPs at the tip of the as-grown Au-GeO<sub>2</sub> N/MWs, on photodetection became clear as the photoresponse for Au NPs decorated Au-GeO<sub>2</sub> N/MWs structures has got enhanced four times compared to non-decoration of Au. Au decorated Au-GeO<sub>2</sub> N/MWs sample has shown photoresponse of  $1.49 \times 10^3$ , responsivity of  $0.25$  A/W and EQE of  $\approx 60$  % that are four times higher in comparisons with non-decorated N/MWs.

Based on the present studies, following works are identified as future scopes in this area of research. It would be both fascinating and beneficial to generalize this *single step* growth technique for the growth of other wide direct band gap oxide semiconductor-metal hetero-nanostructures (HNs), with enhanced visible-light responses.